ADVERTIMENT. La consulta d’aquesta tesi queda condicionada a l’acceptació de les següents condicions d'ús: La difusió d’aquesta tesi per mitjà del servei TDX (www.tesisenxarxa.net) ha estat autoritzada pels titulars dels drets de propietat intel·lectual únicament per a usos privats emmarcats en activitats d’investigació i docència. No s’autoritza la seva reproducció amb finalitats de lucre ni la seva difusió i posada a disposició des d’un lloc aliè al servei TDX. No s’autoritza la presentació del seu contingut en una finestra o marc aliè a TDX (framing). Aquesta reserva de drets afecta tant al resum de presentació de la tesi com als seus continguts. En la utilització o cita de parts de la tesi és obligat indicar el nom de la persona autora.

ADVERTENCIA. La consulta de esta tesis queda condicionada a la aceptación de las siguientes condiciones de uso: La difusión de esta tesis por medio del servicio TDR (www.tesisenred.net) ha sido autorizada por los titulares de los derechos de propiedad intelectual únicamente para usos privados enmarcados en actividades de investigación y docencia. No se autoriza su reproducción con finalidades de lucro ni su difusión y puesta a disposición desde un sitio ajeno al servicio TDR. No se autoriza la presentación de su contenido en una ventana o marco ajeno a TDR (framing). Esta reserva de derechos afecta tanto al resumen de presentación de la tesis como a sus contenidos. En la utilización o cita de partes de la tesis es obligado indicar el nombre de la persona autora.

WARNING. On having consulted this thesis you’re accepting the following use conditions: Spreading this thesis by the TDX (www.tesisenxarxa.net) service has been authorized by the titular of the intellectual property rights only for private uses placed in investigation and teaching activities. Reproduction with lucrative aims is not authorized neither its spreading and availability from a site foreign to the TDX service. Introducing its content in a window or frame foreign to the TDX service is not authorized (framing). This rights affect to the presentation summary of the thesis as well as to its contents. In the using or citation of parts of the thesis it’s obliged to indicate the name of the author

Effects of flow control on Flow past Bluff bodies

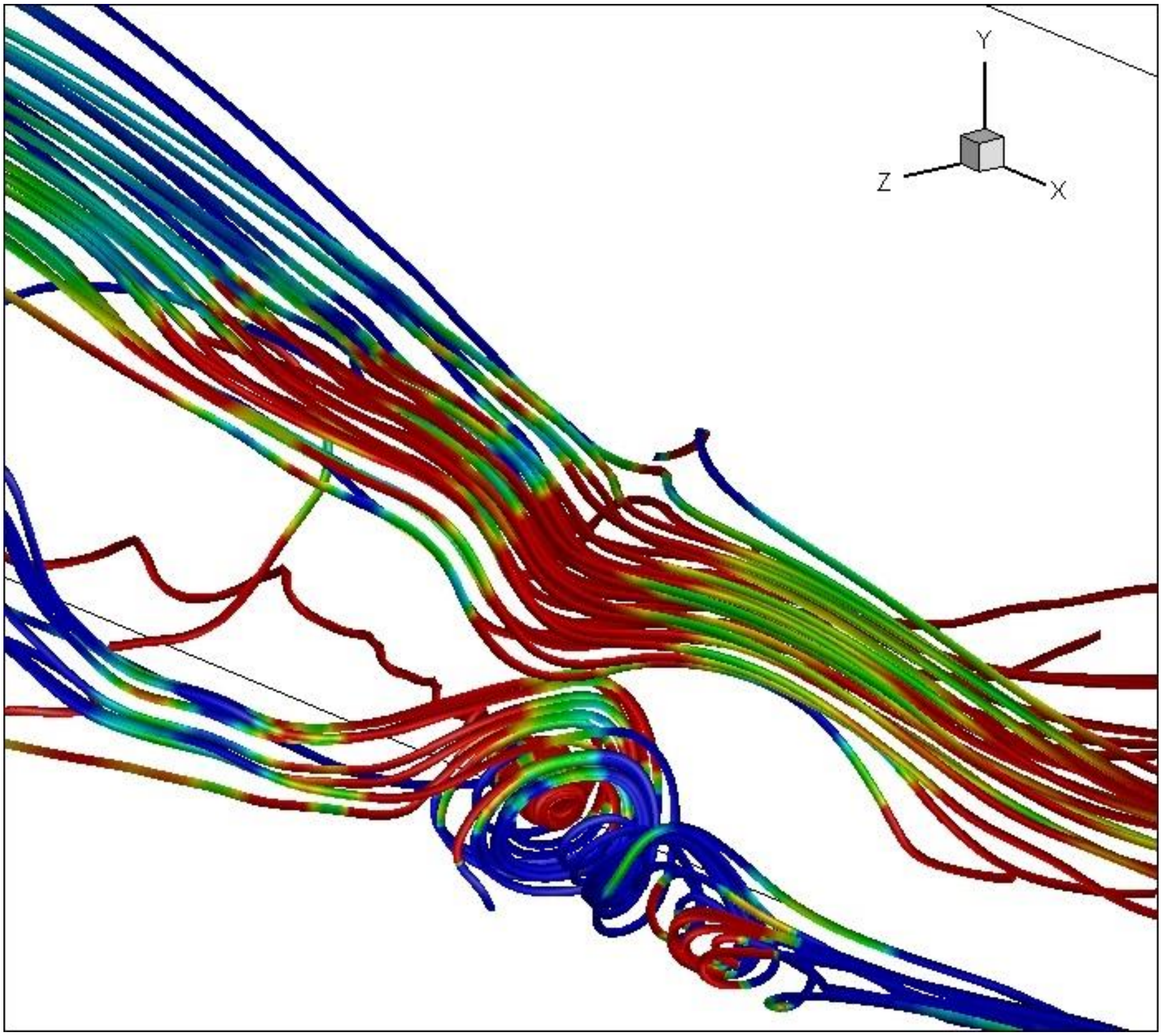

Ph.D. Thesis

Aditya Mushyam

Department of Fluid Mechanics

Technical University of Cataluña

Barcelona

Ph.D. thesis report submitted for a Doctorate degree with International recognition

Title: Effects of flow control on Flow past Bluff bodies

Author: Aditya Mushyam

ISBN: 978-84-617-5013-9

Thesis Supervisor: Dr. Josep M Bergada
Associate Professor
Department of Fluid Mechanics
Technical University of Cataluña
Barcelona

Table of Contents

Introduction

The aim of this Ph.D. thesis, **“Effects of flow control on flow past bluff bodies”** is to study and analyze the effects of Flow Control on various aspects and properties of flow past bluff bodies. Flow control techniques are presently researched and studied across the world to gauge their effectiveness in altering flow properties and patterns in different flow scenarios. The inspiration for the present work is derived from automobile industry, as analyzing the flow over backward step and inclined step shall help in understanding the characteristics of the rear vehicle wake. Since a considerable percentage of the energy needed to propel the vehicle is dissipated by the vorticity generated in the rear of the vehicle, hence it is of utmost importance to understand the properties of the wake. In the present study various possibilities were explored for application and examine effectiveness of active flow control techniques in bluff bodies to increase the aerodynamic efficiency. The primary aim of the study is to reduce the drag acting on bluff bodies by determining an effective active flow control technique and configuration. Two different kinds of Active Flow Control techniques have been used in this thesis namely, **“Zero Net Mass Flow Actuator”** and **“Fluidic Actuator”**. The characteristics of laminar and turbulent boundary layer were analyzed and the effectiveness of flow control in delaying the detachment of the boundary layer was analyzed. Numerical simulation programs were developed in C language for simulating various cases in the thesis and a **3D LES** turbulence modeling finite volume code was developed using **Smagorinsky-Lilly model** in C language for the simulating the flow over backward step in turbulence regime. All the numerical simulation codes were validated with previous research works.

The thesis is divided into five chapters analyzing flow over square cylinder, backward step and inclined step geometries in 2D and 3D in laminar and turbulent regimes. A brief introduction of each chapter is presented below.

Chapter 1 Wake and Mixing layer interaction of Flow past a Square Cylinder

The study of wake and mixing layer interactions was conceived as a case of passive flow control applied to flow over a square cylinder. Aim of the work is to simulate and analyse two dimensional flow past a square cylinder in laminar regime with an interacting mixing layer developed by an axis symmetrical horizontal splitter plate placed upstream of the square cylinder. Mixing layer is generated upstream of the square cylinder by mixing of two uniform flow streams of fluid with different velocities above and below the splitter plate. Observations made from the present study indicate that at low speed ratios, the vortices shed into the wake consists of both clockwise and anticlockwise moment vortices, but as velocity ratio increases only clockwise moment vortices were shed downstream and the anticlockwise vortices were shed as Kelvin-Helmholtz instabilities. In all simulations undertaken the same phenomena appeared independent of the upstream Reynolds number, therefore indicating that velocity ratio is a dominant parameter. Different instability modes were observed and were highly dependent on the upstream velocity ratio. A journal research paper has been published on this work. This is a first study to analyse wake and mixing layer interaction for flow over a square cylinder.

Chapter 2 Laminar flow over a Backward facing Inclined step

In this chapter, analysis of the two dimensional flow over a backward-facing-inclined step in laminar flow regime. An inclined step geometry was selected since the shape is similar to rear of an automobile and analysis of flow over an inclined step shall help in understanding the wake characteristics in the rear of vehicle. The inclined step simulations were carried out by varying different aspects of the geometry for a range of different Reynolds numbers. Critical Reynolds numbers for vortex shedding in the wake of different step inclinations were analysed. Among the conclusions it was found that inclination angle of 15^o was found to be the critical angle for vortex shedding, after which critical Reynolds number remains constant. This is the first time features of flow past an inclined step have been extensively investigated and a journal paper has been published.

Chapter 3 Effects of Active Flow Control on flow past Backward step

In this chapter, two-dimensional flow over a backward step in laminar flow regime with application of active flow control (AFC) technique is analyzed. Two Reynolds numbers of 500 and 800 were evaluated. A parametric non-dimensional analysis was carried out by varying the non-dimensional frequency from 0.005 to 0.1, jet non-dimensional amplitude was varied from 0.025 to 1. Four different positions of the groove were simulated; groove was respectively located at 1.976a, 1.953a, 1.928a and 1.903a, measured downstream from the left side upper edge, where a, is the step height. Three different non-dimensional groove widths of 0.023, 0.048 and 0.073 were also evaluated. It is observed, when using an AFC frequency ± 10% of the vortex shedding one, that maximum drag reduction was achieved. It is also observed that zero net mass flow actuators were more effective than fluidic actuators for drag reduction.

Chapter 4 Effects of Active Flow Control on flow over an Inclined step

In this chapter, two dimensional flow over a backward-facing-inclined step in laminar regime with application of active flow control (AFC) technique was analysed. Flow over an inclined step simulations with angle of inclination of 45^o and 65^o was simulated with application of AFC on the upstream surface to influence the boundary layer and analyze the effects on the downstream vortex shedding and flow properties. Parametric analysis of AFC was carried out by varying the frequency, amplitude, grove position and width to study their effects on the flow and to determine an optimal configuration to reduce the drag on the step and to suppress the vortex dissipation in the wake of the step. It was found that maximum reduction in the drag for an optimum configuration was between 10%-20% depending on the configuration of the AFC technique.

Chapter 5 3D flow over a Backward facing step with Active Flow Control

In this chapter, initially three dimensional flow over a backward facing step in turbulent regime is carried out at Reynolds number, Re=3200 to 1024000. The turbulent flow past backward step is modelled using LES based Smagorinsky-Lilly sub-grid scale model. The aim of the study is to resolve the stream wise vortex in the wake of the step and study its properties to determine optimal configuration for the implementation of AFC in a 3D backward step. It was found that the stream wise vortex formation was observed for Reynolds number, Re>=6400. Subsequently, analysis of the flow over a backward step with application of active flow control technique (AFC)is carried out. The effectiveness of active altering the ocurance of stream wise vortex in the wake of the flow control inbackward step is also studied. A confined flow geometry was chosen to limit the computational domain and to replicate the conditions of a wind tunnel.

Publications

- "A Numerical Investigation of wake and mixing layer interactions of Flow past a Square Cylinder", Mushyam, Aditya et. al. (*Impact Factor* 1.949) http://link.springer.com/article/10.1007/s11012-016-0400-8
- "A Numerical Investigation of Laminar flow over a Backward facing Inclined step", Meccanica (2016), Mushyam, Aditya et. al., Volume 51 Number 8:1739-176, ISSN 0025-6455, DOI 10.1007/s11012-015-0335-5. (*Impact Factor* 1.949)
- "Active Flow Control on Laminar flow over a Backward facing step", Mushyam, Aditya et. al., Journal of Physics-Conference Series, ICM-Square 2015, Volume 633, Conference 1. http://iopscience.iop.org/article/10.1088/1742-6596/633/1/012110
- "A Numerical Simulation of Fluid-Structure Interaction for flow through valves of a hermetic compressor with Immersed Boundary Method." (2012), Mushyam, Aditya et. al., International Compressor Engineering Conference. Paper 2139. http://docs.lib.purdue.edu/icec/2139.

In the process of Submission

- "Effects of Active flow control on flow past an Inclined Backward facing step"
- "3D-Flow over an Backward facing step with Active flow control" (In Preparation)

1

Wake and Mixing Layer interactions of Flow past a Square Cylinder

Abstract:

In the present chapter, interaction of two dimensional flow past a square cylinder in laminar regime with an upstream mixing layer developed by an axis symmetrical horizontal splitter plate is analyzed. Mixing layer is generated upstream of the square cylinder by mixing of two uniform streams of fluid with different velocities above and below the splitter plate. A range of upstream domain lengths, the distance between the splitter plate and the square cylinder, and several upstream velocity ratios between the two streams of fluid have been analyzed. Unconfined flow over a square cylinder placed in uniform upstream flow is initially analyzed as it plays a crucial role in understanding properties of the wake. The results are compared with existing literature to validate the code developed and they were found to be in very good agreement. It was observed from the present study that at smaller velocity ratios, the vortices shed into the wake consists of both clockwise and anticlockwise moment vortices. As velocity ratio is increased only clockwise moment vortices were shed downstream and anticlockwise vortices were shed as Kelvin-Helmholtz instabilities. In all simulations undertaken the same phenomena was observed independent of the upstream Reynolds number, indicating that velocity ratio is a primary parameter influencing the flow. Different instability modes were observed and they were highly dependent on the upstream velocity ratio.

Nomenclature:

a	Side of the square cylinder	
A	Dimensional side of the square cylinder	[m]
C_D	Drag coefficient	
C_L	Lift coefficient	
f	Dimensional frequency	[Hz]
F_D	Dimensional drag force	[N]
F_f	Flux through face f of the control volume	
F_L	Dimensional lift force	[N]
H	Height of the domain	
L	Length of the domain	
$\hat{n}$	Outward normal of the surface S	
p	Non dimensional Pressure	
r	Ratio of Reynolds number above and below the splitter plate	
Re	Reynolds number	
S	Surface onto the control volume	
St	Strouhal number	
spl	Length of the flat plate	
t	Non-dimensional Time	
ul	Upstream Length of the physical domain	
dl	Downstream length of the physical domain	
u	Non-dimensional Velocity in X direction below the splitter plate	
U	Free stream velocity in X direction at the inlet below the splitter plate	[m/sec]
v	Non-dimensional Velocity in Y direction	
$\forall$	Control Volume	
x	Non-Dimensional Eulerian coordinates in horizontal direction	
y	Non-Dimensional Eulerian coordinates in vertical direction	
ρ	Fluid density.	[Kg/m^3]
μ	Fluid viscosity	[Kg/(m s)]

1.1. Introduction.

Introduction is divided and presented in four sections. Initially basic research on flow around circular cylinders is presented. In the second section few prominent research works carried out on flow over square cylinder placed in uniform flow is introduced. Due to the presence of shear in the present study, in third section, vortex shedding characteristics of square cylinder placed in plane shear flow are presented. Lastly, an introduction of research carried out with application of passive flow control on square cylinders is described.

1.1.1 Background Study of flow past circular cylinders.

Flow past bluff bodies, especially cylinders, has been studied extensively. Majority of these studies were performed on circular cylinders in free flow conditions. Excellent reviews on this topic were written by Williamson (1996) and Zdravkovich (1997). The flow around a circular cylinder can be taken as a representative case for the flow around a bluff body. It is a quite complex problem because the flow will not follow the circular cylinder completely, but separates from it and creates wakes. As a result, there are three components in this flow:

a boundary layer, a separating free shear layer and a wake. The generation and shedding of large coherent vortex structures due to flow separation makes the flow around the circular cylinder very difficult to predict. For more than a century, a great number of studies have focused on it. As early as 1912, the milestone for circular cylinder wakes was first established by Von Karman, not only for finding the stability of vortex-street configurations, but also for finding a theoretical link between the vortex-street and the drag acting on the body. In 1954, Roshko first observed the existence of a transition regime in the wake of the circular cylinder. He reported that there exist three different regimes of the flow at low to moderate Reynolds number, which are the laminar, transition and irregular turbulent regime. To characterize these transition regimes and discover their mechanism, many parameters have been traditionally measured, some of them being the Strouhal number, the lift and drag coefficients, the base pressure, the pressure coefficient, the separation points, the surface shear stresses, the recirculation length and the wake velocity.

Vortex shedding around circular cylinders and the Karman vortex street behind it has been the object of numerous experimental and numerical studies because of the fundamental mechanisms that this flow exhibits and its numerous industrial applications. The flow separation and the periodic vortex shedding of the fluid flow from the structures produce fluctuating drag and lift forces on the structures and may cause structural damage under certain unfavorable conditions. The classical view of a vortex street in cross section (2D) consists of regions of concentrated vorticity shed into the downstream flow from alternate sides of the body and with alternate sense of rotation, giving the appearance of an upper row of negative vortices and a lower row of positive vortices. This alternate shedding of vortices in the near wake leads to large fluctuating pressure forces in a direction transverse to the flow and may cause structural vibrations, acoustic noise or resonance. In each shear layer, the instabilities lead to vortex-sheet roll-up. Thus, each sheet can be modeled as an infinite train of co-rotating vortices. Excellent reviews of vortex induced oscillations of bluff bodies were provided by Bearman (1965), (1967) and Williamson (1996), the work presented in Gerrard (1978) clarifies the different regions where discontinuities are likely to appear. Even in well behaved steady laminar flows past bluff bodies, various disturbances develop in the wake and shear layer due to which induced instabilities having time periodicity give rise to formation of periodic vortex street in the wake. In 1996, Williamson discovered the appearance of vortex dislocations and observed two modes of formation of stream-wise vortices in the near wake, which are related to the three-dimensional transition when the Reynolds number ranges from 180 to 260.

1.1.2 Flow past square cylinder with uniform upstream flow.

The analysis of flow around a rectangular/square cylinder is of practical interest since it constitutes a generic configuration with many applications in fields such as nuclear engineering, external aerodynamics and environmental sciences. As an example, mixing properties in heat exchangers play a key role in thermal hydraulic problems related to power plants. Another example is the reduction of aero-acoustic sources generated by the rear-view mirror in car design. A third direct application is the scalar diffusion around buildings and the effect on atmospheric pollution mixing. There exists a non-exhaustive list of practical applications in the field of both engineering and geophysical flows where turbulent wakes interact strongly with the integral scales of the problem to tackle.

Studies on the problems of wake development and vortex shedding behind a rectangular/square cylinder in free-stream flows have been investigated both numerically and experimentally among others by, Franke (1991), Franke et al. (1990), Kelkar and Patankar (1992), Davis and Moore (1982), Davis et al. (1984), Okajima (1982, 1990), Okajima et al (1992), Mukhopadhyay et al. (1992) and Suzuki et al. (1993). Sohankar et al (1998) numerically studied the effect of incidence angle. Owing to fixed separation points for sharp-edged bodies, it is generally accepted that aerodynamic coefficients are less dependent on the Reynolds number than for circular structures.

Depending on the Reynolds number, different flow regimes can be distinguished for a square cylinder, Franke (1991). For example in the case of square cylinder in uniform cross flow, at very low Re, (Re < 1), viscous forces dominate the flow, the flow is laminar and steady, for this creeping flow, no separation takes place at the surface of the cylinder. The behavior of such flows, when Re is increased, undergoes a sequence of well-established bifurcations. With the Reynolds increase, the flow separates from the trailing edge but remains steady and laminar up to Re of about 50, a closed steady recirculation region consisting of two symmetric vortices is observed behind the body, the size of the recirculation region increases with the Reynolds number increase.

Different values of the critical Reynolds number exist in the literature. Based on experimental investigations, Okajima (1982) working with rectangular cylinders, found periodic vortex motion at Re=70. A smaller value of critical Reynolds for periodic vortex motion of Re=54 was determined by Kelkar and Patankar (1992) based on a stability analysis of the flow, they studied unconfined flow past a square cylinder.

When this critical Reynolds number is exceeded, flow undergoes Hopf bifurcation, localized regions of high vorticity are shed alternatively from either side of the cylinder and are convected downstream, the well-known Von Karman vortex street with periodic vortex shedding from the square cylinder is to be detected in the wake, flow is still laminar and 2-D, flow separates at the leading edges of the cylinder. With a further increase of the Reynolds number, the flow undergoes a further bifurcation at around Re = 150–200, Sohankar et al (1999), and becomes three-dimensional but remains time periodic. In reality, the onset of this phenomenon is not clearly defined in the literature, Okajima (1982) and Franke (1991), define a range of Re=100 to 150 for the 3D bifurcation to appear.

Luo et al (2003), (2007), experimentally studied the transition phenomena generated by uniform flow onto a square cylinder. They found two instability modes similar to the ones found by Williamson (1996) in circular cylinders. The modes being clearly differentiated in a St-Re graph. They found mode A appeared at Re=183, being the spanwise wavelength of 5.1D, mode B appeared at about $\mathrm{Re} = 204 \pm 5$, the wavelength associated was about 1.2D. As previously found by Robichaux et al (1999), they observed that as Reynolds increased, the downstream wavelength decreased. By further increasing the Reynolds number, the flow became chaotic and eventually transition to turbulence occurred. Recently, Sau (2009) numerically studied 3D flow performance around a square cylinder, clarifying the physical details of the bifurcation mechanism. It was observed that at Re=100 and even at Re=60 the flow exhibited three dimensional structures originated by spanwise pressure gradients and a clear flow asymmetry was observed at Re=200.

1.1.3 Flow over a square cylinder in planar shear flow.

For investigating the effect of velocity gradient, the simplest case is a uniform shear flow, which has a linear distribution of the longitudinal velocity component along the transverse direction. Practical situations of uniform shear flow may involve obstacles located close to a wall, e.g., flow past a suspension bridge or pipelines near the ground or water surfaces, flow past heat exchanger tubes near walls, etc. The vicinity of a wall can have a distinct influence on the vortex shedding. When there is a gap between the cylinder and the wall, the onset of vortex formation occurs at a critical gap height.

It has been reported by past investigations on circular cylinders, e.g., Jordan and Fromm (1972), Kiya et al. (1980), Kwon et al. (1992), Mukhopadhyay et al. (1999), Xu and Dalton (2001), Sumner and Akosile (2003), that the flow approaching with linear shear greatly altered the vortex dynamics in the wake when compared to the uniform flow case. They attributed this phenomena to the constant vorticity embedded in the free-stream. For square-sectional cylindrical bodies, shear effects have been reported by, e.g., Ayukawa et al. (1993), Hwang and Sue (1997), Saha et al. (2001), Bhattacharyya and Maiti (2004), Cheng et al. (2005, 2007), Lankadasu and Vengadesan (2008). Ayukawa et al. (1993), conducted experiments and performed discrete vortex simulations at Re=4000. They observed that with high shear parameters the flow became self similar downstream of the cylinder. Saha et al. (2001) studied numerically the same problem for a wide range of Reynolds numbers. They showed that due to influence of shear, Karman Vortex Street mainly consisted of clockwise vortices, whose decay was very slow when compared to that of uniform flow. Their studies were limited to low shear parameters and with high blockage ratios. Cheng et al. (2005, 2007) reported that vortex shedding disappeared for large shear parameters. The mean lift and drag coefficients tended to decrease with increasing the shear parameter. They observed that the vortex shedding frequency tended to decrease with the increase of the shear parameter, although they highlighted that this observation was opposite to the one obtained by Kiya et al. (1980) when studying shear flow past circular cylinders. Lankadasu and Vengadesan (2008) also reported a decrease of mean lift and drag coefficients with the increasing shear, for a given Reynolds number. The same phenomenon was observed for a given shear and when Reynolds number was increased. It was also found that the critical Reynolds number at which the flow becomes unsteady periodic, was reduced as shear increased. Bhattacharyya and Maiti (2004) studied laminar shear flow past a square cylinder placed nearby a wall, Reynolds up to 1400. For a gap height of 0.25 times the square cylinder height, vortex shedding suppression and steadiness of the wake was observed up to a Reynolds 250. For a Reynolds number equal and above 500, only negative vortices behind the cylinder at closed proximity to the wall were found.

Hwang and Yao (1997) studied the vortex shedding from a square cylinder in the presence of a thick wall boundary layer in laminar Reynolds number range. In their study the minimum thickness of the wall boundary layer was taken to be 0.8 cylinder height. They found that the vortex shedding was suppressed and the wake behind the cylinder became stationary when the gap between the cylinder and the wall was 0.5 times the cylinder height. Bhattacharyya and Maiti (2006) investigated as well laminar flow over a square cylinder placed nearby a wall, Reynolds <1500. They found that the critical gap height for vortex shedding suppression was dependent on the Reynolds number.

Experimental and numerical studies on high Reynolds number turbulent flow around a square cylinder placed at various heights above a wall were carried out among others by Bosch et al (1996), Bosch and Rodi (1996, 1998), Liou et al (2001) and Wang and Tan (2008). Bosch et al (1996) observed through experimental studies that irregular or intermittent vortex shedding appeared for gap heights just larger than the gap height where complete suppression of vortex shedding occurs. Liou et al (2001), presented a three-dimensional large eddy simulation of the turbulent wake behind a square cylinder placed nearby a wall. Their results showed that, due to the interaction with the wall boundary layer, the celerity of the positive vortex shed from the lower side of the cylinder was smaller than the one shed from the upper side. In all the above studies the Reynolds number which is based on the cylinder height were considered to be of order $O(10^4)$.

1.1.4 Effect of blockage ratio on the flow past square cylinder.

Studying the influence of confining walls on the flow phenomena around square cylinders, also clarifies the effect of shear flow on vortex shedding. Some of the studies in this field are, Davis and Moore, (1982), Davies et al (1984), Mukhopadhyay et al. (1992), Okajima et al (1992), Suzuki et al. (1993), Li and Humphrey (1995), Sohankar et al (1998), Breuer et al (2000), Scarano et al (2009), Islam et al (2012). In comparison with the free flow case, two new parameters have to be taken into account, the inflow profile and the blockage ratio. As presented by Davis et al. (1984), the vortex shedding frequency depends strongly on the inflow profile. In the experimental investigations on circular cylinders by Shair et al. (1963) and on square cylinders by Davis et al. (1984), non-negligible deviations between the velocity profiles far upstream of the cylinder and the parabolic distribution expected for fully developed laminar channel flow were observed. Therefore, this aspect has to be kept in mind for comparison between experimental and numerical investigations which typically apply the theoretical uniform velocity profile as inflow conditions. The second parameter which plays a dominant role in the confined cylinder flow is the blockage ratio of the channel, defined as B=D/H, where D is the diameter of the circular cylinder or the square cylinder side, and H is the channel height.

Suzuki et al. (1993) studied numerically the effect of wall blockage on onset of vortex shedding for the Reynolds number range ($56.3 \leq \mathrm{Re} \leq 225$) and blockage ratios ($\mathrm{BR} = 1/20 - 1/5$). They found that the onset of vortex shedding for flow past square cylinder was delayed with increasing blockage ratio. For a blockage ratio BR=1/5, they computed Strouhal number over a wide Re range and found a maximum Strouhal number at $\mathrm{Re}=\mathrm{Re}_{max}=150$. This study was the first to report the interesting phenomenon showing that for higher blockage ratios ($BR>0.4$) onset of vortex shedding gets preponed.

The widely referred work of Davis et al. (1984) investigated experimentally and numerically, the confined flow past square cylinders for a wide range of Re (Re = 100-1850) and two different blockage ratios (BR= 1/6 and 1/4). Inlet velocity distribution was having a parabolic profile. They found that the presence of confining walls leaded to a drag and Strouhal number increase. Depending on the blockage ratio, a maximum Strouhal number was observed at $\mathrm{Re}=\mathrm{Re}_{max}=200$ to 350. For higher values of Re the Strouhal number decreased again and reached an almost constant level. The computations were based on a finite-volume code and non-equidistant coarse grid of 76x52 grid points.

Two-dimensional laminar numerical simulations on square cylinders were also carried out by Mukhopadhyay et al. (1992) for the Re range of 90-1200, two blockage ratios (BR= 1/8 and 1/4) and a parabolic inflow profile. With respect to the Reynolds number of the corresponding channel flow, the upper limit of Re in this investigation seems to be questionable because a turbulent flow in the channel has to be expected under these conditions. Then according to Okajima et al (1992) when Re>1000 and Scarano et al (2009) when Re>1080, flow should be considered as turbulent. In fact, considering the research undertaken by Luo et al (2003) and Sau (2009), it can be concluded that three dimensional structures are likely to appear at Reynolds numbers as low as 100. It is generally accepted that for a fixed Reynolds number, an increasing blockage ratio leads to an increase in the Strouhal number. This holds true for both circular and square cylinders, although the displacement of the separation points cannot be responsible for this phenomenon for a sharp-edged body as assumed for a round geometry.

1.1.5 Flow past square cylinder with passive flow control.

There are typical situations, where the non-uniformity of the approaching flow is due to the effect of a body located in front or behind the one to be studied. For example, when a small cylinder is placed in the separated shear layer of a large main cylinder to alter the vortex shedding phenomena behind the main cylinder, the small cylinder is inevitably subjected to the effect of shear induced from the large cylinder. Onset of periodic flow from the small cylinder induces oscillatory forces on the body, which may trigger flow-induced vibrations, and in turn alter the vortex shedding on the main cylinder.

Some of the latest most relevant numerical simulations of flow past a square cylinder with the incorporation of a control plate to alter the wake, which is having similarities to the present study were carried out among others by Sudhakar and Vengadesan (2012), case circular cylinder, Lesage and Gartshore (1987), Sakamoto et al (1991), (1997), Zhou et al (2005), Doolan (2009), Sukri et. al. (2011), (2012), and Malekzadeh and Sohankar (2012) and Salinas et al (2014). Some of these studies are presented below.

Sudhakar and Vengadesan (2012), studied numerically in 2D the vortex shedding characteristics of a circular cylinder with an attached oscillating splitter plate located at the cylinder trailing edge. The flow was investigated at a Reynolds number, Re=100. The splitter plate attached in the wake of the circular cylinder was forced to exhibit harmonic oscillations about its attachment point. In order to simulate the oscillating movement a fixed mesh strategy using the immersed boundary method was used to impose the boundary conditions on the body surface. Complex interactions between the vortices shed from the splitter plate and the cylinder were found in the wake and three different patterns of vortex shedding were reported to occur in the wake of the circular cylinder depending on the frequency and amplitude of plate oscillation, namely normal shedding, chain of vortices and shedding from splitter plate. It was reported that the inverse relationship between the vortex formation length and Strouhal number is not applicable when the splitter plate is subjected to oscillation.

Sukri et.al. (2011), carried out a 2D numerical study for flow over a square cylinder with and without a splitter plate at Reynolds number, Re=150. The splitter plate was stationary and attached to the square cylinder trailing face. In order to investigate the flow sensitivity with respect to the splitter plate, the length of the splitter plate was varied from, L=0.5D to L=6D, where D is the side of the square cylinder. Strong hydrodynamic interactions in the near wake of the cylinder were induced by the splitter plate and the length of the plate was found to affect significantly the flow structure. In the study, flow behavior was categorized into three different modes based on the length of the splitter plate, first mode was occurring for splitter plate lengths in the range of $0 \leq L \leq D$, it was observed that the free shear layers were convected further downstream before rolling up and the Strouhal number was decreasing as the plate length was increased. When the length of the splitter plate, L was increased to 1.25D a sharp increase in the Strouhal number was found indicating the onset of new mode. A second mode appeared, for intermediate lengths of the splitter plate in the range of $1.25D \leq L \leq 4.75D$, a secondary vortex was reported to be seen around the trailing edge of the splitter plate and the shear layers began to roll up closer to the trailing edge. The Strouhal number is this mode was first increasing with the increase in length of the splitter plate until L=2D before decreasing with the increase in the length of the splitter plate until L=4.75D. When the length of the splitter plate increased from 4.75D to 5D a sudden decrease in the Strouhal number was found, indicating the onset of the third mode, for long plate lengths $L \geq 5D$. It was observed, that the free shear layers reattached to the splitter plate and the Strouhal number remained constant with the increase in length of the splitter plate. Finally the study also proposed the minimum wake half-width as the length scale for a possible universal Strouhal number, which was found to be valid for $0 \leq L \leq 4D$.

In Sukri et.al. (2012), a 2D numerical study of the square cylinder wake alteration using a detached downstream thin flat plate was carried out. A uniform upstream flow with constant Reynolds number Re=150, based on the side length of the cylinder D, was used. Different detached splitter arrangements were simulated by varying the square cylinder splitter plate gap distance (G) along the wake centerline in the range $0 \leq G \leq 7D$ for a constant plate length, L=D, to investigate the variation in the flow features of the near wake flow structure to the downstream position of the plate. A critical gap distance of G_C=2.3D was reported at which the transition into a different flow mode was observed, indicating the existence of two flow modes. Mode I was characterized by the completion of the vortex formation occurring downstream of the gap but for mode II, formation was found to be occurring within the gap. During the transition between the two modes sudden changes in the integral properties were observed and the plate was found to have no effect on the formation of the Von-Karman vortex street for a gap $G \geq 5.6D$. With the aim to achieve total lift cancellation, the plate length was reduced and was found that for a plate length of L=0.26D at G = 5.6D downstream of the square cylinder, a significant reduction in the lift fluctuation of the system was obtained although a total lift cancellation was not observed. There reason behind non-occurrence of the total lift cancellation was identified as the loss of the sinusoidal form of the fluctuating lift signal of the plate due to plate stall.

Malekzadeh and Sohankar (2012), performed a 2D numerical investigation to reduce the fluid forces acting on a square cylinder in laminar flow regime via using passive control. They used a flat plate located upstream of the cylinder, the inlet flow was uniform. The Reynolds numbers based on the side length of the square cylinder, D and the inlet flow velocity was varied in the range of 50 ≤Re≤200. The width of the control plate, h was varied from 0.1D≤h≤0.9D and the distance between the control plate and the square cylinder, S was chosen within the range of 1.1D≤S≤7D. The different flow patterns and fluid forces magnitude reduction were studied for various arrangements of the control plate and square cylinder to determine the optimum arrangement in the given range of h and S. The results of the heat transfer from the square cylinder in the presence of a control plate were also presented at a constant Reynolds number, Re=160 and Prandtl number, Pr=0.71 for 1.1≤S≤7D and 0.5≤h≤0.9D. It was reported that the optimum distance plate-cylinder and the control plate width, were respectively 3D and 0.5D. Under these conditions, maximum reduction of the fluid forces and minimum reduction of the heat transfer was observed. Three different flow modes were discovered at this Reynolds number, the vortex shedding from the control plate was completely suppressed in modes I and II, in mode III the Karman vortex street was generated behind the control plate and cylinder. Independent of the flow mode, the incorporation of the control plate significantly reduced the mean and fluctuating fluid forces on the cylinder. This reduction was much higher in mode II. A sudden increase in the flow quantities like the lift and drag was observed at the critical distance for each control plate width. It was also found that the total Nusselt number of the cylinder in the presence of the control plate decreased for different gap spacing's, except for S/D = 1.1.

In Salinas et al (2014), a LES 3D numerical analysis of a square cylinder with a vertical flat plate placed upstream was presented. The plate height was varied between 0.2 to 1D and the distance between plate and cylinder varied from 0.5 to 3D while the Reynolds number was maintained constant at 650. Three different flow configurations were observed, in the first one, two quasi stationary symmetric vortices were formed between the two bodies. The second configuration was characterized by asymmetric vortices appearing between the plate and the square cylinder. The appearance of fully developed turbulence in the wake behind the plate, defined the third configuration.

It can be concluded from the literature review that, the incoming flow profile has a primary effect on the bluff body vortex shedding. The effect of placing a bluff body nearby a wall is similar to flow over a bluff body in a planar shear flow. Several modes of shedding oscillation have been observed which are dependent on the degree of the plane shear in the upstream flow.

The use of passive flow control drastically changes bluff body wake profiles and often decreases static and dynamic lift and drag forces acting on them. Wake oscillation modes are highly dependent on passive flow control techniques. The analysis of wake and mixing layer interactions presented in this chapter by generating a mixing layer upstream of the square cylinder using a splitter plate to interact with the wake. Mixing layer intensity depends on the velocity ratio of the flow above and below the splitter plate. The flow in the present case cannot be considered plane shear, but it can be considered as passive flow control.

The rest of the chapter is organized as follows: the description of the physical domain and the numerical strategy adopted are presented in section 2, Code validation and grid refinement study are introduced in Section 3. Results and discussion are presented in section 4.

1.2. Problem Statement.

1.2.1 Physical and computational domains.

Figure 1.1 presents the physical domain with square cylinder and the splitter plate placed upstream of the cylinder. The computational domain consists of a two-dimensional square cylinder of non-dimensional side length, a. Inlet boundary consists of two uniform fluid streams of different velocities above and below the splitter plate, as seen in figure 1.1. The ratio of velocities above and below the splitter plate is defined as velocity ratio, r. The computational domain length, L and height, H considered as 32 times and 16 times the square cylinder length, as seen in figure 1.1.

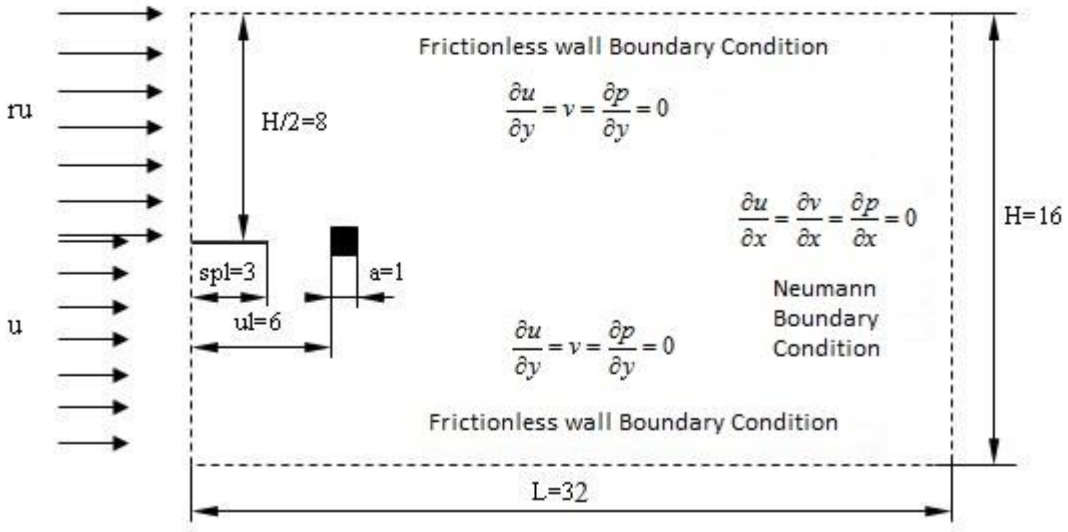

Figure 1.1: Physical Domain of the Inclined Step

According to Sohankar et al (1998), when using Neumann boundary conditions, a minimum downstream length of 20 times the square cylinder side length is required to isolate the effects of outlet boundary on the flow and wake properties. In the present study a downstream length, dl=25a units was considered for all cases simulated.

A frictionless wall boundary condition is applied for the top and bottom boundary of the physical domain as presented in figure 1.1. In Sohankar et al (1995), flow past a square cylinder was analyzed with frictionless wall boundary conditions with a blockage ratio of 7%, which converts to a physical domain height slightly higher than 14 units. It was observed that the boundary conditions above and below were not adversely affecting the flow behavior.

Yoshida et al (1993) when studying unconfined flow past a square cylinder used a height of 16 units for the physical domain and reported that boundary conditions had no effect on the flow. Therefore for the present study, physical domain height was considered as 16 units to make the flow independent of boundary conditions at the top and bottom of the physical domain. Three different upstream lengths, ul, the distance between inlet and the square cylinder leading edge were studied, considering ul=5a, 6a and 7a. For all cases a constant splitter plate length, spl=3a was considered in order to facilitate the development of laminar boundary layer. Splitter plate thickness was considered to be negligible.

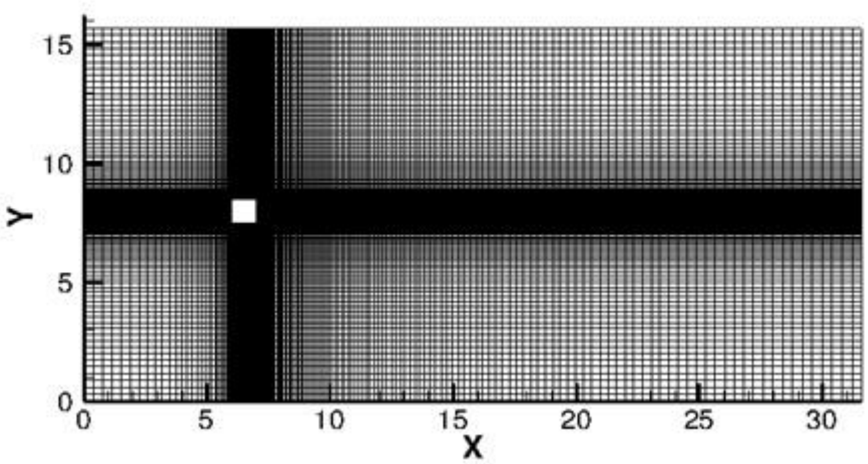

2a.

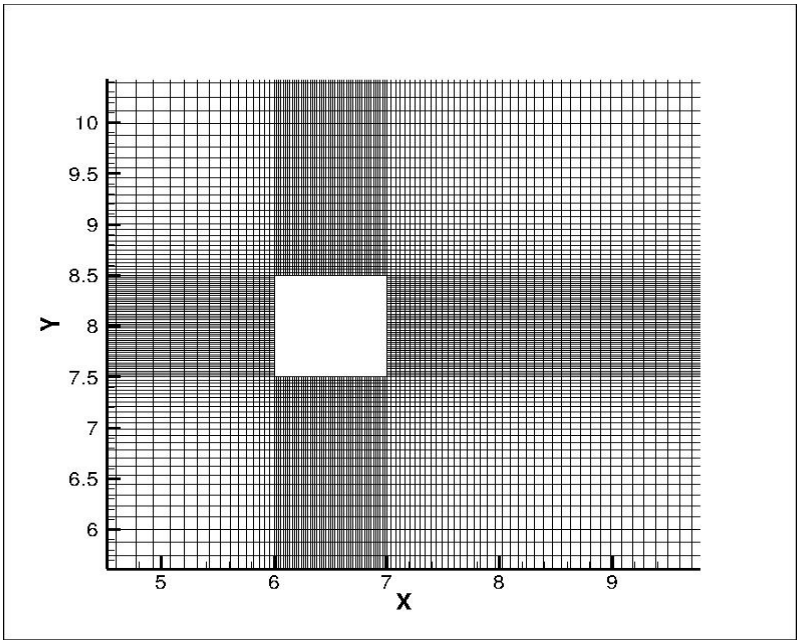

2b.

Figure: 1.2a. Non uniform structured grid for discretization of the domain. 2b. Closer view of the grid point collocation at the wall of the step for accurate resolution of the boundary layer.

Figures 1.2(a), (b), present the grid of the proposed problem, an orthogonal non uniform structured grid was chosen, since it is the most appropriate domain decomposition to resolve the flow dynamics near solid boundaries of the square cylinder and the splitter plate. Figure

1.2(a), clearly shows the four sub domains used to generate the grid. The first sub domain is the region upstream to the square cylinder which includes the horizontal splitter plate. Second and third sub domains are the regions located just below and above the square cylinder respectively. The region downstream of the square cylinder is the fourth sub domain. Non-uniform structured grid has been generated in the four sub-domains using the stretching transformation proposed by Roberts (1971), which refines the grid in the vicinity of the solid walls

1.2.2 Governing Equations.

Non-dimensional form of governing equations have been used to simulate the flow. To non dimensionalize the equations, side of the square cylinder, A, was taken as the characteristic length, the free stream velocity under the splitter plate at the inlet, U, was considered as the characteristic velocity, characteristic pressure was ρU^2 and characteristic time was defined as characteristic length divided by the characteristic velocity, A/U. Reynolds number, Re was defined as $\mathrm{Re} = \frac{\rho U A}{\mu}$. Fluid density, ρ and viscosity, μ were considered to be constant. Flow was regarded as isothermal.

The non-dimensional conservative form of the momentum and continuity equations for laminar flow in two dimensions:

$$\frac{\partial u}{\partial t} + \frac{\partial uu}{\partial x} + \frac{\partial vu}{\partial y} = -\frac{\partial p}{\partial x} + \frac{1}{\mathrm{Re}}\left(\frac{\partial^2 u}{\partial x^2} + \frac{\partial^2 u}{\partial y^2}\right) \tag{1.1}$$

$$\frac{\partial v}{\partial t} + \frac{\partial uv}{\partial x} + \frac{\partial vv}{\partial y} = -\frac{\partial p}{\partial y} + \frac{1}{\mathrm{Re}}\left(\frac{\partial^2 v}{\partial x^2} + \frac{\partial^2 v}{\partial y^2}\right) \tag{1.2}$$

$$\frac{\partial u}{\partial x} + \frac{\partial v}{\partial y} = 0 \tag{1.3}$$

Where u and v are non-dimensional velocity components in X and Y direction and p is the non-dimensional pressure. x and y are non-dimensional Eulerian coordinates in X and Y direction respectively. The non-dimensional time is denoted by t. A Finite volume approach was chosen for the simulation.

1.2.3 Numerical Strategy and Boundary Conditions.

A second-order Adams Bashforth-Crank Nicholson scheme for temporal discretization was applied to Navier Stokes equations in finite volume formulation to obtain equation (1.4). Equation (1.5) is the continuity equation applied over a control volume.

$$\frac{u_{i,P}^{n+1} - u_{i,P}^{n}}{\Delta t}\forall_P + \left(\frac{3}{2}\sum_f F_f^n u_{i,f}^n - \frac{1}{2}\sum_f F_f^{n-1} u_{i,f}^{n-1}\right) = -\sum_f p_f^n S_{f,i} + \frac{1}{2\,\mathrm{Re}}\left(\sum_f F_{dfi}^{n+1} + \sum_f F_{dfi}^{n}\right) \tag{1.4}$$

$$\sum_f F_f^{n+1} = 0 \tag{1.5}$$

Where F_f represents the flux through the face f. Subscript P represents the center of the control volume with volume, $\forall$.

The boundary conditions used in the simulation were depicted in figure 1.1, a brief description of the different boundary conditions follows.

At the inlet, free stream condition for velocity and Neumann boundary condition for pressure were used. Equation (1.6) was used below and equation (1.7) was used above the splitter

$$u = u,\ v = 0,\ \frac{\partial p}{\partial x} = 0 \tag{1.6}$$

$$u = ru,\ v = 0,\ \frac{\partial p}{\partial x} = 0 \tag{1.7}$$

A no-slip boundary condition was applied on solid boundaries as presented in equation (1.8)

$$u = 0, v = 0 \text{ and } \nabla p.\hat{n} = 0 \tag{1.8}$$

Where $\hat{n}$ is the unit normal vector perpendicular to the surface.

At the far field, since in the present study flow past a square cylinder is unconfined, a frictionless wall boundary was considered at a distance 8a measured from the center of the square cylinder as shown in figure 1.1

$$\frac{\partial u}{\partial y} = 0 \text{, v=0 and} \frac{\partial p}{\partial y} = 0 \tag{1.9}$$

The outlet boundary is of paramount importance when studying flows with unsteady wake or convecting vortices, since it not only changes the flow pattern but also affects convergence. In the present case the derivative of all dependent variables was taken equal to zero, which is known as the Newman boundary condition (NBC), as presented in equation (1.10).

$$\frac{\partial \phi}{\partial x} = 0,\ \phi = u, v, p \tag{1.10}$$

MAC (Marker and Cell) method, presented in Harlow and Welch (1965), with velocity and pressure coupling was applied using the predictor-corrector strategy.

A grid of 200x150 was used for all the simulations carried out in the present study with 50 cells on the square cylinder side in both x and y direction. The time step considered was, dt=0.001. In the present study the respective pressure correction factors in all the neighboring cells were also considered, this is an improvisation of the original MAC method to minimize the error involved in the calculation.

Lift and drag coefficients evaluate the average normal and shear stresses acting on the sides of the square cylinder. To calculate lift and drag coefficients, the expressions presented in equation (1.11) were used. It is important to realize that as the flow under study is unsteady and periodic, hence the concept of average lift and drag coefficients has to be used.

$$C_D = \frac{F_D}{\frac{1}{2}\rho U^2 A^2}, \; C_L = \frac{F_L}{\frac{1}{2}\rho U^2 A^2}; \qquad (1.11)$$

F_D and F_L are respectively the dimensional drag and lift forces due to the pressure and shear stresses acting on the square cylinder. Drag force was taken as positive when acting in the positive X axis direction, and Lift force was regarded as positive when acting in the positive Y axis direction. The equation to derive Strouhal number, St is presented in equation (1.12), f being the vortex shedding frequency in the square cylinder wake.

$$St = \frac{f\,A}{U} \qquad (1.12)$$

1.3. Code Validation.

The code was validated by simulating the unconfined flow past a square cylinder, in upstream uniform free stream flow. Results were compared with the ones presented in the existing literature. It was observed that the flow was steady for Reynolds numbers 50 and 52, see figure 1.3, and unsteady periodical at Re=55. According to Sohankar et al (1998), Von Karman vortex street appeared and therefore vortex shedding was happening in the wake of the square cylinder at $Re=51.2\pm1$. Kelkar and Patankar (1992) through stability analysis of the flow found, that the critical Reynolds number for the onset of vortex shedding was 54, which is in line with the results obtained and presented in figure 1.3.
For the unconfined flow past a square cylinder in unsteady periodic flow regime under the Reynolds number range $100\leq Re\leq 200$, average drag coefficients and Strouhal numbers were compared with the results presented by Franke et al (1990) and Sohankar et al (1997), (1998) and (1999). In all cases identical flow and boundary conditions were used.

Figures 1.4(a), (b) present the Drag coefficient, C_D and Strouhal number, St versus upstream flow Reynolds number, the present work and the research undertaken in four previous papers are compared. The present results compare well with the published literature, especially in the case of Strouhal number, St which can be considered as a stringent parameter for comparison.

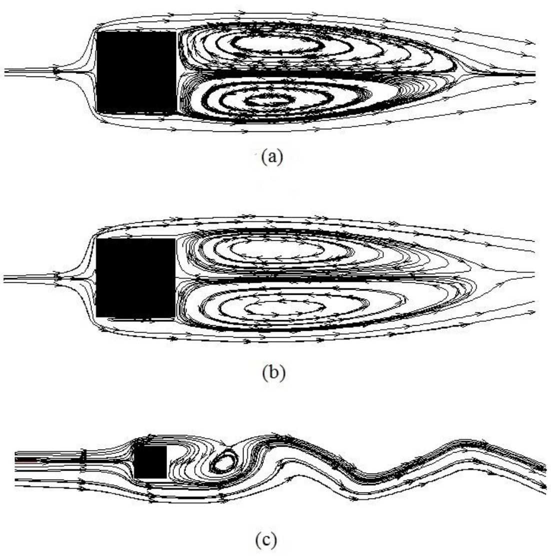

(a)

(b)

(c)

Figure: 1.3. Steady state streamline plot of flow past a square cylinder at Reynolds number, (a) Re=50 and (b) Re=52 and unsteady periodic streamlines (c) Re=55

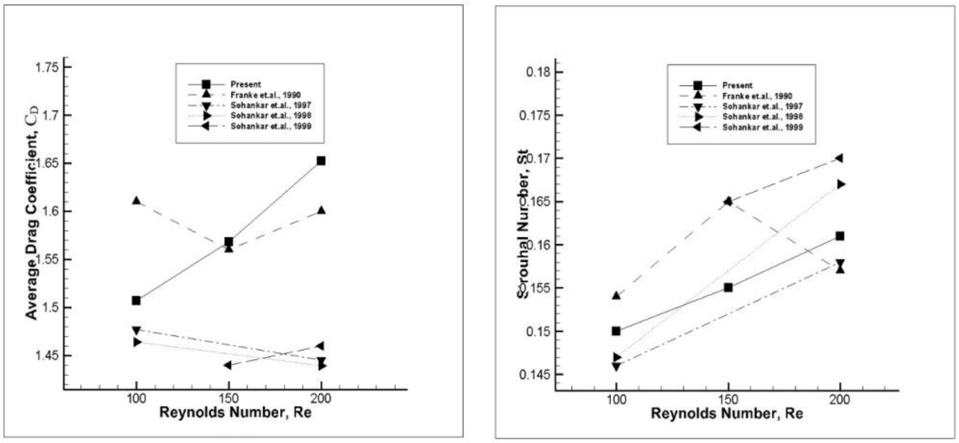

(a)

(b)

Figure: 1.4. (a) Average drag coefficient, C_D versus Reynolds number (b) Strouhal number, St Plots versus Reynolds number for unconfined flow past a square cylinder.

The development of the laminar boundary layer and mixing layer behind the splitter plate can be seen in the vector plots presenting the flow over the splitter plate and upstream of the square cylinder for a Reynolds number, Re100 and ratios, r=2, 3 and 4, figure 1.5. The development of Blasius profile of velocity gradient in the boundary layer over the splitter plate, as expected from a laminar boundary layer, can be clearly seen in figure 1.5 and validates the formation and development of the laminar boundary layer over the splitter plate. The fully developed boundary layer above and below the splitter, merge into a mixing layer in the wake of the splitter plate, due to the difference in the free stream velocities above and below splitter plate, which interacts with the flow in the wake of the square cylinder as seen in figures 1.5.

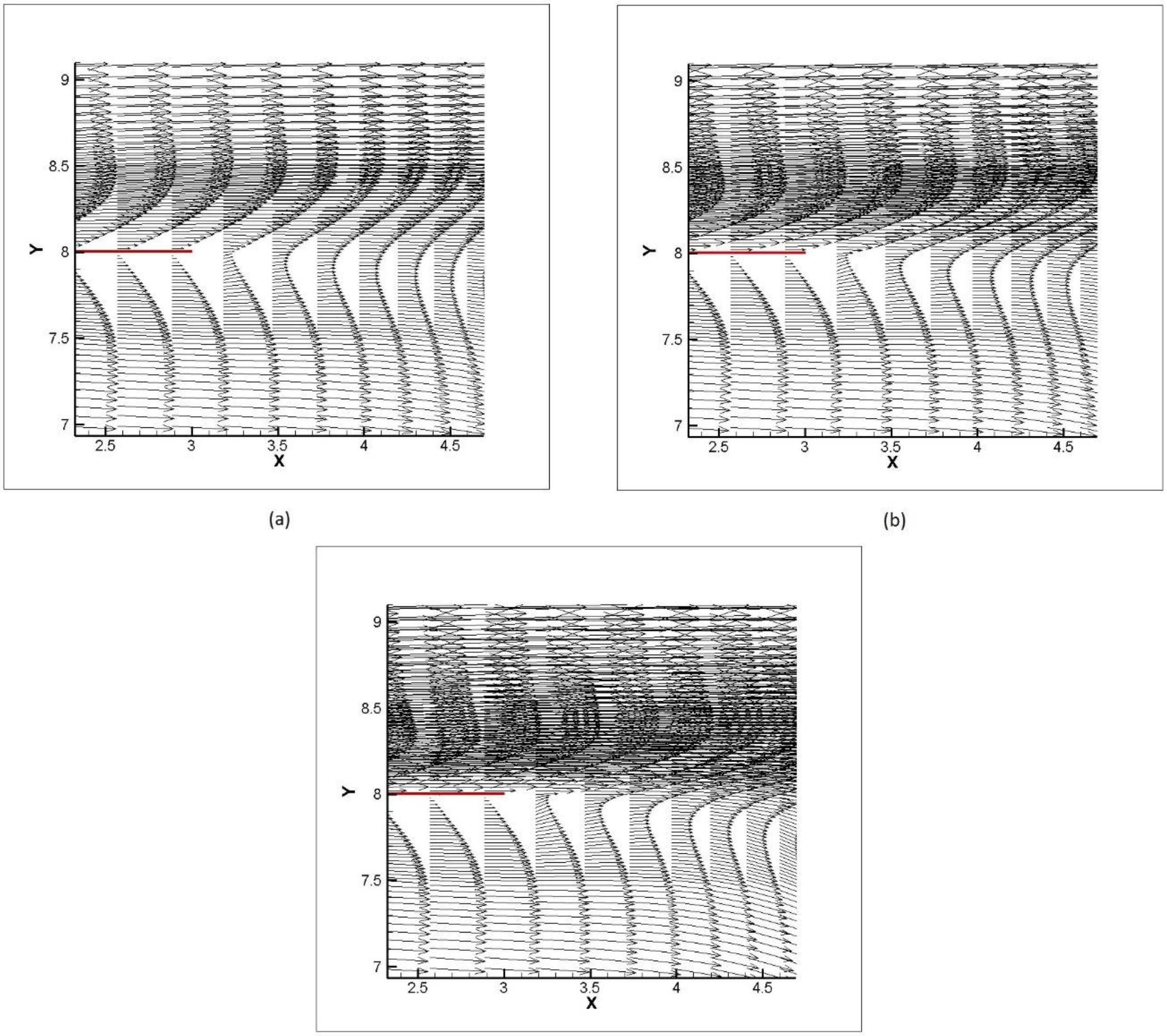

(a)

(b)

(c)

Figure: 1.5. The boundary layer and mixing layer development vector plots of flow over the splitter plate at Reynolds number, Re=100 for (a) r=2 (b) r=3 and (c) r=4.

1.3.1 Effects of Grid Refinement:

A grid refinement study has been carried out on three progressively refined grids for Re=200 and r=4, namely 180×120, 200×150 and 240×180, where the number of grid nodes distributed over the side of the square cylinder are 40, 50 and 60, with cell width mentioned in brackets, respectively.

Grid	180x120	200x150	240x180
No. of Cells on Side of Square	40 (0.025)	50 (0.020)	60 (0.017)
Drag Coefficient	19.125	19.412	19.490

Table 1.1: Results of the grid refinement study

The variation in the drag coefficient, C_D was around 1.5% when the grid was refined from coarsest to the intermediate level. But when the grid was further refined to the finest level, the variation reduced and became close to 0.4%, see table (1.1). Therefore this has led to the use of grid size of 200x150 for the all the simulation.

1.4. Results and Discussion.

1.4.1 Unsteady periodic flow of wake and mixing layer interactions:

In order to evaluate unsteady periodic vortex shedding, simulations were carried out for Reynolds numbers 100, 150 and 200, for each Reynolds number velocity ratios of, r = 1.5, 2, 2.5, 3, 3.5 and 4 were considered. For each case, three different upstream lengths of ul=5a, 6a and 7a, measured between the free stream inlet and the square cylinder leading edge, were studied. Additionally, velocity ratios of r=1.6, 1.8, 1.9, 2.6, 2.8, 2.9, 3.6, 3.8 and 3.9 were also evaluated for ul=6a and ul=7a. Okajima et al (1992), when studying flow past a square cylinder, for a Reynolds number of Re=1000, realized that flow instabilities suffered a sudden increase when compared to the flow patterns appearing at lower Reynolds numbers. Scarano et al (2009) studied experimentally the flow around a square cylinder and observed that the transitional Reynolds number between laminar and turbulent flow happened to be at Re=1080, below which the flow remained laminar. On the other hand, Sau (2009), Luo et al (2003) and Salinas et al (2014) reported the appearance of three dimensional structures at much lower Reynolds numbers. Nevertheless considering this is the first time this flow is being simulated on a wide range of parameters and having in mind the richness of the flow structures appearing, the evaluation of the flow in 2D shall be seen as the first step in understanding the proposed configuration.

The onset of vortex shedding in the case of the wake and mixing layer interaction for flow past the square cylinder is affected by upstream instabilities, which modifies the flapping motion of the vortices on the rear edge of the square cylinder. The flapping motion is due to the periodic separation of boundary layer on both lateral sides of the square cylinder causing the formation of periodic vortices downstream of the square cylinder which get dissipated in the wake. This mechanism is similar to the one appearing in the flow past a square cylinder, with no upstream mixing layer, the vortex shedding occurs due to separation of the boundary layer inducing a flapping motion of the vortices in the rear of the square cylinder and these vortices are eventually shed alternately into the wake.

Laminar periodic vortex shedding is presented in Figures 1.6 to 1.9, in the form of instantaneous vorticity and streamlines contour plots corresponding to six equally spaced time instants within a shedding cycle of time period T. Reynolds number was taken to be 100 in all figures with ratio, r=1.5 for figure 1.6, ratio, r=2 for figure 1.7, ratio, r=3.5 for figure 1.8 and ratio r=4 for Figure 1.9. The distance between the splitter plate and the square cylinder was considered to be 3 units, being the upstream length, ul = 6 units. In all figures, the vortices form at the rear edge of the square cylinder and are shed into the wake. Two types of inviscid critical points, namely ‘centre’ and ‘saddle’ can be seen from the figures. A critical point is a location where slope of streamline becomes indefinite; the point of zero velocity is referred to as the ‘centre’ while the point where two streamlines running in opposite directions touch each other, is referred to as the ‘saddle’ point. From figure 1.6 and 1.7 it is clearly seen that the saddle point of a shed vortex disappears before a new vortex is shed. Instantaneous vorticity contours, shown in Figure 1.6-1.9, further reveals the formation and shedding of vortices from the rear edge of the square cylinder. The positive and negative vorticity, corresponding respectively to counter-clockwise and clockwise motion, are presented by solid and dashed lines. The two vortices in the rear of the cylinder exhibit a flapping motion while the mixing layer moves into these growing vortices in the wake, only to be convected downstream in the form of a vortical structure which scales with the height of the cylinder.

As seen in figure 1.6 for ratio, r=1.5 the vortex shedding occurs alternatively with positive and negative moment vortices. It was also found that alternate shedding was occurring at ratios r=1.6 to 1.9, ul=6a. A similar shedding pattern was found for ul=5a and 7a, r<2. As velocity ratio increased, the dissipation frequency of positive moment vortices decreased before finally being dissipated as Kelvin-Helmholtz (KH) instability. This was found to be occurring from ratio, r=2 and above, as seen in figure 1.7. The KH instability became more prominent as the ratio increased to r=4, as presented in figures 1.7, 1.8 and 1.9. According to the results obtained, the threshold velocity ratio separating the cases for which positive and negative vortices are dissipated alternatively into the wake and the cases in which only the negative moment vortex is being shed and the positive moment vortex is being shed as Kelvin-Helmholtz instability, just a single negative vortex appears downstream, was found to be around r =2.

When comparing figure 1.8 and 1.9 with figure 1.6 and 1.7, it can be observed that whenever the ratio is below r=3, the vortex dissipation has a higher regularity, but the simulations at r >3, show much faster and disorganized vortex dissipation, as more random vortical structures are being dissipated in the wake. Some of these vortical structures can be seen just below the square cylinder in figure 1.8 and especially in figures 1.9(d) to (f) and 1.10(a) to (f). These small vortical structures appear because as velocity ratio increases, the kinetic energy associated to each fluid particle increases as well, momentum interchange between particles also increases, producing a quicker and higher disorganized vortex breakdown.

It was also found that for r >3, the mixing layer formed upstream of the square cylinder tended to break before reaching the square cylinder, therefore inducing very random vortex shedding into the wake with no regular pattern or single shedding frequency, as seen in figure 1.14 from the FFT analysis of the drag signal. As Reynolds number increases from 100 to 150 and 200, the mixing layer tends to break upstream of the square cylinder, but this phenomena is much weaker than the similar one happening when the Reynolds number is maintained constant and the ratio r increases.

After simulating the wake and mixing layer interactions for an upstream length ul=5a and 7a, it was found that the critical point for onset of KH instability is at velocity ratio r=2, as already observed for ul=6a. It is interesting to highlight that this happens independently of the upstream Reynolds number. It was also found that for ul=7a, Reynolds 100 and velocity ratio r=4, the mixing layer tends to break just upstream of the square cylinder, creating random small vortical structures which are converted into the wake of the square cylinder causing disorganized downstream vortex shedding. It was observed that the same phenomena occurred when ul=6a, ratio 4 but the Reynolds number was 150. This can be attributed to the fact that when ul=7a the mixing layer has a longer development length and therefore the shear stresses have more time to induce flow instabilities in the upstream mixing layer and causing it to break away. For ul=5a, the mixing layer was breaking upstream when r=4 and Reynolds number was 200. Therefore, it can be concluded that for shorter upstream lengths the mixing layer tends to break at higher Reynolds number, following the trend previously clarified. The breaking up of the mixing layer can be clearly seen with the help of the vorticity contours in figure 1.10 for ul=6a. It is at this point interesting to highlight that mixing layer wavering motion increases with the velocity ratio increase.

From the present study it has been observed, that the free shear layers shed from top and bottom edges of the square cylinder, become naturally unstable and roll up alternately to form a large scale Vortex Street. Detailed inspections of flow visualization in the wake show that there are a few distinct features in the flow structure for each of the studied cases, figure 1.6 to 1.9. For the unmodified square cylinder, the separated shear layers are deflected inwards immediately after they pass the cylinder base. This is believed to be due to the lower fluid velocity and pressure behind the rear edge of the square cylinder. In this region, the roll up of the shear layer from the top side of the cylinder entrains fluid from the adjacent irrotational flow into the growing vortex. The resulting backflow, due to this fluid entrainment, engulfs the rear face causing the negative moment vortex to be shed downstream. A similar mechanism occurs for the shedding of the positive moment vortices. As a result of the present study, this phenomenon is observed to be occurring for ratios up to r=1.9. It can be noted that for these small velocity ratios, the upstream mixing layer is too weak to alter the vortex formation mechanism already introduced above. In the next section this phenomena will be addressed as the first oscillation mode.

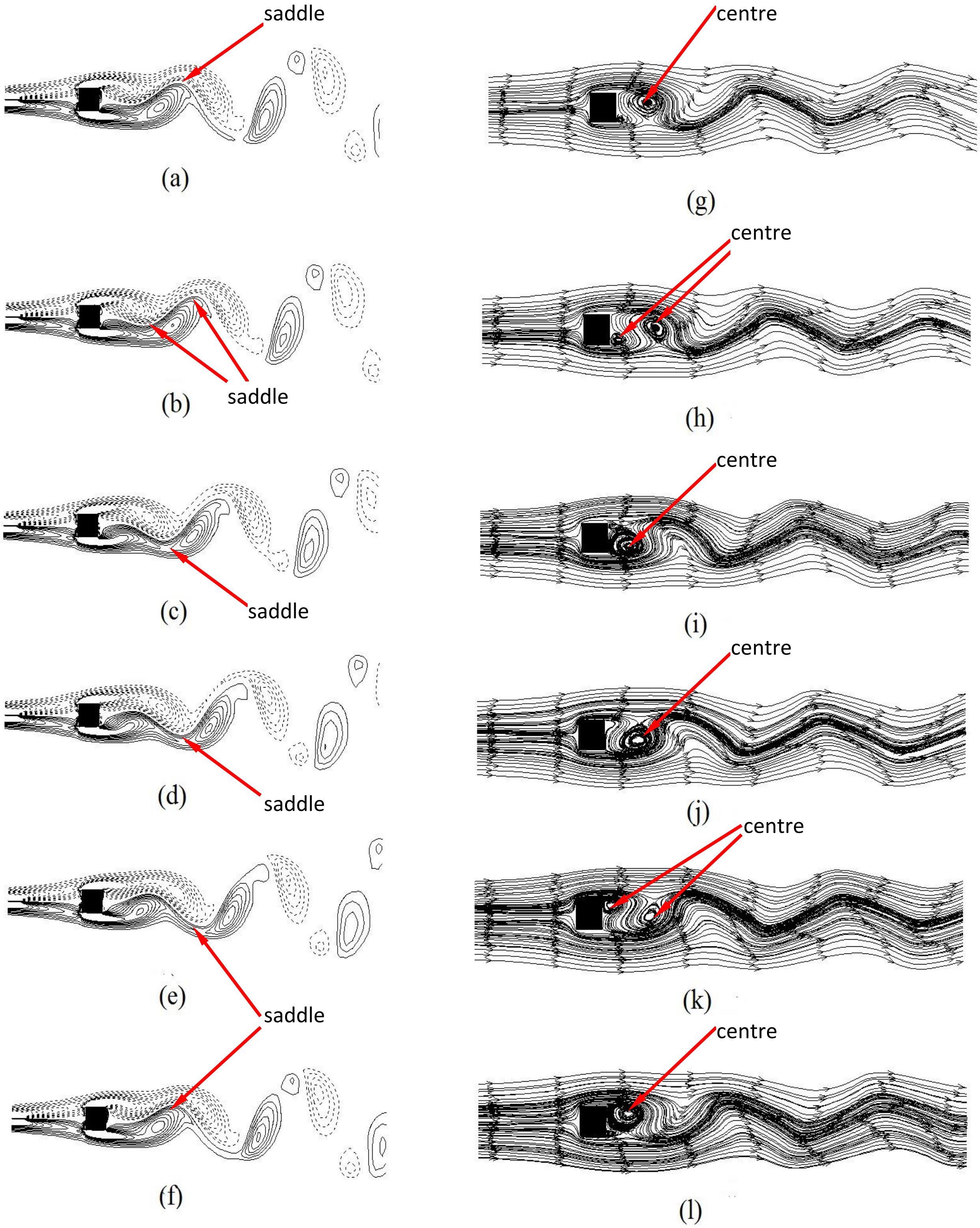

Figure (1.6): Vorticity and corresponding streamline plots of vortex shedding cycle in the wake of the square cylinder for ul=6a, Re=100 and r=1.5, (a, g) T/6; (b, h) T/3; (c, i) T/2; (d, j) 2T/3; (e, k) 5T/6; (f, l) T.

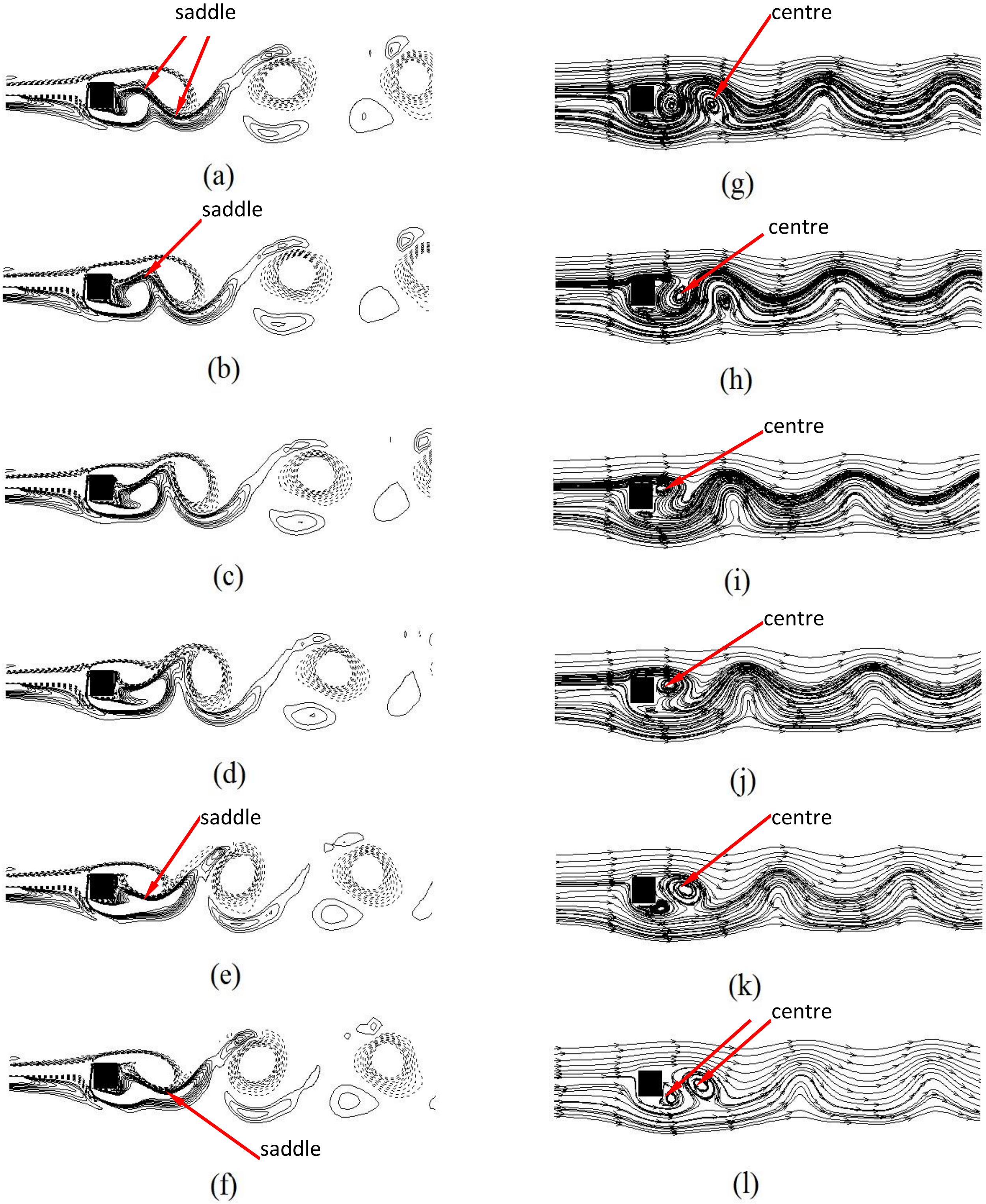

Figure (1.7): Vorticity and corresponding streamline plots of vortex shedding cycle in the wake of the square cylinder for ul=6a, Re=100 and r=2, (a, g) T/6; (b, h) T/3; (c, i) T/2; (d, j) 2T/3; (e, k) 5T/6; (f, l) T.

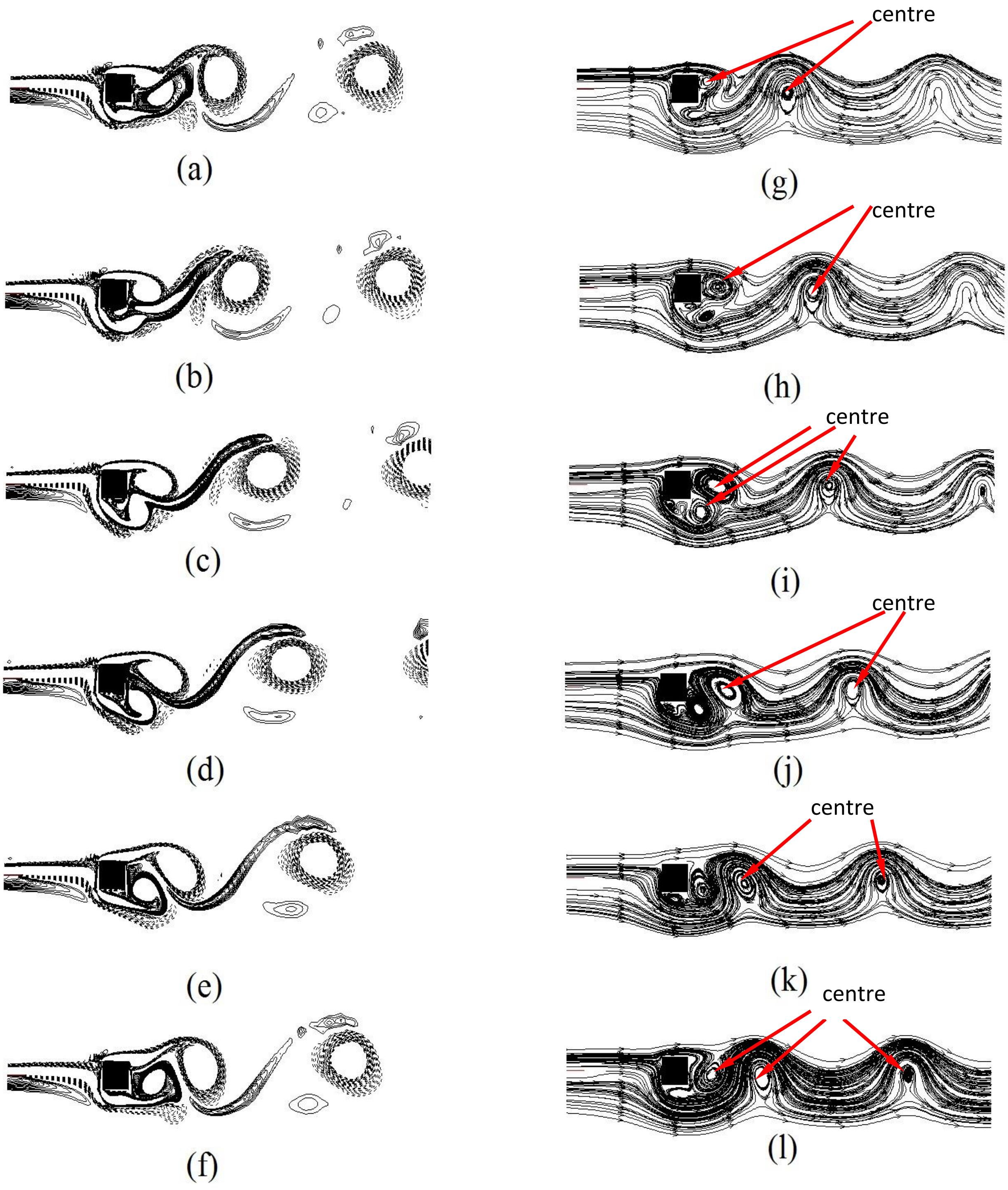

(a) (g)
(b) (h)
(c) (i)
(d) (j)
(e) (k)
(f) (l)

Figure (1.8): Vorticity and corresponding streamline plots of vortex shedding cycle in the wake of the square cylinder for ul=6a, Re=100 and r=3.5, (a, g) T/6; (b, h) T/3; (c, i) T/2; (d, j) 2T/3; (e, k) 5T/6; (f, l) T.

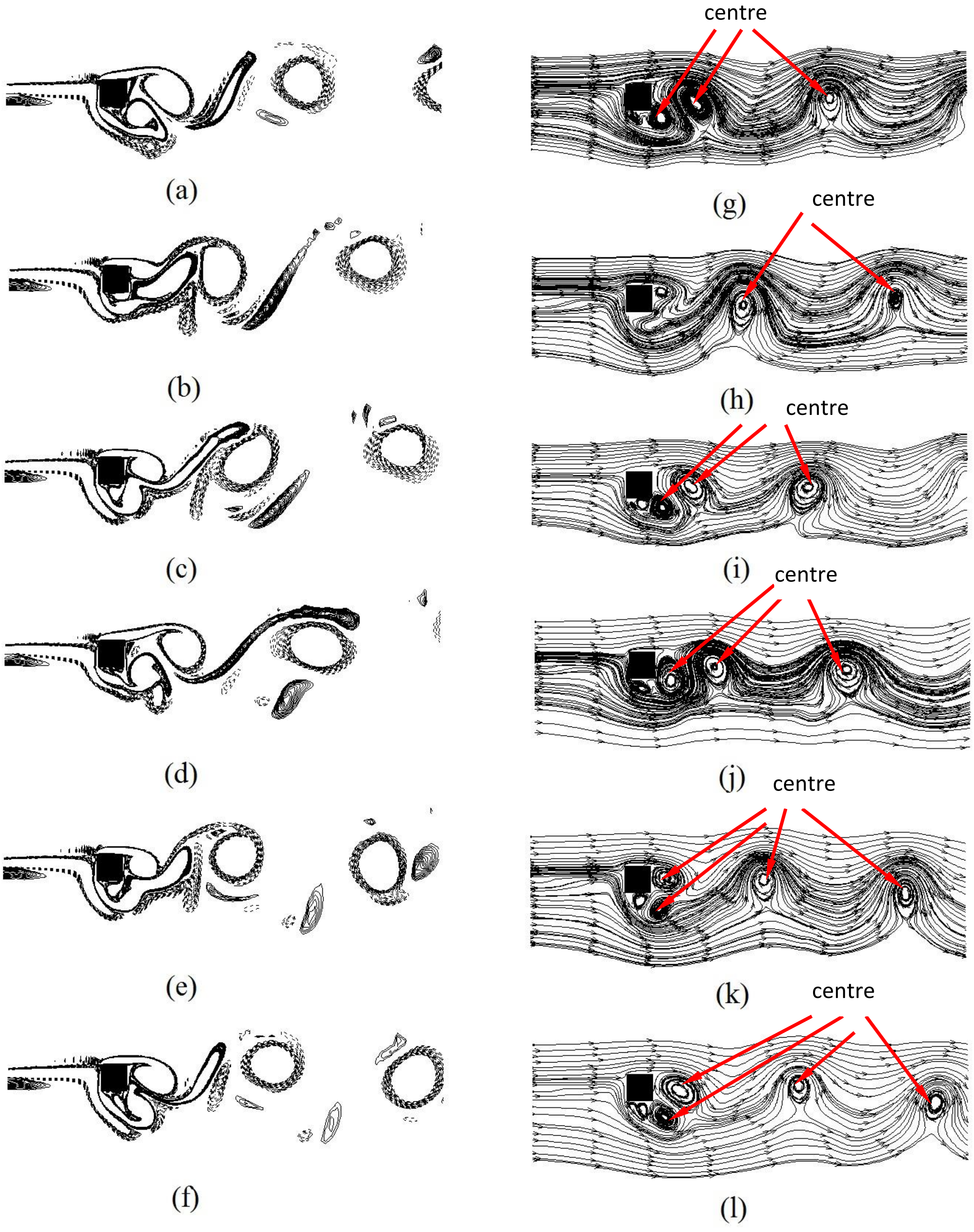

Figure (1.9): Vorticity and corresponding streamline plots of vortex shedding cycle in the wake of the square cylinder for ul=6a, Re=100 and r=4, (a, g) T/6; (b, h) T/3; (c, i) T/2; (d, j) 2T/3; (e, k) 5T/6; (f, l) T.

At higher ratios r, the interaction of the mixing layer with the laminar boundary layer emanating from the stagnation point, causes the free shear layer at the bottom of the square cylinder to separate at the lower corner of the front face, whereas the free shear layer on top of the square cylinder is attached to the surface and separates at the rear vertex of the top edge. This causes the positive vortex formed at the bottom of the square cylinder to become unstable, tending to break away from the free shear layer before reaching the rear edge of the square cylinder, as seen in figures 1.6 to 1.9. Since the energy associated to the primary vortex is much higher than the one corresponding to the secondary vortex, the primary vortex grows faster and entrains into the slowly growing secondary vortex at the bottom of the square cylinder, causing it to be dissipated as Kelvin-Helmholtz instability. This phenomenon of vortex shedding was found to be occurring for a relatively stable mixing layer, the breaking of the mixing layer upstream was not observed. For Re=100 and ul=6a, the above explained shedding mechanism, was found to be occurring from r=2 until r=3.9, as presented in figures 1.7 and 1.8. As ratio r increased, the stagnation point tended to move up on the front face of the square cylinder, causing the laminar boundary layer to separate before reaching the lower corner of the front face.

In general it can be said that there are similarities in the vorticity contours for all cases studied. The flow structures around the front and side faces of the square cylinder are qualitatively unchanged when the splitter plate is moved upstream of the square cylinder. On the front face, a well-defined stagnation point was observed in all cases. From this point, the fluid is forced to move over the body and laminar boundary layers are developed along the front surface. At the front corners of the square cylinder, the abrupt change in geometry induces separation and free shear layers are initiated at these points. From figure 1.6 to 1.10 a distinct stagnation point was observed for each case on the square cylinder front face, the stagnation point displacement as a function of the velocity ratio r, ul=6a and for a Reynolds number 100, is presented in figure 1.11. From figure 1.9, Re=100 and r=4, considering the streamlines plots 9g to 9l, minor variations with respect to the change in the stagnation point position can be observed. In one periodic shedding cycle, stagnation point oscillates between the positions (6; 8.25) and (6; 8.38), measured from the coordinate axes origin, see figure 1.2. This stagnation point oscillation is attributed to the unstable oscillating upstream mixing layer, tending to break. In figure 1.10, for Re=200 and ratio r=4, the stagnation point oscillates between the top and bottom corner of the square cylinder front face, positions (6; 8.1) and (6; 8.45). It can be noted that the stagnation point oscillation amplitude is for this second case about three times bigger than for the previous one. This is due to the breaking up of the mixing layer upstream of the square cylinder, which induces a wavering motion of the vortical structures generated upstream in tandem with the vortices generated on the rear edge of the square cylinder. At this ratio r=4, the free shear layer generated at the bottom of the square cylinder becomes unstable and separates before reaching the leading edge lower corner. As a consequence, the positive vortex at the bottom of the square cylinder separates before reaching the rear edge of the square cylinder as it interacts with the breaking mixing layer formed upstream, causing a very random and unstructured vortex dissipation in the wake of the square cylinder as seen in the vorticity plots in figures (1.9) and (1.10) when compared to figure (1.6) to (1.8). This random dissipation will be clearly seen from the FFT analysis of drag and lift coefficients presented in figure (1.14) and (1.15) on the right side.

Due to high velocity ratio, r=4, the negative vortical structures generated by the breaking mixing layer, interact with the positive vortex produced by the free shear layer at the bottom of the square cylinder, suppressing its formation. As a result, the vortices generated at the bottom of the square cylinder are weakened while the vortex formed at the top are shed downstream as primary vortical structures. Despite the fact that the incoming negative vortical structures tend to weaken the positive vortex generated below the square cylinder, the positive vortical structures gradually grow in size until they are eventually shed downstream as KH instability. During the growing process, the stagnation point at the square cylinder front face moves downward. The lowest position of the stagnation point is reached when the vortex formed below the square cylinder is about to be shed. As soon as the vortex at the bottom is shed, the stagnation point moves up reaching its highest position and the cycle is repeated again.

A general trend characterizing all cases studied shows that as ratio r increases from 1.5 to 4, the stagnation point average position tends move upwards on the front face of square cylinder. This phenomenon has been previously reported by Cheng et al (2007), when studying plane shear flow around a square cylinder.

Figure 1.11 summarizes the stagnation point oscillation as a function of the velocity ratio r for Re =100. Different patterns of oscillation can be seen with changing amplitudes by varying the velocity ratio r. This shows that the splitter plate is altering the process of vortex formation in the cylinder wake by generating various types of mixing layer and wake interactions. Different modes of vortex shedding based on the similarities in the stagnation point oscillations are presented in figure 1.11. The ranges of velocity ratios, r where the displacement amplitude of the stagnation point remains constant, will constitute a mode. The change in modes of dissipation is occurring at r = 1.9, 2.9, 3.9. Dissipation mode occurring from r = 1.5 to 1.9 will be called as mode 1, vortex shedding from r = 2 to 2.9 as mode 2, for 3< r <3.9 will be called mode 3 and at r = 4 is mode 4.

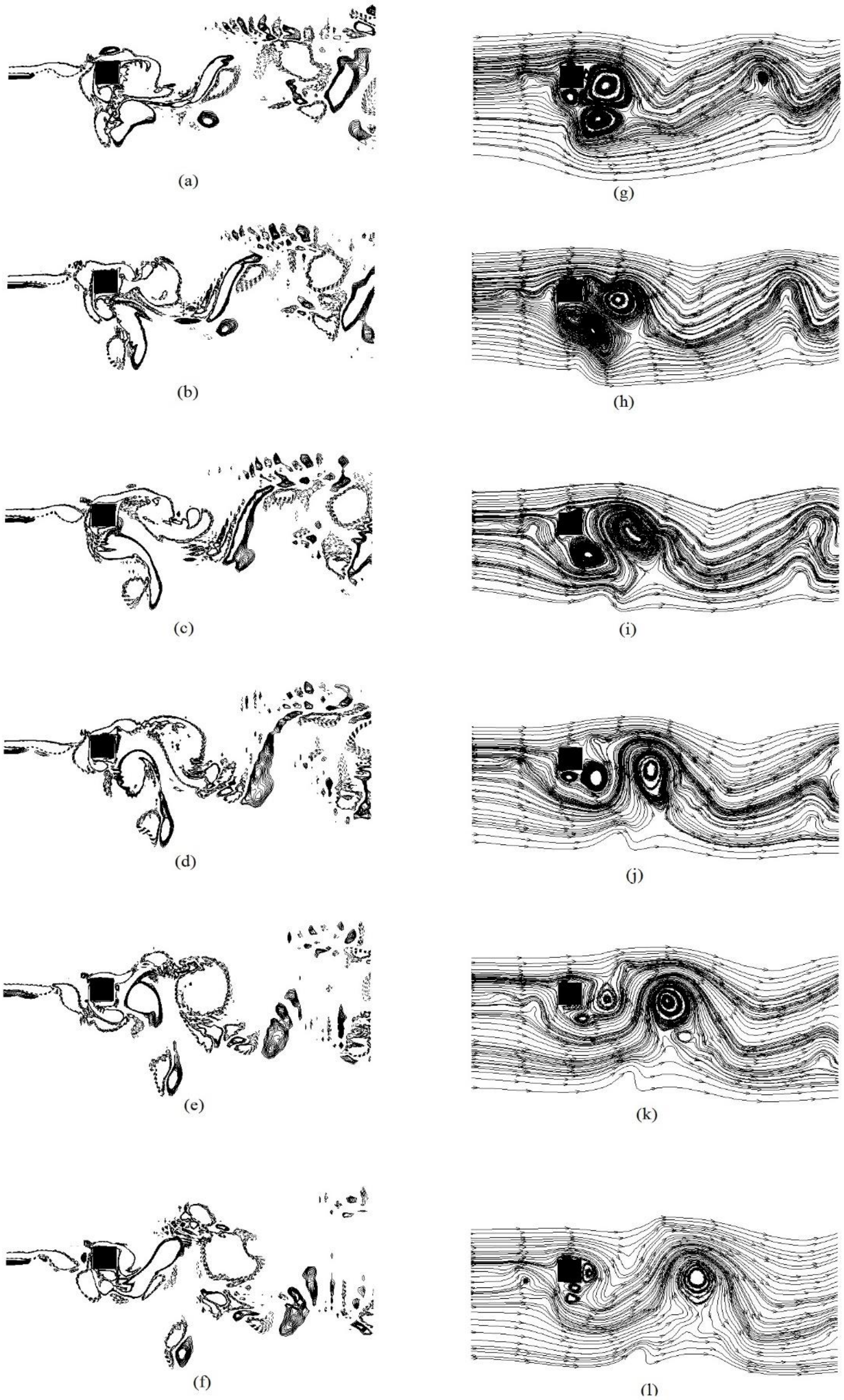

Figure (1.10): Vorticity contour and corresponding streamline plots of vortex shedding in the wake of the square cylinder for ul=6a, Re=200 and r=4, (a, g) T/6; (b, h) T/3; (c, i) T/2; (d, j) 2T/3; (e, k) 5T/6; (f, l) T.

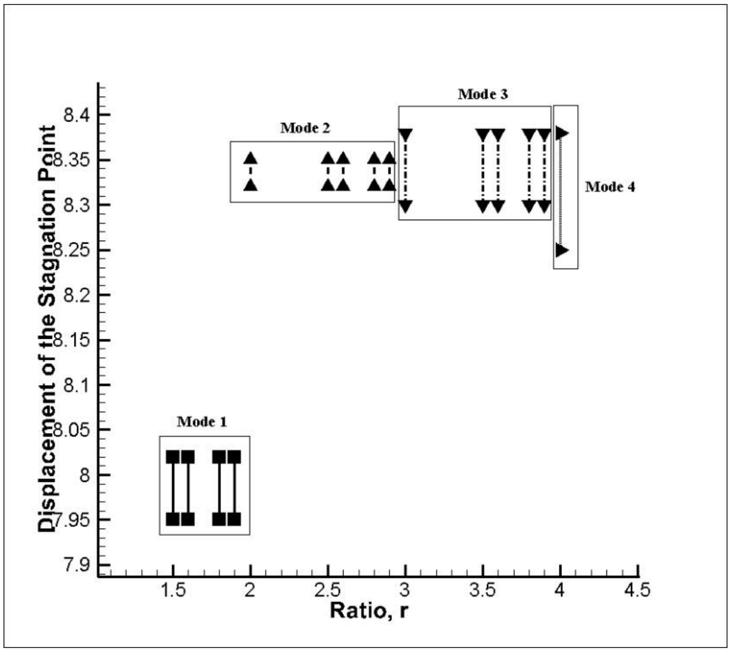

Figure (1.11): Displacement of the stagnation point vs. the Ratio, r for Reynolds number, Re=100 and upstream length, ul=6a

The first observation to realize from figure (1.11) is that the stagnation point oscillation for mode 1 consisting of small velocity ratios, is located around the square cylinder center line, while for higher velocity ratios the stagnation point oscillation average values are located much above the center line. This can be explained by considering that at small velocity ratios the vortex shedding pattern in the wake is similar to the one appearing in a square cylinder with uniform upstream flow, where the stagnation point is located on the front face centerline.

1.4.2 Lift and Drag Coefficients, C_D & C_L.

Figure 1.12 introduces the average lift, C_L and drag coefficients, C_D for all velocity ratios studied, ul=6a, Re=100, 150 and 200. The first observation that can be made is that both coefficients exhibit a stepwise profile, indicating the existence of different modes of vortex dissipation in the wake of the square cylinder as in the case of the stagnation point oscialltions.

At this point it is interesting to recall the work done by Williamson (1996), which presented that for an isolated circular cylinder placed in a laminar two dimensional flow regime, the transition from two dimensional to three dimensional laminar regime was characterized by two distinct discontinuities i.e. two different vibration modes. Sukri et al (2012) also found two oscillation modes when studying uniform flow around a square cylinder with a detached downstream thin flat plate. Also Malekzadeh and Sohankar (2012) while studying laminar flow around a square cylinder with a splitter plate located upstream, found three different oscillation modes. The existence of several oscillation modes in circular and square cylinders have been found by many researchers but never for the conditions of flow simulated and presented in this study.

Regarding the averaged drag coefficient, figure 1.12(a) shows that it increases with the increase of ratio r, remaining constant for a given mode, regardless of the upstream value of Reynolds number. This behavior can be explained when considering that as the velocity ratio r increases the normal pressure acting onto the square cylinder front face will gradually increase, while the pressure acting onto the trailing square cylinder face is slightly being affected by the velocity ratio modifications. From the simulations undertaken it was observed that as Reynolds number increases, while maintaining a constant velocity ratio, the pressure acting onto the front square cylinder surface, which is the major component of the drag, will also increase, the shear stresses on the top and bottom square cylinder surfaces also increase therefore causing the shear drag and the overall drag on the body to increase. The occurrence of the modes of dissipation could be attributed to the energy thresholds of the flow where the flow exhibits a new mode of dissipation when the increase in the velocity ratio, r leads to a certain level of energy for the flow, sufficient to cause different vortex shedding pattern in the wake. This phenomenon can be observed from the figure (1.11) also. The stagnation point position oscillation have the same amplitude in a given mode until the energy associated with the flow increases and reaches a level which initiates the onset of a new mode. Similar variations in the behaviour of the upstream mixing layer can also be seen from the vorticity plots of Figures (1.6-1.10), between different modes. In a given mode the stability of the upstream mixing layer remains constant and as the velocity ratio, r increases the stability of the mixing layer decreases when the onset of a new mode is triggered. As the velocity ratio r increases, the upstream mixing layer becomes more unstable and finally tends to break before reaching the front face of the square cylinder at ratio r=4 as seen figure (1.10).

The average lift coefficient presented in figure 1.12(b) shows that as the ratio r increases, for a given Reynolds number, the average lift coefficient increases due to an increase in the pressure difference above and below the square cylinder. This can be attributed to the fact that as the ratio increases the velocity over the top surface of the square cylinder increases, causing the normal pressure on the top surface to decrease with respect to the bottom surface of the square cylinder, where the flow velocity remains constant. Consequently the pressure difference between the top and bottom surfaces increases, leading to an increase in the lift on the body.

It is interesting to observe that at ratio r=4, the increase in average lift coefficient, is very much affected by the increase of Reynolds number, when compared to the increase suffered by the average drag coefficient, see figures 1.13(a) and (b). Notice that at ratio r=4, the velocity difference between the upper and lower square cylinder surfaces is at highest, therefore the pressure difference between both surfaces suffer a drastic increase, this pressure increase directly influences the lift coefficient, whereas the drag coefficient is essentially dependent on the normal forces acting on the lateral sides of the square cylinder.

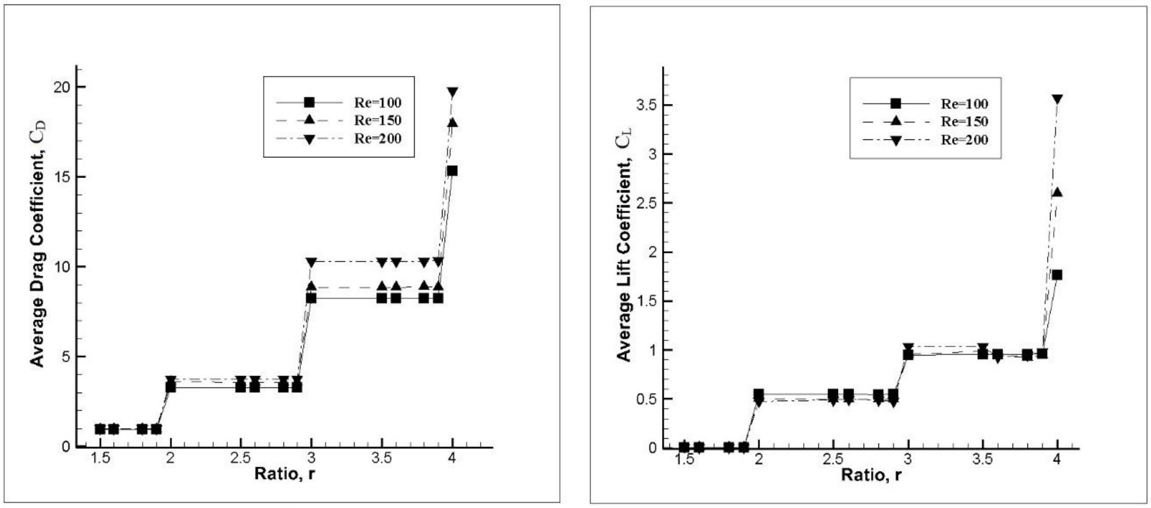

(a) (b)

Figure 1.12 (a) Average drag coefficient, C_{Davg} versus ratio, r. (b) Average Lift coefficient, C_{Lavg} versus ratio, r. Upstream length ul = 6a.

Nevertheless the velocity increase between the upper and lower square cylinder faces, cannot explain why at smaller velocity ratios, lift coefficient remains, in a given mode and for different Reynolds numbers, rather constant. The explanation in fact relies on vortex shedding. As observed in figure 1.12 (b), the average lift coefficient remains constant for ratio, r<4 and increases suddenly at r=4 when the Reynolds number is increased from100 to 200. At lower ratios the mixing layer is relatively stable and coupled with the stable shear layers on top and bottom of the square cylinder, leading to smaller pressure fluctuations. But at r=4, as the Reynolds number increased from 100 to 200, the mixing layer becomes more unstable and breaks, inducing instability in the shear layers and causing larger pressure fluctuations. The result is a higher increase in the average lift on the body.

Figure 1.13 presents the average drag and lift profiles with respect to the ratio r and for ul=7a. When comparing figure 1.12 and 1.13, it is to be seen that the profiles are very similar. In both cases the four different modes of dissipation were observed. Both figures show that onset of each mode is occurring at the same velocity ratio. It was observed that the different vortex shedding mechanisms which characterize each mode, already presented in figure 1.6 to 1.10 for ul=6a, occur as well for ul=7a and ul=5a, emphasizing the global nature of the dissipation modes.

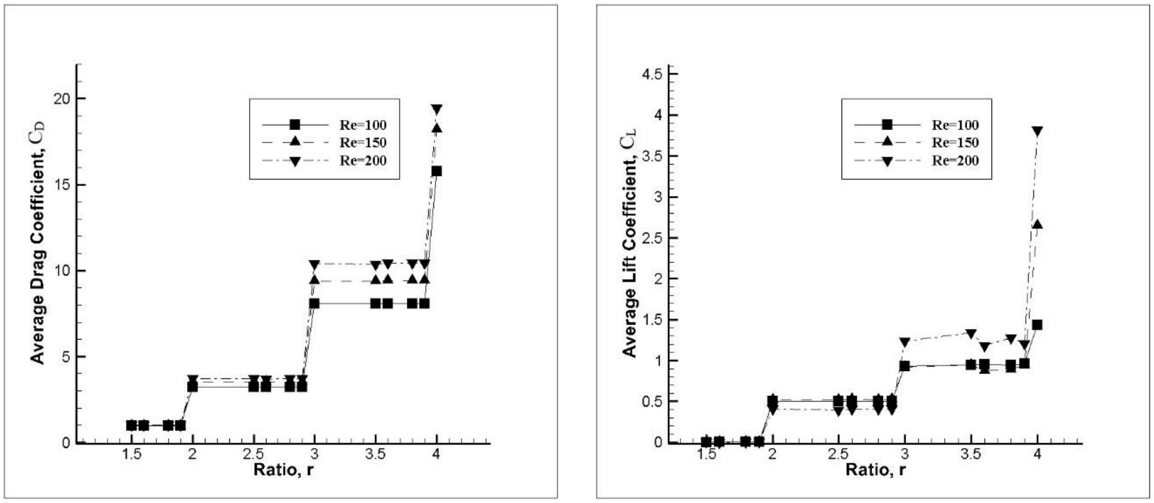

(a) (b)

Figure 1.13 (a) Average drag coefficient, C_{Davg} versus ratio, r. (b) Average Lift coefficient, C_{Lavg} versus ratio, r. Upstream length ul = 7a.

In figure 1.14 are being introduced the time dependent profiles for the drag coefficient as a function of the velocity ratio increase r and for the three upstream Reynolds numbers, ul=6a. It can be seen that oscillation amplitude increases with the increase of ratio r, the increase being over 80% of the latter when the ratio, r is increased from 2 to 3. Very similar increase of amplitude is spotted for the three Reynolds numbers studied Re=100, 150 and 200. For a given velocity ratio r, the oscillation amplitude also increases with the increase of the Reynolds number, this increase is smaller than the one occurring when the velocity ratio r is modified. As an example, for r=2 and Reynolds number changing from 100 to 150, the oscillation amplitude increase is about 46%. As previously stated, vortex shedding for the case of ratio r=4, is much more unstable and disorganized than at lower velocity ratios, instability increases with the Reynolds number increase although the parameter generating the highest flow instability is the velocity ratio. Flow instability is directly linked with the mixing layer instability. Under these conditions, wavering motion of the wake becomes severe and the flow undergoes random fluctuations. These effects are clearly seen in figure 1.14 (a) (b) (c), r=4.

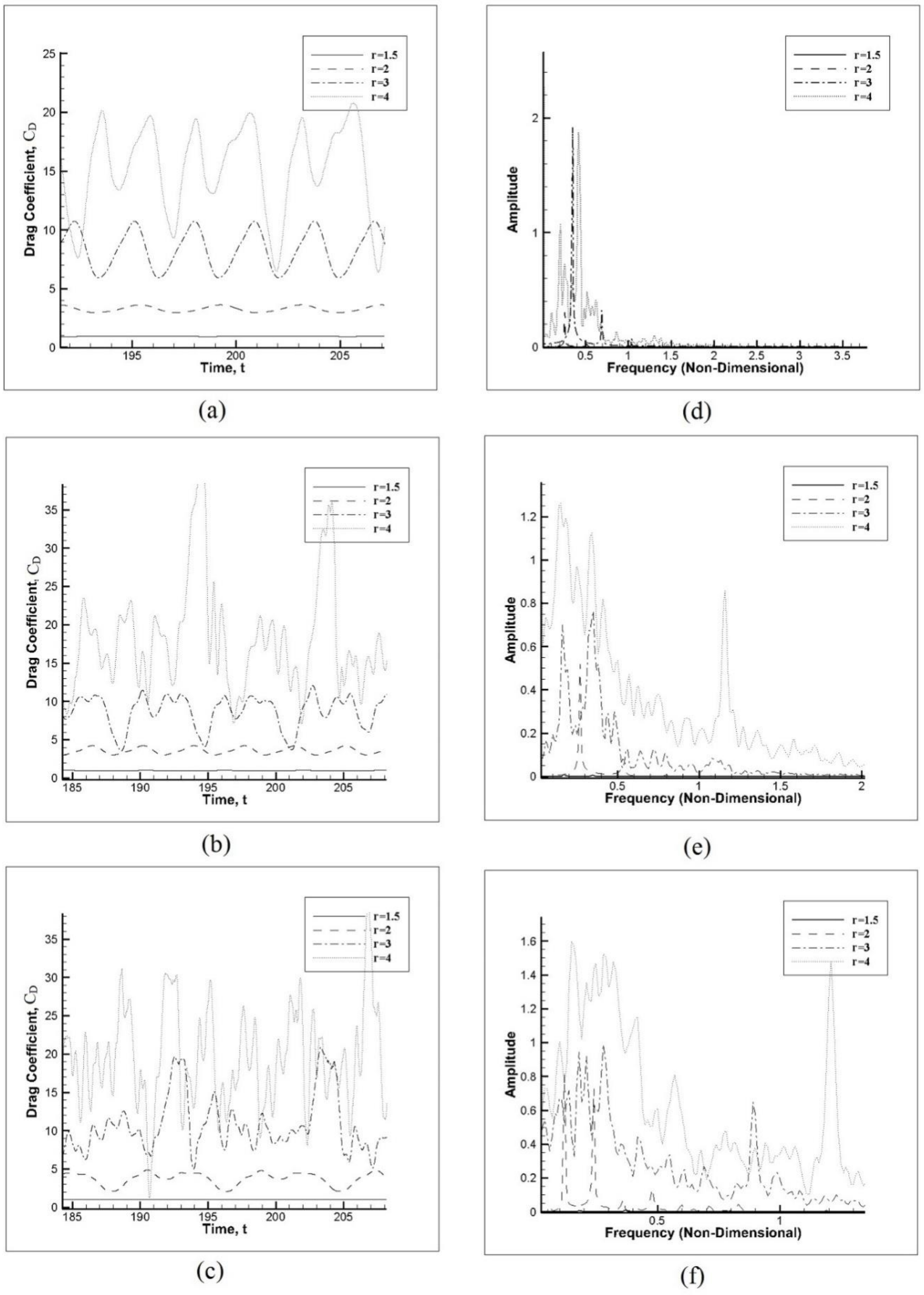

(a) (d)

(b) (e)

(c) (f)

Figure 1.14: Drag coefficient versus time, as a function of upstream velocity ratio r. ul = 6a. (a) Re=100, (b) Re=150, (c) Re=200 and their respective FFT analysis in (d), (e) and (f)

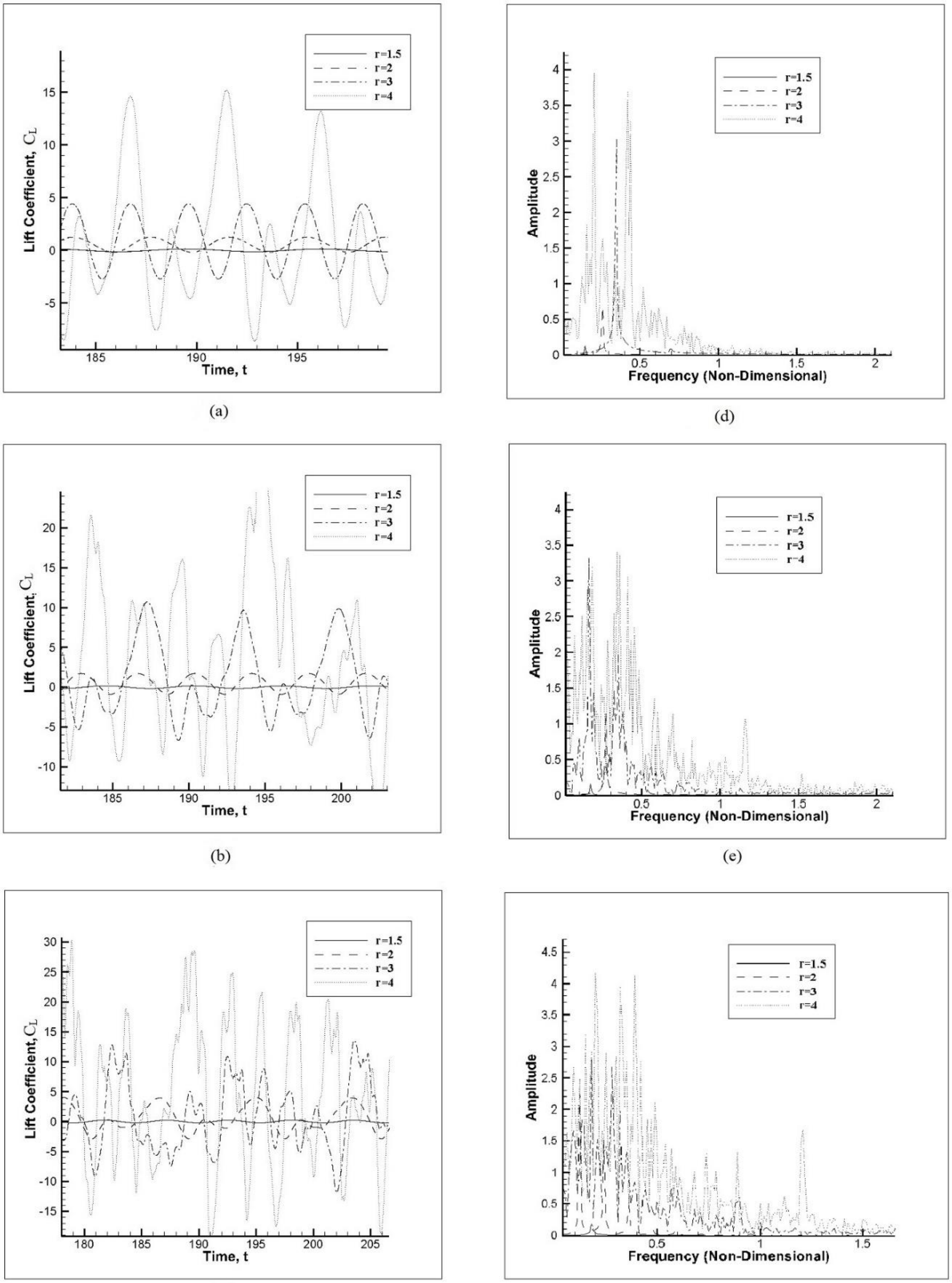

(a) (d)

(b) (e)

(c) (f)

Figure 1.15: Lift coefficient versus time, as a function of upstream velocity ratio r. ul = 6a. (a) Re=100, (b) Re=150, (c) Re=200 and their respective FFT analysis in (d), (e) and (f)

The time dependent lift coefficient profile for the same velocity ratios and Reynolds numbers evaluated in figure 1.14 is presented in figure 1.15. From the comparison of both figures, it can be concluded that the change in oscillation amplitude with velocity ratio r and Reynolds number, are presenting the same trend as presented in figure (1.14). Notice that the oscillation amplitude variation with the increase of ratio r and or Reynolds number, is similar to the one observed for the drag coefficient. In other words, the lift amplitude has an increase of 74% when velocity ratio increases from 2 to 3, Reynolds number Re=100, the increase is of 80% in the case of drag coefficient.

The increase of time dependent drag and lift oscillation amplitude as velocity ratio r increases is due of two main phenomena. The first one is an earlier shear layer separation from the square cylinder surfaces; the second one is the tendency of the mixing layer to break. These two factors complement each other causing higher pressure fluctuations, as can be seen from figure 1.14(d) to (f) and 1.15(d) to (f).

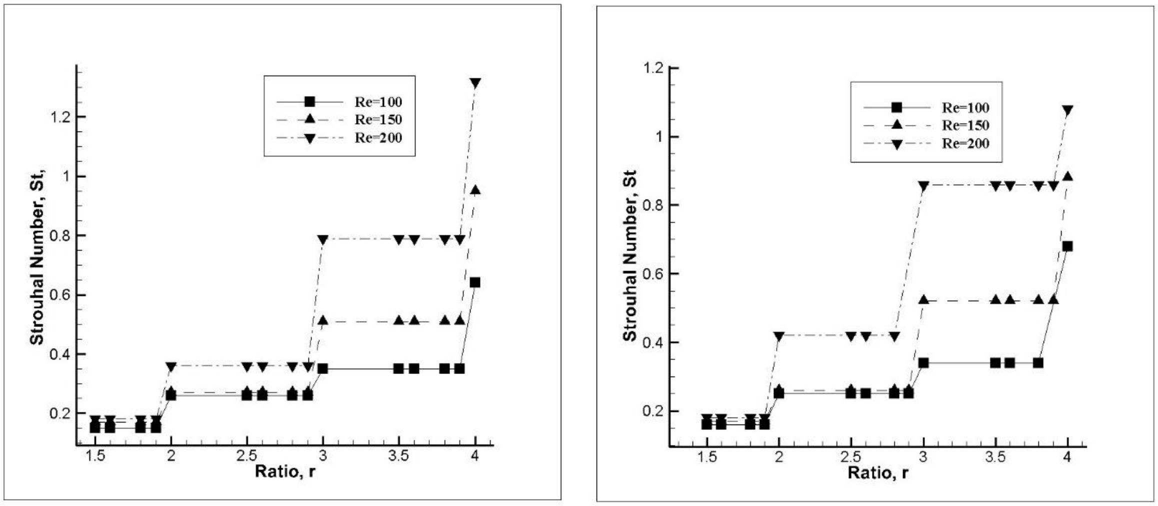

(a) (b)

Figure 1.16: Strouhal Number, St versus Ratio, r for (a) ul=6a and (b) ul=7a

The Strouhal number, for different velocity ratios r and at Reynolds numbers, 100, 150, 200, upstream distance ul=6a is presented in figure 1.16. For a given Reynolds, the Strouhal number is increasing with the increase of ratio, r and remains constant for a given oscillation mode. In mode 1, for Reynolds =100, Strouhal number has a value of 0.15, when Reynolds = 200, Stouhal number has a value of 0.17. For a Reynolds number of 100, the Strouhal number increase when going from mode 1 to mode 2 is about 80%. This increase drops to 44% when moving from mode 2 to mode 3, and increases to 94% between modes 3 and 4.

The evaluation of Strouhal number variation at a given mode, from figure 1.16 (a), shows that for velocity ratio, r =2, mode 2, when Reynolds number increases from 100 to 200, the Strouhal number increases about 38%. In mode 3, the Strouhal number increase when Reynolds number goes from 100 to 200 is of 128% and at mode 4 the increase is about 103%

When comparing figure 1.16(a), (b), it can be seen that although the splitter plate distance increases, the modes of vibration still follow the same pattern, clearly indicating a global nature of the flow even in terms of Strouhal numbers. For a Reynolds number of 100, in mode 1, the increase of Strouhal number between ul=6a and ul=7a is of 6%, for mode 2 there is a small decrease of 3.8%, for mode 3 the decrease is 2.8% and for mode 4 there is an increase of 6%. Similar results are obtained for the other two Reynolds numbers studied. Since the Strouhal number variation with the increase of splitter plate distance is very small, it can be concluded that, for the cases studied, the splitter plate distance is not affecting the downstream vortex shedding frequency.

The increase in Strouhal number between two consecutive modes is larger for higher velocity ratios and higher Reynolds numbers, because as the velocity ratio increases, it leads to an increase in flow kinetic energy causing higher oscillations in the mixing layer making it unstable and enhancing the vortex shedding frequency downstream. It is observed that in modes 1 and 2 the predominant effect when considering the Strouhal number change is due to velocity ratio r, whereas in modes 3 and 4, the Reynolds number increase generates a higher variation in Strouhal number. This is due to difference in the fluid kinetic energy above and below the splitter plate, which for ratios 3 and 4 is 8 and 15 times the kinetic energy below the splitter plate respectively. On the other hand, as Reynolds number increases from 100 to 200, while maintaining the same two ratios, the value of kinetic energy increase between above and below the splitter plate, is respectively 32 times and 60 times the kinetic energy below the splitter plate at Re=100.

Based on understanding of the global nature of flow, the velocity ratio, r is the primary factor influencing the flow, since the onset of various modes of dissipation occur irrespective of the Reynolds number and is also the important contributor of the shear stresses induced into the flow by the upstream mixing layer. The effects of Reynolds number on the flow characteristics is secondary and is considerable in some cases studied.

1.5 Summary:

The wake and mixing layer interactions analyzed in the present study are primarily dependent on the velocity ratios and four different modes of vortex dissipation were observed as the velocity ratio increases from 1.5 to 4. Vortex shedding mechanism in mode 1 was similar to the flow past a square cylinder with shedding of positive and negative moment vortices alternatively due to smaller velocity ratios. But in the case of modes 2, 3 and 4, only negative vortices are shed downstream and the positive moment vortices are dissipated in the form of Kelvin-Helmholtz instabilities. The onset of Kelvin-Helmholtz instabilities in the wake occurs at velocity ratio 2, independent of the upstream Reynolds number and length, ul. Physical characteristics of the flow such as upstream mixing layer, stagnation point oscillation amplitude, vortex shedding pattern, Strouhal number and average lift and drag remain constant in a given mode. The tendency for the free shear layer to separate before reaching the lower vertex of leading edge, increases with the increase of ratio r. It was observed that Stagnation point moves upwards on the square cylinder front face as ratio r increases. A sudden variation in the position of the stagnation point was observed from mode 1 to mode 2 due to the change in the vortex shedding mechanism. Since as the instability of the upstream mixing layer increases as the flow progresses from mode 2 to 4 the stagnation point oscillation amplitude also increases.

Acknowledgement:
The first author would like to acknowledge the work carried out during the Bachelor of Technology thesis at the Department of Mechanical Engineering, Indian Institute of Technology, Guwahati, has inspired and helped in the research carried out in this study. He is thankful for the knowledge acquired in CFD at the institute during the Bachelor Degree program in Mechanical Engineering. The first author also sincerely acknowledges the computing facility of the Department of Mechanical engineering at the institute, for acquiring valuable experience in developing the CFD programs and understanding different numerical methods.

References:

Ayukawa, K., Ochi, J., Kawahara, G., Hirao, T., “Effects of shear rate on the flow around a square cylinder in uniform a shear flow,” J. Wind Engineering and industrial Aerodynamics. 50: 97-106, (1993).

Bearman, P.W., “Investigation of the flow behind a two-dimensional model with a blunt trailing edge and fitted with splitter plates,” J. Fluid Mechanics 21:2, 241-255, (1965).

Bearman, P.W., “On vortex street wakes,” J. Fluid Mechanics 28:4, 625-641, (1967).

Bhattacharyya, S., Maiti, D.K., “Shear flow past a square cylinder near a wall.” International Journal of Engineering Science 42, 2119-2134, (2004).

Bhattacharyya, S., Maiti, D.K., “Vortex shedding suppression for laminar flow past a square cylinder near a plane wall: a two-dimensional analysis,” Acta Mechanica 184: 15-31, (2006).

Bosch, G., Kappler, M., Rodi, W., “Experiments on the flow past a square cylinder placed near a wall,” Experimental thermal and fluid Science. 13: 292-305, (1996).

Bosch, G., Rodi, W., “Simulation of vortex shedding past a square cylinder near a wall,” Int. J Heat and Fluid Flow. 17: 267-275, (1996).

Bosch, G., Rodi. W., “Simulation of vortex shedding past a square cylinder with different turbulent models”. Int. J Num. Meth. Fluids 28: 601-616, (1998).

Breuer, M., Bernsdorf, J., Zeiser, T., Durst, F., “Accurate computations of the laminar flow past a square cylinder based on two different methods: Lattice-Boltzmann and Finite-volume,” Int. Journal of Heat and Fluid Flow. 21: 186-196, (2000).

Cheng, M., Tan, S.H.N., Hung, C., “Linear shear flow over a square cylinder at low Reynolds number,” Physics of Fluids 17: 078103-1/4, (2005).

Cheng, M., Whyte, D.S., Lou, J., “Numerical simulation of flow around a square cylinder in uniform-shear flow,” Journal of Fluids and Structures. 23: 207-226, (2007).

Davis, R.W., Moore, E.F., “A numerical Study of vortex shedding from rectangles,” J Fluid Mech. 116; 475-506, (1982).

Davis, R.W., Moore, E.F., Purtell, L.P., "A numerical-experimental study of confined flow around rectangular cylinders," Phys. Fluids. 27: 46-59, (1984).

Doolan, C.J., "Flat-plate interaction with the near wake of a square cylinder," AIAA Journal. 47;2: 475-478, (2009).

Franke, R., "Numerische Berechnung der instationären Wirbelablösung hinter zylindrischen Körpern," Ph.D. Thesis, University of Karlsruhe. (1991).

Franke, R., Rodi, W., Schonung. B., "Numerical calculation of laminar vortex shedding flow past cylinders," Journal of wind energy and industrial Aerodynamics. 35, 237-257, (1990).

Gerrard, J.H. "The wakes of cylindrical bluff bodies at low Reynolds number", Phil. Trans soc. London. 288: 1354, 351-382 (1978).

Harlow, F.H., Welch. J.E., "Numerical calculation of time-dependent viscous incompressible flow of fluid with free surface". Physics of Fluids. 8, 2182-2189. (1965).

Huang, L.S., Ho C.M., "Small-scale transition in a plane mixing layer", J Fluid. Mech. 210, 475-500, (1990).

Hwang, R.R., Sue. Y.C., "Numerical simulation of shear effect on vortex shedding behind a square cylinder," Int. J. for Numerical Methods in Fluids. 25:12, 1409-1420, (1997).

Hwang, R.R., Yao, C., "A numerical study of vortex shedding from a square cylinder with ground effect," J. Fluids Engineering, 119:3, 512-518, (1997).

Islam, S.U.I., Zhou, C.Y., Shah, A., Xie, P., "Numerical simulation of flow past rectangular cylinders with different aspect ratios using the incompressible Lattice Boltzmann method," Journal of Mechanical Science and Technology, 26:4, 1027-1041, (2012).

Jordan, S.K., Fromm, J.E., "Laminar flow past a circle in a shear-flow," Physics of Fluids, 15:6, 972, (1972).

Kelkar, K.M., Patankar, S.V., "Numerical prediction of vortex shedding behind a square cylinder," International Journal for Numerical Methods in Fluids, 14, 327-341, (1992).

Kiya, M.; Tamura, H., Arie, M., "Vortex shedding from a circular cylinder in moderate-Reynolds number shear flow," J Fluid Mech, 141:4, 721-735, (1980).

Kwon, T.S.; Sung, H.J., Hyun, J.M., "Experimental investigation of uniform-shear flow past a circular cylinder," J Fluids. Eng, 114, 457, (1992).

Lankadasu, A., Vengadesan, S., "Onset of vortex shedding in planar shear flow past a square cylinder," Int. Journal of Heat and Fluid Flow, 29, 1054-1059, (2008).

Lesage, F.; Gartshore, I.S., "A method of reducing drag and fluctuating side force on bluff bodies," Journal of Wind Engineering and Industrial aerodynamics, 25, 229-245, (1987).

Liou, T., Chen, S., Hwang, P., "Large eddy simulation of turbulent wake behind a square cylinder with a nearby wall," J Fluids Engineering, 124:1, 81-90, (2001).

Li, G., Humphrey, J.A.C., "Numerical Modelling of confined flow past a cylinder of square cross-section at various orientations," Int. Journal of Numerical Methods in Fluids, 20, 1215-1236, (1995).

Luo, S.C., Tong, X.H., Khoo, B.C., "Transition phenomena in the wake of a square cylinder," J. of Fluids and Structures, 23, 227-248, (2007).

Luo, S.C., Chew, Y.T., Ng, Y.T., "Characteristics of square cylinder wake transition flows" Physics of Fluids, 15, 2549 (2003).

Malekzadeh, S., Sohankar, A., "Reduction of Fluid forces and heat transfer on a square cylinder in a laminar flow regime using a control plate," Int. Journal of Heat and Fluid flow, 34, 15-27, (2012).

Mukhopadhyay, A., Biswa, G., Sundararajan, T., "Numerical Investigation of confined wakes behind a square cylinder in a channel," International Journal for Numerical Methods in Fluids, 14, 1473-1484, (1992).

Mukhopadhyay, A., Venugopal, P., Vanka, S.P., "Numerical study of vortex shedding from a circular cylinder in linear shear flow," J Fluid Engineering, 121:2, 462-468, (1999).

Nakamura, Y., "Vortex shedding from bluff bodies with splitter plates," Journal of Fluids and Structures, 10, 147-158, (1996).

Okajima, A., "Strouhal numbers of rectangular cylinders," J Fluid Mech, 123, 379-398, (1982).

Okajima, A., "Numerical simulation of flow around rectangular cylinders," J. Wind Eng. Ind. Aerodyn, 33, 171-180, (1990).

Okajima, A., Ueno, H., Sakai, H., "Numerical Simulation of Laminar and Turbulent Flows around Rectangular Cylinders," Int. Journal for Numerical Methods in Fluids, 15, 999-1012, (1992).

Roberts, G.O., "Computational meshes for boundary layer problems," Proceedings of the second international conference on numerical methods and fluid dynamics, Lecture notes in physics, 8, 171-177, Springer-Verlag New York, (1971).

Robicaux, J., Balachandar, S., Vanka, S.P., "Three dimensional Floquet instability of the wake of square cylinder," Physics of Fluids, 11:3, 560-578, (1999).

Roshko, A., "On the development of turbulent wakes from vortex streets," NACA Technical Note, No: 1190, (1954).

Saha, A.K., Biswas, G., Muralidhar, K., "Two dimensional study of the turbulent wake behind a square cylinder subject to uniform shear," J. Fluid Engineering, 123:3, 595-603, (2001).

Sakamoto, H., Tan, K., Haniu, H., "An optimum suppression of fluid forces by controlling a shear layer separated from a square prism," ASME Journal of Fluids Engineering, 113:2, 183-189, (1991).

Sakamoto, H., Tan, K., Takeuchi, N., Haniu, H., "Suppresion of fluid forces acting on a square prism by passive control," ASME Journal of Fluids Engineering, 119, 506-511, (1997).

Salinas-Vazquez, M., Vicente, W., Barrera, E, Martinez, E. "Numerical Analysis of the drag force of the flow in a square cylinder with a flat plate in front". Revista Mexicana de Física, 60, 102-108 (2014).

Sau A. "Hopf bifurcations in the wake of a square cylinder", Physics of Fluids, 21, 034105 (2009).

Scarano, F., Poel, M.C., "Three-dimensional vorticity pattern of cylinder wakes," Exp. Fluids, 47, 69-83, (2009).

Shair, F.H., Grove, A.S., Petersen, E.E., Acrivos, A., "The effect of confining walls on the stability of the steady wake behind a circular cylinder," J Fluid Mechanics, 17:4, 546-550, (1963).

Sohankar, A., Davidson, L., Norberg, C., "Numerical simulation of unsteady flow around a square two dimensional cylinder," 12th Australian Fluid Mechanics Conference, University of Sydney, Australia, 517-520, (1995).

Sohankar, A., Norberg, C., Davidson. L., "Numerical Simulation of Unsteady low-Reynolds number flow around Rectangular cylinders at incidence," Journal of Wind Engineering and Industrial Aerodynamics, 69:71, 189-201, (1997).

Sohankar, A., Norberg, C., Davidson, L., "Low Reynolds number flow around a square cylinder at incidence: Study of blockage, onset of vortex shedding and outlet boundary condition," Int Journal for Numerical Methods in Fluids, 26, 39-56, (1998).

Sohankar, A., Norberg, C., Davidson, L., "Simulation of three-dimensional flow around a square cylinder at moderate Reynolds numbers," Phys. Fluids, 11, 288-306, (1999).

Sudhakar, Y., Vengadesan, S., "Vortex shedding characteristics of a circular cylinder with an oscillating wake splitter plate," Computers & Fluids, 53, 40-52, (2012).

Sukri, M.A.M., Doolan, C.J., Wheatley,V., “Low Reynolds number flow over a square cylinder with a splitter plate,” Phys. Fluids, 23, 033602, (2011).

Sukri, M. A. M., Doolan, C.J., Wheatley, V., “Low Reynolds number flow over a square cylinder with a detached flat plate,” International Journal of Heat and Fluid Flow, 36, 133-141, (2012).

Sumner, D., Akosile, O.O., “On uniform planar shear flow around a circular cylinder at subcritical Reynolds number,” J. Fluids and Structures, 18, 441-454, (2003).

Suzuki, H., Inoue, Y., Nishimura, T., Fukutani, K., Suzuki, K., “Unsteady flow in a channel obstructed by a square rod. (crisscross motion of vortex),” Int. Journal of Heat and Fluid Flow, 14:1, 2-9, (1993).

Wang, X.K., Tan, S.K., “Comparison of flow patterns in the near wake of a circular cylinder and a square cylinder placed near a plane wall,” Ocean Engineering, 35, 458-472, (2008).

Williamson, C.H.K., “Vortex Dynamics in the Cylinder Wake,” Annu. Rev. Fluid Mech, 28, 477-539, (1996).

Xu, Y., Dalton, C., “Computational force on a cylinder in a shear flow,” Journal of Fluids and Structures, 15, 941-954, (2001).

Yoshida, T., Watanabe, T., Nakamura, I., “Numerical Analysis of open boundary conditions for incompressible viscous flow past a square cylinder,” Transactions of JSME, 59, 2799-2806, (1993).

Zdravkovich, M.M., “Flow around Circular Cylinders. Fundamentals,” Oxford University, New York, 1, (1997).

Zhou, L., Cheng, M., Hung, K.C., “Suppression of fluid force on a square cylinder by flow control,” Journal of Fluids and Structures, 21, 151-167, (2005).

2

Laminar flow over a Backward facing Inclined step

Abstract:
In this chapter. two dimensional flow over a backward-facing-inclined step in laminar flow regime is analyzed. The inspiration for the present work is derived from the fact that in automobile industry, analyzing the flow over an inclined step shall help in understanding the characteristics of the rear vehicle wake. A considerable percentage of the energy needed to propel the vehicle is dissipated by the vorticity generated in the rear of the vehicle, hence it is of utmost importance to understand the properties of the wake. The flow over a backward step is initially analyzed and the results are compared with the existing literature to validate the code developed. The inclined step simulations were carried out by varying different aspects of the geometry i.e. different tilts, several upstream lengths and a range of different Reynolds numbers. Critical Reynolds numbers for vortex shedding in the wake of different step inclinations have been analyzed for all cases studied. A discussion on the time-averaged drag and lift coefficients as a function of Reynolds number and for all cases undertaken, are among the results presented. Among the conclusions, it is particularly interesting that the inclination angle of 15º was found to be the critical angle for vortex shedding, after which critical Reynolds number remains constant.

Nomenclature:

a	Height of the inclined step	(m)
C_D	Drag coefficient	
C_L	Lift coefficient	
F_D	Dimensional drag force	(N)

F_f	Flux through face f of the control volume	
F_L	Dimensional lift force	(N)
F_p	Dimensional normal force	(N)
F_s	Dimensional shear force	(N)
h	Height of the non-orthogonal physical domain	
l	Length of the non-orthogonal physical domain	
L_r	Non dimensional vortex recirculation length	
$\hat{n}$	Outward normal of the surface S	
p	Non dimensional Pressure	
Re	Reynolds number	
S	Surface onto the control volume	
t	Non-dimensional Time	
ul	Upstream Length of the physical domain	
u	Non-dimensional Velocity X direction	
U	Free stream velocity in X direction at the inlet	(m/sec)
v	Non-dimensional Velocity Y direction	
$\forall$	Control Volume	(m^3)
x	Non-Dimensional Eulerian coordinates in horizontal direction	
x_p	Dimensional horizontal coordinate of the physical domain	(m)
y	Non-Dimensional Eulerian coordinates in vertical direction	
y_p	Dimensional vertical coordinate of the physical domain	(m)
δ	Non-Dimensional Boundary Layer thickness on the upstream surface	
η	Non-dimensional coordinates of transformed domain in vertical direction	
θ	Angle of inclination	(deg)
ξ	Non-dimensional coordinates of transformed domain in horizontal direction	

2.1. Introduction:

In the present study a two dimensional flow over a backward facing inclined step in laminar flow regime is analyzed. Most of the research undertaken until now has been focused on studying the flow over a backward-facing step. As a matter of fact, a comprehensive analysis of the flow over an inclined backward facing step has not been carried out. Flow past an inclined step is expected to have similarities to that of the backward facing case, hence this study was carried out to analyze the vortex dynamics associated with inclined step configurations. A brief introduction of some important research carried out on backward facing step and backward facing inclined step is presented in the following section.

2.1.1 Flow over a Backward-Facing Step:

The interest in studying the flow over a backward facing step was intensified with the experimental and numerical work of Armaly et al (1983). They presented a detailed experimental investigation in a backward-facing step geometry located inside a rectangular channel for an expansion ratio H/h=1.94, h being the inlet channel height and H the outlet channel height, an aspect ratio W/h=35 and Reynolds numbers ranging from 70 to 8000 were evaluated, W is the downstream channel length measured from the step. The flow appeared to be three-dimensional above Reynolds numbers close to 400. Around this Reynolds number, they observed a discrepancy in the primary recirculation length between the experimental results and the numerical predictions. Also, around this Reynolds number, a secondary recirculation zone was observed at the channel upper wall. They also conjectured that the discrepancy between the experimental measurements and the numerical prediction was due to the secondary recirculation zone which perturbed the two-dimensional character of the flow. The normalized value of the reattachment length showed a peak at Re 1200. The decrease in recirculation length beyond a Reynolds number of 1200 was attributed to the effect of Reynolds stresses. Flow was found to be transitional for Reynolds numbers between 1200 and 6600.

Kim and Moin (1985) computed the flow over a backward-facing step using a method which was second-order accurate in both space and time. They found a dependence of the reattachment length on Reynolds number in good agreement with the experimental data of Armaly et al (1983) up to about Re=500. At Re=600 the computed results of Kim and Moin (1985) started to deviate from the experimental values. The difference was attributed to the three-dimensionality of the experimental flow around a Reynolds number of 600. Gartling (1990) developed a solution procedure using a Galerkin- based finite-element method for steady incompressible flow over a backward-facing step geometry. His results compared well with the results from Kim and Moin (1985) especially with respect to the bottom wall separation zone. Kaiktsis et al (1991) identified the bifurcation of two-dimensional laminar flow to three-dimensional flow as the primary source of discrepancies appearing in comparisons of numerical predictions and experimental data. They also observed that irrespective of the accuracy of the numerical schemes, the experimentally measured recirculation lengths were consistently under-estimated above a Reynolds number of Re=600. They found that all unsteady states of the flow were three-dimensional and developed for Reynolds number Re>700. Furthermore, they detected that the downstream flow region was excited through the upstream shear layer with a characteristic frequency f1. The supercritical states Re>700 were found to be periodic with another frequency f2.

Durst et al (1993) studied experimentally and numerically the formation of secondary separation zones in the two-dimensional numerical simulations of a symmetric sudden-expansion flow. Both the experiments and the predictions confirmed a symmetry-breaking bifurcation leading to one short and one long primary separation zone. Kaiktsis et al. (1996) revisited the backward-facing step flow and found that the unsteadiness in step flow was created by convective instabilities. The flow was found to be convective unstable for Reynolds numbers ranging $700 \le \mathrm{Re} \le 2500$. A conclusion of this study was that the upstream-generated small disturbances propagated downstream at exponentially amplified amplitude with a space-dependent speed. Williams and Baker (1997) investigated the laminar flow over three dimensional backward-facing step geometry. They carried on a full three-dimensional simulation of the geometry used by Armaly et al (1983) for 100<Re<800 and found that the simulation correctly predicted the reattachment lengths and confirmed the effect of three-dimensionality. They also found that the side walls resulted in the creation of a wall jet, located at the lower channel wall and pointing from the side wall towards the channel mid-plane.

Heenan and Morrison (1998) conducted experiments for a Reynolds number (Re_S) based on the step height S of 1.9×10^5 and suggested that while the flow was likely to be convectively unstable over a large region, the global unsteadiness, driven by the impingement of large eddies at reattachment was the cause of low frequency oscillations called flapping. Le et al (1997) conducted direct numerical simulations of turbulent flow over a backward-facing step at a Reynolds number of $\mathrm{Re}_S = 5100$ based on step height S and inlet free-stream velocity, the expansion ratio was of 1.2. The instantaneous velocity fields revealed that the variation of reattachment length in the spanwise direction oscillated about a mean value of 6.28 S. The flow exhibited strong streamwise vortical structures. Lee and Mateescu (1998) performed an experimental and numerical investigation of air flow over a two-dimensional backward-facing step for $\mathrm{Re} \le 3000$. The hot film sensor measurements at Re=805 and expansion ratio H/h=2.0 were found to be in agreement with their numerical predictions with respect to the locations of the separation and reattachment points on the upper and lower walls.

Chiang and Sheu (1999) studied numerically three dimensionally and under laminar conditions, the flow behind the same backwards facing step geometry used by Armaly et al (1983). Several Reynolds numbers and aspect ratios were considered. They found that the flow developed a two dimensional like profile only when the channel width was increased up to 100 times the step height, therefore establishing the boundaries of three dimensional flow. Barkley et al (2002) carried out a three-dimensional linear stability analysis for the backward-facing step flow with an expansion ratio of 2. They showed that the primary bifurcation of the steady two-dimensional flow was a steady three-dimensional instability. Furthermore, the critical Eigen-mode was localized as the primary recirculation region consisting of a flat roll. Nie and Armaly (2002) presented the results of laminar forced convection flow in backward-facing step geometry. They showed that the size of the primary recirculation zone and the maximum Nusselt number increase with increasing step height. They also indicated that a jet-like flow developed in the separating shear layer downstream from the step. This jet-like flow and its impingement with the step wall are responsible from developing a minimum in the reattachment length and a maximum in the Nusselt number.

Armaly et al. (2003), reported the velocity measurements for three-dimensional laminar separated airflow adjacent to a backward-facing step using two-component laser Doppler velocimeter. The investigation revealed that a swirling jet like flow developed near the sidewall in the separating shear layer, and reverse and recirculation flow regions developed adjacent to both the sidewall and the step. These regions increased in size with the increase in Reynolds number. Velocity distributions measured at various planes downstream from the step, were presented in the paper. They found that the flow was laminar and steady for Reynolds number smaller than 500. Some interesting flow features not visible in the two-dimensional studies were also observed in the experimental analysis presented in the paper.

Kung et al (2004) performed a numerical study using a step located inside a rectangular closed channel, fluid was regarded as viscoelastic. They considered the effect of mixed convection. It was found that the reattachment length increased with the increase of Reynolds number and the increase of inclination angle, the maximum was located for inclination angles between 150º and 180º. Reattachment length increased with the decrease of fluid elastic coefficient. At an inclination angle of 120º they found a second recirculation zone located just below the top plate. This second recirculation zone was on the bottom plate whenever the inclination angle was 180º. Kim et al. (2005), evaluated the flow over a backward facing step under turbulent conditions. The authors analyzed several near-wall treatment methods and turbulence models. They concluded saying that to properly predict the flow pattern it is necessary a proper combination of turbulence models and near wall treatment methods. Schäfer et al. (2009), used direct numerical simulation to evaluate the fluid performance over a backward facing step in the transitional regime $Re_D = 6000$, D being the hydraulic diameter of the inlet channel. Their work focused in investigating the downstream vortex oscillations and reattachment length. They concluded that the vortical structures generated in the unstable shear layer, is the cause of flow flapping from reattachment to separation of downstream flow.

Reddeppa and Gai (2011) studied the flow configuration as well as heat transfer of a backward facing step at Hypersonic Mach number of 7.6. Under these conditions they found that flow needed about 10 steps heights measured downstream of the backwards facing step to become reattached. Barri and Andersson (2010) applied direct numerical simulation to study the flow reattachment and separation over a backward facing step under turbulent conditions and when flow was affected by rotation. They realized that as rotation rate increased, the size of separation bubble decreased. Flow rotation tended to stabilize and damp turbulence. They observed that orientation of vortex cells and roller eddies were disrupted by the enhanced flow turbulence. Premixed combustion flow over a backward facing step, was investigated by Park and Ko (2011). Flow was regarded as turbulent and large eddy simulation along with a dynamic sub-grid G-equation flamelet model was employed to model the fluid. The objective of their work was to validate the G-equation flamelet model for this kind of flow. They obtained good agreement between experimental and simulated results.

The particularities of three-dimensional flow separation in rectangular ducts sudden expansions, was investigated numerically by Mistrangelo (2011). He derived scaling laws which described the evolution of the reattachment length of the vortical structures appearing downstream of the expansion. The fluid studied was liquid metal. Lanzerstorfer and

Kuhlmann (2012) studied the flow stability over a backward facing step. Flow was considered as two dimensional and incompressible, different expansion ratios were studied. Stability analysis showed that basic flow became unstable to different three-dimensional modes which depended on the expansion ratio. For large expansion ratios they identified an elliptical instability mechanism, instabilities were amplified by the strong shear generated at the sharp corner of the step.

2.1.2 Backward facing inclined step:

Weber and Danberg (1992) are among the first papers to be found in this category. These authors studied experimentally the subsonic turbulent flow evolution onto a backward facing inclined step. They studied three different inclination angles and were able to measure mean velocities using a hot-film anemometer. It needs to be pointed out that the step inclination angle was measured horizontally and versus the flow direction. Kaltenbach and Janke (2000) investigated the effect of sweep on the transitional separation bubble behind a backward-facing step using direct numerical simulation. In this context they also performed simulations for the un-swept case at $Re_s = 3000$, S being the step height. The flow upstream of the step was laminar and shear-layer transition took place prior to reattachment. Comparing the results for zero sweep from two simulations using either steady inflow conditions or the same velocity profiles with superimposed low-amplitude random disturbances, they found out that the flow field downstream of the step is very sensitive to the type of inlet boundary conditions. The changes in global flow features which are due to sweep, seem to be fairly independent of the specific transition scenario. Seven different sweep angles were studied inclination angle being measured versus the same reference as in the paper from Weber and Danberg (1992). In a further paper, Kaltenbach (2004) used Large Eddy Simulation to study turbulent flow over a swept backward facing step when $Re_s = 5000$ and for a range of swept angles. The configuration studied was the same as the one presented in Kaltenbach and Janke (2000) and Weber and Danberg (1992). He observed that the inclusion of a swept affected the dynamics of the near wall region upstream of the reattachment, upstream conditions strongly influenced flow dynamics, especially in the first half of the separation region.

Three dimensional laminar flow flowing inside a rectangular duct and over an inclined step was numerically studied in Chen et al (2006), the channel bottom wall was heated with constant head flux. Inclination slant angles of 0º, 45º, 60º and 75º were considered, angles were measured along a plane perpendicular to the flow field. Temperature, Nusselt number distributions, streamlines configuration and saddle and nodal points as a function of the inclination angle, were presented. The location where the streamwise velocity component was cero, at the center of the duct, changed from a saddle point to a nodal point as the inclination angle decreased. For small inclination angles, the maximum Nusselt number was located at the center of the duct. A single Reynolds number of 343 was used to perform the simulations.

Gandjalikhan Nassab et al (2009), studied the turbulent forced convection of flow progressing inside a rectangular duct where an inclined forward step was located. Flow was regarded as turbulent and they used the k-ε turbulence model to solve Navier-Stokes equations, non-orthogonal grid was transformed to orthogonal via using the Schwarz-Christoffel transformation. The channel bottom wall was heated at a constant temperature. They concluded saying that the step length and inclination angle played a decisive role in the fluid hydrodynamic behavior. El-Askary (2011) simulated supersonic turbulent flow over a two dimensional inclined backwards facing step for a single slant angle of 25º and an upstream Mach number of 2.9. He demonstrated that the use of Large Eddy simulation allowed analyse the supersonic flow clearly showing the locations where expansion waves and shock waves appeared. The near-wall flow over inclined and curved backward and forward facing steps was recently measured via using Particle image velocimetry (PIV) by Nguyen et al (2012). In this paper they presented an extension of the IPIV measuring technique previously developed by the authors. The new technique allows measuring tangential and wall normal velocity components and allows measuring the three velocity components when applied to stereoscopic PIV.

2.1.3 Bodies with geometry similar to Backward facing step in the rear:

Cogotti (1998), studied experimentally the aerodynamic characteristics of a full scale simplified car model. Different parts of the car were modified to investigate the ground effect. This was the first time a systematic study into ground effect at full scale was published. Large scale unsteady structures in the wake of a real car model were experimentally investigated by Sims-Williams et al (2001). They were able to measure symmetric and anti-symmetric oscillations in the strength of the rear-pillar vortices. They observed that parameters like the radii of the vehicle surface have a little impact on wake unsteadiness. Unsteady flow was found to be much less periodic than for the two dimensional cases. They estimated that fluctuating forces due to flow unsteadiness will be less than 0.010 on C_D or C_L.

In Khalighi et al (2001), simple devices capable of reducing bluff body aerodynamic drag more than 20%, were presented. The devices were tested experimentally using PIV techniques and numerically via using the unsteady RANS-CFD turbulence model. All simulations were done using the software Fluent. The authors realized that the drag reduction device minimized large-scale turbulent intensity and deflected the underbody flow. Howard and Pourquie (2002), simulated the three dimensional flow around an Ahmed reference model with a rear slant angle of 28º. They used large eddy simulation turbulent model along with a non-structured tetrahedral grid. Flow downstream, vorticity, dynamic drag coefficient, and flow velocity distributions were among the results presented. They observed that at the rear of the body appeared a periodic horseshoe vortex shedding process. In Leinhart et al (2003), flow measurements on an Ahmed body trailing edge were undertaken via using 2-component laser-Doppler anemometer. Two different slant angles of 25º and 35º were evaluated. Fluid used was air and the upstream incoming velocity was of 40 m/s. The authors said that the results obtained should be used to validate CFD turbulent models applied to this geometry. Kapadia et al (2003), numerically studied the flow on the trailing edge of an Ahmed car model with 25º slant angle. Spallart-Allamaras detached eddy simulation hybrid model and One-equation RANS model were used to perform the simulations. The paper also discussed the different turbulence modeling techniques available. Flow structure downstream was perfectly captured, static and dynamic drag coefficients were also analyzed.

Le Good and Garry (2004), presented a thorough review of the different key reference models used in car aerodynamics. They conclude saying that when a researcher choose to use a simple model, existing reference models should be employed. Krajnovic and Davidson (2004), modeled the flow over an Ahmed body with 25º slant angle via using LES, fluid was considered as incompressible, the flow Reynolds number based on the Ahmed body height was $7.68x10^5$. Vortex generation on the car trailing edge was clearly seen; they realized that whenever the Reynolds number was high enough, a further increase of the Reynolds number had a small influence in the separated flow around a car. Vino et al (2005), presented a time-averaged and time-dependent nature of the Ahmed model near- and far-wake experimentally. The use of a new multi-hole probe allowed for measurement in regions exhibiting large flow angles (including flow reversals), and high levels of unsteadiness, allowing examination of flow regions previously difficult to investigate. Although time-averaged results of the far-wake showed good agreement with previously published work, the near-wake structure was found to be somewhat different, with much of the inconsistency being found in the interaction between a separated region over the slant and the re-circulating flows behind the model. Time-dependant analysis revealed that the shedding behind the model was analogous to vortex shedding behind bluff bodies, with most of the fluctuations confined to the axial direction. In addition, the shedding characteristics on the slant showed very similar behaviour to the vertical base, indicating strong turbulent mixing between the two regions, emphasizing time-averaged findings.

Fares (2006), used the software Power Flow 4.0 to simulate the three dimensional unsteady flow around an Ahmed body via employing the turbulent Lattice Boltzmann model. Two different slant angles of 25º and 35º were studied, air velocity was 40 m/s. Results were compared with the experimental ones done by Leinhart et al (2003), and Becker and Leinhart (2003), obtaining a good agreement. They realized that at 25º angle, vortical structures were clearly seen, while at 35º flow exhibited a separation region. The Ahmed body used by Fares resembled the one used by Howard and Pourquie (2002), but the Fares model considered flow between the Ahmed body bottom and the ground. Guilmineau (2008), studied computationally the flow over an Ahmed body with two slant angles 25º and 35º. He used a flow solver called ISIS and unsteady Reynolds averaged Navier-Stokes equations URANS as turbulence model. Results were compared with other turbulence models. They had a good agreement for slant angle of 35º since the flow was mostly two dimensional, for 25º slant angle the flow was fully three-dimensional and they said further research was needed to properly model such flow.

Schröck et al (2009), studied experimentally the aerodynamic properties over a SAE reference model with rounded rear edge. Measurements were undertaken for turbulent flow conditions and when the incoming flow turbulence was reduced to practically zero, smooth conditions. Analysis of the periodic surface pressure fluctuations in the area where separation occurs as well as flow structures on the car trailing edge were presented. They found that the unsteady structures were modified with the increase of turbulence on the incoming flow. Franck et al (2009), applied LES turbulent model along with Smagorinsky model modified with the Van Driest near wall Damping, to study the flow over an Ahmed body with 12.5 degrees slant angle. The finite element approach was used. In conclusions they said that the model used was feasible to study vehicle aerodynamics. Gaylard (2009), evaluated the pros and cons of using wind tunnels or using CFD approaches to study flow over a real car. The author concluded by saying that CFD models give a valuable information to the designer and therefore have to be considered as a very important tool. Heft et al (2011), Presented a new reference car model called DrivAer body, which was more realistic than the Ahmed body. They applied LES, k-ω-SAS-SST and k-ω-SST turbulence models to both car configurations and compared the results from the Ahmed body with the measurements done by Leinhart et al (2003). They noticed that the steady state RANS simulations performed with the k-ω-SST model was highly dependent on the turbulent parameters of the incoming flow. They concluded by saying that the steady state simulations can't predict the dynamic flow structures generated on a car trailing edge, and therefore the use of unsteady turbulence models like the ones used in their paper is strongly recommended. Heft et al (2012), studied experimentally the flow configuration over the new car reference model introduced in Heft et al (2011). Three different car configurations and four incoming flow speeds of 10, 20, 30 and 40 m/s were evaluated. Drag and pressure coefficients as well as pressure distributions were presented. Comparisons between the drag coefficient of different real car models and the new reference model were undertaken.

It can be said that a detailed analysis of inclination angle effects on flow past an inclined step, in laminar regime, has not been carried out with the different flow parameters deeply analyzed. This was a major inspiration for the present study along with the compelling similarity of the incline step geometry with the automobiles. Although the flow over automobiles is turbulent, the present study of the inclined step was carried out in laminar regime as a preliminary step towards understanding the effects of inclination the flow past the step.

2.2. Problem Statement:

Figure 2.1 presents the physical domain of the inclined step. In order to determine the effect of boundary layer on the downstream vorticity, several upstream lengths were evaluated. On the right hand side of the horizontal surface, it is found the inclined step. For the present study, several inclination angles θ ranging from 5 to 75 degrees have been studied, also a comparison with previous studies undertaken by other researchers at $\theta=0$ degrees was carried out. Figure 2.1 also presents the dimensions of the inclined step and the boundary conditions used for the simulation. No slip boundary condition was used at all solid boundaries. As the flow is unconstrained at the top, a free slip boundary condition was used, and the open boundary was located at a distance of 8a, according to Sohankar et.al. (1995). Neumann boundary condition was used at the outlet. In order to simulate a far field downstream boundary, the outlet boundary was located at a distance of 20a, downstream of the inclined step lower vertex, as suggested by Sohankar et.al. (1998).

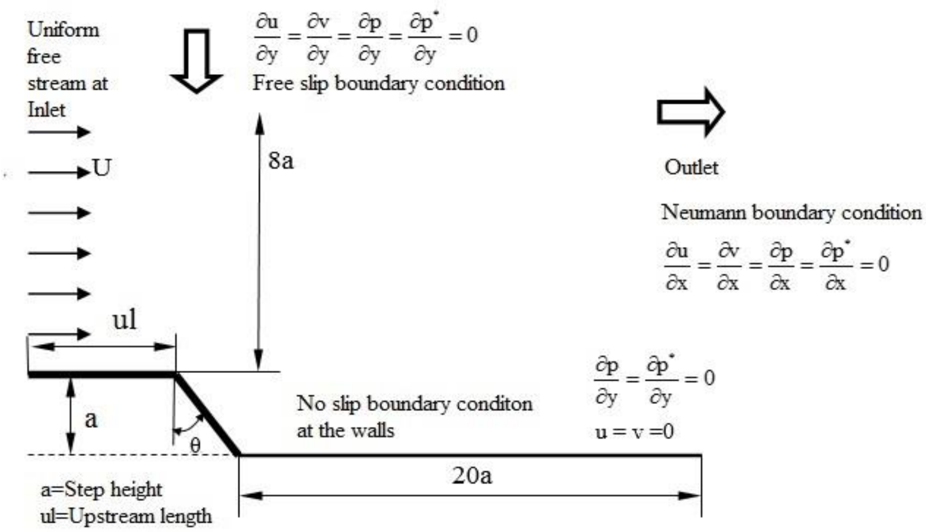

Figure 2.1: Physical Domain of the Inclined Step

Figures 2.2(a), (b), present the grid of the proposed problem. A non-orthogonal non uniform structured grid was chosen, since it is most appropriate to simulate the flow dynamics in the presence of an inclined edge. Figure 2.2(b), shows the three sub domains used to generate the grid. The first sub domain is the region above the upstream horizontal surface, the second sub domain is the region starting at the vertex where the horizontal and inclined step meet, and covers the upper right hand side region. The grid region located on the right hand side of the inclined step wall is the third sub domain.

Structured grid has been generated in the three sub-domains using the stretching transformation proposed by Roberts (1971), which refines the grid in the vicinity of the solid walls. The domain on the right hand side of the inclined edge is transformed into an orthogonal domain by using a grid transformation as defined by Anderson (1995).

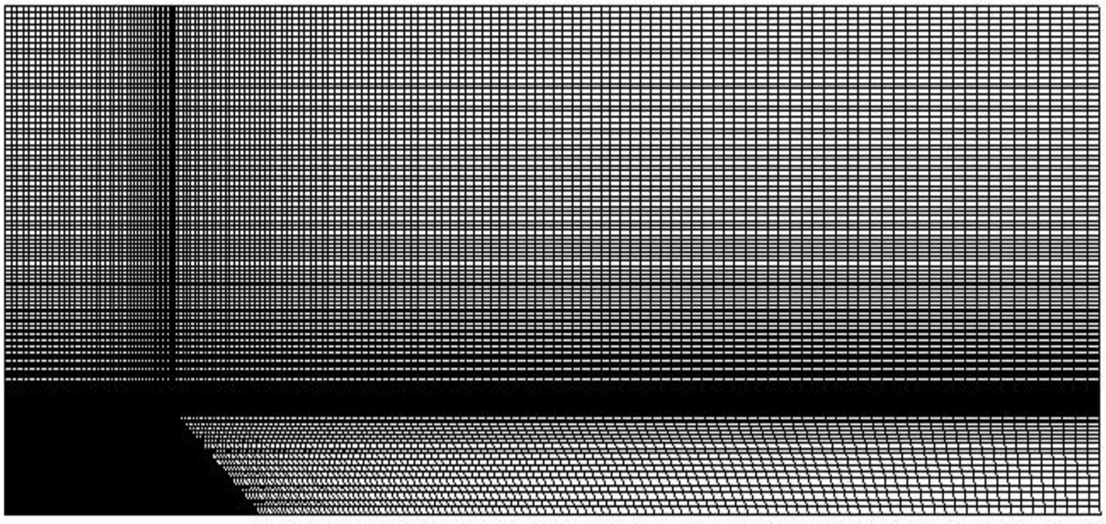

(a)

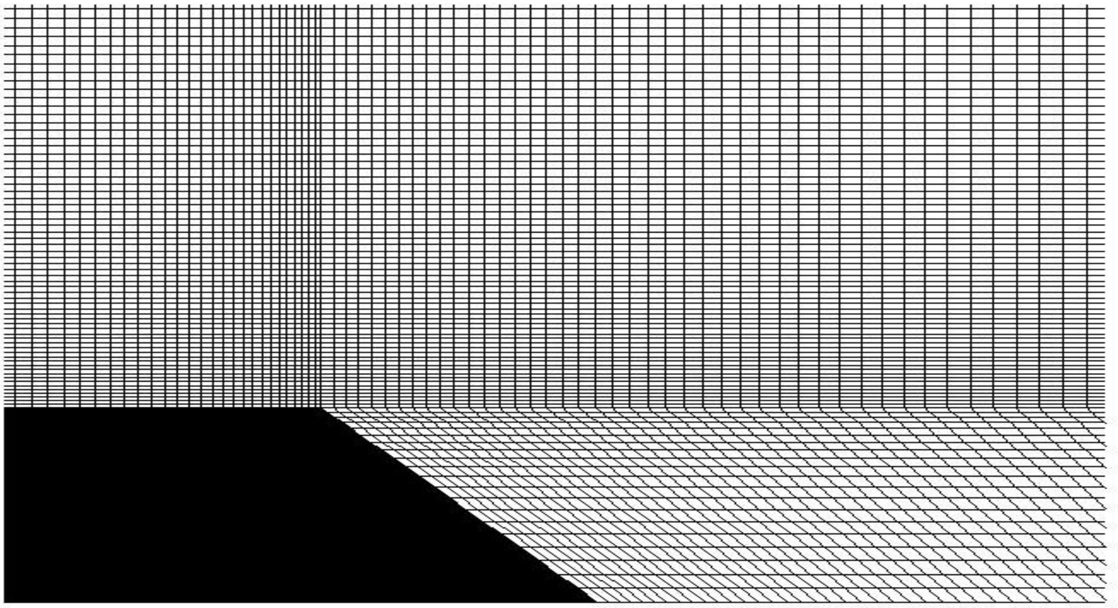

b)

Figure: 2.2(a) Non uniform structured grid for discretization of the domain. 2(b) Closer view of the grid point collocation at the wall of the step for accurate resolution of the boundary layer.

2.2.1 Governing Equations:

Simulations have been done with non-dimensional form of Navier-Stokes equations. To non dimensionalize the equations, the height of the step, a, was taken as the characteristic length, the free stream velocity U was taken as the characteristic velocity, the characteristic pressure was ρU^2, the characteristic time was defined as the characteristic length divided by the characteristic velocity a/U and the characteristic frequency was U/a. Reynolds number was defined as $Re = \frac{\rho U a}{\mu}$; notice that fluid density and viscosity were taken as constant. Flow was considered as isothermal.

The non-dimensional form of the momentum and continuity equations for laminar flow is represented as:

$$\frac{\partial u}{\partial t} + \frac{\partial u\, u}{\partial x} + \frac{\partial vu}{\partial y} = -\frac{\partial p}{\partial x} + \frac{1}{Re}\left(\frac{\partial^2 u}{\partial x^2} + \frac{\partial^2 u}{\partial y^2}\right) \qquad (2.1)$$

$$\frac{\partial v}{\partial t} + \frac{\partial uv}{\partial x} + \frac{\partial vv}{\partial y} = -\frac{\partial p}{\partial y} + \frac{1}{Re}\left(\frac{\partial^2 v}{\partial x^2} + \frac{\partial^2 v}{\partial y^2}\right) \qquad (2.2)$$

$$\frac{\partial u}{\partial x} + \frac{\partial v}{\partial y} = 0 \qquad (2.3)$$

The finite volume approach was chosen for the simulation

2.2.2 Numerical Strategy and Boundary Conditions:

A second-order Adams Bashforth-Crank Nicholson scheme for temporal discretization was applied to Navier Stokes equations in finite volume formulation to obtain equation (2.4). Equation (2.5) is the continuity equation applied over a control volume.

$$\frac{u_{i,P}^{n+1} - u_{i,P}^{n}}{\Delta t} V_P + \left(\frac{3}{2} \sum_f F_f^n u_{i,f}^n - \frac{1}{2} \sum_f F_f^{n-1} u_{i,f}^{n-1} \right) = -\sum_f p_f^n S_{f,i} + \frac{1}{2\,\mathrm{Re}} \left(\sum_f F_{dfi}^{n+1} + \sum_f F_{dfi}^{n} \right) \tag{2.4}$$

$$\sum_f F_f^{n+1} = 0 \tag{2.5}$$

Equations (2.4) and (2.5) were solved by using the bi-conjugate gradient stabilized method. The boundary conditions used in the simulation were depicted in figure 2.1, a brief description of the different boundary conditions follows.

At the inlet, uniform free stream condition for velocity and Neumann boundary condition for pressure were used.

$$u = U, \quad v = 0, \ \frac{\partial p}{\partial x} = 0 \tag{2.6}$$

In all solid boundaries, no-slip boundary condition for velocity and normal gradient condition for pressure was employed.

$$u = 0, v = 0 \text{ and } \nabla p.\hat{n} = 0 \tag{2.7}$$

Where $\hat{n}$ is the unit normal vector perpendicular to the surface.

At the far field, as the present study focuses on the unconfined flow past an inclined step, a free slip boundary was applied at a distance of 8a, measured from the upstream horizontal surface, see figure 2.1.

$$\frac{\partial \phi}{\partial y} = 0; \ \phi = u, v; \ \frac{\partial p}{\partial y} = 0 \tag{2.8}$$

The outlet boundary, right hand side of figure 2.1, posed the biggest difficulty in computational modeling, especially when studying flows with unsteady wake or convecting vortices. The definition of this boundary condition is of paramount importance, since it not only changes the flow pattern but also affects convergence. For the present case the derivative of all dependent variables was taken equal to zero, which is known as Neumann boundary condition (NBC), condition presented in equation (2,9).

$$\frac{\partial \phi}{\partial x} = 0, \ \ \phi = u, v, p; \tag{2.9}$$

The distance between the inclined step bottom edge and outlet boundary, where the Newman boundary condition is applied, was considered as 20a as seen in figure 2.1.

MAC (Marker and Cell) method with velocity and pressure coupling was applied using a predictor-corrector strategy. In the present study, the respective pressure correction factor in all the neighboring cells were also considered, notice that this is a further improvement with respect to the original MAC method and minimizes the error involved in the calculation. In this method the momentum equations are solved to calculate provisional values for the velocity components for the next time step using the predictor step and thereafter calculating the pressure and velocity correction factors for achieving the incompressibility condition of mass conservation.

For the inclined step case, the grid located on the right hand side of the inclined boundary edge, has a non-orthogonal domain, (x,y) this domain was transformed into an orthogonal domain (ξ, η).

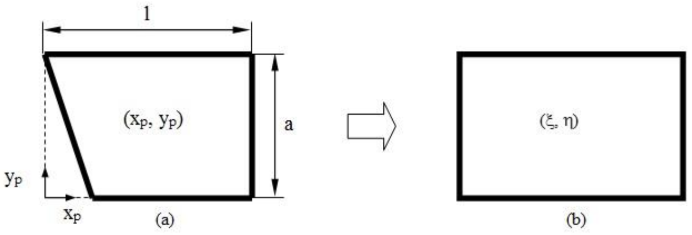

Figure: 2.3. Transformation of the physical domain to computational domain (a) Physical domain (b) Computational domain

The transformation equations used to transform the physical domain to a computational domain are presented as equations (2.10), (2.11) and (2.12).

$$\xi = \left(\frac{x_p - c}{l - c} \right) \tag{2.10}$$

$$\eta = \left(\frac{y_p}{a} \right) \tag{2.11}$$

Where l and a are the length and height of the physical domain as shown in figure 2.3 and c is a constant defined by:

$$c = \left(\frac{a - y_p}{\cot \theta} \right). \tag{2.12}$$

To transform Navier-Stokes equations from non-orthogonal to orthogonal coordinates, the transformation mentioned in Anderson (1995) was used, for the first and second derivatives.

The non-dimensional form of momentum and continuity equations, (2.1) to (2.3), can be transformed into equations in the orthogonal domain, equations (2.13) to (2.15) using transformation equations (2.10) to (2.12)

$$\frac{\partial u}{\partial t}+\xi_x\frac{\partial uu}{\partial x}+\eta_y\frac{\partial vu}{\partial y}=-\xi_x\frac{\partial p}{\partial x}+\frac{1}{Re}\left(\xi_x^2\frac{\partial^2 u}{\partial x^2}+\eta_y^2\frac{\partial^2 u}{\partial y^2}\right) \tag{2.13}$$

$$\frac{\partial v}{\partial t}+\xi_x\frac{\partial uv}{\partial x}+\eta_y\frac{\partial vv}{\partial y}=-\eta_y\frac{\partial p}{\partial y}+\frac{1}{Re}\left(\xi_x^2\frac{\partial^2 v}{\partial x^2}+\eta_y^2\frac{\partial^2 v}{\partial y^2}\right) \tag{2.14}$$

$$\xi_x\frac{\partial u}{\partial x}+\eta_y\frac{\partial v}{\partial y}=0 \tag{2.15}$$

The transformed equations, (2.13) to (2.15), can be discretized using the second-order Adams Bashforth-Crank Nicholson scheme, as it was previously used to discretize the non-dimensional equations (2.1) to (2.3), into (2.4) and (2.5).

2.3. Code Validation:

The code was validated by simulating the flow over a backward step and the results were compared with the results presented in the literature. Figure 2.4 presents the streamline plots for the backward facing step case. The left side plots, present the results obtained from the code developed and the graphs presented on the right hand side, were obtained by Chowdhary and Dhiman (2011). Three Reynolds numbers of 100, 150 and 200 were studied in both cases. The comparison was in complete agreement in all cases studied, flow configuration was very much alike, the downstream vortices were steady in all cases and their respective length was the same in all comparisons undertaken. It is necessary to point out that as the plots presented in the right hand side of figure 2.4 were extracted from Chowdhary and Dhiman (2011), their quality has been compromised when reducing their dimensions. A grid of size (200x150), with 50 and 40 cells on the upstream and inclined surface of the step respectively, was used to simulate the flow in these validation cases.

From the present code, it has also been found, from a further analysis of the backward step geometry and for a flow simulation at Reynolds 498, that downstream vortex flow was steady, on the other hand, when Reynolds number was 500, downstream flow became unsteady and periodic. It therefore can be inferred that the onset of vortex shedding is observed to be around Reynolds number 500, as found originally by Armaly et al (2003), also Chen et al (2006) mentioned this flow behavior. They pointed out that the critical Reynolds number, for flow transition from steady state to unsteady periodic vortex dissipation in the wake of the backward step, was around 500.

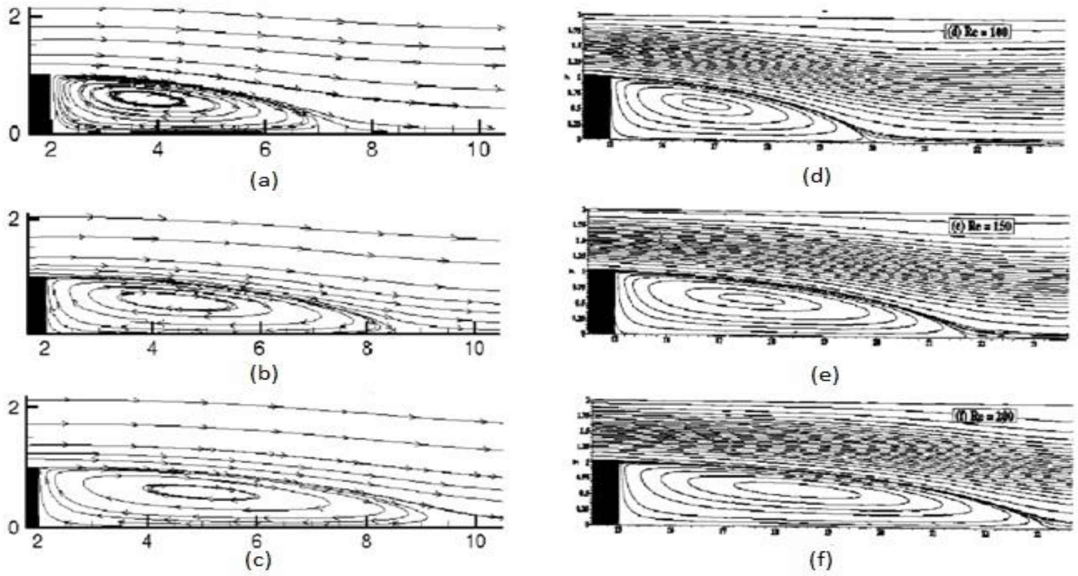

Figure 2.4: Instantaneous Streamline plots for Reynolds Numbers: (a), (d) Re=100, (b), (e) Re=150 and (c), (f) Re=200. Left side plots were generated by the present code, right side plots are presented in Chowdhary and Dhiman (2011).

2.3.1 Effect of Grid Refinement:

A grid refinement study has been carried out on three progressively refined grids, namely 160×140, 200×150 and 220×160 where the number of grid nodes distributed over the inclined edge of the step are 30, 40 and 50, respectively. An inclination angle, $\theta=60^0$ and ul=4a was considered for the grid refinement study at Reynolds number, Re=500. During the refinement, the smallest and the largest cell size on the inclined edge is maintained approximately at 0.02 and 0.033, respectively.

The variation in the drag coefficient, C_D was around 0.8% when the grid was refined from coarsest to the intermediate level. But when the grid was further refined to the finest level, the variation reduced and became close to 0.3%, see table 2.1. However, the non-dimensional frequency of vortex shedding remained constant during the refinement. Therefore based on these results, a grid size of 200x150 was considered for the simulation with ul=2a and 4a and for ul=a, a grid size of 160x150 was used for all Reynolds numbers.

Grid	160x140	200x150	220x160
Drag Coefficient, C_D	0.2093	0.2110	0.2118
Frequency, f	0.05	0.05	0.05

Table 2.1: Results of the grid refinement study

2.4. Results and Discussion:

In order to evaluate the flow over and inclined backwards facing step, the results for various simulations carried out will be presented in this section. Simulations were performed for an inclination angles of, θ = 15º, 30º, 45º, 60º and 75º, three different upstream lengths of ul=a, ul=2a and ul=4a were chosen, to study the boundary layer development on the horizontal surface and also to analyze the effects of boundary layer on the wake of the flow past an inclined step. Firstly the steady state flow will be presented for inclination angles, θ =15º, 30º, 45º, 60º and 75º, upstream channel lengths of ul=4a and Reynolds numbers of 100, 200, 349 and 350. Reynolds numbers 349 and 350 were analyzed to understand the flow transition from steady to unsteady. Simulations for angles of inclination, θ =5º, 10º, 12º, 14º were undertaken to analyze the trend followed in the angles less than θ =15º for attaining criticality. Secondly, the unsteady flow analysis for the same angles and upstream lengths ul=a, 2a and 4a are presented for Reynolds numbers Re = 500 and 800. The temporal averaged and dynamic lift and drag coefficients are also presented in the final part of this section.

2.4.1 Boundary Layer development on the upstream surface, ul:

The development of the boundary layer on the upstream surface length, ul plays an important role in the dynamics of the flow past an inclined step. Three different upstream lengths ul=a, 2a and 4a were simulated to understand evolution and development of the boundary layer and its effects on the flow properties.

For the inclined step geometry with ul=a and all inclination angles a grid of size (160x150 was used with 20 cells on the upstream surface, figure 2.5(d), Similarly for the step with ul=2a and 4a, as observed in figure 2.5(c) and figure 2.5(a, b) respectively for all inclination angles, a grid size of (200x150) was used with 40 and 50 cells respectively on the upstream surface. In all cases, for different upstream lengths and inclination angles, 40 cells have been used on the inclined surface. The non-dimensional time step was considered as 0.001. The same grid size was used in both steady and unsteady flow cases. Figure 2.5 presents instantaneous vector plots over the upstream surface of the step for all different upstream lengths, ul. Figure 2.5(a) and (b) respectively present the boundary layer development for Re=500 and Re=800, for upstream length ul=4a. The non-dimensional boundary layer thickness, δ at the step corner is similar for both cases, with δ≈0.2 as presented in Figure 2.5(a) and (b).

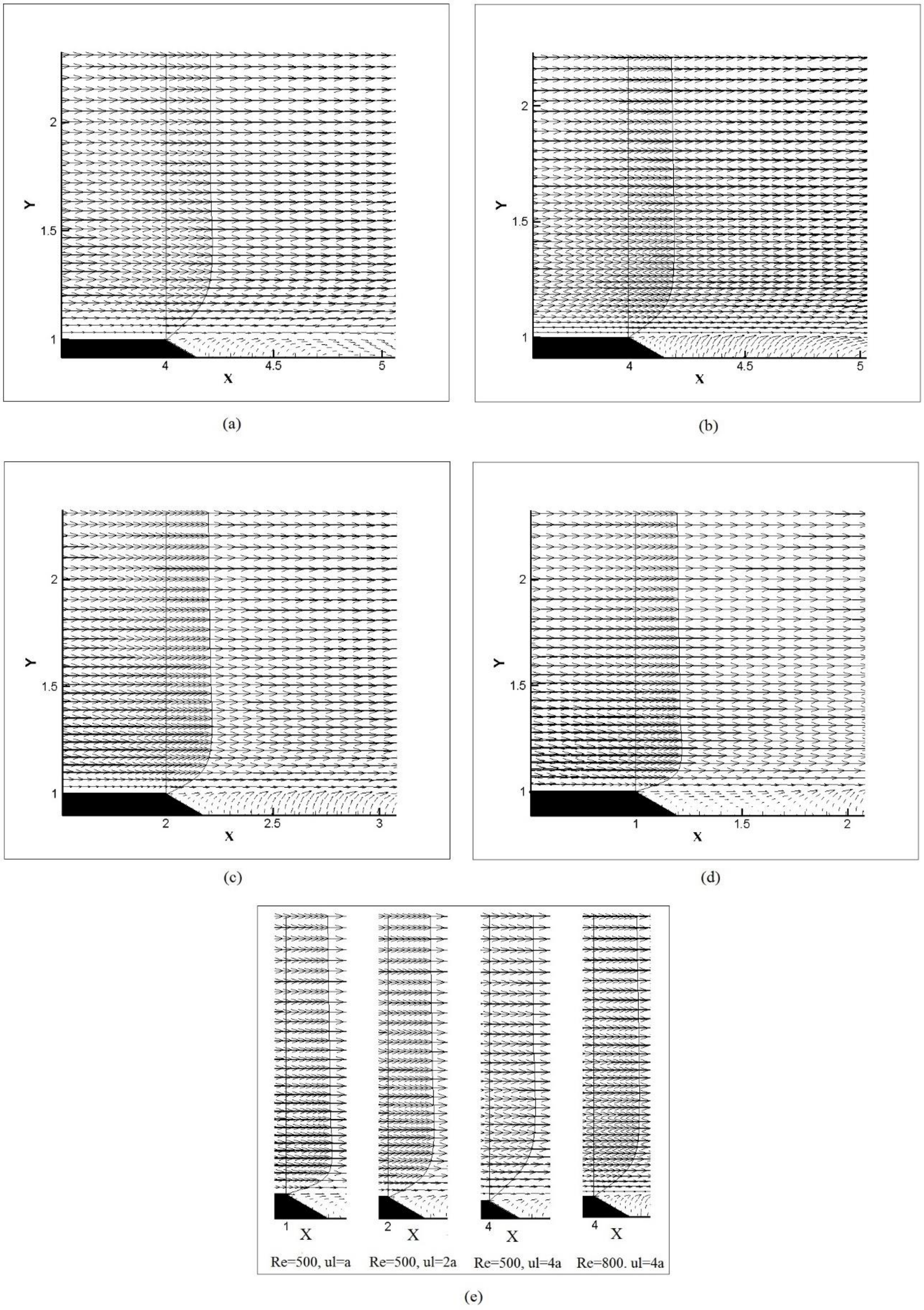

(a) (b) (c) (d) (e)

Figure 2.5: Instantaneous vector plots on the upstream surface, ul for θ=60^{o} (a) Re=500, ul=4a, (b) Re=800, ul=4a, (c) Re=500, ul=2a and (d) Re=500, ul=a (e) Comparison of boundary layer profile development at the inclined step corner.

A similar thickness value of δ≈0.2 can be found for ul=2a in figure 2.5(c), but in figure 2.5(d) for ul=a, the boundary layer thickness, δ reduces to approximately 0.15. This can be attributed to the shorter upstream length, ul=a, which is not sufficient for the complete development of the laminar boundary layer which appears to be fully developed for ul=2a and remains constant until ul=4a. It can be inferred that a minimum of ul=2a is needed for the laminar boundary to develop completely. This can also be seen as a validation for the grid used for simulating different upstream lengths. The non-dimensional width of the cell on the upstream surface is 0.032, the boundary layer thickness for ul=2a and 4a accommodates approximately 6 cells of the refined grid near the upstream surface. In the case of ul=a, about four cells are contained inside the boundary layer at the inclined step corner. The comparison between boundary layer profiles at the inclined step corner for different upstream lengths, ul=a, 2a and 4a is presented in figure 2.5(e). It can be observed from figure 2.5(e) that as the upstream length, ul increases the parabolic profile of the boundary layer is more developed and evident. For ul=4a at both Reynolds numbers, Re=500 and 800 boundary later profile is parabolic but for ul=a, parabolic profile is not fully developed, as expected in the case of laminar boundary layer development. When ul=2a boundary layer profile is similar to ul=4a but not fully parabolic.

2.4.2 Steady state flow analysis:

Figures 2.6 and 2.7 present the steady state analysis of five different inclination angles of θ =15º, 30º, 45º, 60º and 75º, for a single Reynolds number and upstream length, ul=4a. Since the recirculation vortex in the wake were found to be similar for all upstream lengths, ul=a, 2a and 4a, results for ul=4a are only presented. In all cases, a grid size of (200x150) was used, with 50 cells located on the upstream surface. Figure 2.6 presents Reynolds number, Re=100 and 200 and figure 2.7 presents Re=349. When simulating flow at Reynolds number, Re=350 for all five inclination angles, downstream vortical flow was found to be unsteady, periodic vortex shedding appeared in all cases. During the simulations it was realized that the modification of the upstream length produced no appreciable variation in the flow properties, since the boundary layer development is similar for different lengths and not affecting much the flow past the inclined step.

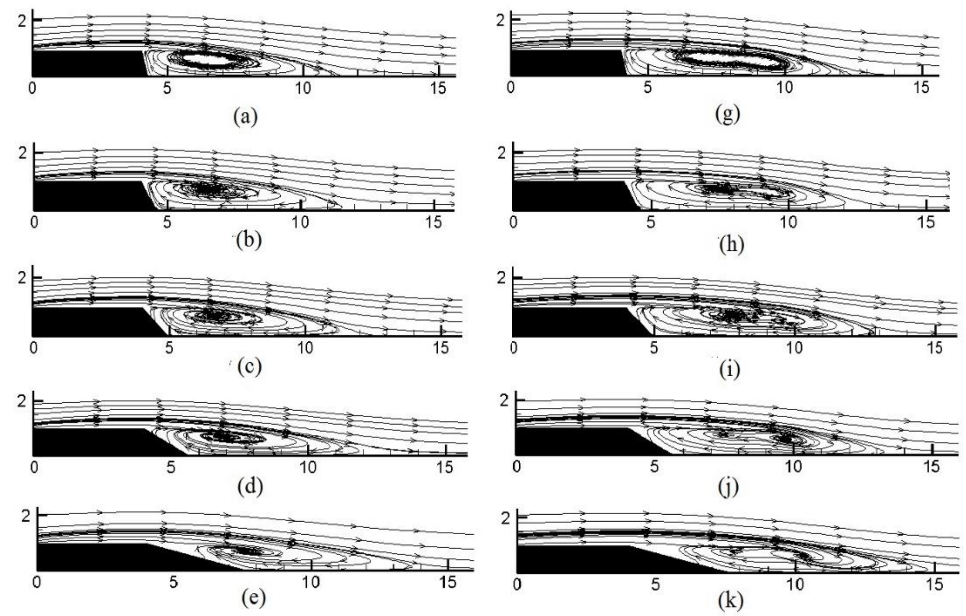

Figure 2.6: Steady state streamline plots for Reynolds Number 100 for inclination angles. a) θ=15º, b) θ=30º, c) θ=45º, d) θ=60º, (e) θ=75º and Reynolds number 200 for inclination angles. (g) θ=15º, (h) θ=30º, (i) θ=45º, (j) θ=60º, (k) θ=75º Upstream channel length ul=4a.

When comparing figure 2.6 and 2.7, it can be noticed that for a given Reynolds number, the downstream static recirculation vortex length, remains pretty much constant and independent of the inclination angle. Similar phenomenon was also reported by Chen et.al. (2006), Kotapati et.al. (2014) and Makiola et.al. (1992). Downstream static recirculating vortex length (L_r) increases with the increase of Reynolds number. The variations of recirculating vortex length (L_r) were calculated for three different static cases, Reynolds numbers Re=100, 200 and 349, their respective values were fitted into a polynomial to obtain a relation given in equation (2.16).

$$L_r = (-4.96804\text{x}10^{-12})\text{Re}^5 + (3.31561\text{x}10^{-9})\text{Re}^4 - (2.11322\text{x}10^{-7})\text{Re}^3 - (2.77175\text{x}10^{-4})\text{Re}^2 + (7.72119\text{x}10^{-2})\text{Re} + 9.75374\text{x}10^{-6} \tag{2.16}$$

2.4.3 Critical Reynolds number for onset of vortex shedding:

The point of criticality at which flow becomes unsteady and periodic from steady state is called the critical Reynolds number. $Re=Re_{cr.}$

From figure 2.7 it can be seen that the flow is steady for all angles from 15º to 75º until Reynolds number 349. The critical Reynolds number for angles of inclination from 15º to 75º was found to be 350, since the flow was unsteady and periodic at Re=350. It was also determined that for angles below θ=15º flow behavior was different with respect to the criticality, it appears as if critical Reynolds number decreases as the angle of inclination is increased from θ=0º to θ=15º. To analyze this trend of the flow characteristics for angles of inclination smaller than 15º, at small Reynolds numbers, a set of new simulations were carried out for θ=5º, 10º, 12º, and 14º, at Reynolds numbers, Re=350, 351, 352, 358, 359, 360, 370, 372, 374, 375, 380, 382, 385, 400, 404 and 405 in order to determine their respective critical Reynolds numbers. Therefore a critical angle of inclination is expected, all angles of inclination above which will have the constant critical Reynolds number for the flow to become periodic and unsteady.

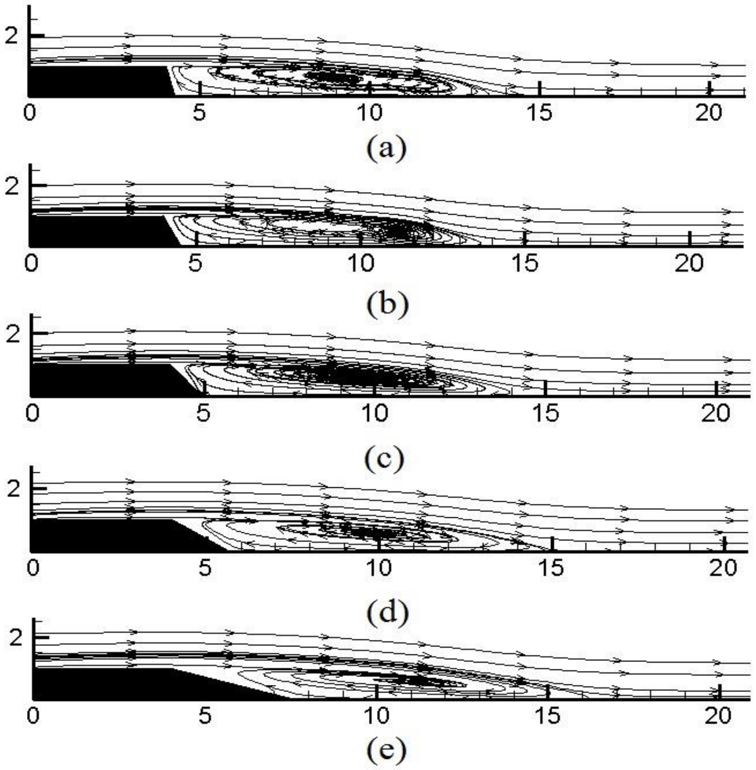

Figure 2.7: Steady state streamline plots for Reynolds Number 349 and inclination angles. (a) θ=15º, (b) θ=30º, (c) θ=45º, (d) θ=60º and (e) θ=75º Upstream channel length ul=4a.

It was determined from the simulations that flow is steady when θ=5º, 10º, 12º and 14º at Reynolds number, Re=404, 374, 359 and 351 respectively, which implies that the critical Reynolds number for these angles of inclination is above 350. Therefore it can be concluded that the critical angle of inclination is θ_{cr}=15º, above which the flow critical Reynolds number, Re_{cr}=350, remains constant.

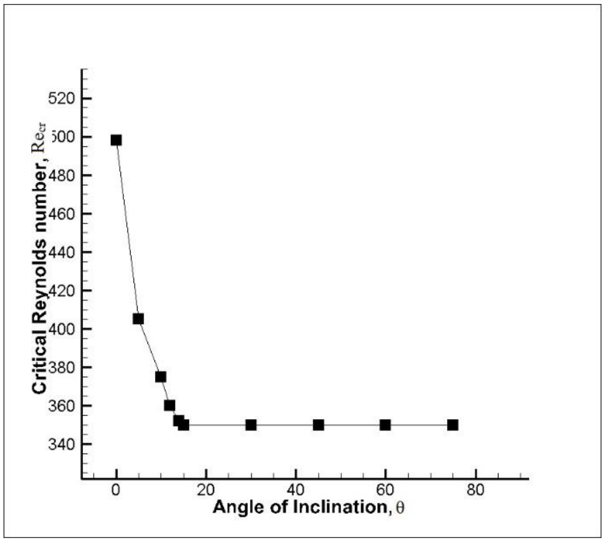

Figure 2.8: Critical Reynolds number Re_{cr} vs. Angle of Inclination, θ.

Figure 2.8 shows that the critical Reynolds number for angles between θ=0º and 15º is decreasing with the increase of the angle of inclination. The critical Reynolds number for backward facing step for θ=0º was reported to be around 500 (Armaly et.al. 2003) (Chen et.al. 2006) and was found in the present study to be at Re=498. For θ=5º the flow critical Reynolds number was found to be at Re=405. This trend of decreasing critical Reynolds number with the increase in the angle of inclination from θ=0º and 15º, could be attributed to the length of the neck of the vortex in the wake of the inclined step. As the angle of inclination increases the length of the vortex neck increases, therefore the rolling up shear layer can separate the vortex from the neck and dissipate more easily into the wake of the inclined step than in the case of the backward step. The various critical Reynolds numbers obtained for different angles of inclination were fitted into a polynomial to derive a generic equation representing the variation of critical Reynolds number with the increase of inclination angle, presented in equation (2.17).

$$\mathrm{Re}_{\mathrm{cr}} = (-0.0000018)\theta^5 + (0.000395)\theta^4 - (0.032748)\theta^3 + (1.264546)\theta^2 - (22.514803)\theta + 496.159 \qquad (2.17)$$

It is also important to realize that the steady state vortex presented in figure 2.6 from Chen et al (2006), for an angle of inclination, θ=45º and for a Reynolds number of Re=343, is identical to the vortex presented in figure 2.7(c) in the present study. The analysis done in Chen et.al. (2006) was in 3-Dimensions and in a constrained flow setup, to simulate the flow in a duct with an inclined edge. The characteristics of the flow are expected to be similar to that of the steady state vortex presented herein, as the vortex at the center of the domain in a duct is most comparable to the 2D vortex in the wake of the unconfined flow past an inclined step.

2.4.4 Unsteady and periodic flow analysis:

As presented in the previous section, the critical Reynolds number for inclination angles between 15º and 75º was found to be 350, therefore in order to visualize unsteady periodic vortex shedding, in the present section simulations were undertaken for Reynolds numbers of 500 and 800. Laminar periodic vortex shedding is presented in Figures 2.9 to 2.14, for ul=4a and mesh size of 200x150, with the help of instantaneous streamlines and vorticity contours corresponding to six equally spaced time instants within a shedding cycle of time period T. Since the vortex shedding patters were found to be similar for all upstream lengths, ul=a, 2a and 4a, only results for ul=4a are presented. The flow remains laminar under these conditions, since as determined by Armaly et al (1983) the flow over an inclined step is laminar whenever Reynolds number is below 1200.

The onset of vortex shedding in the case of the backward facing step or inclined step occurs due to the rolling up shear layer, located downstream of the inclined step. The rolling up shear layer is generated due to the interaction between the negative momentum of the vortex in the wake of the step and the solid constrained boundary located below the vortex. This mechanism is different from the one appearing in a generic bluff body, where vortex shedding occurs due to the flapping motion of the upper and lower vortices appearing at the body trailing edge, vortices shed alternately into the wake.

Reynolds number was taken to be 500 in figures 2.9 to 2.13 and 800 in figure 2.14. Each figure presents the results for a given inclination angle. Inclination angles vary between 15º in figure 2.8 to 75º in figure 2.12, the inclination angle of figure 2.13 is 15º. Notice that in all figures, the vortex forms at the inclined edge vertices of the inclined step and is shed into the wake. Two types of inviscid critical points, namely ‘centre’ and ‘saddle’ can be seen from the figures. A critical point is a location where slope of streamline becomes indefinite; the point of zero velocity is referred to as the ‘centre’ while the point where two streamlines running in opposite direction touch each other is referred to as the ‘saddle’. From the present study, it is realized that whenever Re >350, the saddle point of a shed vortex, disappears before a new vortex is shed. Instantaneous vorticity contours, shown in Figure 2.9 to 2.14, further reveals the formation and shedding of vortices from the inclined edge vertex of the step. Due to its streamlined shape, separation in an inclined step always occurs at the inclined edge vertex leading to a separated shear layer from the vertex which is stretched, bent and finally convected into the wake. The neck between the tip and the main body of a growing vortex stretches and bends, leading to separation from the main body.

The positive and negative vorticity, corresponding to counter-clockwise and clockwise motion, is shown by solid and dashed lines, respectively. The rolling up shear layer exhibits a flapping motion while the shear layer moves into the growing vortex in the wake only to be convected downstream in the form of vortical structure which scales with the height of the inclined step. It is interesting to point out that, the same mechanism and features of vortex shedding has been found for all different angles studied. The evolution of the recirculating vortex in the wake of the step before being shed can be clearly seen in the figures 2.9-2.14

The results at Re=800, shown in Figure 2.14, reveals the same shedding mechanism as the one found at lower Reynolds. Based on quantitative observations made from the simulations, it was evident that at Reynolds number 500, the vortex dissipation is more organized, but the simulations at Reynolds 800, showed much faster and disorganized vortex dissipation. This is due to the fact that as Reynolds number increases, the kinetic energy associated to each fluid particle also increases and momentum interchange between particles increases, producing a quicker and higher disorganized vortex dissipation. Vortex shedding frequency for all the cases studied, which is presented in the next section, was found to be very similar regardless of the Reynolds number and inclination angle. This fact emphasizes the global nature of flow dynamics. A detailed three-dimensional calculation is needed to explore the three-dimensional nature of the flow at moderate Re and to determine the exact Reynolds number for the flow transition from two-dimensions to three-dimensions.

The vortex recirculation length, under unsteady state conditions, varies with time from the formation of the vortex until it is finally dissipated into the wake after its separation. From figure 2.9(i) the vortex recirculation length, when the vortex is just formed, was 2 units, and it increased to 4 units when it was finally separated by the rolling up shear layer, as presented in figure 2.9(g), (h). Similar movement of recirculating vortex can also be observed in figures 2.10 to 2.14 within a vortex shedding cycle.

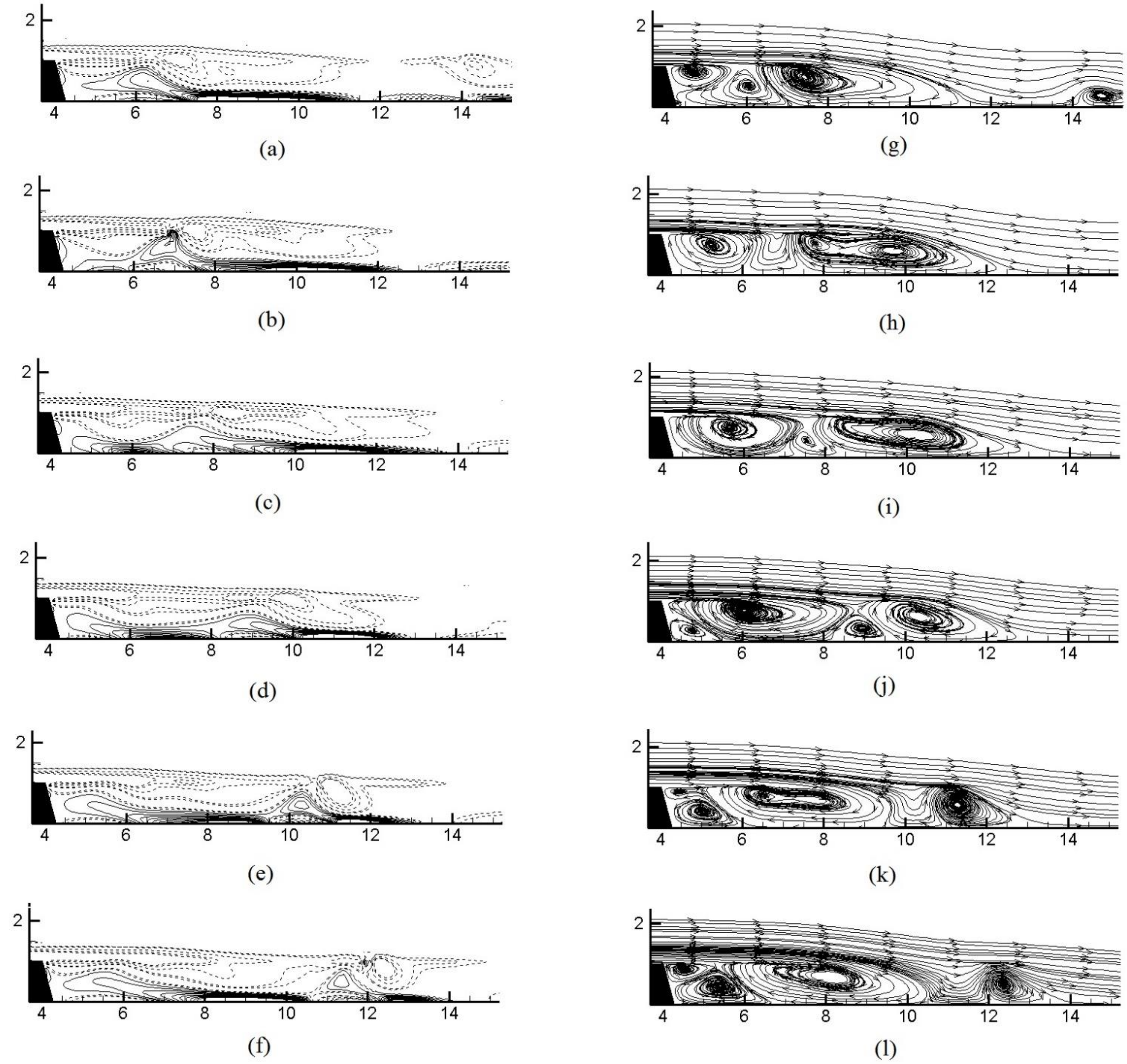

Figure 2.9: Vorticity and corresponding Streamline plots of vortex shedding cycle in the wake of Inclined Step with inclination angle θ=15º, for Re 500, upstream length ul=4a, and six time steps: (a, g) T/6; (b, h) T/3; (c, i) T/2; (d, j) 2T/3; (e, k) 5T/6; (f, l) T.

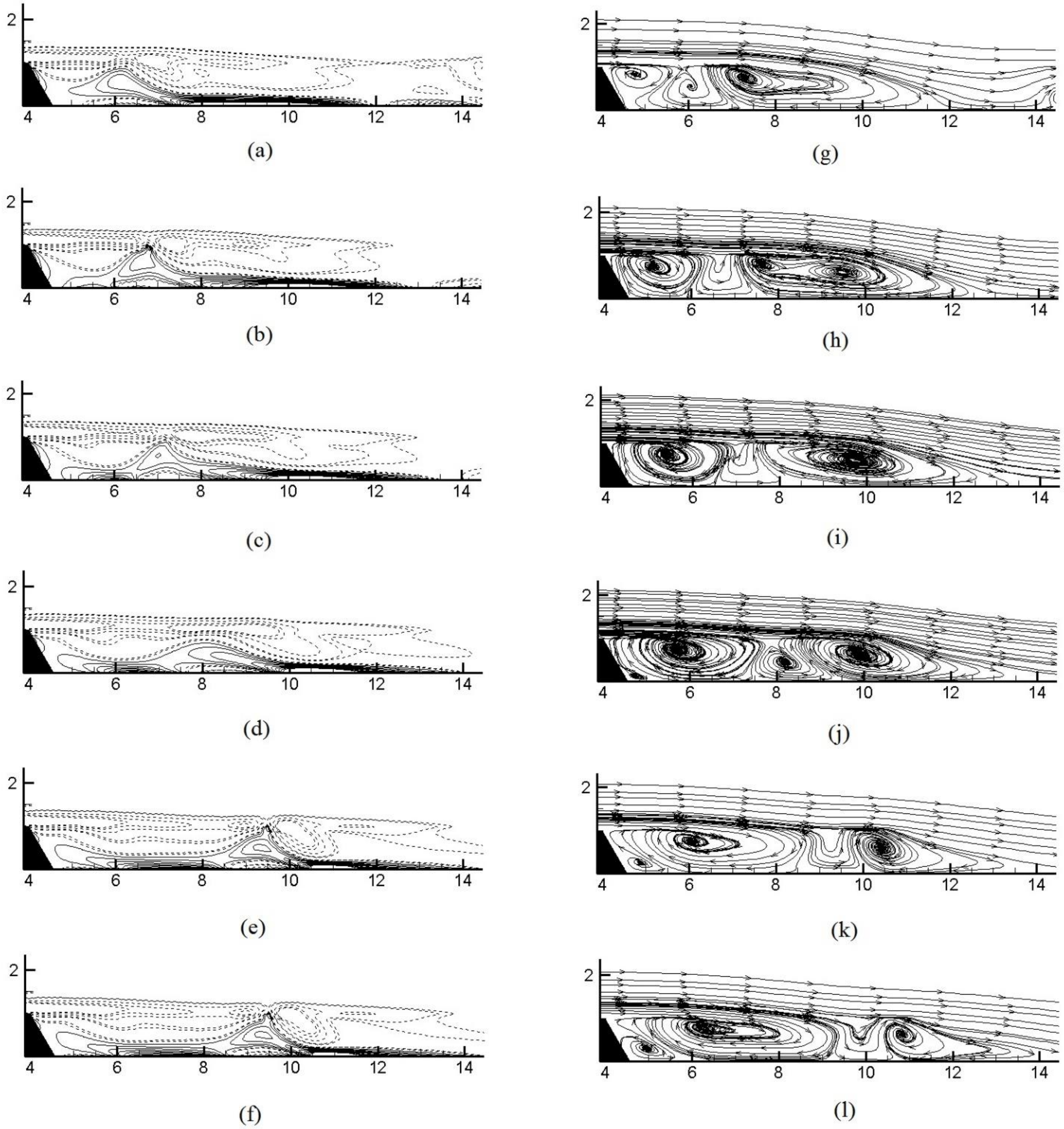

Figure 2.10: Vorticity and corresponding Streamline plots of vortex shedding cycle in the wake of Inclined Step with inclination angle θ=30º, for Re 500, upstream length ul=4a, and six time steps: (a, g) T/6; (b, h) T/3; (c, i) T/2; (d, j) 2T/3; (e, k) 5T/6; (f, l) T.

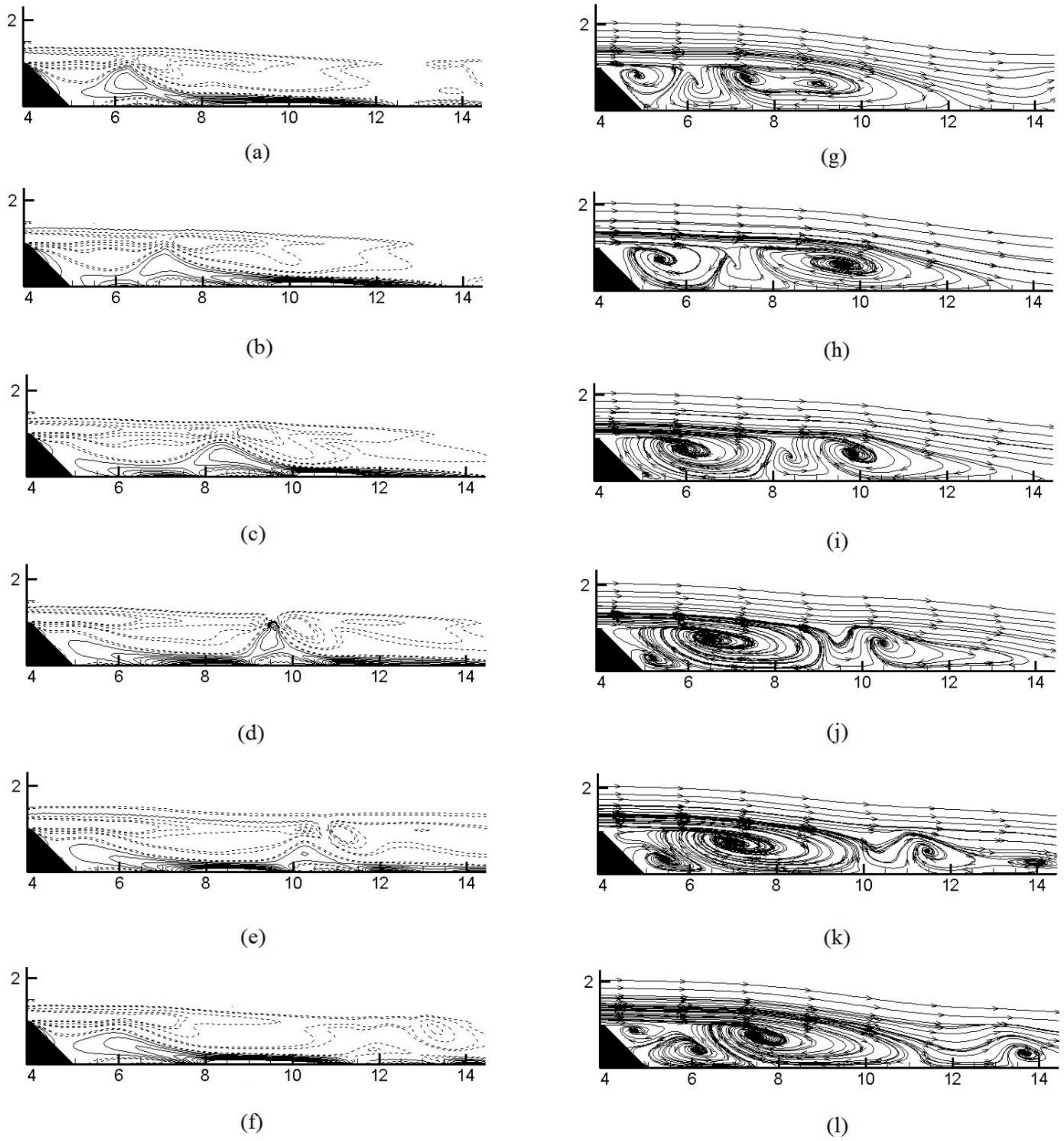

(a) (g)

(b) (h)

(c) (i)

(d) (j)

(e) (k)

(f) (l)

Figure 2.11: Vorticity and corresponding Streamline plots of vortex shedding cycle in the wake of Inclined Step with inclination angle θ=45º, for Re 500, upstream length ul=4a, and six time steps: (a, g) T/6; (b, h) T/3; (c, i) T/2; (d, j) 2T/3; (e, k) 5T/6; (f, l) T.

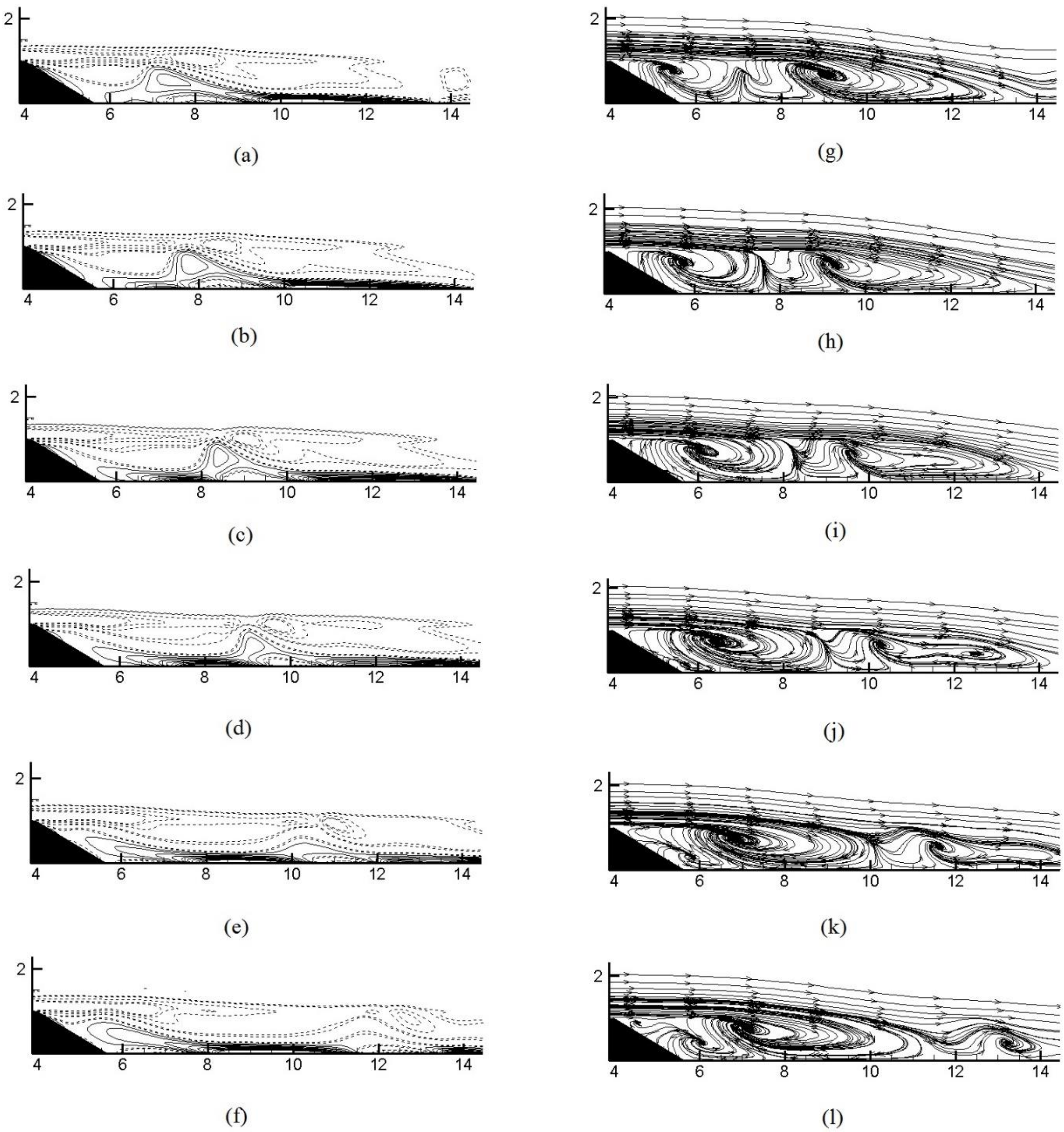

Figure 2.12: Vorticity and corresponding Streamline plots of vortex shedding cycle in the wake of Inclined Step with inclination angle θ=60º, for Re 500, upstream length ul=4a, and six time steps: (a, g) T/6; (b, h) T/3; (c, i) T/2; (d, j) 2T/3; (e, k) 5T/6; (f, l) T.

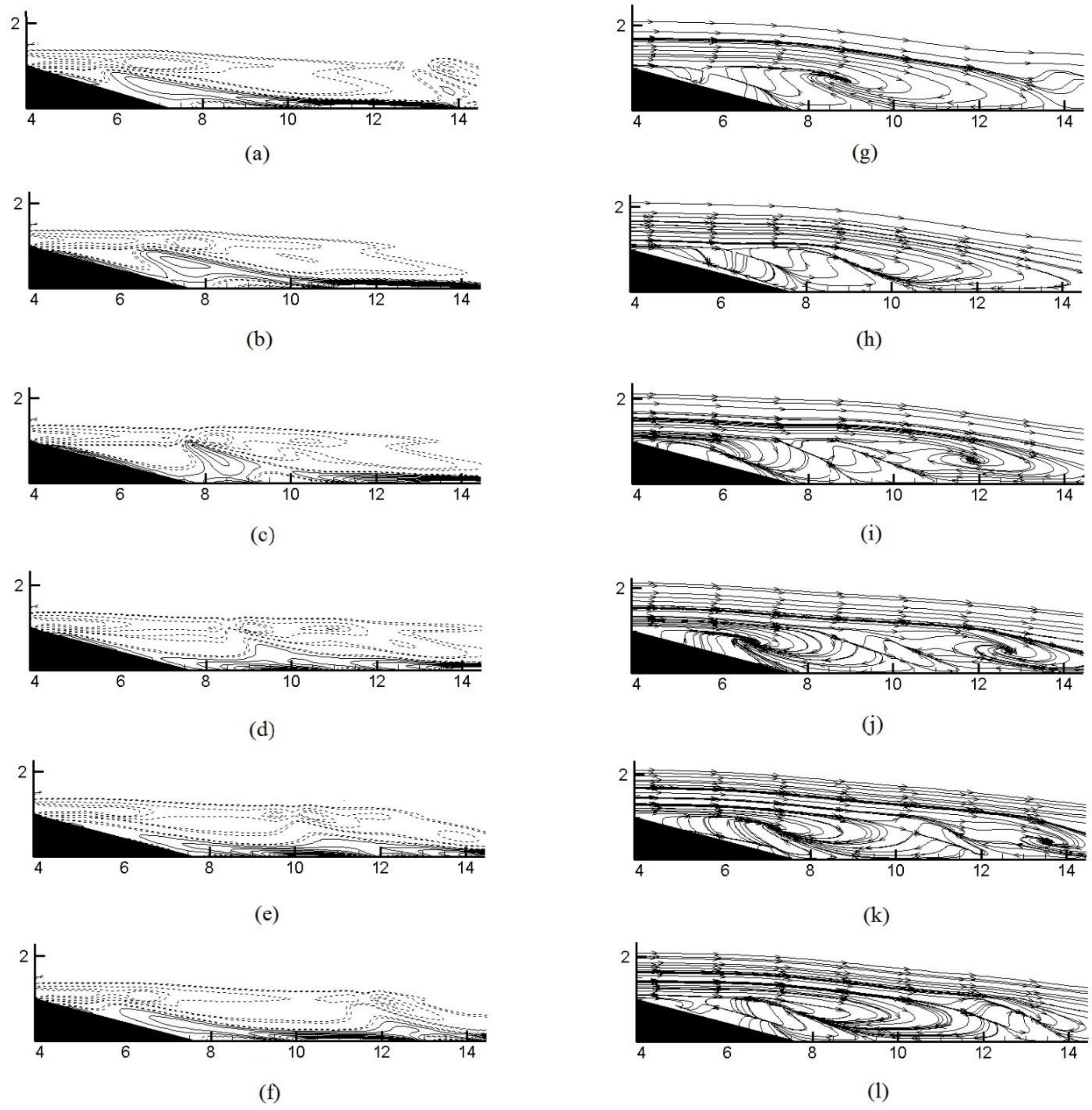

Figure 2.13: Vorticity and corresponding Streamline plots of vortex shedding cycle in the wake of Inclined Step with inclination angle θ=75º, for Re 500, upstream length ul=4a, and six time steps: (a, g) T/6; (b, h) T/3; (c, i) T/2; (d, j) 2T/3; (e, k) 5T/6; (f, l) T.

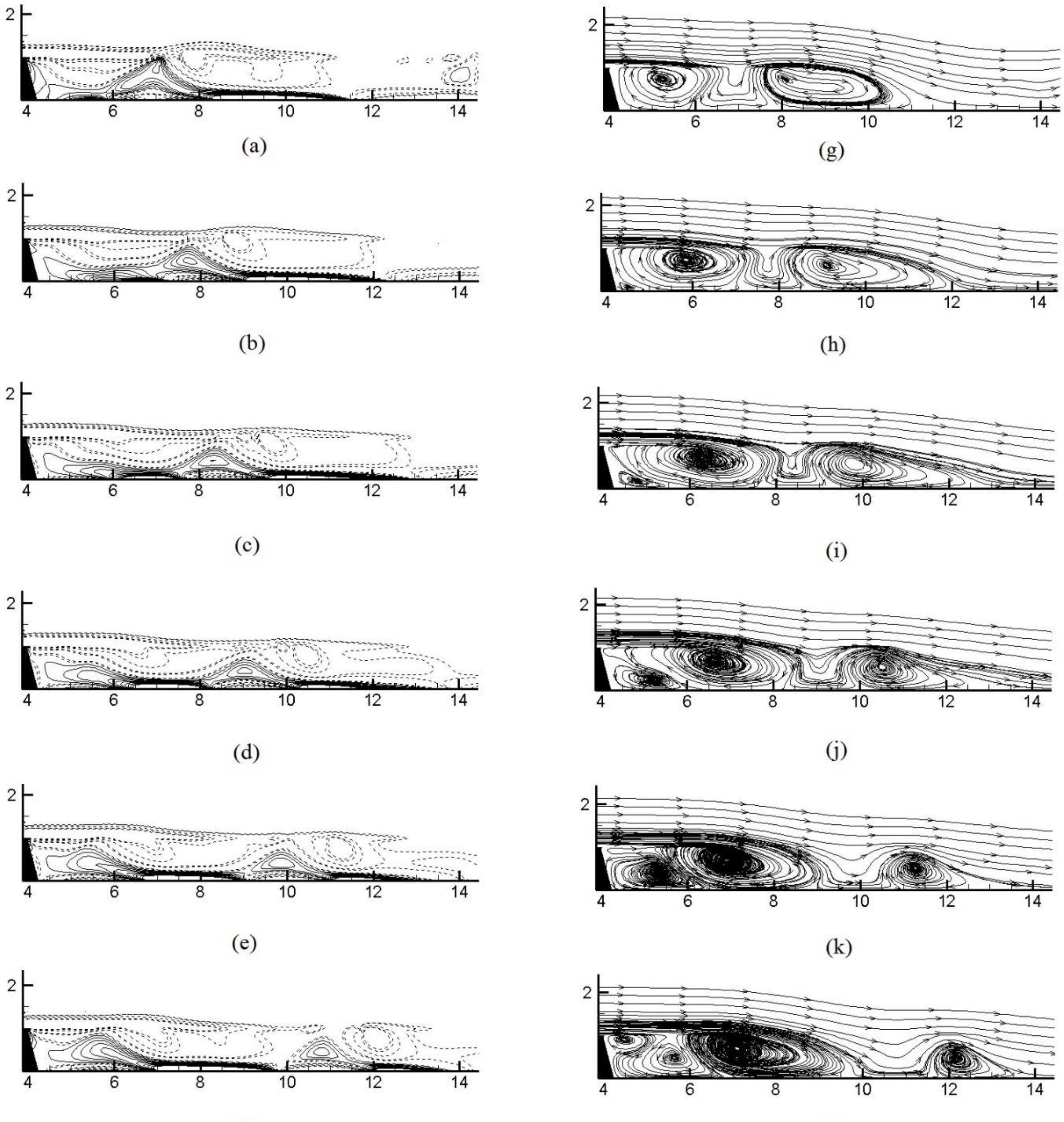

Figure 2.14: Vorticity and corresponding Streamline plots of vortex shedding cycle in the wake of Inclined Step with inclination angle θ=15º, for Re 800, upstream length ul=4a, and six time steps: (a, g) T/6; (b, h) T/3; (c, i) T/2; (d, j) 2T/3; (e, k) 5T/6; (f, l) T.

2.4.5 Lift and drag coefficients.

Figures 2.15 and 2.16, present the variation of averaged lift and drag coefficients acting on the inclined step with the change of inclination angle. These coefficients consider the average normal and shear stresses acting on the upstream horizontal surface and the inclined step surface. To calculate lift and drag coefficients, the expressions presented in equation (2.18) were used. It is important to realize that as the flow under study is unsteady and periodic, the concept of average lift and drag coefficients has to be used.

$$\mathrm{C_D} = \frac{\mathrm{F_D}}{\frac{1}{2}\rho\,\mathrm{U}^2\,\mathrm{a}^2}, \qquad \mathrm{C_L} = \frac{\mathrm{F_L}}{\frac{1}{2}\rho\,\mathrm{U}^2\,\mathrm{a}^2} \tag{2.18}$$

F_D and F_L are respectively the dimensional drag and lift forces consisting of their respective components of normal, F_p and shear, F_s forces acting on the upstream horizontal and inclined surfaces. The pressure and shear forces acting on the inclined step are calculated by the expressions presented in equation (2.19).

$$F_p = -\,(p.A)\,\hat{n}, \qquad \mathrm{F}_s = -\mu \mathrm{A}\left(\frac{\partial u_i}{\partial x_j}\right).\hat{n} \tag{2.19}$$

Where $\hat{n}$ is the unit normal vector perpendicular to the surface. Drag force was taken as positive when pointing towards the positive X axis direction, and Lift force was regarded as positive when pointing towards the positive Y axis direction.

From figures 2.15 and 2.16, it can be observed that regardless of the Reynolds number and the upstream horizontal length used, the averaged drag coefficient, C_D is inversely proportional to the angle of inclination increase and averaged lift coefficient, C_L is directly proportional to the angle of inclination. This trend is due to the fact that as the inclination angle increases, the inclined surface area also increases, therefore, the component of the vertical force in the Y direction due to the pressure acting on the inclined surface will also increase, see figure 2.16 (a) and (b). It can also be observed that, regardless of the inclination angle, lift coefficient for an upstream horizontal length of ul=4a, is always higher than for smaller lengths, because as the horizontal upstream length increases, the area where the normal pressure is acting also increases. Lift coefficient increase, is smaller when the upstream horizontal length goes from a to 2a than from 2a to 4a due to the smaller increase in the upstream surface area in the former case than in the latter and this happens regardless of the angle of inclination and Reynolds number. When comparing figures 2.16(a) and (b), it is realized that, regardless of the inclination angle, as Reynolds number increases the lift coefficient suffers a small increase. This can be attributed to the pressure distribution on the surface of the inclined step, as Reynolds number increases the relative pressure acting on the upstream surface suffers a small decrease and the pressure decrease over the inclined surface is even smaller, as seen in figures 2.17 (a) and (d).

Regarding the averaged drag coefficient, figure 2.15 shows that drag coefficient decreases with the inclination angle increase. This can be attributed to the fact that as the angle of inclination increases, shear stresses acting on the inclined surface increase, due to the area increase. As a result of the downstream vorticity generated the component of shear stresses in x direction, acting on the inclined surface, has an opposite direction to the shear forces acting on the upstream surface. Therefore, the overall shear stresses component acting in the X direction will decrease with the inclination angle increase. Figures 2.17 (a) and (d), show that pressure on the inclined surface increases marginally as the inclined step angle increases. Hence the drag component due to the normal pressure acting over the inclined surface generates a force rather constant and independent of the inclined step angle. This force will pull the step towards the positive direction, because the relative pressure onto the inclined surface is negative. Since pressure forces are remain constant and the inclined surface shear forces increase in the opposite direction with the increase of inclined step angle, the drag on the body will decrease as the inclination angle increases.

For a given angle of inclination, as the upstream horizontal length increases the shear stresses on the horizontal surface also increase, but the pressure acting on the inclined surface vary marginally as seen in figure 2.17 (c) and (f), causing the drag coefficient to increase.

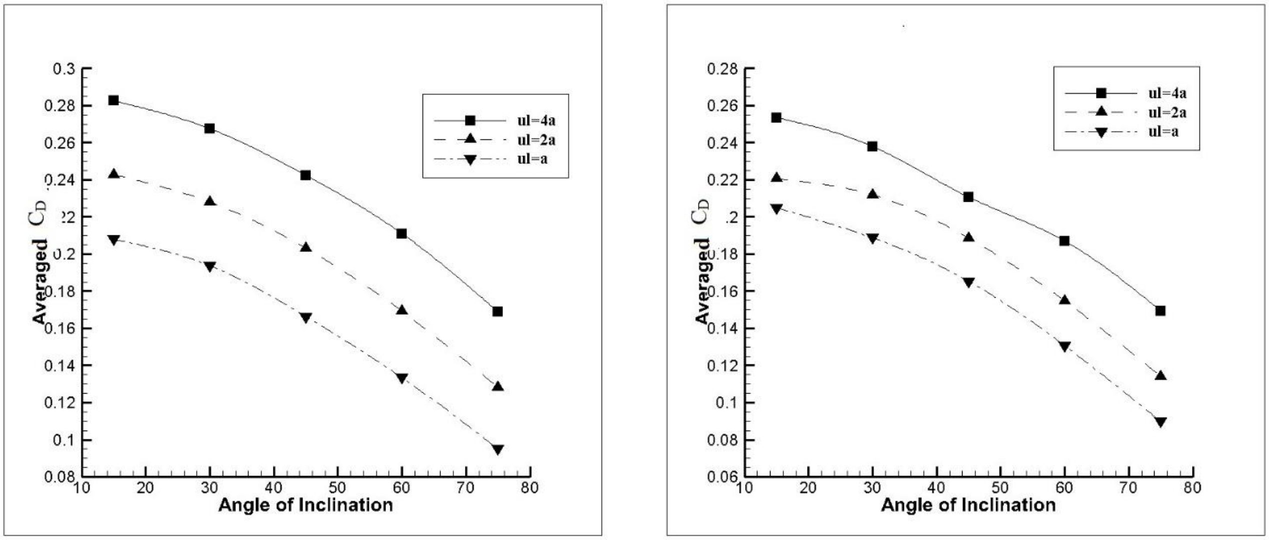

(a) (b)

Figure 2.15: Averaged Drag coefficient versus angle of Inclination: (a) Re=500 (b) Re=800

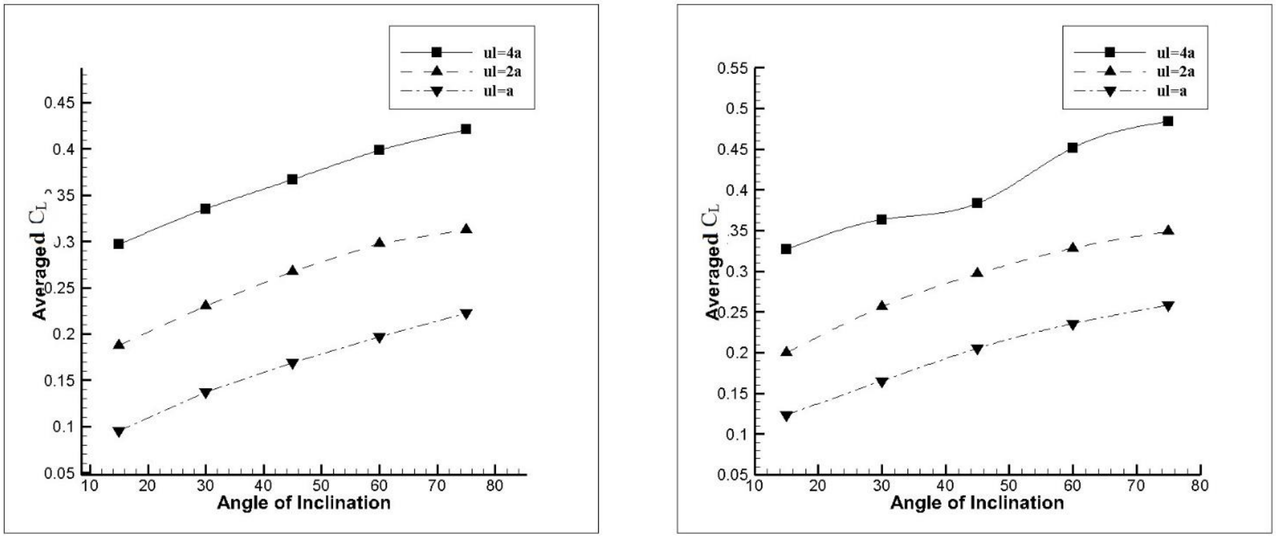

(a) (b)

Figure 2.16: Averaged Lift coefficient versus angle of Inclination. (a) Re=500 (b) Re=800

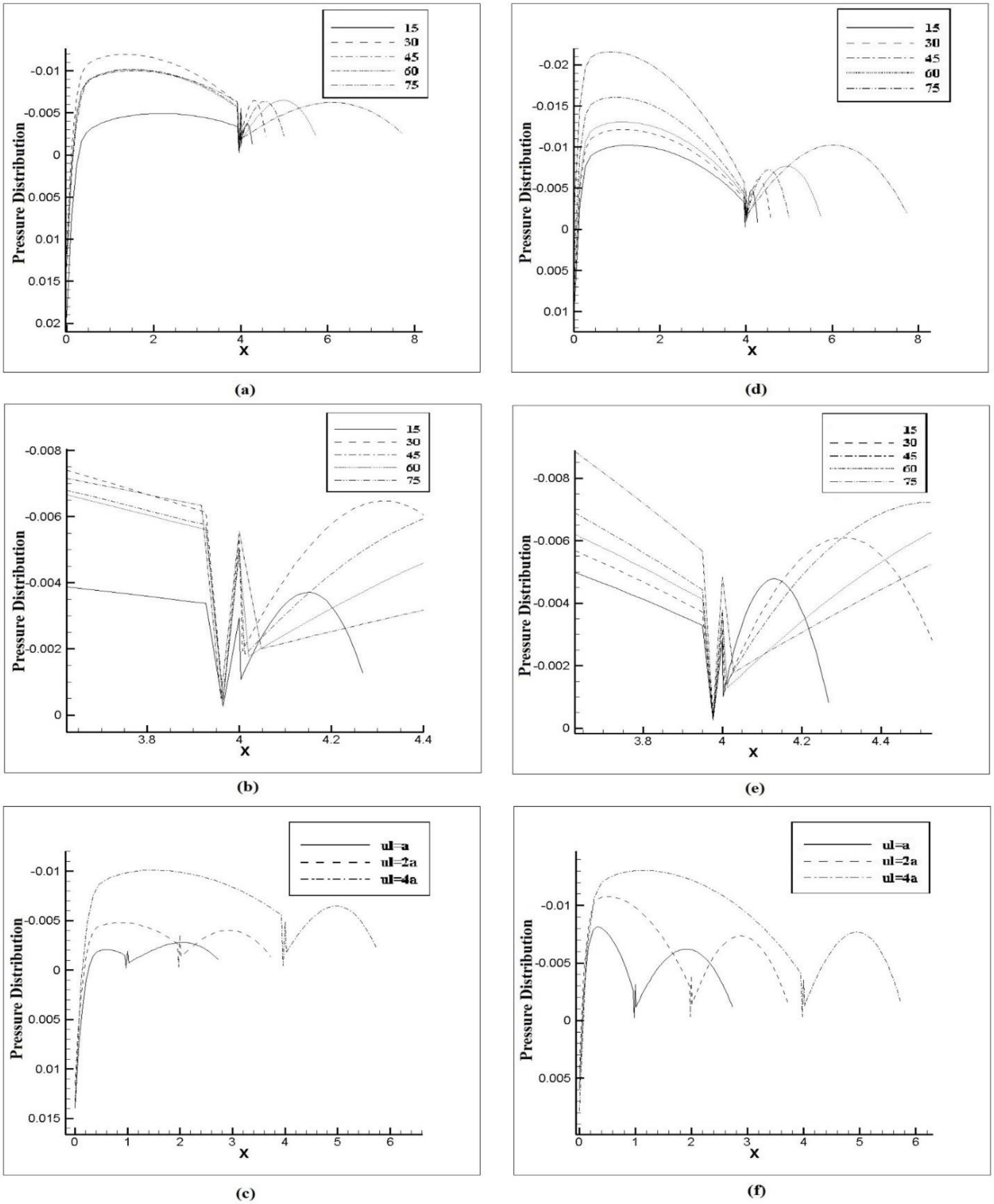

(a) (d)

(b) (e)

(c) (f)

Figure 2.17: Instantaneous relative pressure Distribution plots on the inclined step surface. (a) For different angles of inclination, θ at Re=500. (b) Close up view of the step corner at Re=500. (c) For different upstream length, ul at Re=500 and θ=60°. (d) For different angles of inclination, θ at Re=800. (e) Close up view of the step corner at Re=800. (f) For different upstream length, ul at Re=800, θ=60°.

Figure 2.17 presents the instantaneous non dimensional relative pressure distribution plots on the complete inclined step surface. Relative pressure, with respect to the free stream or ambient pressure, acting on the step surface is negative since the velocity of fluid is higher over the surface of the step than the free stream velocity as in the case of flow over the top surface of an airfoil. In figures 2.17 (a) and (d), the pressure distribution on the step surface is presented for all the inclination angles simulated at Re=500 and 800 respectively. It can be observed that as the as the angle of inclination increases, the pressure acting on the upstream surface decreases, causing the lift on the body to increase, as seen in figure 2.16(a) and (b). The variation of pressure on the inclined surface suffers a marginal increase with the increase in the Reynolds number, as can be seen in figures 2.17(a) and (d); (c) and (f). An interesting observation that can be made on the right corner of the upstream surface, where the inclined surface of the step starts, is the pressure fluctuation. The close up view of these pressure fluctuations can be seen clearly in figure 2.17 (b) and (e). These pressure fluctuations could be due to the sudden change in geometry at the corner, leading to variations in the velocity of the flow. An important phenomenon observed in figures 2.17 (a) and (d) is that the pressure on the upstream surfaces, first decreases until reaching the stagnation point, formed close to the leading edge, due to the abrupt change in the flow conditions caused by the sudden interaction of the free stream with the upstream surface. Pressure distribution then tends to stabilize as the boundary layer develops on the upstream surface. This phenomenon is identical to the pressure distribution on the upper surface of an airfoil. Similarly on the inclined surface, the pressure decreases until reaching the midpoint of the surface and then increases. This is due to the flow separation at the upper corner inclined surface, resulting in a vortex dissipation in the wake along with the rolling up shear layer appearing at the lower edge of the inclined surface. When the upstream surface is increased for a given angle of inclination, the pressure on the upstream surface tends to decrease and this decrease directly proportional to the upstream surface length increase, as presented in figure 2.17 (c) and (f). But the increase in the upstream surface length, have a minimal effect on the pressure distribution over the inclined surface, the pressure tends to marginally decrease. The decrease in pressure when the Reynolds number is increased for a given angle and upstream surface is also very marginal, as presented in figures 2.17 (a) and (d) and figures 2.17 (c) and (f).

Figure 2.18, presents the time dependent drag profile for different angles of inclination, 15º, 45º, 75º and at different Reynolds numbers 500 and 800. It can be observed that for a given Reynolds number, the frequency of oscillation has a negligible change with the increase of inclination angle, see figure 2.18 (b) and (d). It can also be observed that if the inclination angle is maintained constant and Reynolds number is increased, the oscillation frequency increases about 30% when the Reynolds number goes from 500 to 800. This pattern shows the global nature of the flow.

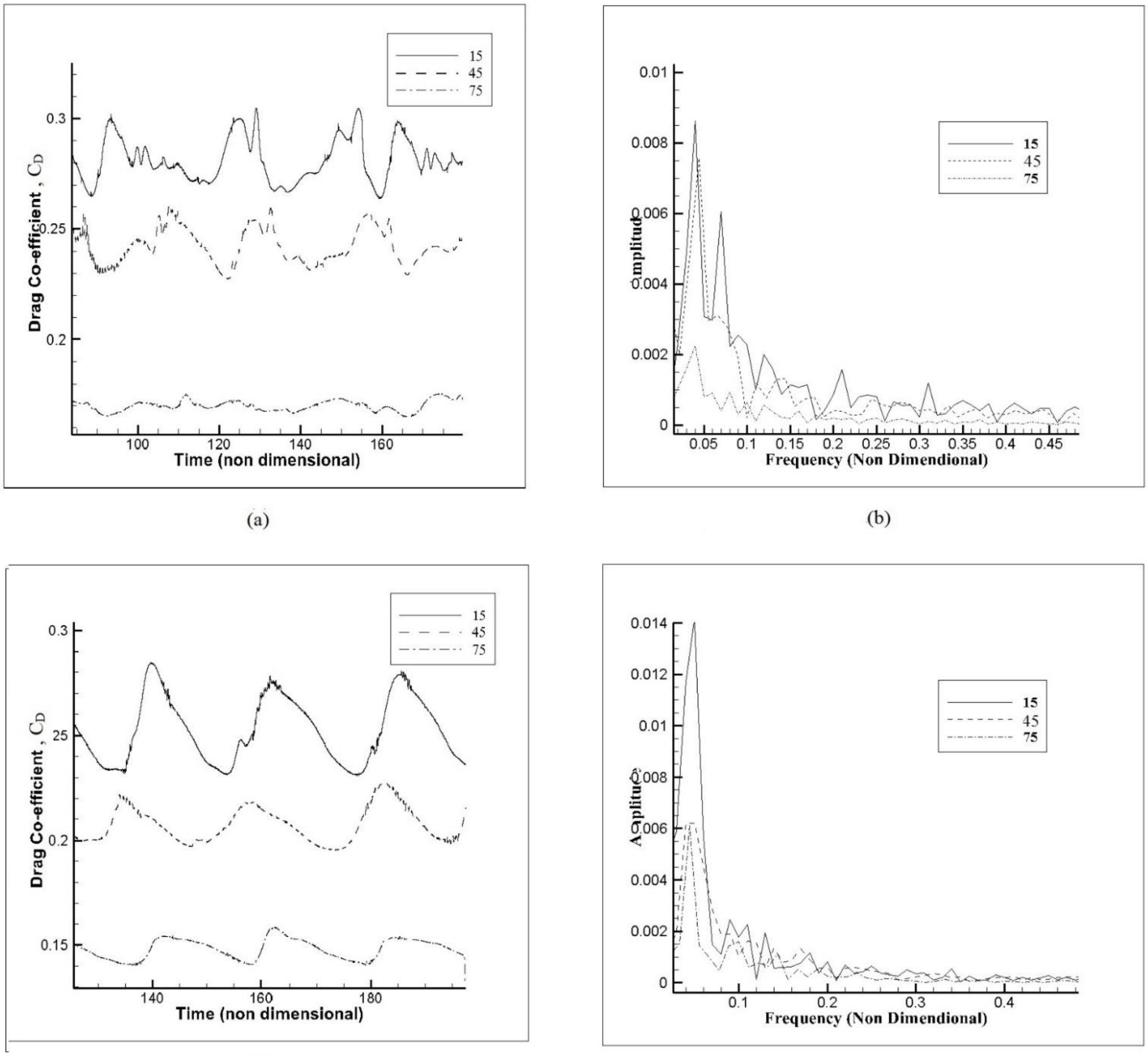

(a) (b)

(c) (d)

Figure 2.18: Drag coefficient versus time for L=4a. (a) Re=500. (b) FFT analysis of C_D at Re=500.(c) Re=800. (d) FFT analysis of C_D at Re=800

The drag coefficient amplitude of oscillation decreases with the increase of inclination angle, the decrease being of over 75% when the inclination angle goes from 15º to 75º for Re=500, see figures 2.18 (b) and (d). The amplitude decrease with the inclination angle increase is smaller as the Reynolds number increases.

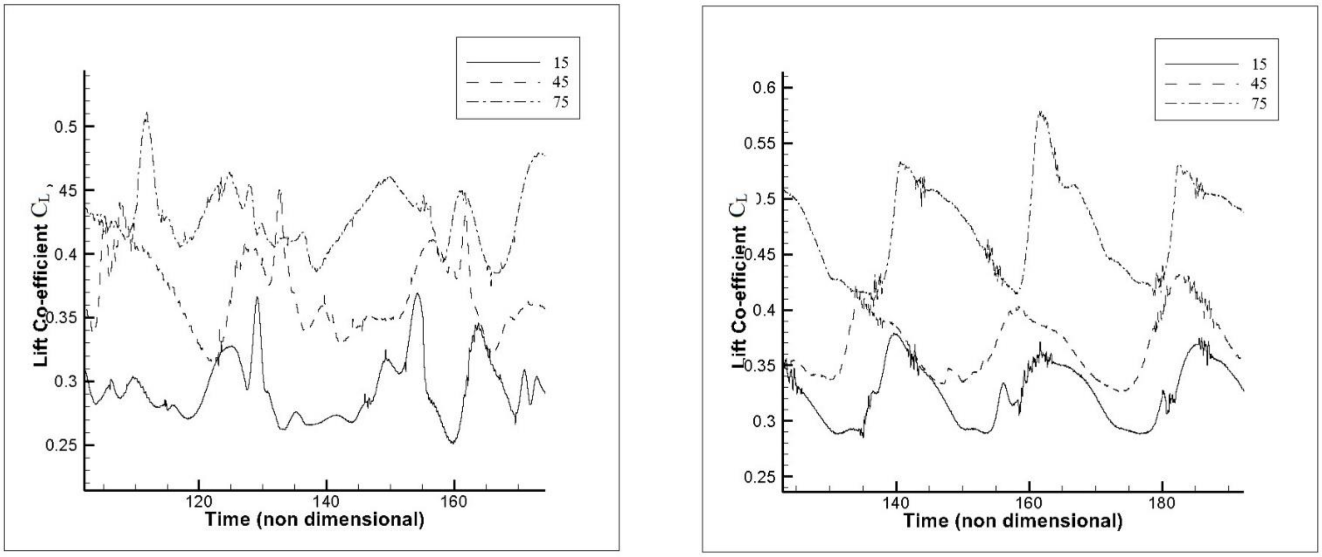

(a)

(b)

Figure 2.19: Lift Coefficient versus time for L=4a (a) Re=500 (b) Re=800

Figure 2.19, presents the time dependent lift coefficient profile for the same different angles of inclination and Reynolds numbers introduced in figure 2.18. It is interesting to note that the oscillation amplitude variation with the inclination angle or Reynolds number increase is much smaller than in the case of drag coefficient. In other words, the amplitude has an increase of 50% when inclination angle goes from 15º to 75º, but this happens at Reynolds number 800, for Reynolds number = 500, no appreciable variation was observed.

2.5. Conclusions:

- In the steady state analysis, it has been found that the vortex recirculation length has a strong dependency of Reynolds number. Recirculation length remains constant for all angles of inclination studied.
- The effect of the boundary layer onto the upstream horizontal surface has a negligible effect on the vortex recirculation length, and on the downstream periodic flow.
- Vortex shedding was found to be occurring at Reynolds number of 350 and inclination angles between 15º and 75º. For angles of inclination below 15º the critical Reynolds number for flow transition from steady state to periodic unsteady (vortex shedding), increases with the decrease of inclination angle.
- The average drag coefficient on the body decreases as the angle of inclination increases. This is attributed to the inclined surface shear drag increase, in the opposite direction of the pressure and upstream surface shear drag.
- Average lift coefficient increases with the angle of inclination increase. This is because the force component due to the pressure acting on the inclined surface increases with the inclination angle, due to the increase of the inclined surface area.
- The average lift and drag acting on the inclined step increases with the increase in the

upstream horizontal surface length for a given Reynolds number and angle of inclination.

- From the quantitative observations of vorticity plots, for the cases studied, flow appears to be more unsteady and disorganized with the Reynolds number increase.
- Amplitude of oscillation tends to decrease as angle of inclination increases, the vortex shedding frequency increases by 30% as Reynolds number increases from 500 to 800.

References:

Anderson J.D. (1995) Computational Fluid Dynamics. McGraw Hill.

Armaly, B. F., Durst, F., Peireira, J. C. F., Schonung, B. (1983). Experimental and theoretical investigation of backward-facing step flow. J. Fluid Mech. 127: 473– 96.

Armaly, B. F., Li A, Nie JH. (2003). Measurements in the three-dimensional laminar separated flow. Int. J. Heat and Mass Transfer. 46: 3573-3582.

Barkley D; Gomes M. G. M; Henderson R. D. (2002). Three-dimensional instability in flow over a backward-facing step, J. Fluid Mech. 473: 167–190.

Barri M; Anderson HI. (2010). Turbulent flow over a backward-facing step. Part 1. Effects of anti-cyclonic system rotation. J. Fluid Mechanics. 665: 382-417.

Becker S; Leienhart H. (2003). Flow and turbulence structures in the wake of a simplified car model. SAE Paper 01-0656.

Chen Y.T., Nie J.H., Hsieh H.T., Sun L.J. (2006), Three-dimensional convection flow adjacent to inclined backward-facing step. Int. Journal of Heat and Mass Transfer. 49: 4795-4803.

Chiang, T. P; Sheu T. W. H. (1999). A numerical revisit of backward-facing step flow problem. Physics of Fluids, 11; N4: 862–874.

Chowdhary H., Dhiman A., (2011). Two-Dimensional Laminar Fluid Flow and Heat Transfer over a Backward-Facing Step: Effects of Reynolds and Prandtl Numbers. Heat transfer research journal. 42, 4, 379-402

Cogotti A. (1998). A parametric study on the ground effect of a simplified car model. SAE paper 980031; 37-63.

Durst F; Peireira J. C. F; Tropea C. (1993). The plane symmetric sudden-expansion flow at low Reynolds numbers. J. Fluid Mech. 248: 567–581.

El-Askary WA. (2011). Simulation of supersonic turbulent flow in the vicinity of an inclined backward-facing step. International Journal of Computational Fluid Dynamics. 25: N7; 407-423.

Fares E. (2006). Unsteady flow simulation of the Ahmed reference body using a lattice

Boltzmann approach. Computers and Fluids. 35; 940-950.

Franck G; Nigro N; Storti M; D'elía J. (2009). Numerical simulation of the flow around the Ahmed vehicle model. Latin American Applied Research. 39: 295-306.

Gandjalikhan Nassab SA; Moosavi R; Hosseini Sarvari SM. (2009). Turbulent forced convection flow adjacent to inclined forward step in a duct. International Journal of thermal sciences. 48: 1319-1326.

Gartling, D. K. (1990). A test problem for outflow boundary condition flow over a backward-facing step. Int. J. Numer. Methods Fluids 11: 953–967.

Gaylard AP. (2009). The appropriate use of CFD in the automotive design process. SAE paper 01-1162. 337-348.

Guilmineau E. (2008). Computational study of flow around a simplified car body. Journal of wind engineering. 96: 1207-1217.

Heenan, A. F. Morrison, J. F. (1998) Passive control of backstep flow. Exp. Therm. Fluid Sci. 16: 122–132.

Heft AI; Indinger T; Adams NA. (2011). Investigation of unsteady flow structures in the wake of a realistic generic car model. AIAA Applied aerodynamic conference. Hawaii USA. Paper 3669. 1-14.

Heft AI; Indiger T; Adams NA. (2012). Introduction of a new realistic car model for aerodynamic investigations. SAE International. Paper 01-0168. 1-14.

Howard RJA; Pourquie M. (2002). Large eddy simulation of an Ahmed reference model. Journal of Turbulence 3; N12.

Kaiktsis L; Karniadakis G. E; Orszag, S. A. (1991). Onset of three-dimensionality, equilibria, and early transition in flow over a backward-facing step. J. Fluid Mech. 231: 501–528.

Kaiktsis L; Karniadakis, G. E; Orszag, S. A. (1996). Unsteadiness and convective instabilities in a two-dimensional flow over a backward-facing step. J. Fluid Mech. 321: 157–187.

Kaltenbach, HJ; Janke, G.. (2000). Direct numerical simulation of flow separation behind a swept rearward-facing step at $Re_H = 3000$. Physics of Fluids, 129: 2320–2337.

Kaltenbach HJ. (2004). Turbulent flow over a swept backward-facing step. European Journal of Mechanics B/Fluids. 23; 501-518.

Kapadia S; Roy S; Wurtzler K. (2003). Detached eddy simulation over a reference Ahmed car model. AIAA paper 0857: 1-10.

Khalighi B; Zhang S; Koromilas C; Balkanyi SR; Bernal LP; Laccarino G; Moin P. (2001).

Experimental and computational study of unsteady wake flow behind a bluff body with a drag reduction device. SAE paper 01B-207: 1-15.

Kim, J; Moin, P. (1985), Application of a fractional-step method to incompressible Navier-Stokes equations, J. Comput. Phys., 59: 308–323.

Kim JY; Ghajar AJ; Tang C; Foutch GL. (2005). Comparison of near-wall treatment methods for high Reynolds number backward-facing step flow. 19; N7: 493-500.

Krajnovic S; Davidson L. (2004). Large-eddy simulation of the flow around simplified car model. SAE World congress, Detroit USA. Paper 01-0227: 1-10

Kung KY; Hsu H.CH; Chiang HL. (2004). Transient mixed convection flow of a second grade viscoelastic fluid past an inclined backward facing step. 39; 427-439.

Lanzerstorfer D; Kuhlmann HC. (2012). Global stability of the two-dimensional flow over a backward-facing step. J Fluid Mechanics. 693: 1-27.

Le, H; Moin P; Kim J. (1997). Direct numerical simulation of turbulent flow over a backward-facing step. J. Fluid Mech. 330: 349–374.

Lee T; Mateescu D. (1998). Experimental and numerical investigation of 2D backward-facing step flow. J. Fluids Struct. 12: 703–716.

Le Good GM; Garry KP. (2004). On the use of reference models in automotive aerodynamics. SAE paper 01-1308: 375-400.

Leinhart H; Stoots C; Becker S. (2003). Flow and turbulence structures in the wake of a simplified car model (Ahmed model). SAE Technical paper series. Paper 01-1315. 1-8.

Mistrangelo C. (2011). Topological analysis of separation phenomena in liquid metal flow in sudden expansions. Part 1. Hydrodynamic flow. J. Fluid Mechanics. 674: 120-131.

Nguyen TD; Wells JC; Nguyen CV. (2012). Velocity measurement of near-wall flow over inclined and curved boundaries by extended interfacial particle image velocimetry. Flow measurement and instrumentation. 23: 33-39.

Nie, J. H., Armaly, B. F. (2002). Three-dimensional convective flow adjacent to backward-facing step effects of step height, Int. J. Heat Mass Transfer, 45: 2431–2438.

Park NS; Ko SC. (2011). Large eddy simulation of turbulent premixed combustion flows over backward facing step. Journal of mechanical science and technology. 25; (3) 713-719.

Reddeppa P; Gai SL. (2011). Measurement of heat transfer rate on backward-facing steps at hypersonic mach number. Journal of Thermophysics and heat transfer. 25; N3: 321-328

Roberts GO.(1971). Computational meshes for boundary layer problems. Proceedings of the

Second International Conference on Numerical Methods and Fluid Dynamics, Lecture Notes in Physics. Springer-Verlag: New York. 8:171–177.

Schäfer F; Breuer M; Durst F. (2009). The dynamics of the transitional flow over a backward-facing step. J. Fluid Mechanics. 623: 85-119.

Schröck D; Widdecke N; Wiedemann J. (2009). The effect of high turbulence intensities on surface pressure fluctuations and wake structures of a vehicle model. SAE Int. J. Passeng. Cars-Mech.Syst. 2; N1 paper 01-0001: 98-110.

Sims-Williams DB; Dominy RG; Howell JP. (2001). An investigation into large scale unsteady structures in the wake of real and idealized hatchback car models. SAE paper 01-1041; 1197-1208.

Sohankar, A., Davidson, L., Norberg, C., "Numerical simulation of unsteady flow around a square two dimensional cylinder," 12th Australian Fluid Mechanics Conference, University of Sydney,Australia, 517-520, (1995).

Sohankar, A., Norberg, C., Davidson, L., "Low Reynolds number flow around a square cylinder at incidence: Study of blockage, onset of vortex shedding and outlet boundary condition," Int Journal for Numerical Methods in Fluids,26, 39-56, (1998).

Vino G; Watkins S; Mousley P; Wattmuff J; Prasad S. (2005) Flow structures in the near wake of the Ahmed body. Journal of fluids and structures. 20: 673-695.

Weber JD; Danberg JE. (1992). Correlation of mean velocity measurements downstream of a swept backward-facing step. AIAA Journal. 30:11, 2701-2706

Williams, P. T., and Baker, A. J. (1997), Numerical simulations of laminar flow over a 3D backward-facing step. Int. J. Numer. Methods Fluids 24: 1159–1183.

3

Effects of Active Flow Control on flow past Backward step

Abstract:

In the present study, two-dimensional flow over a backward-facing step in laminar flow regime with application of active flow control (AFC) technique is analyzed; two Reynolds numbers of 500 and 800 were evaluated. The aim of the present research is to gauge the effectiveness of implementing AFC to reduce drag and study its effects on flow characteristics. In order to analyze the influence of AFC on the boundary layer and the downstream vortex shedding, two different kinds of AFC techniques were used in this study namely zero net mass flow actuators and fluidic actuators. A parametric non-dimensional analysis was carried out by varying the non-dimensional frequency from 0.005 to 0.1, jet non-dimensional amplitude was varied from 0.025 to 1. Four different positions of the groove were simulated; groove was respectively located at 1.976a, 1.953a, 1.928a and 1.903a, measured downstream from the left side upper edge, where a, is the step height. Three different non-dimensional groove widths of 0.023, 0.048 and 0.073 were also evaluated. The idea behind this study was to determine an optimal configuration to reduce the drag on the step and to suppress the vortex dissipation in the wake of the step. It was observed, when using an AFC frequency ± 10% of the vortex shedding one, that maximum drag reduction was obtained. It is observed that zero net mass flow actuators were more effective than fluidic actuators for drag reduction.

Nomenclature.

a	Height of the inclined step	(m)
A	Non-dimensional amplitude of the AFC jet	
C_D	Drag coefficient	
C_L	Lift coefficient	
f	Non dimensional frequency of AFC	
f_v	AFC frequency	(Hz)
F_D	Drag force	(N)
F_L	Lift force	(N)
h	Height of the non-orthogonal physical domain	
l	Length of the non-orthogonal physical domain	
p	Non dimensional Pressure	
Re	Reynolds number	
t	Non-dimensional Time	
ul	Upstream Length of the physical domain	
u	Non-dimensional Velocity X direction	
U	Free stream non-dimensional velocity in X direction at the inlet	
v	Non-dimensional Velocity Y direction	
V_{av}	Average half cycle velocity of the AFC jet	(m/s)
V_{jet}	AFC jet velocity in Y direction	(m/s)
w	Non-dimensional groove width	
W	Groove width	(m)
x	Non-Dimensional Eulerian coordinates in horizontal direction	
y	Non-Dimensional Eulerian coordinates in vertical direction	
ϕ	Generic parameter	
Ψ	Additional default velocity amplitude of the AFC jet	
ρ	Incoming fluid density	(Kg/m^3)
ρ_{jet}	Actuating jet density	(Kg/m^3)

Abbreviations.

AFC	Active flow control
FA	Fluidic actuator
ZNMF	Zero net mass flow
BFS	Backward facing step.

3.1. Introduction.

Flow control, whether passive or active, has a wide range of applications. Aviation industry, for example, is interested in using active flow control to modify lift and drag on aircraft wings. Automobile industry, is aiming to suppress vortex formation at the rear of cars/trucks to reduce drag and therefore decrease fuel consumption. Construction industry has traditionally used passive flow control to minimize or even suppress downstream undesirable vortices on bridges, buildings, pipes placed perpendicular to a flow, etc; the use of active flow control is also currently under study. Several methods were studied to analyze their efficiency, reliability and simplicity regarding the active flow control approach.

The use of injection, absorption and both periodic injection and absorption, involving devices like fluidic actuators or zero net mass flow actuators, is presently being tested in many fields. Important parameters related to active flow control actuators are, the precise location and width of the groove, the fluid jet amplitude, the jet frequency if pulsating flow is used and the momentum coefficient. In the present chapter, several of these parameters will be evaluated in a backwards facing step under laminar flow conditions.

Among the previous research undertaken by applying AFC on backwards facing step, Dahan et al (2012) carried out an interesting study. They performed a 2D and 3D numerical study using Reynolds numbers Re=280 and 1500 respectively, and employing both open and closed loop control. Two different locations of the zero net mass flow actuators were considered, namely near the separation border and close to the step foot. They observed that perturbing the flow with a frequency close to the shedding frequency, increased the turbulent kinetic energy in the near separation region and decreased the base pressure. Actuator location was found to be a significant parameter. Feedback control produced similar flow behavior in laminar and turbulent conditions. Open loop frequencies employed ranged St_h =0.04 to 0.3.

Dejoan et al (2005) numerically studied the effect of a 2D ZNMF actuator located just before the separation corner with a jet inclination of 45°, the same inclination was also used by Dahan et al (2012). Synthetic jet actuation frequencies employed ranged from St_h =0.077 to 0.2, the frequency St_h= 0.2 was associated to the natural roll-up process instability mode of the shear layer and was the most effective to reduce downstream bubble length. When studying boundary layer performance in low-pressure turbines with AFC, Sondergaad et al (2002) and Postl et al (2003), observed that unsteady suction was more effective that steady one, and AFC jets located perpendicular to the surface were more effective than tangential ones. Marrot et al (2005) used a loudspeaker located downstream of the step to activate the boundary layer, the maximum effect was observed when the loudspeaker frequency was equal to the boundary layer instability mode, at these conditions a small reduction of the recirculation length was obtained. The pre-excited flow was controlled using two rows of synthetic jets located on the vertical side of the step. A similar method, consisting of two arrays of jets located on the vertical side of the step of which the upper row steadily absorbs and the lower row steadily injects, was analyzed numerically in 2D by Creusé et al (2009), in fact different AFC techniques including pulsating flow were evaluated. In Dahan et al (2012), and Marrot et al (2005), open loop and closed loop control were studied. For open loop control, the optimum actuation frequency, as already found by many other researchers, coincided with the fundamental frequency, which was St_h =0.14, the optimum amplitude being A=0.2, this was the same amplitude used by Dahan et al (2012). According to the work presented by Hassan (1992), in laminar flow conditions, the shear layer has two instability modes, the first one defined by a Strouhal number, $S_{r\theta} = f\,\theta/U$, where θ is the momentum thickness of the boundary layer on the step edge, f is the natural roll up frequency of the shear layer and U is the free stream velocity. The step mode based on the step height h, and defined by Strouhal number, $S_{rh} = f\,h/U$ characterizes the second instability mode. He observed these values to be around $S_{r\theta}$ = 0.012 and S_{rh} = 0.185 respectively, these values match with the values obtained lately by Marrot et al (2005), St_h =0.14 and Dejoan et al (2005), St_h =0.2. In Vukasinovic et al (2010), active flow control in a backwards facing step under turbulent conditions was studied, it was reported that a slight waviness of energy in the boundary layer results in a low scale periodic vortex train. They observed that the actuation induced time periodic modulation of the vorticity flux within the boundary layer, which was the primary source of vorticity for the separated shear layer. The vorticity flux within the boundary layer is responsible for the formation and advection of a train of discrete vortices having a characteristic cross-stream scale and streamwise spacing than are typically smaller than the boundary layer thickness. They observed three different domains in the near field of the forced shear layer. In Brunn and Nitsche (2006), an experimental research of flow around a backwards facing inclined step with 25 degrees slant angle at Reynolds $Re_H = 4*10^4$ was undertaken, they also studied an Ahmed body configuration, being the slant angle and Reynolds number respectively of 35 degrees and $4.9*10^4$, flow was evaluated via using PIV. They observed the flow was characterized by two fundamental frequencies, one was associated to the shear layer instability and the second one was the vortex shedding frequency. It was also realized that the optimum forcing frequency, whenever using AFC periodic forcing, was linked with the formation of the large-scale structures, the vortex shedding structures. In the experimental study carried out by Joseph et al (2012) on a backwards inclined step, the authors observed three unsteady mechanisms which could be characterized by a constant value of Strouhal number. The first unsteady mechanism was linked with the ring-shaped structure observed in the wake, the second one was associated with the natural Kelvin-Helmholtz instability of the shear layer, and the third one was due to the flapping of the shear layer. As already observed in Brunn and Nitsche (2006) and Leclerc et al (2006), they also noticed that the most effective forcing frequency was the one associated to the downstream vortex shedding.

Groove width and location, frequency, amplitude and of course, the overall amount of energy of the AFC to be applied in each particular application, evaluated as momentum coefficient, is nowadays an interesting field of research. What so far appears to be clear is that when using periodic forcing, frequency employed should be around the vortex-shedding frequency.

The rest of the chapter is divided into following sections. In section 3.2, the definition of the problem including grid used, boundary conditions, equations applied, numerical method used and the active flow control techniques employed are defined. Section 3.3 will present the validation of the model. In section 3.4, the results obtained are discussed.

3.2. Problem Statement.

Figure 3.1 presents the physical domain of the backward facing step. Flow over a Backward facing step with upstream length, ul=2a and downstream length dl=20a, was simulated at Reynolds number, Re=500 and 800. Figure 3.1 also presents the boundary conditions used for the simulation. No slip boundary condition was used at all solid boundaries. As the flow is unconstrained at the top, free slip boundary condition was used at the top and the open boundary was located at a distance of 8a, according to Sohankar et.al. (1995). Neumann boundary condition was used at the outlet. In order to prevent the far field downstream boundary to affect vortex shedding, the outlet boundary was located at a distance of 20a, downstream of the inclined step lower vertex, as suggested by Sohankar et.al. (1998). Flow was evaluated in two dimensions under laminar regime.

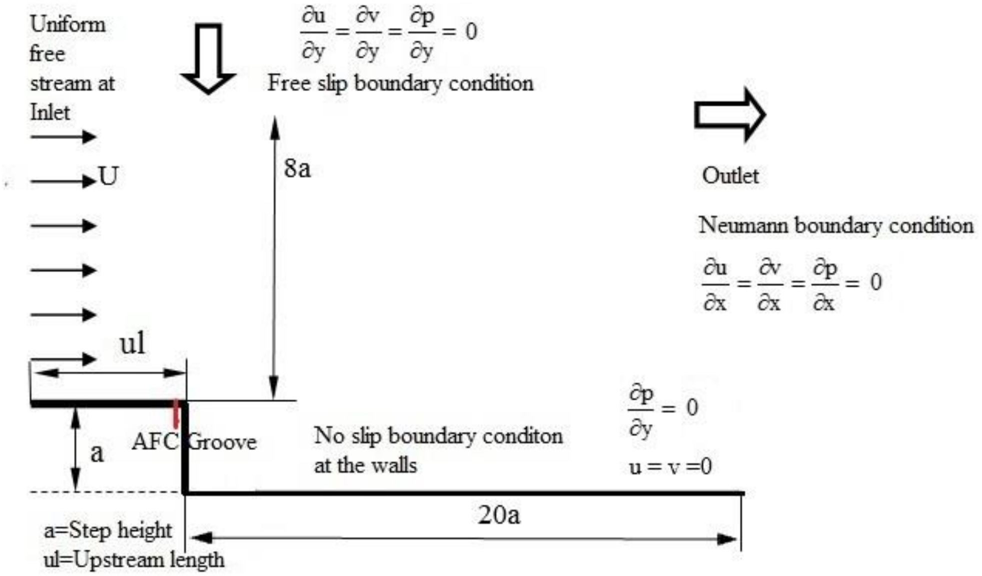

Figure 3.1: Physical domain and boundary conditions of the backwards facing step.

Figures 3.2(a), (b), present the grid of the proposed problem. An orthogonal non uniform structured grid was chosen, since it is most appropriate to simulate the flow dynamics over the step. Figure 3.2(b), shows the three sub-domains of the grid. The first sub domain is the region over the upstream surface of the backward step. The second sub-domain is located behind the step on the rear edge of the step. The region over the second sub-domain and behind the first sub-domain is the third sub-domain. Structured grid has been generated in the three sub-domains using the stretching transformation proposed by Roberts (1971), which refines the grid in the vicinity of the solid walls.

Simulations were performed using two different types of active flow control techniques, Zero Net Mass Flow Actuators (ZNMFA) and Fluidic Actuators (FA), applied on the upstream length of the step at four different locations, x=1.976a, x=1.953a, x=1.928a and x=1.903a, measured downstream from the upper left hand side step origin, a being the step height. Three different non-dimensional groove widths of 0.023, 0.048 and 0.073 were also evaluated.

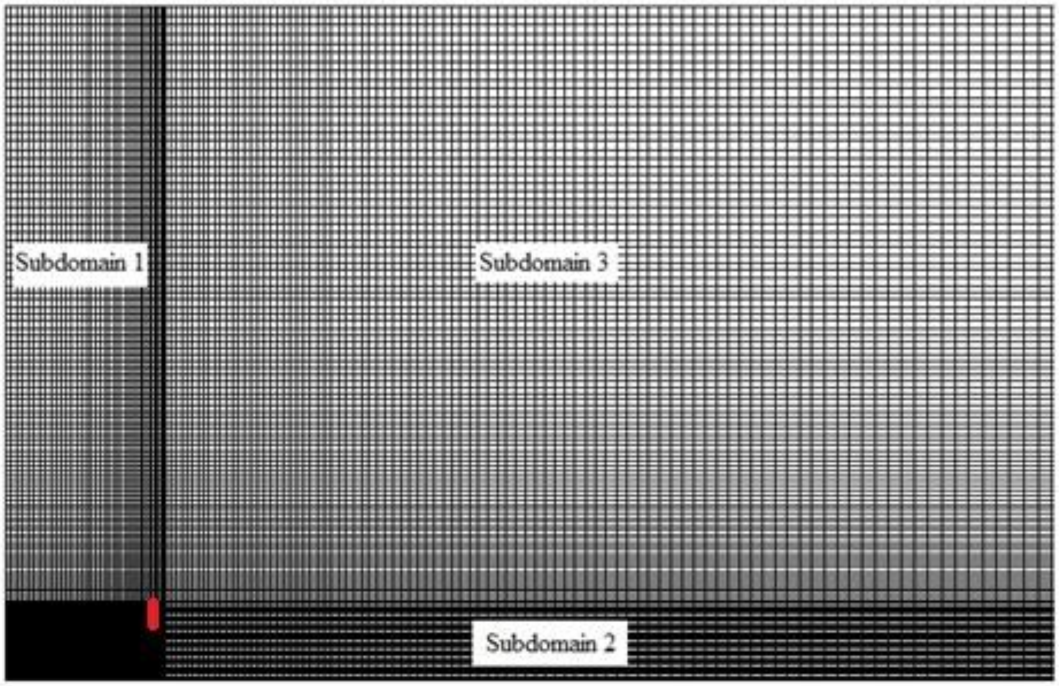

2(a)

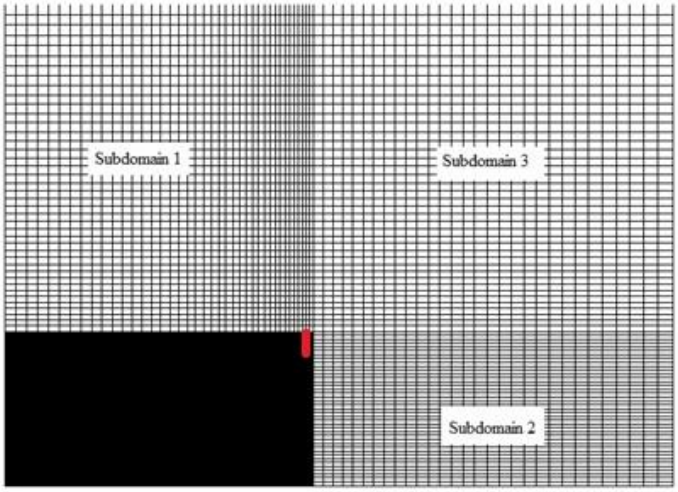

2(b)

Figure: 3.2(a) Non uniform structured grid for discretization of the domain. 2(b) Closer view of the grid collocation at the wall of the step for accurate resolution of the boundary layer.

Studies were carried out to understand the effects of the active flow control techniques on the boundary layer development on the horizontal surface and subsequently on the flow downstream of the step. Two different parameters of the active flow control techniques were varied to study their effects of the flow, amplitude and frequency. The non-dimensional frequency, f of active flow control jet, was varied from f=0.005 to f=0.1, eight different jet non-dimensional velocity amplitudes, A varying form A=0.025 to 1 were also considered.

3.2.1 Governing Equations.

Simulations were done with non-dimensional form of Navier-Stokes equations. To non dimensionalize the equations, the height of the step, a, was considered as the characteristic length, the free stream velocity, U as the characteristic velocity. The characteristic pressure was ρU^2 and the characteristic time was defined as the characteristic length divided by the characteristic velocity a/U. Reynolds number was defined as $Re = \frac{\rho U a}{\mu}$; notice that fluid density and viscosity were taken as constant. Flow was considered as isothermal.

The non-dimensional form of the momentum and continuity equations for laminar flow is represented as:

$$\frac{\partial u}{\partial t} + u\frac{\partial u}{\partial x} + v\frac{\partial u}{\partial y} = -\frac{\partial p}{\partial x} + \frac{1}{Re}\left(\frac{\partial^2 u}{\partial x^2} + \frac{\partial^2 u}{\partial y^2}\right) \qquad (3.1)$$

$$\frac{\partial v}{\partial t} + u\frac{\partial v}{\partial x} + v\frac{\partial v}{\partial y} = -\frac{\partial p}{\partial y} + \frac{1}{Re}\left(\frac{\partial^2 v}{\partial x^2} + \frac{\partial^2 v}{\partial y^2}\right) \qquad (3.2)$$

$$\frac{\partial u}{\partial x} + \frac{\partial v}{\partial y} = 0 \qquad (3.3)$$

The finite volume approach was chosen for the simulation

3.2.2 Numerical Strategy and Boundary Conditions.

A second-order Adams Bashforth-Crank Nicholson scheme for temporal discretization was applied to Navier Stokes equations in finite volume formulation to obtain equation (3.4). Equation (3.5) is the continuity equation applied over a control volume.

$$\frac{u_{i,P}^{n+1} - u_{i,P}^{n}}{\Delta t} V_P + \left(\frac{3}{2}\sum_f F_f^n u_{i,f}^n - \frac{1}{2}\sum_f F_f^{n-1} u_{i,f}^{n-1}\right) = -\sum_f p_f^n S_{f,i} + \frac{1}{2Re}\left(\sum_f F_{dfi}^{n+1} + \sum_f F_{dfi}^{n}\right) \qquad (3.4)$$

$$\sum_f F_f^{n+1} = 0 \qquad (3.5)$$

Equations (3.4) and (3.5) were solved by using the bi-conjugate gradient stabilized method. The boundary conditions used in the simulation were depicted in figure 3.1, a brief description of the different boundary conditions follows.

At the inlet, uniform free stream condition for velocity and Neumann boundary condition for pressure were used.

$$u = U, \quad v = 0, \ \frac{\partial p}{\partial x} = 0 \tag{3.6}$$

In all solid boundaries, no-slip boundary condition for velocity and normal gradient condition for pressure was employed.

$$u = 0, v = 0 \text{ and } \nabla p.\hat{n} = 0 \tag{3.7}$$

Where $\hat{n}$ is the unit normal vector perpendicular to the surface.

At the far field, as the present study focuses on the unconfined flow past an inclined step, a free slip boundary was applied at a distance of 8a, measured from the upstream horizontal surface, see figure 3.1.

$$\frac{\partial \phi}{\partial y} = 0; \ \phi = u, v; \ \frac{\partial p}{\partial y} = 0 \tag{3.8}$$

The outlet boundary, right hand side of figure 3.1, posed the biggest difficulty in computational modeling, especially when studying flows with unsteady wake or convecting vortices. The definition of this boundary condition is of paramount importance, since it not only changes the flow pattern but also affects convergence. For the present case the derivative of all dependent variables was taken equal to zero, which is known as Neumann boundary condition (NBC), condition presented in equation (3.9).

$$\frac{\partial \phi}{\partial x} = 0, \ \phi = u, v, p; \tag{3.9}$$

The distance between the step bottom edge and outlet boundary, where the Newman boundary condition is applied, was considered as 20a as seen in figure 3.1.

MAC (Marker and Cell) method with velocity and pressure coupling was applied using a predictor-corrector strategy. In the present study, the respective pressure correction factor in all the neighboring cells were also considered, notice that this is a further improvement with respect to the original MAC method and minimizes the error involved in the calculation. In this method the momentum equations are solved to calculate provisional values for the velocity components for the next time step using the predictor step and thereafter calculating the pressure and velocity correction factors for achieving the incompressibility condition of mass conservation.

3.2.3 Zero-net mass flow control technique.

In this technique the flow control is induced into the flow upstream of the step in such a way that the net mass flow from the groove in zero. A sinusoidal form of wave equation was used to induce the active flow control technique as presented in equation (3.10).

$u=0$

$$v=AU\sin(2\pi f t) \tag{3.10}$$

Where u and v are respectively the non-dimensional horizontal x-component and vertical y-component of fluid velocity, f is the non-dimensional frequency of the active flow control jet and t is the non-dimensional time. A is the non-dimensional velocity amplitude of the oscillating jet.

3.2.4 Fluidic Actuator flow control technique.

In fluidic actuators, the flow control is induced into the flow upstream of the step in such a way that the net mass flow from the groove in outwards. This is the primary difference from the flow control in the case of zero net mass flow technique. This is applied by inducing a default amplitude Ψ added to the sinusoidal form of wave equation used in zero net mass flow technique as presented in equation (3.11).

$u=0$

$$v=\Psi+A\,U\sin(2\pi f\,t) \tag{3.11}$$

Where Ψ is the additional default non-dimensional velocity amplitude, in the present study the default amplitude Ψ was considered equal to the amplitude A of the jet, so that the minimum velocity of the injected jet is zero.

The primary difference between zero net mass flow and fluidic actuator techniques is that in case of former, the fluid is injected and absorbed into the upstream boundary layer but in the case of the fluidic actuator the fluid is only injected due to the predefined additional velocity amplitude, Ψ. In both cases the fluid is injected perpendicular to the upstream surface, since according to Sondergaad et al (2002) and Postl et al (2003), perpendicular forcing is more effective.

3.2.5 Non dimensional parameters.

Lift and drag coefficients evaluate the average normal and shear stresses acting on the horizontal upper and vertical walls of the step. To calculate lift and drag coefficients, the expressions presented in equation (3.12) were used. It is important to realize that as the flow under study is unsteady and periodic, hence the concept of average lift and drag coefficients has to be used.

$$C_D=\frac{F_D}{\frac{1}{2}\rho U^2 a^2}; \qquad C_L=\frac{F_L}{\frac{1}{2}\rho U^2 a^2}; \tag{3.12}$$

F_D and F_L are respectively the dimensional drag and lift forces due to the pressure and shear stresses acting on the step walls. Drag force was taken as positive when acting in the positive X axis direction, and Lift force was regarded as positive when acting towards the positive Y axis direction. The expression to derive the Strouhal number St, which is equal to the non-dimensional frequency f, is presented in equation (3.13). f_v is the dimensional frequency.

$$\mathrm{St} = f = \frac{f_v\, a}{U} \tag{3.13}$$

Momentum coefficient, C_μ, used in the present study is presented in equation (3.14).

$$C_\mu = \frac{\rho_{jet} V_{av}^2 W}{\rho U^2 a} \tag{3.14}$$

Where ρ_{jet} is the jet density, ρ is the incoming fluid density, V_{av} is the average half cycle velocity of the AFC jet, W is the width of the AFC groove on the upstream surface, a is the height of the inclined step and U is the fluid free stream velocity, as presented in figure 3.1.

3.3. Code Validation.

The code was validated by simulating the flow over a backward step and the results were compared with the results presented in the literature. Figure 3.3 shows the streamline plots for the backward facing step case. Figures 3.3(a, b, c), present the results obtained from the code developed and the graphs presented in figure 3.4(d, e, f), were obtained by Chowdhary and Dhiman (2011). The quality of the figure 3.4(d, e, f) was compromised when extracted from the paper. Three Reynolds numbers of 100, 150 and 200 were studied in both cases. The comparison of the results was in complete agreement in all cases, in case of the downstream vortex recirculation length.

From the present code, it was observed that the flow over a backward step geometry was steady at Reynolds number, Re=498 but the flow was unsteady and periodic for Re=500. It can be inferred that the onset of vortex shedding occurs around Reynolds number 500, as reported by Armaly et. al. (2003), and also by Chen Y.T. et. al. (2006). The non-dimensional vortex shedding frequency was found to be f=0.05.

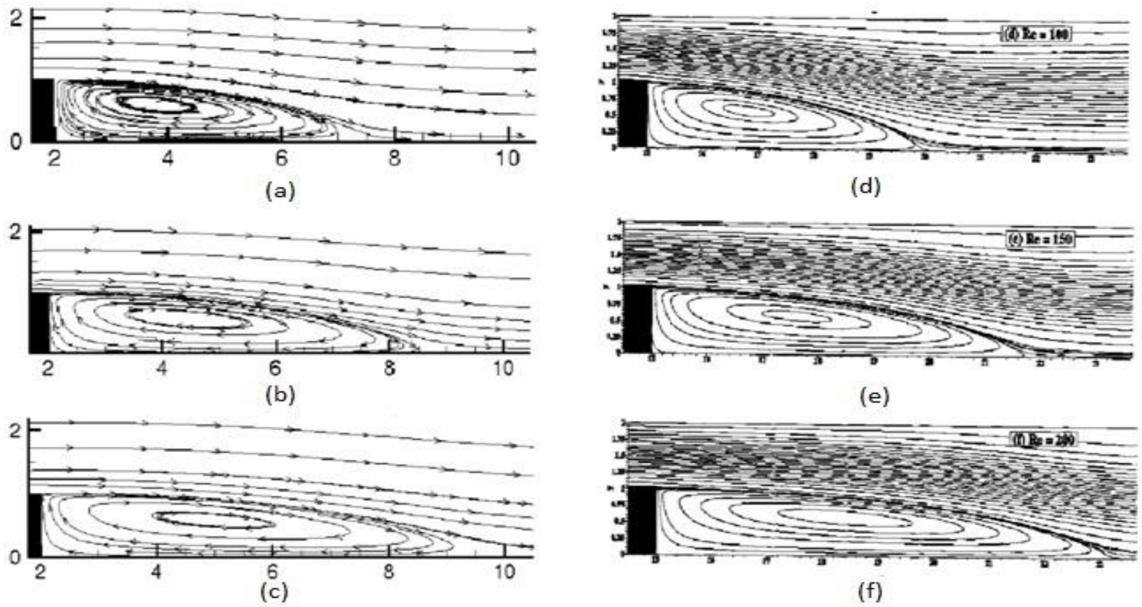

Figure 3.3: Instantaneous Streamline plots for Reynolds Numbers: (a), (d) Re=100, (b), (e) Re=150 and (c), (f) Re=200. Left figures were generated by the present code, right figures were created by Chowdhary and Dhiman (2011).

3.3.1 Effects of grid refinement.

A grid refinement study was carried out on three progressively refined grids, namely 160×140, 200×150 and 240×160 where the number of grid nodes distributed over the rear edge of the backward step were 30, 40 and 50, respectively. An upstream length, ul=2a was considered for the grid refinement study at Reynolds number, Re=800. During the refinement, the non-dimensional smallest and the largest cell size on the backwards facing step edge was maintained approximately at 0.02 and 0.033, respectively.

Grid	160x140	200x150	240x160
Drag Coefficient, C_D	0.2571370	0.2559677	0.2554021
Lift Coefficient, C_L	0.2783731	0.2806993	0.2782181

Table 3.1: Grid refinement for flow past backward facing step

The variation in the drag coefficient, C_D was around 0.455% when the grid was refined from coarsest to the intermediate level. But when the grid was further refined to the finest level, the variation reduced to 0.221%, see table 3.1. Therefore, based on the grid refinement analysis results, a grid size of 200x150 was considered for all simulations.

3.4 Results and Discussion.

3.4.1 Streamlines and vorticity plots.

In order to visualize unsteady periodic laminar vortex shedding past the backward step, in the present section, simulations at Reynolds number Re=500 and 800 are presented in figures 3.4 to 3.8, with the help of instantaneous streamlines and vorticity plots at six equally spaced time intervals within a shedding cycle of time period T. The flow remains laminar under these conditions, since as determined by Armaly et al (1983) the flow over a backwards facing step is laminar whenever Reynolds number is below 1200. From the global flow characteristics, it can be said that the use of ZNMFA and FA produce a very similar effect on the downstream wake patterns.

The onset of vortex shedding in the case of the backward facing step occurs due to the rolling up shear layer, located downstream of the inclined step. The rolling up shear layer is formed due to the interaction between the negative momentum of the vortex in the wake of the step and the solid constrained boundary located below the vortex. As the rolling up shear layer develops, its intensity increases, causing the entrainment of the rolling up shear layer into the neck of growing recirculating vortex at the rear of the step, which leads to the separation of the vortex from the neck and it is consequently shed into the wake of the step. This mechanism is different from the shedding mechanism in case of generic bluff body, where vortex shedding occurs due to the flapping motion of the upper and lower vortices appearing at the body trailing edge, vortices were shed alternately into the wake.

Figure 3.4 presents the vortex shedding cycle for flow over the backward step when ZNMF technique is applied, six equally spaced temporal streamline and vorticity plots are presented, Reynolds number evaluated was Re=500. It was observed that, at frequency f=0.055, amplitude A = 0.1 and momentum coefficient, C_μ =0.0001, vortex shedding was subdued and the drag reduction was found to be maximum. This suppression of vortex shedding can be attributed to the fact that, Reynolds number Re=500 is near to the critical Reynold number, and AFC frequency applied is close to the natural vortex shedding frequency. The groove was placed at (x=1.953a, y=a) and the non-dimensional width of the groove was considered as w=0.023. Vortex shedding occurs in the rear of the step, due to the interaction of the rolling up shear layer formed below the growing recirculating vortex with the neck of the vortex, causing the vortex separation and subsequently dissipation in the wake of the step as seen in figure 3.4(g, h, i). Identical vortex shedding mechanism was observed, as seen in figures 3.4 and 3.5, in all the simulations studied in the present study irrespective of the Reynolds number, AFC technique used and groove configuration. However, some variations in the recirculation and neck lengths of the vortices in the wake of the step were observed. Primarily differences in different cases concerning the characteristics of the flow over a backward step when the AFC techniques were applied on the upstream length of the step were the pressure variation on the upstream and rear surfaces of the step. Also in some cases the separation of the boundary layer in the upstream length due to the interactions of the injected jet into the upstream boundary layer. It was also observed that upstream boundary layer oscillates in harmony with the injection and absorption of the fluid when ZNMF technique was applied, see figure 3.5, where the thickness of the boundary layer varies along the vortex shedding cycle with respect to the upstream surface near the step corner.

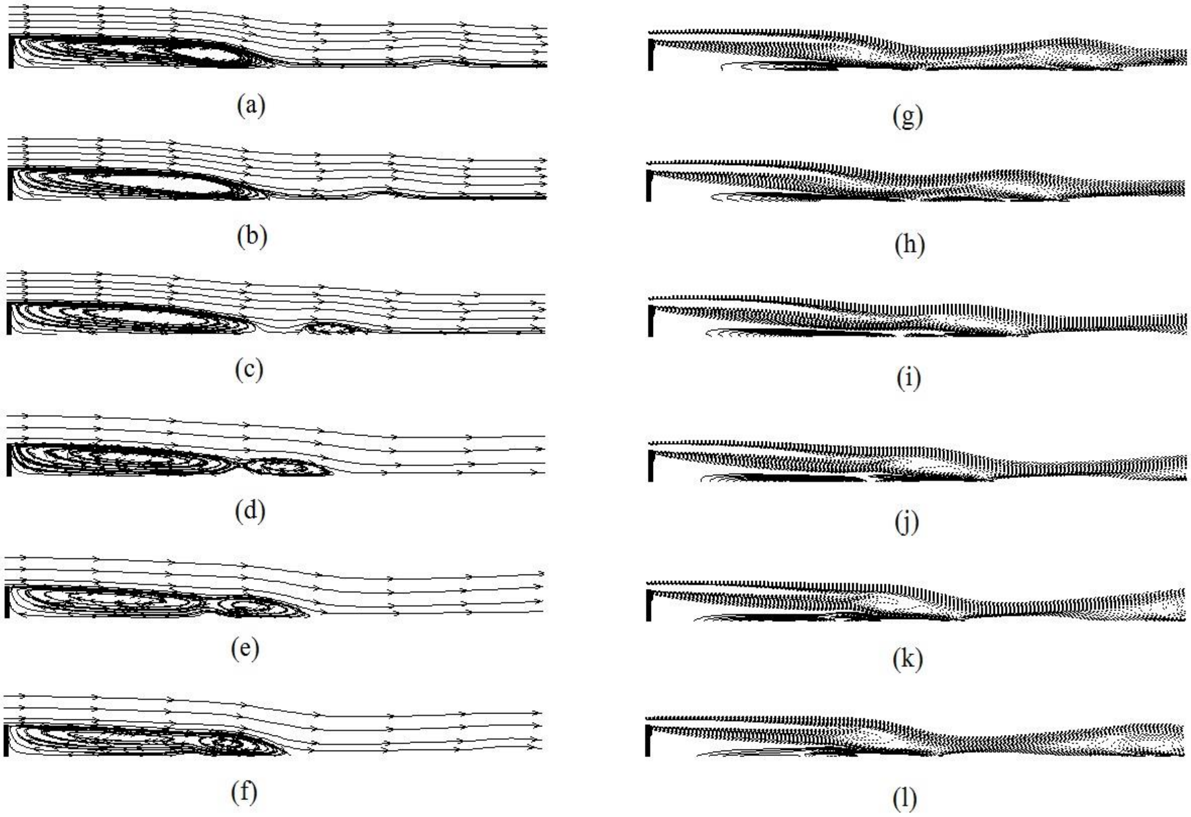

Figure 3.4: Streamline and corresponding Vorticity plots of vortex shedding cycle in the wake of Backward Step at Re=500, with upstream zero net mass flow control frequency f=0.055, A=0.1, w=0.023, C_{μ} =0.0001 and groove position x=1.953a: (a, g) T/6; (b, h) T/3; (c, i) T/2; (d, j) 2T/3; (e, k) 5T/6; (f, l) T.

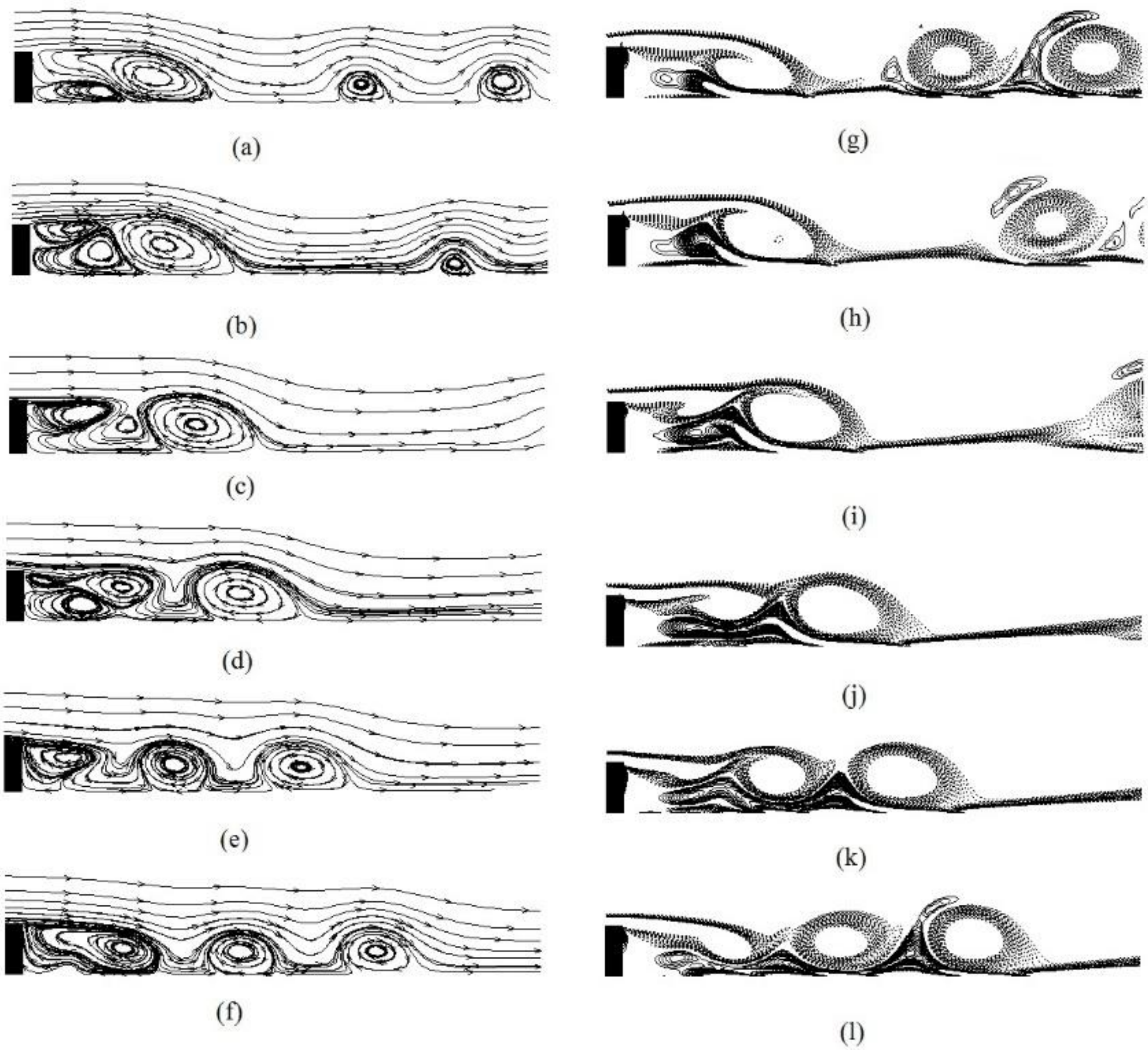

Figure 3.5: Streamline and corresponding Vorticity plots of vortex shedding cycle in the wake of Backward Step at Re=500, with upstream zero net mass flow control frequency f=0.055, A =1 w=0.023, C_μ=0.0093 and groove position x=1.953a: (a, g) T/6; (b, h) T/3; (c, i) T/2; (d, j) 2T/3; (e, k) 5T/6; (f, l) T.

Figure 3.5 presents the vortex shedding cycle for flow over the backward step with ZNMF technique applied, with six equally spaced temporal streamline and vorticity plots. The frequency of the flow control was f=0.055, amplitude A=1 and momentum coefficient, C_μ=0.0093, groove width was w=0.023. Vortex shedding was found to be more random and disorganized than as observed in figure 3.4. It appears as if, at high forcing amplitudes, the energy of the dissipating vortex increases, leading to higher tendency of separation, as seen figures 3.5 (a, g) and 3.5 (f, l). Shear stresses on the upstream surface also increase causing the drag acting on the backward step to increase. In reality, the use of high forcing amplitudes whenever a low Reynolds number is used, delivers the jet forcing associated energy whether onto the upper part of the boundary layer or simply outside the boundary layer, producing very often an undesired effect, shear stresses increase, vortex shedding enhancement, backwards facing vertical wall pressure decrease.

Figure 3.6 presents the vorticity plots along a vortex shedding cycle, at Re=800 and when using ZNMFA, frequency, f=0.051, amplitude, A=1, non-dimensional width w=0.023, grove position x=1.953a and momentum coefficient, C_μ=0.0093. Corresponding vorticity plots of the AFC injection of the fluid on the upstream surface into the boundary layer in a vortex shedding cycle are presented. A gradual increase of fluid injection into the upstream boundary layer can be observed in figures 3.6(j, k, l) and the decrease in the fluid injection can be seen in figures 3.6(l, g, h). The upstream boundary layer remains attached to the surface until reaching the step corner and detaches form the surface forming the neck of the vortex, which then elongates along with the growing recirculating vortex in the wake. The growing recirculating vortex leads to the formation of rolling up shear layer, which interacts with the growing recirculating vortex leading to dissipation of the vortex in the wake of the step as seen in the vorticity plots. In figures 3.6(j, k, l), boundary layer thickness slightly increases and bends up, while in figures 3.6(g, h, i), boundary layer bends down. Notice that the boundary layer fluctuates with the jet forcing frequency. In figure 3.7, the FA technique applied to the backward step, at Re=800, frequency f=0.055, amplitude A=1 and momentum coefficient, C_μ=0.0616, is introduced, groove non-dimensional width and position are respectively: w=0.023 and x=1.953a. Since the momentum coefficient corresponding to figure 3.7 is much higher than the one used in figure 3.6, which is due to higher velocity amplitude of the injected jet associated to FA, therefore determining the maximum velocity at which the fluid is injected, the AFC jet is breaking the upstream boundary layer as seen in figure 3.7(l). This phenomenon is called boundary layer tripping, and has associated a relatively high upstream pressure. This effect also leads to the separation and re-attachment of the upstream boundary layer just before the AFC groove.

From figure 3.6 and 3.7, it can be observed that in case of former, the fluid injection is within the boundary layer, whereas in case of latter, the injected jet is breaking through the boundary layer causing it to separate upstream of the groove. The boundary layer then reattaches just before reaching the groove as seen in figure 3.7(l). It is important to realize that, the momentum coefficient for FA, is around 7 times the one for ZNMFA and this explains why, especially when A=1, fluidic actuators generate boundary layer tripping. This boundary layer separation upstream of the step upper corner, leads to a pressure increase acting on the upstream horizontal surface leading to a drastic decrease in the body lift due to the increase in the downward force acting on the upstream surface as presented in figures 3.11(c), (d). Due to the high velocity of the injected jet in case of figure (3.7), FA, the recirculating vortex is also much larger and tends to grow further than in case of figure (3.6), ZNMFA, as observed form the vorticity plots. In figure (3.6) the vortex size is about the height of the step but in case of figure (3.7) the size is larger than the height of the step, indicating an earlier boundary layer separation at the step edge.

A preliminary conclusion derived from that analysis ia that amplitude of the fluid injection, which has a quadratic effect to the momentum coefficient C_μ, is the primary factor influencing the flow over the step. It was found that the variation of frequency, f had secondary effect on the upstream boundary layer in terms of separation and reattachment but the variation of amplitude had a maximum effect on the properties of the upstream boundary layer. In order to investigate the effects of the amplitude of AFC on the flow, 8 different cases were simulated by varying amplitude from 2.5 % to 100% of the flow free stream velocity, which corresponds to A=0.025 to 1 respectively.

Figure 3.8 presents the vorticity plots for identical conditions presented in figure 3.4 but with a groove width of w=0.073, and respective momentum coefficient, C_μ=0.00032. By comparing vorticity plots from figures 3.4 and 3.8, as momentum coefficient increases 32 times causing enhanced vortex shedding in wake of the step which was suppressed in case of former. This can be attributed to the increased volume of fluid injected and absorbed into the upstream boundary on the step leading to inducing of higher energy. It was observed that in case of figure 3.8, the upstream boundary layer oscillated in harmony with the ZNMFA frequency. From this comparison, it can be also deduced that increase in groove width leads to enhanced vortex shedding and influences the flow properties considerably apart from amplitude of the jet as observed by comparing figure 3.4 and 3.5.

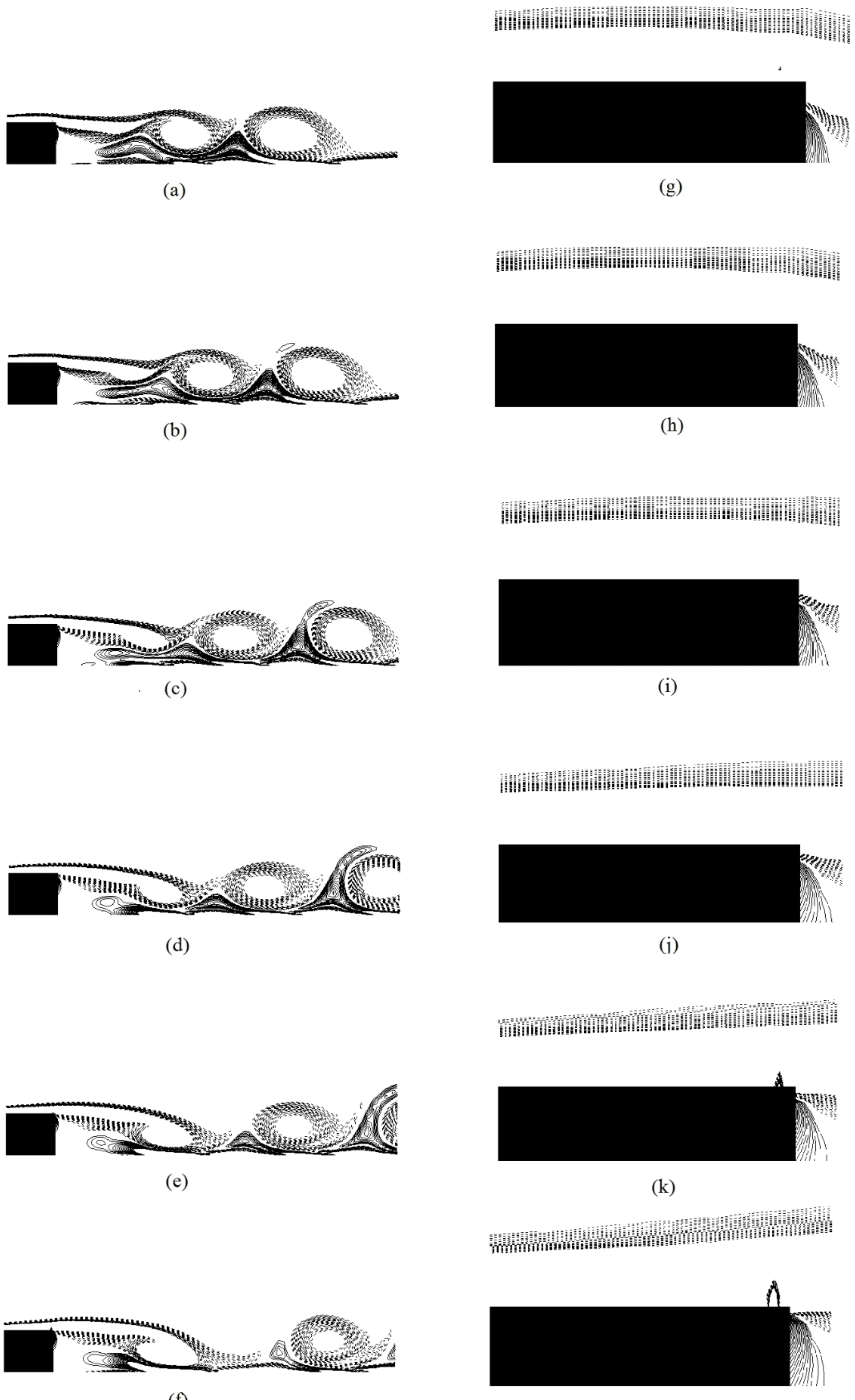

(a) (g)

(b) (h)

(c) (i)

(d) (j)

(e) (k)

(f) (l)

Figure 3.6: Vorticity plots of vortex shedding cycle and corresponding plots of AFC on the upstream surface of the step at Re=800, with upstream zero net mass flow control frequency f=0.051, amplitude A=1, width w= 0.023, C_μ=0.0093 and grove position x=1.953a: (a, g) T/6; (b, h) T/3; (c, i) T/2; (d, j) 2T/3; (e, k) 5T/6; (f, l) T

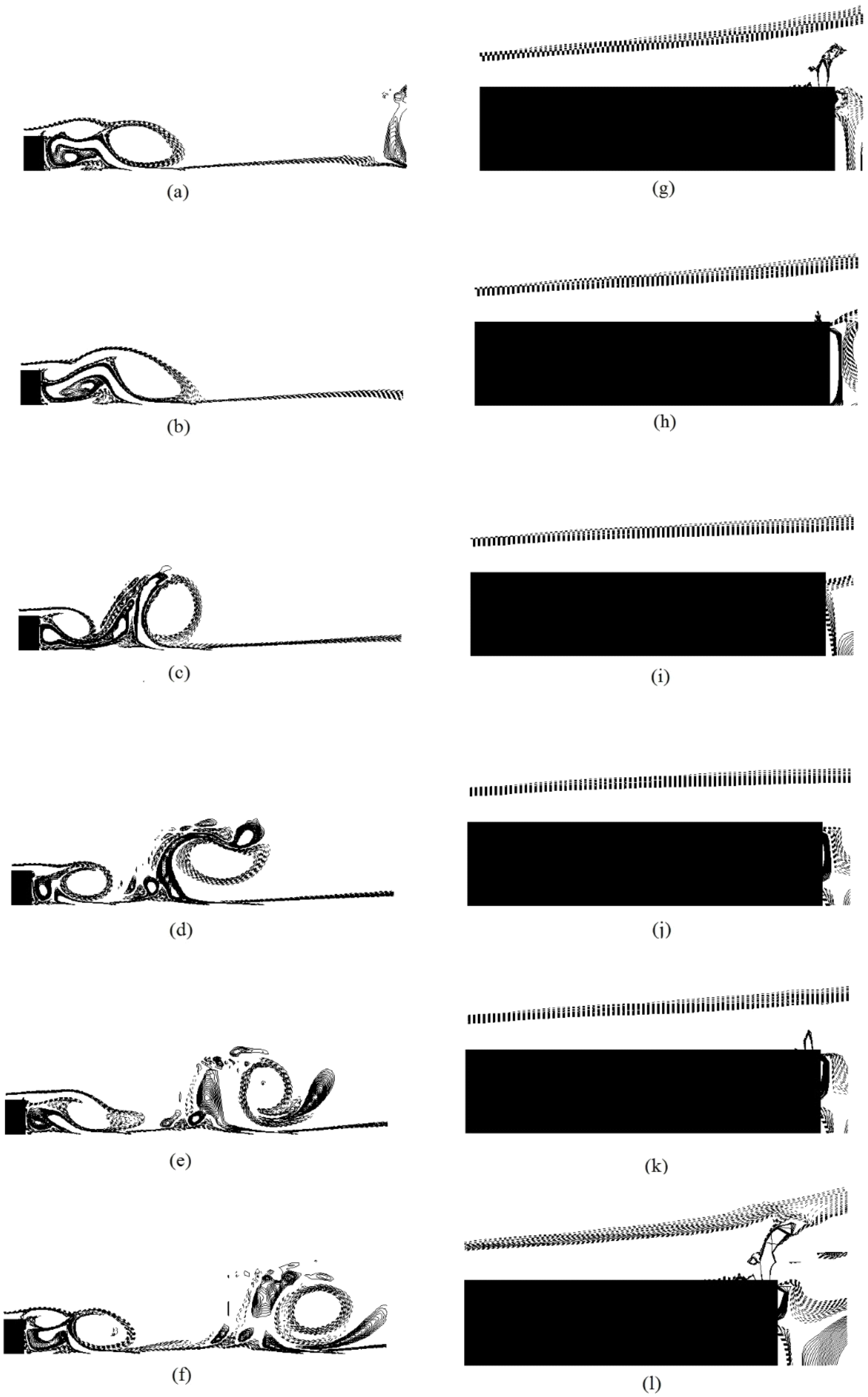

(a) (g)

(b) (h)

(c) (i)

(d) (j)

(e) (k)

(f) (l)

Figure 3.7: Vorticity plots of vortex shedding cycle and corresponding plots of AFC on the upstream surface of the inclined step at Re=800, with upstream fluidic actuator flow control frequency f=0.055, amplitude A=1, width =0.023, C_{μ}=0.0616 and grove positioned at x=1.953a: (a, g) T/6; (b, h) T/3; (c, i) T/2; (d, j) 2T/3; (e, k) 5T/6; (f, l) T

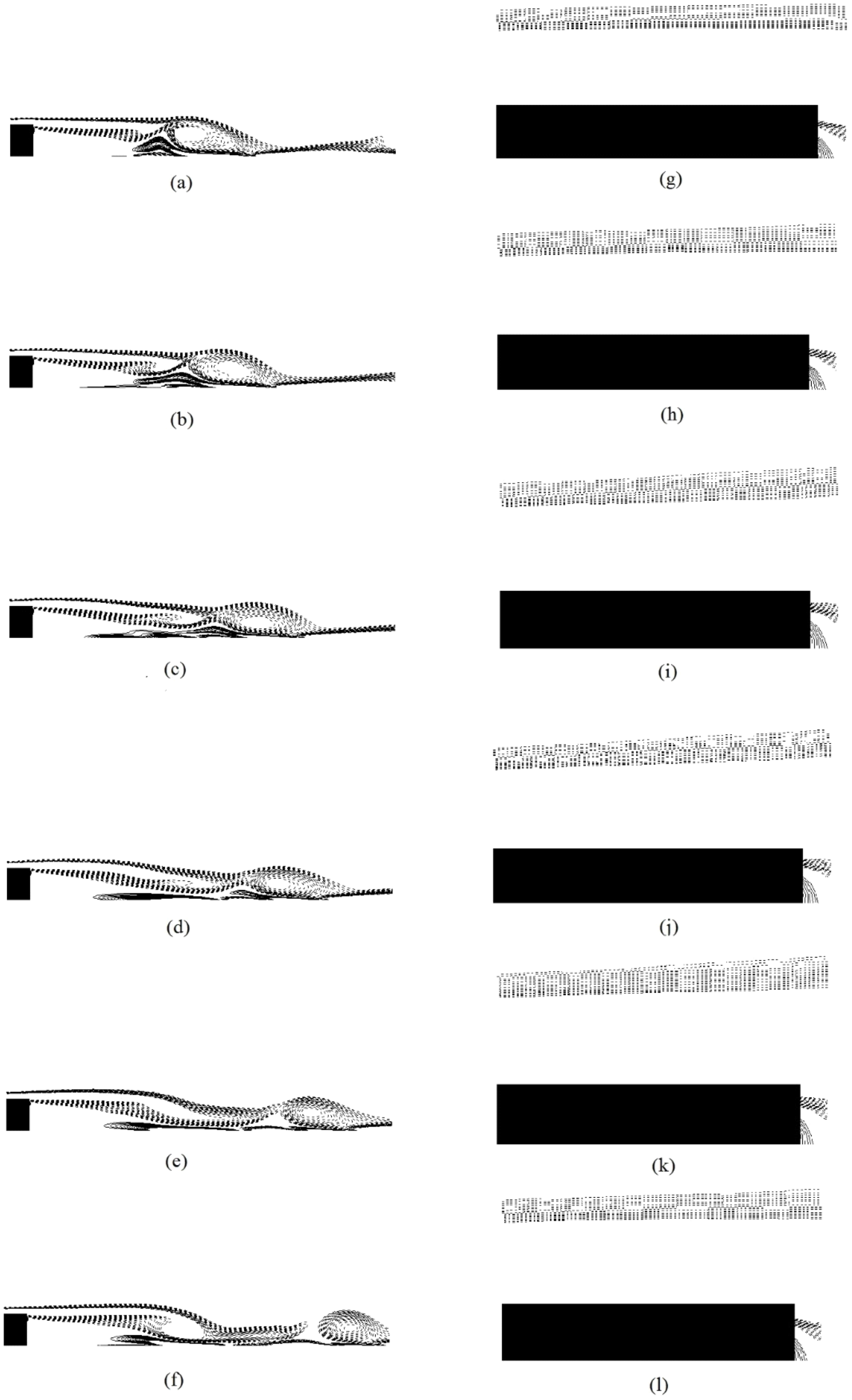

Figure 3.8: Vorticity plots of vortex shedding cycle and corresponding plots of AFC on the upstream surface of the inclined step at Re=500, with upstream zero net mass flow control frequency f=0.055, amplitude A=0.1, groove width w= 0.073, C_μ=0.00032 and grove position x=1.953a: (a, g) T/6; (b, h) T/3; (c, i) T/2; (d, j) 2T/3; (e, k) 5T/6; (f, l) T.

3.4.2 Average lift and drag coefficients.

At Reynolds Re=500, for a jet non-dimensional velocity amplitude A=0.1, momentum coefficient C_μ=0.0001 and optimum frequency f=0.055, the drag on the step was minimum, this can now be better seen in figure 3.9(a). As the velocity amplitude of the AFC jet was increased above 0.1, the drag acting onto the body also increased, figures 3.9(c) and (d). Similar trend was observed in both zero net mass flow and fluidic actuator techniques, but in case of FA the increase was observed to be higher than when using ZNMFA. Especially when using FA, even at relatively small amplitudes, boundary layer suffers an earlier separation due to boundary layer tripping, which generates more active downstream vorticity and makes downstream pressure acting onto the step vertical wall to keep decreasing as jet amplitude increases, this effect is the main factor of the drag coefficient increase.

In figures 3.9(a) and (b), the variation of Drag coefficient with active flow control frequency is presented. The minimum drag values appear at f=0.045 and f=0.055, which happens to be ±10% of the natural vortex shedding frequency when no flow control is applied. In the present case +10% i.e. f=0.055 is found to be slightly more effective than -10% in drag reduction, as seen in figure 3.9(a), hence flow patterns in figures 3.4 and 3.5 were presented at this frequency. The results presented in these two figures, are in complete agreement of previous studies undertaken by, Creusé et al (2009), Dahan et al (2012), Hassan (1992), among others, then in all these investigations it was proved that exciting the flow with a frequency around the vortex shedding natural one, diminishes downstream vorticity, whenever the injected jet amplitude is the appropriate. It is interesting to observe that between the two effective frequencies 0.045 and 0.055 and in both control techniques, the drag seems to increase and decrease following a zigzag cycle. This appears to be due to the nonlinear interaction between the forcing jet frequency and the shear layer natural frequency. Therefore, a small change in the jet forcing frequency from the natural vortex shedding frequency, it leads to uncoupling effects until reaching an effective frequency of f=0.05±10%. The frequencies f=0.055 and f=0.045 were observed to be the limits of oscillations in the drag coefficient and frequencies above and below them lead to an increase of the drag coefficient.

When carefully observing figures 3.9(c), (d), it is noticed that, the flow control amplitudes at which the minimum drag was acting on the body, at Reynolds number Re=500 were, A=0.2 and 0.05 for ZNMF and FA techniques respectively. Nevertheless, at Reynolds 500 and for ZNMFA, the amplitude of A=0.1 produced almost the same effect. At Reynolds number Re=800, the optimum amplitudes for drag reduction were respectively A=0.1 and 0.025 for ZNMF and FA techniques. From figure 3.9(d), Re=800, it is noticed that at very small amplitudes, FA appears to be more effective than ZNMFA in reducing the drag coefficient, this indicates that as Reynolds number increases a higher momentum coefficient may be required to activate the boundary layer.

Another interesting phenomenon observed from figure 3.9 and 3.10, is with the variation of the frequency and amplitude of the injected jet, both flow control techniques exhibit similar behavior. Zero net mass flow technique is more effective than the fluidic actuator for drag reduction at the optimum frequency and amplitude of the control jet.

In the present study, four different groove locations were evaluated, x=1.976a, x=1.953a, x=1.928a and x=1.903a, measured downstream from the left hand side upper horizontal surface edge. The groove optimum position for both actuating techniques, with respect to maximum drag reduction was x=1.953a, as presented in figure 3.10(a) and (b). At this position, flow control seems to influence the boundary layer in an efficient manner, delaying boundary layer separation and thereby reducing the drag on the body. When the groove is moved further upstream, it leads to boundary layer earlier separation and the drag on the body increases. When the groove is very close to the right edge, the boundary layers seems to become more unstable and also separate earlier than in the case of optimum position, thereby enhancing the vortex dissipation and causing the drag to increase.

Drag coefficient obtained from the analysis of flow over the backwards facing step, without any flow control implemented on the upstream length, at Reynolds number, Re=500 and 800 was found to be C_D=0.2951 and 0.256 respectively. The optimum frequency where maximum drag reduction occurred at Reynolds number Re=500 for both ZNMF and FA techniques was found to be the same, f=0.055. At Re=800, the optimum frequency for maximum drag reduction in case of ZNMF technique was observed to be f=0.051, but in case of FA technique the optimum frequency was f=0.055. This observation again confirms, that the optimum frequency where maximum effects on drag can be found is, at or near the natural vortex shedding frequency. It also justifies the strategy adopted in this study to analyze the effects of flow control by applying frequencies around the natural vortex shedding frequency.

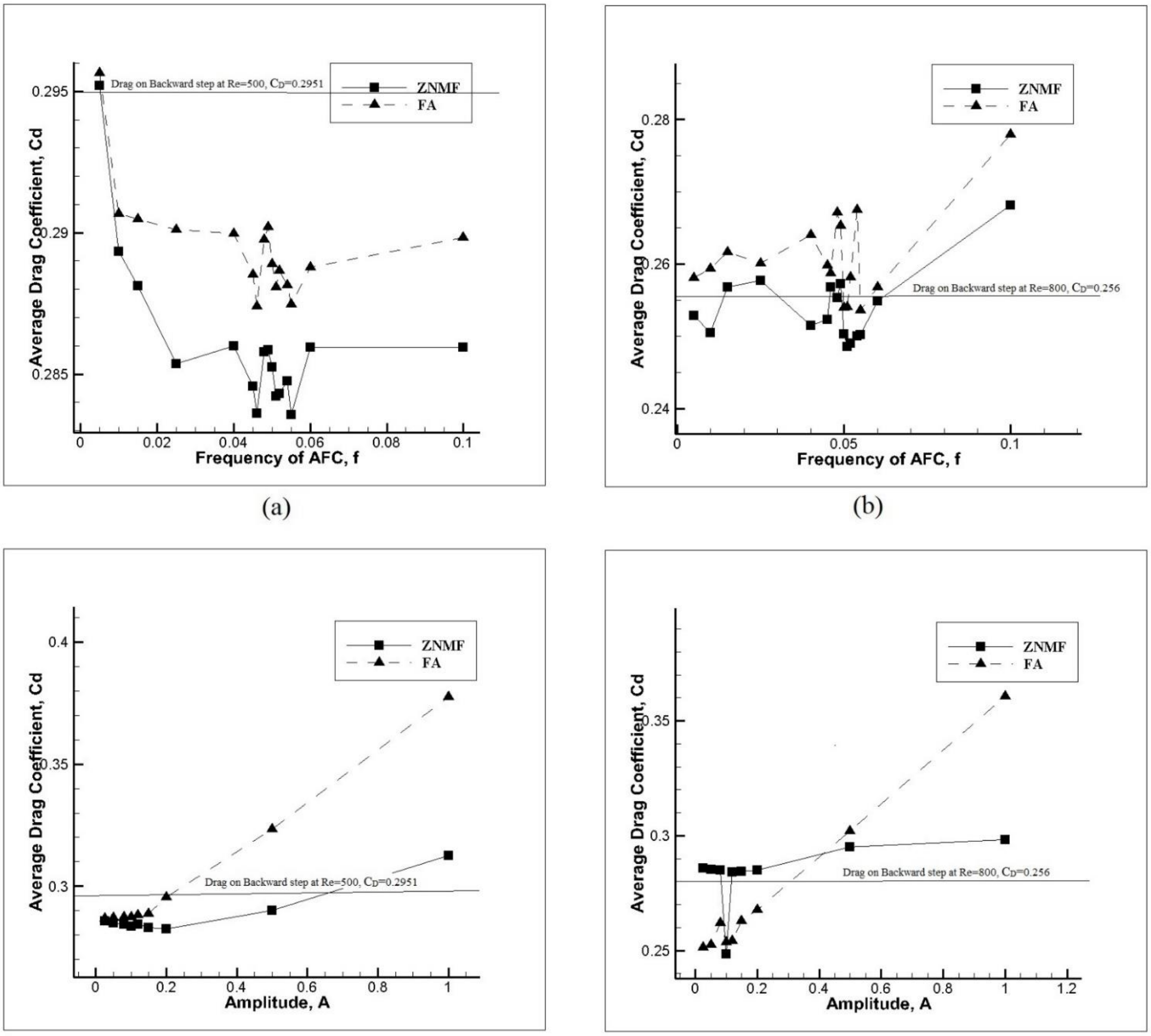

(a) (b)

(c) (d)

Figure 3.9: Average Drag coefficient versus frequency, f of active flow control (AFC) with amplitude A=0.1 (a) Re=500 (b) Re=800, Average Drag coefficient versus Amplitude, A of active flow control (AFC), f = 0.055 (c) Re=500 (d) Re=800. Width was considered as, w= 0.023 and grove position was x=1.953a

Groove width also plays an important role regarding the body drag reduction, in the case of fluidic actuators, the drag acting on the body is almost directly proportional to the groove width, see figures 3.10(c) and (d). This effect is mostly due to the boundary layer tripping generated by the high jet velocity amplitude and momentum coefficient associated to FA. As the groove width increases, the mass flow into the boundary layer also increases, leading to more energy being induced into or even outside the boundary layer, which leads to early separation. This causes downstream vorticity enhancement and reduction in downstream pressure, therefore increasing the drag acting on the body. In the case of zero net mass flow, the drag decreases when the groove width is increased from 0.023a to 0.048a and increases when the width is further increased to 0.074a, indicating that as the energy injected to the boundary layer crosses a threshold value, leads to enhanced vortex shedding and increase in drag coefficient. The effective groove width for maximum reduction in drag and boundary layer stability for ZNMF and FA technique is around 5% and 2% of the step height, as seen in figure 3.10(c) and (d).

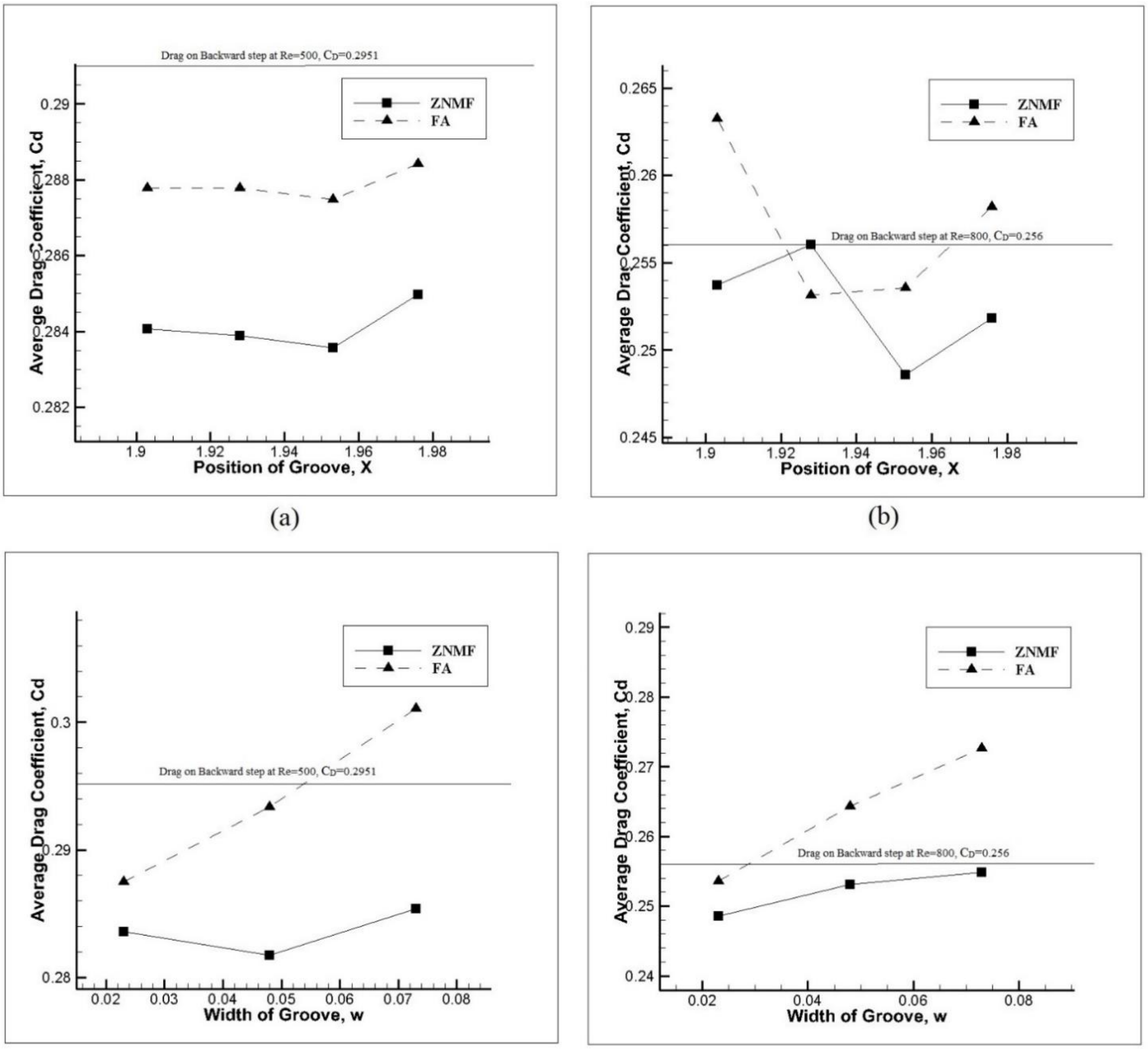

(a) (b)

(c) (d)

Figure 3.10: Average Drag coefficient versus groove position, groove width, w=0.023 (a) Re=500 (b) Re=800, Average Drag coefficient versus groove width, grove positioned at 1.953a (a) Re=500 (b) Re=800

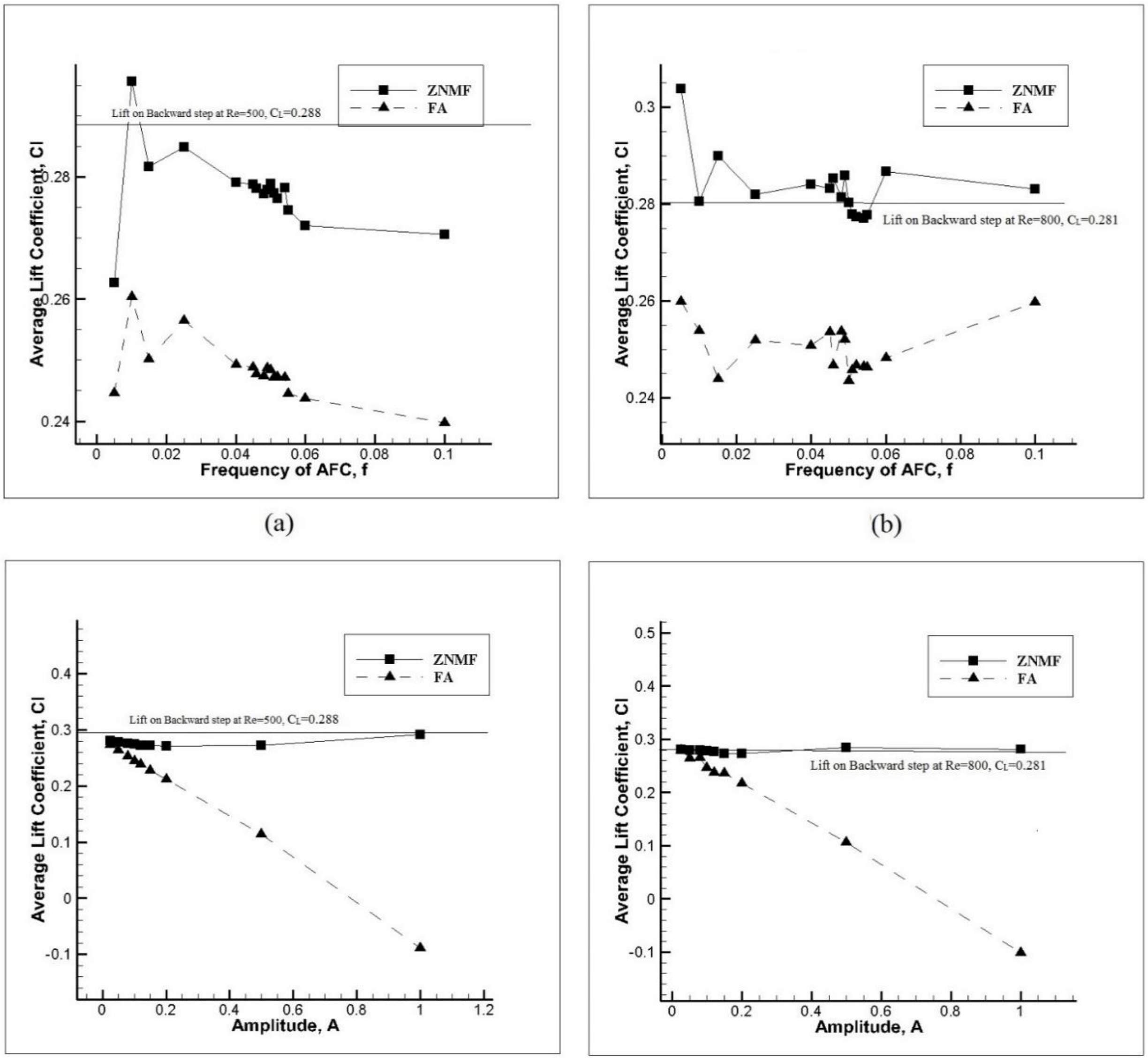

(a) (b)

(c) (d)

Figure 3.11: Average Lift coefficient versus frequency, f of active flow control (AFC) with amplitude A=0.1 (a) Re=500 (b) Re=800, Average Lift coefficient versus amplitude, A of active flow control (AFC) (a) Re=500 (b) Re=800. Width was considered as, w= 0.023, f=0.055 and the grove was positioned at x=1.953a

Figure 3.11(a), (b) present the variation of lift coefficient with active flow control frequency and figure 3.11 (c), (d) present the variation of lift coefficient with amplitude of the flow control jet at Reynolds number, Re=500 and 800 respectively. The first thing to notice is that, at Re=500 and regardless of the actuating system employed, nearly at all frequencies and amplitudes studied average lift coefficient was smaller than the one obtained without AFC, at Re=800 the trend was the same when using FA, but when using ZNMFA, lift was fluctuating around the one obtained without forcing. It is also to be highlighted that frequency had a small effect on the lift coefficient, at Re=500 as frequency increased lift tended to decrease, while at Re=800 frequency was not affecting much except when it was around the vortex shedding one, where the minimum lift was obtained. Regarding the effect of jet forcing amplitude, from figure 3.11(c) and (d), it is noticed that when using FA, as amplitude increases lift coefficient decreases, but when using ZNMFA amplitude modification has a much smaller effect on lift and in reality an optimum amplitude around A=0.2 is to be seen. Pressure acting on the upstream surface is the predominant component contributing to the lift acting on the step and as the amplitude of the jet increase pressure acting on the upstream surface also increase as seen in figure 3.11. This increase in pressure, especially in case of FA technique, irrespective of Reynolds number can be attributed to boundary layer separation on the upstream surface or boundary layer tripping, as shown in figure 3.7. This boundary separation occurs because, as the amplitude A increases boundary layer instability increases, leading to an early separation and the increase in pressure acting on the upstream surface of the backward step. This separation can be observed in figures 3.7 (k), (l) and (g).

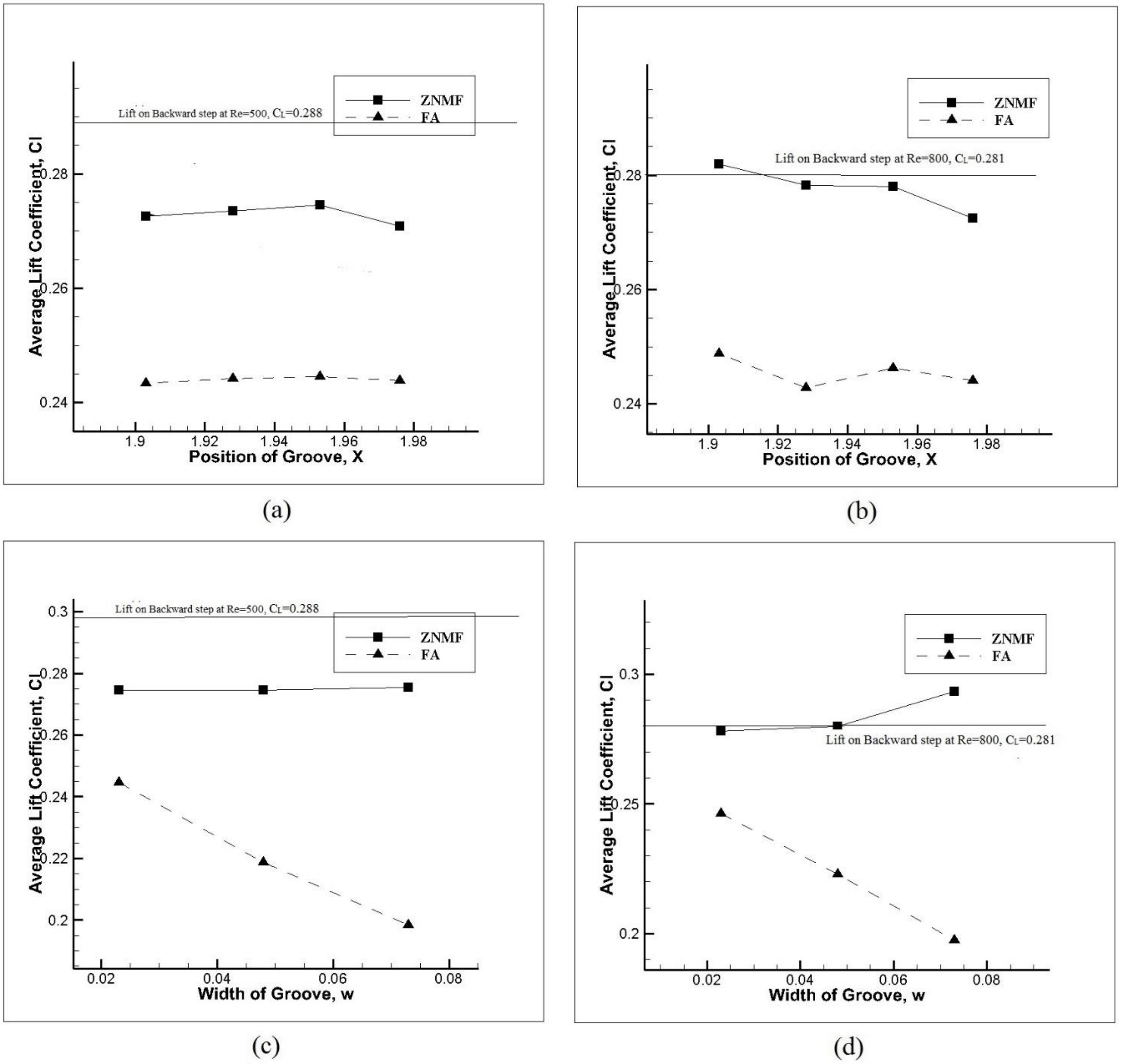

(a) (b)

(c) (d)

Figure 3.12: Average Lift coefficient versus position of groove with width, w=0.023 (a) Re=500 (b) Re=800, Average Lift coefficient versus width of groove, w grove positioned at 1.953a(a) Re=500 (b) Re=800

Figures 3.12(a) and (b) present the variation of lift coefficient with the groove position on the upstream surface of the backward step. It can be observed that, for the different positions studied, for both control techniques and Reynolds numbers, lift coefficient remains rather stable around a mean value, just at Re=800 it seems that lift coefficient tends to decrease as groove is positioned near the step corner. From figures 3.12(c) and (d), the variation of lift coefficient with groove width was found to be minimum for ZNMF technique, whereas when using FA technique, a drastic decrease in lift is observed as the width of the groove is increased. The drastic decrease in lift, is attributed to a pressure increase acting on the upstream surface of the step, caused by early separation of the boundary layer generated by boundary layer tripping. Clearly the effect of groove position is much smaller when compared to grove width, especially in case of FA technique, as seen when comparing figures 3.12(c) and (d) with 12 (a) and (b) at both Reynolds numbers. This can be attributed to the variation in magnitude of the momentum coefficient especially in case of FA when compared to ZNMFA and its effects on the earlier boundary layer separation.

3.5. Conclusions.

- It was found that ZNMF and FA exhibit a similar global behavior.
- The predominant factor affecting the flow is the AFC amplitude.
- The second factor affecting the flow is the AFC frequency.
- The optimum frequency was found to be ± 10% of the flow vortex shedding frequency.
- Effective amplitude for both cases of AFC techniques was found to 10% of the upstream velocity.
- The most effective position of the groove was 1.953a.
- Optimum groove width for ZNMF was about 5% of the step height, while for FA the optimum groove width was 2% of the step height.
- ZNMF technique has minimum effect on lift acting on the body at the optimum frequency when the amplitude of the flow control jet is varied.
- In FA technique the lift acting on the body decreases drastically as the amplitude A is increased.
- For the cases studied, the effect of groove position is much smaller when compared to grove width especially in case of FA technique.

References.

Armaly, B. F.; Durst F; Pereira JCF; Schonung B. (1983). Experimental and theoretical investigation of backward-facing step flow. J. Fluid Mech. 127; 473-496.

Armaly, B. F; Li A; Nie JH. (2003). Measurements in the three-dimensional laminar separated flow. Int. J. Heat and Mass Transfer. 46; 3573-3582.

Brunn A.; W Nitsche. (2006). Active control of turbulent separated flows over slanted surfaces. International Journal of heat and Fluid flow. 26: 748-755.

Chen Y.T., Nie J.H., Hsieh H.T., Sun L.J. (2006). Three-dimensional convection flow adjacent to inclined backward-facing step. Int. Journal of Heat and Mass Transfer. 49: 25-26; 4795-4803.

Chowdhary H., Dhiman A. (2011). Two-Dimensional Laminar Fluid Flow and Heat Transfer over a Backward-Facing Step: Effects of Reynolds and Prandtl Numbers. Heat transfer research journal. 42: 4; 379-402.

Creusé E., Giovannini A., Mortazavi I. (2009).Vortex simulation of active control strategies for transitional backward-facing step flows. Conputers & Fluids 38; 1348-1360.

Dahan Jeremy A., Morgans A.S., Lardeau S. (2012).Feedback control for form-drag reduction on a bluff body with a blunt trailing edge. J. Fluid Mech. 704; 360-387.

Dejoan A., Jang Y.-J., Leschziner M.A. (2005). Comparative LES and Unsteady RANS Computations for a Periodically-Perturbed Separated Flow Over a Backward-Facing Step. ASME-Journal of Fluids Engineering. 127; 872-878.

Hasan M. A. Z. (1992). The flow over a backward-facing step under controlled perturbation: laminar separation. J Fluid Mech. 238; 73-96.

Joseph P; Amadolèse X; Aider JL. (2012). Drag reduction on the 25º slant angle Ahmed reference body using pulsed jets. Exp. Fluids 52: 1169-1185.

Lecrec C.; Levallois E.; Gallas Q.; Gulliéron P.; Kourta A. (2006). Phase locked analysis of a simplified car geometry wake flow control using synthetic jet. Proceedings of the FEDSM2006 ASME Joint US-European Fluids Engineering Summer Meeting. July 17-20, Miami, FL. Paper N 98469.

Marrot F., Gajan P., Pauzin S., Simon F. (2005). Experimental Application of an Active Control Loop on Backward-Facing Step Flow. AIAA Journal, 43:6; 1176-1186.

Postl D., Gross A., Faselz HF. (2003) Numerical investigation of low-pressure turbine blade separation control. AIAA 2003-614.

Sohankar, A., Davidson, L., Norberg, C. (1995). Numerical simulation of unsteady flow around a square two dimensional cylinder. 12th Australian Fluid Mechanics Conference, University of Sydney,Australia, 517-520.

Sohankar, A., Norberg, C., Davidson, L. (1998). Low Reynolds number flow around a square cylinder at incidence: Study of blockage, onset of vortex shedding and outlet boundary condition. Int Journal for Numerical Methods in Fluids,26; 39-56.

Sondergaard R., Rivir RB., Bons JP. (2002). Control of low-pressure turbine separation using vortex-generator jets. Journal of propulsion and power 18, 889-895.

Roberts GO.(1971) Computational meshes for boundary layer problems. Proceedings of the Second International Conference on Numerical Methods and Fluid Dynamics, Lecture Notes in Physics. Springer-Verlag: New York. 8;171–177.

Vukasinovic B., Rusak Z., Glezer A. (2010). Dissipative small-scale actuation of turbulent shear layer. J Fluid Mech. 656; 51-81.

4

Effects of Active Flow Control on flow over an Inclined step

Abstract:
This chapter presents two dimensional flow over an inclined backward facing step in laminar flow regime with application of active flow control technique (AFC). The motive for the present work is to gauge the effectiveness of implementing active flow control to reduce the drag acting on the inclined step. An inclined step was studied, since its shape is similar to the rear of a car and considerable amount of the energy needed for a vehicle to move is dissipated by the drag acting on the vehicle. Backward facing inclined step simulations with angles of inclination of 45^{o} and 65^{o} were carried out with application of active flow control on the upstream horizontal surface to influence the boundary layer and to analyse the effects on the downstream vortex shedding properties of the flow. Two different kinds of flow control techniques were analyzed in this study namely zero net mass flow actuators and fluidic actuators. Parametric analysis of active flow control was carried out by varying the frequency, amplitude, groove position and width, to study their respective effects on the flow and vortex dissipation in the wake of the step. It is attempted to determine an optimal configuration to reduce the drag on the step and suppress the vortex shedding in the wake. It is found that maximum drag reduction for an optimum configuration was between 10%-20% depending on the geometry.

Nomenclature

a	Height of the inclined step	(m)
A	Amplitude of the AFC jet	
C_D	Drag coefficient	
C_L	Lift coefficient	
C_μ	Momentum Coefficient	
f	Non-dimensional frequency of AFC,	
f_v	Dimensional frequency	(H_z)
F_D	Dimensional drag force	(N)
F_f	Flux through face f of the control volume	
F_L	Dimensional lift force	(N)
h	Height of the non-orthogonal physical domain	
l	Length of the non-orthogonal physical domain	
L_r	Non dimensional vortex recirculation length	
$\hat{n}$	Outward normal of the surface S	
p	Non dimensional Pressure	
Re	Reynolds number	
S	Surface onto the control volume	
t	Non-dimensional Time	
ul	Upstream Length of the physical domain	
u	Non-dimensional Velocity Y direction	
u_{av}	Average half cycle velocity of the AFC jet	(m/s)
U	Free stream velocity in X direction at the inlet	(m/s)
v	Non-dimensional Velocity Y direction	
V_{afc}	Non-dimensional Velocity Y direction of the jet	
w	Width of the groove, non-dimensional	
W	Groove width	(m)

$\forall$	Control Volume	(m^3)
x	Non-Dimensional Eulerian coordinates in horizontal direction	
x_p	Dimensional horizontal coordinate of the physical domain	(m)
y	Non-Dimensional Eulerian coordinates in vertical direction	
y_p	Dimensional vertical coordinate of the physical domain	(m)
ρ	Incoming fluid density	(Kg/m^3)
ρ_{jet}	Actuating jet density	(Kg/m^3)
η	Non-dimensional coordinates of transformed domain in vertical direction	
θ	Angle of inclination	(deg)
ξ	Non-dimensional coordinates of transformed domain in horizontal direction	
Ψ	Additional default amplitude of the AFC jet	

Abbreviations.

AFC	Active flow control
ZNMF	Zero net mass flow
FA	Fluidic Actuator

4.1. Introduction.

Flow control, whether passive or active, has a wide range of applications. Aircraft industry, for example, it is interested in using active flow control to modify lift and drag on aircraft wings. Car industry, is aiming to reduce vortex formation on the rear of cars/trucks to diminish drag and therefore reduce fuel consumption. Construction industry has traditionally used passive flow control to minimize or even suppress downstream undesirable vortices on bridges, buildings, pipes placed perpendicular to a flow, etc; the use of active flow control is also currently under study. Several methods have been so far tested to find out its efficiency, reliability and simplicity regarding the active flow control approach.

The use of constant blowing, constant suction, periodic blowing and suction, involving devices like synthetic jets or fluidic actuators is nowadays being tested in many fields. Important parameters related to active flow control actuators are, the precise location of the actuation system, the fluid jet amplitude, the momentum coefficient and the jet frequency if pulsating flow is used. In the present study all these parameters will be evaluated on a backwards facing inclined step under laminar flow conditions. The idea is, initially, to gather a good knowledge on downstream vortex shedding and then use active flow control to reduce or suppress downstream vortices. The present research has to be seen as a basis one, having direct applications to vehicle and building industries.

Active flow control applied to backwards facing inclined step, has quite recently gained the attention of the scientific community. Flow over a rounded ramp, was numerically studied in 2D by Newmann and Wengle (2004), and in 3D by Dandois et al (2006, 2007), in both cases synthetic jets were used as AFC. The respective incoming flow Reynolds numbers were $Re_h = 9100$ and $Re_h = 28275$. In the first paper, the location of downstream separation and reattachment points was obtained. For active flow control, two different groove positions of the synthetic jets were used; two different jet amplitudes and three different Strouhal numbers were evaluated. The optimum drag reduction was obtained when St = 0.1, jet amplitude = 0.2 and groove position $X_b = 1.3$. Their results were compared with the experimental ones undertaken by Song (2002), being the agreement very good. In Dandois et al (2006, 2007), two actuation frequencies were used, a lower one $F^+ = 0.5$ which was close to the shedding frequency and a higher one $F^+ = 4$, in both cases the momentum coefficient was set at 1%. They noticed, when using the lower actuation frequency, that the turbulent kinetic energy level increased and the downstream separation length was reduced by 54%, the opposite happened at high actuation frequencies, the turbulent kinetic energy decreased and the separation length increased by 43%.

The Lattice Boltzman method, to study AFC over the Ahmed body configuration with a slant angle of 25 degrees, was used in 2D by Leclerc et al (2006), and in 3D by Rouméas et al (2008, 2009) and Lehugeur et al (2006, 2008). Respectively, the upcoming flow Reynolds numbers they evaluated were, $Re_L= 2.8*10^6$, $Re_L=2.8*10^6$ and $Re_L= 1.4*10^6$. Leclerc et al (2006), located synthetic jets at the top surface, just before the inclined surface top vertex. Initially they obtained the vortex shedding frequencies generated at the top and bottom of the body; they also observed that a frequency associated to a third vortex was appearing due to the coupling of the previous two structures generated. They confirmed the fact that the time evolution of C_D and C_L is directly associated with the vortices developed in the wake. To obtain the maximum synthetic jets efficiency, maximum attenuation of the natural shedding structures, the excitation frequency had to be synchronized with the vortex shedding frequency. Furthermore, they observed that the momentum coefficient introduced by the jet, C_μ, reduced the boundary layer thickness and increased the mean maximum velocity on the boundary layer. Regarding the C_μ applied, they realized it exists a lower and upper threshold value, below the lower threshold the momentum associated to the synthetic jets is too small to produce any effect on the boundary layer, and if on the other hand the momentum overcomes a certain value, the energy associated to the jets is delivered onto the upper part or above the boundary layer, in both cases the drag coefficient increases. The efficiency of the jet, was mostly determined by the C_μ associated to the blowing phase. C_μ controls the height inside the boundary layer, at which the synthetic jet delivers its energy. When C_μ increases, the velocity fluctuations between the blowing and suction phases also increase. Two phenomena appeared to induce the efficiency loss on the synthetic jets for higher values of C_μ; the energy of the jet in the blowing phase represented an obstacle in the boundary layer, and the energy induced by the jet in the upcoming flow and the vortical structures generated occurred too high up in the boundary layer. In their study, the optimum values were $F^+= 0.68$ and $C_\mu = 2.4*10^{-4}$, for which drag coefficient was reduced by 30%. Rouméas et al (2008, 2009), controlled the flow via using a continuous suction slot of 1mm width located along the upper corner of the backwards inclined window. They noticed the drag reduction was 12.7% when the suction velocity was $U_{suction} = 0.374*U_\infty$, the drag kept reducing when increasing suction velocity until reaching a reduction of 17,2% for a jet velocity of $U_{suction} = 0.6*U_\infty$. A further increase of suction velocity caused a negligible effect on the drag performance. The authors also realized that the suction generated caused no effect on the lateral longitudinal vortex structures, but did modify the vortex structures on the inclined window at the car rear. Lehugeur et al (2006, 2008), studied via using the 3D Lattice Boltzman method and experimentally, the longitudinal vortices formed at the sides of an Ahmed body slant surface. They located blowing jets at both sides of the slanted surface and observed that they could modify the longitudinal vortices main axis direction and the swirl number associated to it. It was also realized that as the jet blowing velocity increased from $0.5*U_\infty$ to $1.5*U_\infty$, the vorticity associated to the longitudinal vortices also increased, and once reached a threshold, vortex breakdown was observed. Maximum drag reduction of about 6% was obtained, drag reduction was mostly due to the pressure increase observed at the slant surface whenever AFC was used. Numerical and experimental results were in good agreement.

A two dimensional hump via using LES was simulated by Avdis et al (2009), an experimental study was also undertaken, in fact the downstream part of the hump resembled the rounder ramp studied by Dandois et al(2007). The synthetic jet was located in both cases approximately in the same position, but in Avdis et al the injection section formed a small angle versus the ramp surface while in Dandois et al the angle was of 90 degrees. Synthetic jet actuation frequency was $F^+ = 0.77$ being the momentum coefficient $C_\mu = 0.0011$, Reynolds number based on the chord length was 935892. Agreement between experimental and numerical results was good, the vortex length reduction obtained experimentally was of 28%; numerically it was obtained a 30%.

Bruneau et al. (2012) studied via 3D numerical simulation, the rear part of an Ahmed body. They evaluated the effect of locating a suction line on the upper corner of the rear window, which was having a slant angle of 25 degrees, and a blowing line on the car rear vertical section, the effect of using two blowing lines located along the two lateral borders of the inclined window, was also considered. In all cases studied drag coefficient was reduced, the minimum drag coefficient value was achieved when combining all previous actuations, the use of the transversal suction and blowing lines also produced a drag reduction of 11%. On the other hand, the use of lateral blowing lines produced a small drag reduction. For all cases studied, jet velocity, whether for suction or blowing, was taken as $U_{jet} = 0.6*U_\infty$ and remained constant. Bruneau's work needs to be seen as a continuation of Rouméas et al (2009) research, yet the outcome appears to be more successful in the previous case.

In reality, active flow control on backwards facing inclined step and vehicles rear side, has been mostly studied experimentally. Geropp and Odental (2000), used two constant blowing jets located onto the upper and lower corners of a car rear vertical plane, blowing jets velocity was taken as two to six times the free stream velocity, $U_{jet} = (2 \text{ to } 6)*U_\infty$. For a blowing rate of 2 they found a decrease of drag coefficient of 10%, Reynolds number was $9.9*10^5$. The large difference between the jet velocity used in Bruneau et al and Geropp and Odental, is explained when noticing that in reality the two experiments are not comparable, one of the main aims in Bruneau`s work was to produce a flow reattachment onto the car rear inclined window, while in Geropp and Odental they were using the jets onto the car rear vertical plane to generate a Coanda effect and reattach the flow to the vehicle rear.

In Brunn and Nitsche (2006), an experimental research of flow around a backwards facing inclined step with 25 degrees' slant angle at Reynolds $Re_H = 4*10^4$ was undertaken, they also studied an Ahmed body configuration, being the slant angle and Reynolds number respectively of 35 degrees and $4.9*10^4$, flow was evaluated via using PIV. They observed the flow was characterized by two fundamental frequencies, one was associated to the shear layer instability and the second one was the vortex shedding frequency. It was as well realized that the optimum forcing frequency, whenever using AFC periodic forcing, was linked with the formation of the large scale structures, the vortex shedding structures. In Park et al (2013), the rear part of a three dimensional Ahmed body was experimentally studied, they considered two slant angles of 25 and 35 degrees, the flow Reynolds number, based on the model length, was $4.29*10^5$. They used an array of 12 synthetic jets located at the roof end edge, just before the inclined rear window, another 12 synthetic jets were located along the slanted side edges, six on each side. The inclination of roof jets, versus the surface, was arranged to be of 30º, 60º and 90º, the jets located onto the slanted side edges were having inclination angles of 30 and 60 degrees. Eight different momentum coefficients were evaluated; their minimum and maximum values were respectively of $2.34*10^{-4}$ and $1.09*10^{-2}$. Eleven jet driving frequencies F^+ ranging from 0.4 to 1.74 were also considered. As a general trend, they noticed that independently of the injection angle, the driving frequency and the momentum coefficient used, for a slant angle of 35 degrees the drag coefficient was always higher than the conventional Ahmed body one, a maximum drag coefficient reduction of 5.2% could be obtained for a slant angle of 25 degrees and when using the synthetic jets located at the body roof. The jets located at the slant side edges produced a negligible effect on the body drag when the slant angle was 25º. For a slant angle of 35º the drag increase was smaller than the one obtained for the same angle and when the jet array was located at the roof. It is interesting to notice that although Rouméas et al (2009), Bruneau et al (2012) and Park et al (2013) studied the same model the results obtained by Park et al are much less promising than the ones obtained numerically by Rouméas et al and Bruneau et al. A key difference is that Park et al used synthetic jets while the other two researchers employed a suction line and one or several blowing lines. The location of the actuating devices was also different.

Aubrun et al (2011) performed a 3D experimental study of an Ahmed body with 25 degrees' slant angle. An array of microjets, 0.4 mm diameter and separated every 5 mm, was located on the inclined surface, just 6 mm below the upper corner, steady blowing was used as AFC, PIV was used to visualize the flow field. Three different Reynolds numbers $Re_L = 0.97*10^6$; $1.46*10^6$ and $1.95*10^6$ were evaluated, momentum coefficients used ranged from $C_\mu = 0\%$ to 10%. They observed that the most effective velocity ratio was about $U_{jet}/U_\infty = 2$ to 2.1, being the drag coefficient decrease between 9 and 14%. When plotting the lift C_L and drag C_D coefficients as a function of the momentum coefficient C_μ, they observed that, for each Reynols number, it exist an optimum value of C_μ for which lift and drag coefficient falls to a minimum, once this threshold is overcome, both coefficients appear to be rather independent of the momentum coefficient applied. The optimum momentum coefficient was found to be around 2.5% regardless of the Reynolds number studied. It is interesting to realize that this threshold agrees pretty well with the results obtained by Leclerc et al (2006), in both cases, it is observed that the jet delivers energy onto the upper part or outside the boundary layer, therefore not producing the desired effect. A similar study to the one undertaken by Aubrun et al (2011), was performed by Joseph et al (2012). Both studies were experimental, an Ahmed body was used and the inclined surface slant angle was 25 degrees. One of the main differences between these two studies is that in the later one, the following four different AFC geometric configurations were studied; discontinuous rectangular slots located at the roof end and at the slant top edge, 15 mm below the top corner, a continuous slot located at slant top edge, and winglets located at the roof end. Regardless of the configuration chosen, pulsating flow was used, two Reynolds numbers of $Re_L = 1.4*10^6$ and $2.8*10^6$ were evaluated. For each of the four configurations, a range of frequencies and momentum coefficients were analyzed, obtaining for each case the optimum pair of values, St, C_μ, which produced minimum drag, drag reduction of 6 to 8% was observed in all cases. The optimum of the four configurations was the one using a continuous slot located at the slant top edge, then for this case the momentum coefficient used was minimum, $0.4*10^{-3} < C_\mu < 0.9*10^{-3}$, being the Strouhal number St = 0.35. The authors observed three unsteady mechanisms which could be characterized by a constant value of Strouhal number. The first unsteady mechanism was liked with the ring-shaped structure observed in the wake, the second one was associated with the natural Kelvin-Helmholtz instability of the shear layer, and the third one was due to the flapping of the shear layer. As already observed in Brunn and Nitsche (2006) and Leclerc et al (2006), they also noticed that the most effective forcing frequency was the one associated to the downstream vortex shedding. Mestiri et al (2014), studied experimentally an Ahmed body with 25º slant angle. They used a slit width of 1 mm located at the upper corner of the inclined wall, active flow control was evaluated via using steady blowing. The incoming flow Reynolds numbers evaluated, based on the Ahmed body length, ranged from $1.74*10^6$ to $2.78*10^6$, the corresponding free stream velocities being 25 and 40 m/s. Blowing velocity range oscillated between 0 and 22 m/s. The maximum drag reduction observed was about 10% for a Reynolds number of $1,74*10^6$ and a velocity ratio of $0,65 = U_{blowing}/U_\infty$, they also observed that the actuation was not efficient whenever the velocity ratio ($U_{blowing}/U_\infty$) was smaller than 0.4. Via using the energetic efficiency criteria proposed by Roumeas et al (2009) they realized that maximum efficiency was obtained for velocity ratios ($U_{blowing}/U_\infty$) around 0.5.

A numerical and experimental study of an entire car profile was presented by Kumar-Singh and Bandyopadhyay (2012). The numerical study was done in 2D and using the K-ε turbulence model, measurements were done in a 3D car model. On the car top, just before the car rear inclined window, a set of six rectangular splices having a width of 1 mm and separated 20mm from each other, were located perpendicular to the flow direction, also on the car rear vertical surface, an array of six slots having the same width and separation were used. It is important to highlight that in the studies presented until now, see for example Rouméas et al (2009), Bruneau et al (2012) and Park et al (2013), the suction or blowing lines consisted always of a single line, Kumar-Singh and Bandyopadhyay (2012) were using a set of six lines located one next to the other, it can therefore be expected an increase of accuracy regarding the flow control. The top car splices were used to suck air while the rear car vertical plane splices were blowing the air previously sucked. Car velocity was maintained constant at 25m/s, the Reynolds number associated was 427866, sucking and blowing velocities were always the same, and ranged from 10 to 90 m/s. The slots intake angle was also varied from 40 to 90 degrees. As suction angle increased, drag coefficient decreased and lift coefficient increased. Regarding the suction/blowing air velocity, a maximum drag decrease of 20.25% was obtained at 60m/s, for these conditions lift increased by 19.4%.

Heinemann et al (2014), studied experimentally the flow field around a real car via using Laser Doppler Anemometry LDA and for a Reynolds number of $Re_L = 2.1*10^6$. They used three different AFC configurations to evaluate its effectiveness, for all cases steady blowing was employed. In the first configuration, a slot was located on the top of the rear window, flow was blowing perpendicular to the surface, on the second configuration the slot was located at the bottom of the rear window, for this case the flow was injected perpendicular to the surface and also tangentially, upwards, to it. When injecting the fluid on the upper part of the rear window, the pressure distribution on the car rear window decreased, as a result the drag increased. When flow was injected at the rear window lower part and normal to the surface, lift and drag coefficients were slightly affected, the variation was smaller than 2%, but when tangential blowing was used, lift coefficient was reduced by 7%, while drag coefficient remained constant. In fact, the low effectiveness of using a groove located at the bottom of the rear window, can be explained when understanding that, very especially, the drag coefficient is affected by the pressure distribution on the rear window, see among others, Lehueur et al (2006,2008), Leclerc et al (2006), Aubrun et al (2011), Joseph et al (2012), and clearly, this particular groove location is not affecting much the flow and pressure distribution onto the rear car inclined surface.

When comparing the different studies presented, it is interesting to see that for constant sucking and or blowing Rouméas et al (2009) used a relation $U_{jet} = (0.374 \text{ to } 0.6)*U_\infty$; Bruneau et al (2012) used $U_{jet} = 0.6*U_\infty$; Geropp and Odental (2000) used $U_{jet} = (2 \text{ to } 6)*U_\infty$; and Kumar-Singh and Bandyopadhyay (2012) used $U_{jet} = (0.4 \text{ to } 3.6)*U_\infty$ and obtained the optimum results at $U_{jet} = 2.4*U_\infty$. Despite the fact that the location of the jet arrays and Reynolds number is not the same for all these studies, this comparison gives an idea of the order of magnitude to be employed under turbulent conditions.

In the present chapter laminar flow over an inclined backwards facing step is studied, several inclined step angles will be evaluated, for each case, different slot locations, momentum coefficients and active flow control methodologies, will be considered, the optimization of these parameters is presented. Advantages of using laminar flow are, it allows to fully evaluate the downstream vortical structures, allowing to better understand the effect of AFC on them. A disadvantage is that real cars move at higher Reynolds numbers. In any case, the optimal configuration obtained under laminar conditions, shall provide good indications of how to proceed under turbulent ones.

4.2. Problem Statement.

4.2.1 Physical domain.

Figure 4.1 presents the physical domain of the inclined step. Flow over a backward facing inclined step with upstream length, ul=2a and downstream length, dl=20a was simulated at Reynolds number, Re= 500 and 800 for two different angles of Inclination, $\theta=45^o$ and 65^o. Figure 4.1 also presents the boundary conditions used for the simulation. No slip boundary condition was used at all solid boundaries. As the flow is unconstrained at the top, free slip boundary conditions was used at the top, which was located at a distance of 8a, according to Sohankar et al. (1995). In order to simulate a far field downstream boundary, Neumann boundary condition was used at the outlet, the outlet boundary was located at a distance of 20a downstream of the inclined step lower vertex, as suggested by Sohankar et al. (1998). Flow was evaluated in two dimensions under laminar regime.

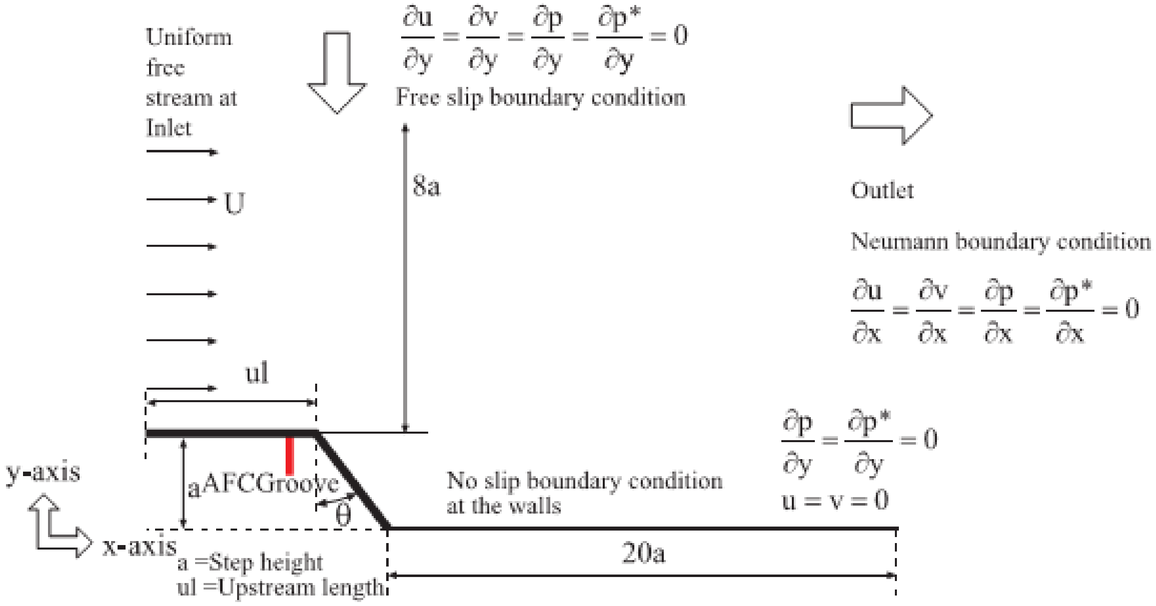

Figure 4.1: Physical Domain of the Inclined Step

Figures 4.2(a), (b), present the grid of the proposed problem. A non-orthogonal non uniform structured grid was chosen, since it is most appropriate to simulate the flow dynamics in the presence of an inclined edge. Figure 4.2b, shows the three sub-domains of the grid. The first sub domain is the region over the upstream surface of the inclined step. Second sub-domain is located on the right hand side of the inclined surface. The region over the second sub-domain and on the right side of the first sub-domain is the third sub-domain. Structured grid has been generated in the three sub-domains using the stretching transformation proposed by Roberts (1971), which refines the grid in the vicinity of the solid walls. The domain on the right hand side of the inclined edge is transformed into an orthogonal domain by using a grid transformation as defined by Anderson (1995).

Simulations were performed using two different types of active flow control techniques, zero net mass flow and fluidic actuators. For each actuator technique, five different non-dimensional frequencies ranging from f = 0.005 to f = 0.1 and eight different non-dimensional velocity amplitudes A, from 0.025 to 1, were evaluated. The grove was placed at four different locations on the upstream length just before the upper right hand side corner, these non-dimensional locations measured from the coordinate system, see figure 4.2, were: (x =1.903a, y = a), (x =1.928a, y = a), (x =1.953a, y = a) and (x =1.976a, y = a). For all cases, the groove right end was positioned at the mentioned locations. Three different non-dimensional groove widths of w = 0.023, 0.048 and 0.073, were also analyzed. These studies were designed to understand the effects of the active flow control techniques on the horizontal surface boundary layer development and subsequently on the inclined surface downstream flow.

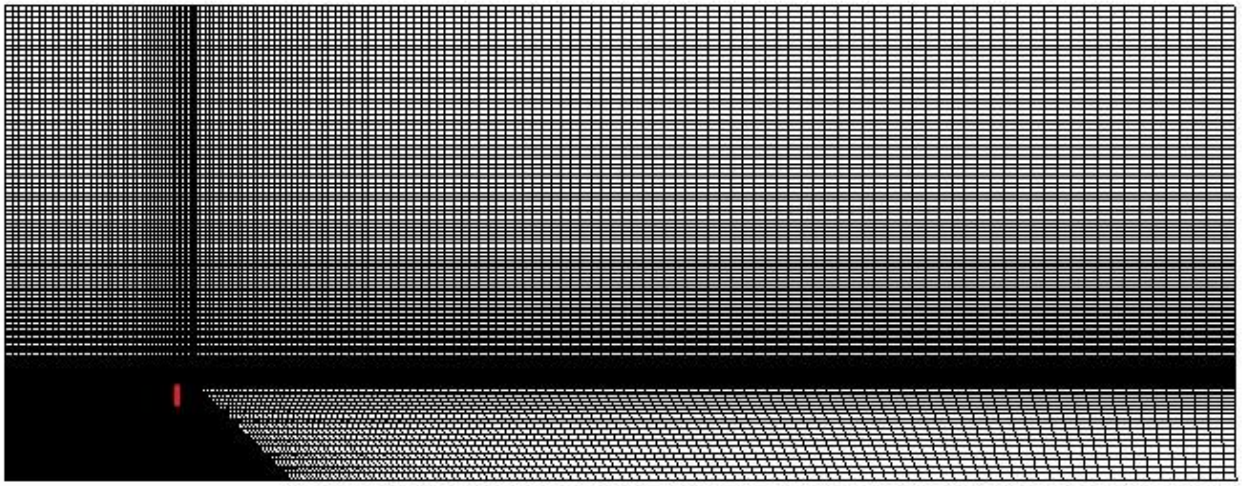

4.2(a)

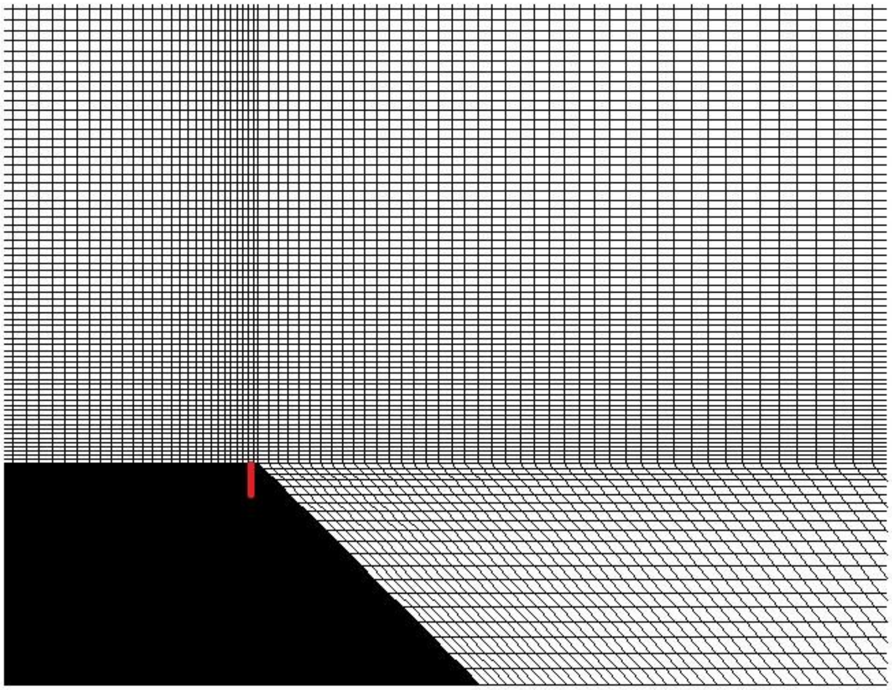

4.2(b)

Figure: 4.2(a) Non uniform structured grid for discretization of the domain. 2(b) Closer view of the grid point collocation at the wall of the step for accurate resolution of the boundary layer.

4.2.2 Governing Equations.

Simulations have been done with non-dimensional form of Navier-Stokes equations. To non dimensionalize the equations, the height of the step, a, was taken as the characteristic length, the free stream velocity U, was taken as the characteristic velocity, the characteristic pressure was ρU^2 and the characteristic time was defined as the characteristic length divided by the characteristic velocity a/U. Reynolds number was defined as $\mathrm{Re} = \frac{\rho U a}{\mu}$; notice that fluid density and viscosity were taken as constant. Flow was considered as isothermal.

The non-dimensional form of the momentum and continuity equations for laminar flow is represented as:

$$\frac{\partial u}{\partial t} + u\frac{\partial u}{\partial x} + v\frac{\partial u}{\partial y} = -\frac{\partial p}{\partial x} + \frac{1}{\mathrm{Re}}\left(\frac{\partial^2 u}{\partial x^2} + \frac{\partial^2 u}{\partial y^2}\right) \tag{4.1}$$

$$\frac{\partial v}{\partial t} + u\frac{\partial v}{\partial x} + v\frac{\partial v}{\partial y} = -\frac{\partial p}{\partial y} + \frac{1}{\mathrm{Re}}\left(\frac{\partial^2 v}{\partial x^2} + \frac{\partial^2 v}{\partial y^2}\right) \tag{4.2}$$

$$\frac{\partial u}{\partial x} + \frac{\partial v}{\partial y} = 0 \tag{4.3}$$

The finite volume approach was chosen for the simulation

4.2.3 Numerical Strategy and Boundary Conditions.

A second-order Adams Bashforth-Crank Nicholson scheme for temporal discretization was applied to Navier Stokes equations in finite volume formulation to obtain equation (4.4). Equation (4.5) is the continuity equation applied over a control volume.

$$\frac{u_{i,P}^{n+1} - u_{i,P}^{n}}{\Delta t} V_P + \left(\frac{3}{2}\sum_f F_f^n u_{i,f}^n - \frac{1}{2}\sum_f F_f^{n-1} u_{i,f}^{n-1}\right) = -\sum_f p_f^n S_{f,i} + \frac{1}{2\,\mathrm{Re}}\left(\sum_f F_{dfi}^{n+1} + \sum_f F_{dfi}^{n}\right) \tag{4.4}$$

$$\sum_f F_f^{n+1} = 0 \tag{4.5}$$

Equations (4.4) and (4.5) were solved by using the bi-conjugate gradient stabilized method. The boundary conditions used in the simulation were depicted in figure 4.1, a brief description of the different boundary conditions follows.

At the inlet, uniform free stream condition for velocity and Neumann boundary condition for pressure were used.

$$u = U, \quad v = 0, \quad \frac{\partial p}{\partial x} = 0 \tag{4.6}$$

In all solid boundaries, no-slip boundary condition for velocity and normal gradient condition for pressure was employed.

$$u = 0, v = 0 \text{ and } \nabla p.\hat{n} = 0 \qquad (4.7)$$

Where $\hat{n}$ is the unit normal vector perpendicular to the surface.

At the far field, as the present study focuses on the unconfined flow past an inclined step, a free slip boundary was applied at a distance of 8a, measured from the upstream horizontal surface, see figure 4.1.

$$\frac{\partial \phi}{\partial y} = 0; \ \ \phi = u, v; \ \frac{\partial p}{\partial y} = 0 \qquad (4.8)$$

The outlet boundary, right hand side of figure 4.1, posed the biggest difficulty in computational modeling, especially when studying flows with unsteady wake or convecting vortices. The definition of this boundary condition is of paramount importance, since it not only changes the flow pattern but also affects convergence. For the present case the derivative of all dependent variables was taken equal to zero, which is known as Neumann Boundary Condition (NBC), condition presented in equation (4.9).

$$\frac{\partial \phi}{\partial x} = 0, \ \ \phi = u, v, p; \qquad (4.9)$$

The distance between the inclined step bottom edge and outlet boundary, where the Newman boundary condition is applied, was considered as 20a as seen in figure 4.1.

MAC (Marker and Cell) method with velocity and pressure coupling was applied using a predictor-corrector strategy. In the present study, the respective pressure correction factor in all the neighboring cells were also considered, notice that this is a further improvement with respect to the original MAC method and minimizes the error involved in the calculation. In this method the momentum equations are solved to calculate provisional values for the velocity components for the next time step using the predictor step and thereafter calculating the pressure and velocity correction factors for achieving the incompressibility condition of mass conservation.

For the inclined step case, the grid located on the right hand side of the inclined boundary edge, has a non-orthogonal domain, (x,y) this domain was transformed into an orthogonal domain (ξ, η). See figure 4.3.

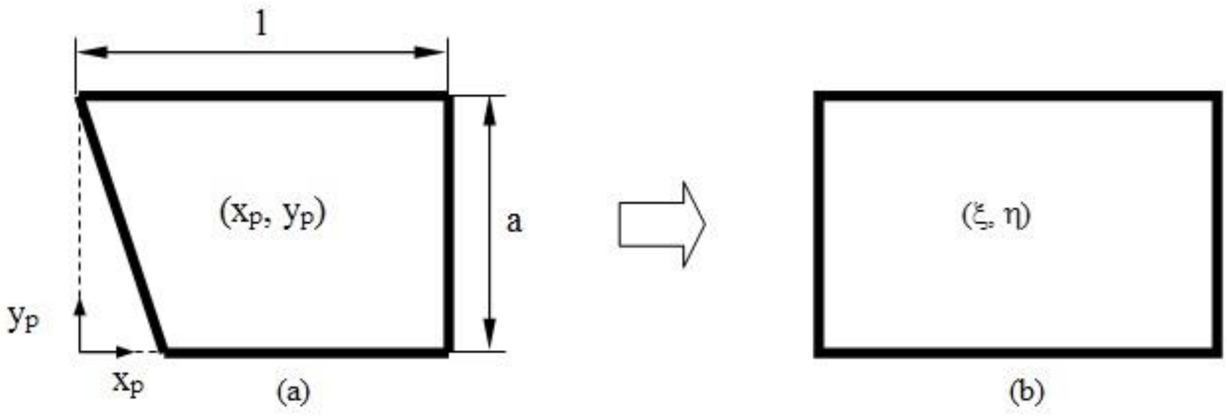

(a) (b)

Figure: 4.3. Transformation of the physical domain to computational domain (a) Physical domain (b) Computational domain

The transformation equations used to transform the physical domain to a computational domain are presented as equations (4.10), (4.11) and (4.12).

$$\xi = \left(\frac{x_p - c}{1 - c} \right) \tag{4.10}$$

$$\eta = \left(\frac{y_p}{a} \right) \tag{4.11}$$

Where "l" and "a" are the length and height of the physical domain as shown in the figure 4.3 and "c" is a constant defined by:

$$c = \left(\frac{a - y_p}{\cot\theta} \right). \tag{4.12}$$

To transform Navier-Stokes equations from non-orthogonal to orthogonal coordinates, the transformation mentioned in Anderson (1995) was used, for the first and second derivatives.

The non-dimensional form of momentum and continuity equations, (4.1) to (4.3), were transformed into equations in the orthogonal domain, equations (4.13) to (4.15) using transformation equations (4.10) to (4.12).

$$\frac{\partial u}{\partial t} + \xi_x u \frac{\partial u}{\partial x} + \eta_y v \frac{\partial v}{\partial y} = -\xi_x \frac{\partial p}{\partial x} + \frac{1}{Re} \left(\xi_x^2 \frac{\partial^2 u}{\partial x^2} + \eta_y^2 \frac{\partial^2 u}{\partial y^2} \right) \tag{4.13}$$

$$\frac{\partial v}{\partial t} + \xi_x u \frac{\partial v}{\partial x} + \eta_y v \frac{\partial v}{\partial y} = -\eta_y \frac{\partial p}{\partial y} + \frac{1}{Re} \left(\xi_x^2 \frac{\partial^2 v}{\partial x^2} + \eta_y^2 \frac{\partial^2 v}{\partial y^2} \right) \tag{4.14}$$

$$\xi_x \frac{\partial u}{\partial x} + \eta_y \frac{\partial v}{\partial y} = 0 \tag{4.15}$$

The transformed equations, (4.13) to (4.15), were discretized using the second-order Adams Bashforth-Crank Nicholson scheme, as it was previously used to discretize the non-dimensional equations (4.1) to (4.3), into (4.4) and (4.5).

4.2.4 Zero-net mass flow control technique.

In this technique the flow control is induced into the flow upstream of the step in such a way that the net mass flow from the groove is zero. A sinusoidal form of wave equation was used to induce the active flow control technique as presented in equation 4.16.

$u=0$

$v=A.\sin(2\pi f t)$ (4.16)

Where u and v are respectively the non-dimensional horizontal x-component and vertical y-component of fluid velocity, f is the non-dimensional frequency of the active flow control jet and t is the non-dimensional time. A is the non-dimensional velocity amplitude of the oscillating jet $A=V_{jet}/U$.

4.2.5 Fluidic Actuator flow control technique.

In fluidic actuators, the flow control is induced into the flow upstream of the step in such a way that the net mass flow from the groove is outwards. This is applied by inducing a default amplitude Ψ added to the sinusoidal form of wave equation used in zero net mass flow technique as presented in equation (4.17).

$u=0$

$v= \Psi +A.\sin(2\pi ft)$ (4.17)

Where Ψ is the additional default non-dimensional velocity amplitude, in the present study the default amplitude Ψ was considered equal to the amplitude A of the jet, so that the minimum velocity of the injected jet is zero.

The primary difference between zero net mass flow and fluidic actuator techniques is that, in case of former the fluid is injected and absorbed into the upstream boundary layer, but in case of fluidic actuator the fluid is only injected. In both cases the fluid is injected perpendicular to the upstream surface, since as mentioned in Sondergaad et al (2002) and Postl et al (2003), perpendicular forcing is most effective.

4.2.6 Non dimensional Coefficients.

Lift and drag coefficients evaluate the average normal and shear stresses acting on upper horizontal and inclined walls. To calculate lift and drag coefficients, the expressions presented in equation (4.18) were used. Since the flow analyzed is unsteady and periodic, average lift and drag coefficients were used.

$$C_D = \frac{F_D}{\frac{1}{2}\rho U^2 a^2}, \; C_L = \frac{F_L}{\frac{1}{2}\rho U^2 a^2}; \tag{4.18}$$

F_D and F_L are respectively the dimensional drag and lift forces due to the pressure and shear stresses acting on the upper horizontal and inclined surfaces. Drag force was taken as positive when acting towards the positive X axis direction, and Lift force was regarded as positive when acting towards the positive Y axis direction. The equation to derive the Strouhal number, St is presented in equation (4.19), f_v being the vortex shedding frequency in the inclined backwards step wake.

$$St = f = \frac{f_v \, a}{U} \tag{4.19}$$

The momentum coefficient, C_μ, used in the present study is according to equation (4.20).

$$C_\mu = \frac{\rho_{jet} u_{av}^2 W}{\rho U^2 a} \tag{4.20}$$

Where ρ_{jet} and ρ are respectively the jet and incoming flow density, u_{av} is the average half cycle velocity of the AFC jet, W is the width of the AFC groove, a is the height of the inclined step and U is the free stream velocity of the fluid at the inlet as seen in figure 4.1.

4.3. Code Validation.

The code was validated by simulating the flow over a backward step and the results were compared with the results presented in the literature. Figure 4.4 presents the streamline plots for the backward facing step case. The left side of the figure, presents the results obtained from the code developed and the graphs presented on the right side, were obtained by Chowdhary and Dhiman (2011). Three Reynolds numbers of 100, 150 and 200 were studied in both cases. The comparison was in complete agreement in all cases studied, flow configuration was very much alike, the downstream vortexes were steady in all cases and their respective length was the same in all comparisons undertaken. It is necessary to point out that as the plots presented in the right hand side of figure 4.4 were extracted from Chowdhary and Dhiman (2011), their quality has been compromised when reducing their dimensions.

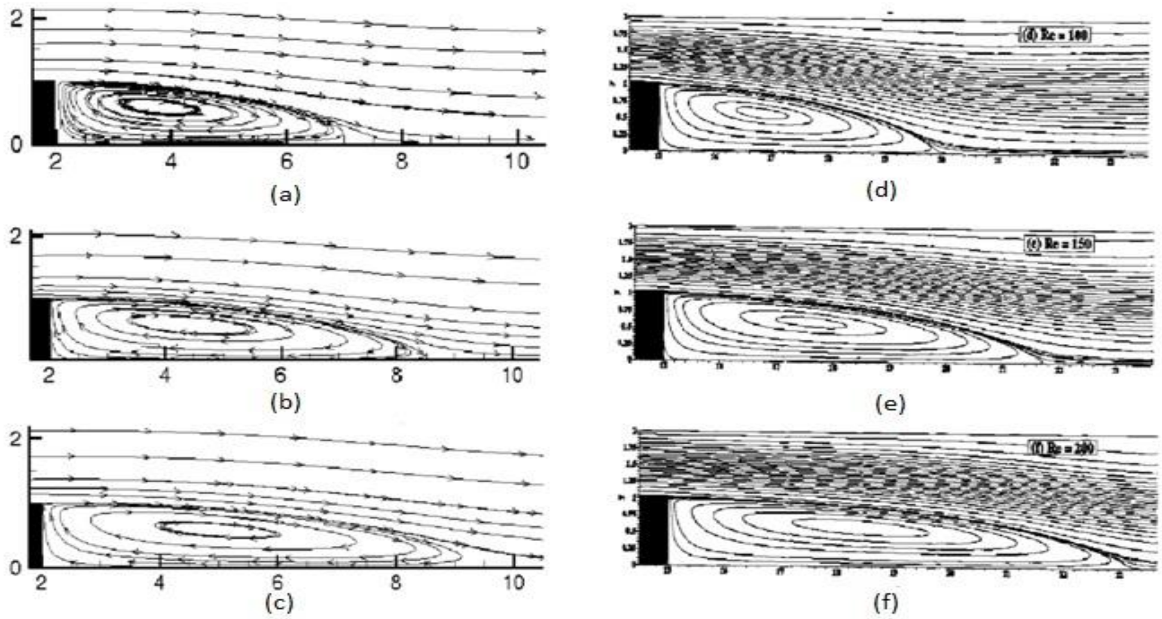

Figure 4.4: Instantaneous Streamline plots for Reynolds Numbers: (a), (d) Re=100, (b), (e) Re=150 and (c), (f) Re=200. Left side figures were generated by the present code, right side figures were created by Chowdhary and Dhiman (2011).

From the present code, it was observed that the flow over a backward step geometry was steady at Reynolds number, Re=498 but the flow was unsteady and periodic for Re=500. It can be inferred that the onset of vortex shedding occurs around Reynolds number 500, as previously reported by Armaly et al (2003) and also by Chen et al (2006).

4.3.1 Effects of Grid refinement.

A grid refinement study was carried out on three progressively refined grids, namely 160×140, 200×150 and 240×160 where the number of grid nodes distributed over the inclined edge of the step are 30, 40 and 50, respectively. An inclination angle, $\theta=65^0$ and ul=2a was considered for the grid refinement study at Reynolds number, Re=500. During the refinement, the non-dimensional smallest and the largest cell size on the inclined edge was maintained approximately at 0.02 and 0.033, respectively.

Grid	160x140	200x150	240x160
Drag Coefficient, C_D	0.1557714	0.1561975	0.1562214
Lift Coefficient, C_L	0.3022320	0.3053222	0.3051489

Table 4.1: Grid refinement for flow past backward facing inclined step

The variation of the drag coefficient, C_D was around 0.274% when the grid was refined from coarsest to the intermediate level. But when the grid was further refined to the finest level, the change reduced to 0.015% as seen table 4.1.The variation in lift coefficient was also found to be similar. Therefore, from results of the grid refinement analysis, a grid size of 200x150 was considered for all the simulations.

4.4. Results and Discussion.

This section is divided into three parts, initially the unsteady flow dynamics is analyzed with the help of streamline and vorticity plots. Secondly, average lift and drag coefficients as a function of AFC frequency and amplitude will be introduced. Finally both lift and drag coefficients will again be presented as a function of groove position and width to understand their variation, based on the pressure profiles of inclined step surface.

4.4.1 Unsteady periodic flow over inclined backward facing step.

In order to visualize unsteady periodic laminar vortex shedding past an inclined step, in the present section simulations at Reynolds number, Re=500 and 800 are presented in figure 4.5 to 4.11, with the help of instantaneous streamlines and vorticity plots at six equally spaced time intervals within a shedding cycle of time period T. Figure 4.5 presents the flow without application of AFC, while the rest of the figures present the flow when considering AFC. In all cases, an upstream length, ul=2a was considered. The flow remains laminar under these conditions, since as determined by Armaly et al (1983) the flow over an inclined step is laminar whenever Reynolds number is below 1200.

The onset of vortex shedding in the case of the backward facing step or inclined step, occurs due to the rolling up shear layer, located downstream of the inclined step. The rolling up shear layer is formed due to the interaction between the negative momentum of the vortex in the wake of the step and the solid constrained boundary located below the vortex. As the rolling up shear layer develops, its intensity increases, causing the entrainment of the rolling up shear layer into the neck of growing recirculating vortex at the rear of the inclined step, which leads to the separation of the vortex from the neck and it is consequently shed into the wake of the step. This mechanism is different from the shedding mechanism in case of generic bluff body, where vortex shedding occurs due to the flapping motion of the upper and lower vortices appearing at the body trailing edge, vortices shed alternately into the wake.

The vortex shedding cycle for flow over an inclined step for $\theta=45^0$, Re = 500, is presented in figure 4.5. The recirculating vortex is formed at the inclined edge of the step and is gradually shed into the wake. Two types of inviscid critical points, namely ‘center’ and ‘saddle’ can be seen from the figure. A critical point is a location where slope of streamline becomes indefinite; the point of zero velocity is referred to as the ‘center’ while the point where two streamlines running in opposite direction touch each other is referred to as the ‘saddle’. From the present study it is noticed that the saddle point of a shed vortex, disappears before a new vortex is shed. Instantaneous vorticity contours, further reveals the formation and shedding of vortices from the inclined step upper corner. Due to its streamlined shape, separation in an inclined step always occurs at the inclined edge corner leading to a separated shear layer from the vertex which is stretched, bent and finally convected into the wake. The neck between the tip and the main body of a growing vortex stretches and bends, leading to separation from the main body as seen in figure 4.5(j, k, l). The positive and negative vorticity, corresponding to counter-clockwise and clockwise motion, is shown by solid and dashed lines, respectively.

The rolling up shear layer exhibits a flapping motion while the shear layer moves into the growing vortex in the wake only to be convected downstream in the form of vortical structure which scales with the height of the inclined step. Similar vortex shedding patterns were obtained for both inclination angles $\theta=45^0$ and 65^0 and Reynolds numbers, Re=500 and 800, emphasizing the global nature of the flow. Non-dimensional vortex shedding frequency was found to be, St=f=0.05, minor variations were seen with the modification of inclination angle or Reynolds number, indicating that for all cases studied the phenomena remained in the same mode. From quantitative observations of simulations, it was also found that flow at Re=500 is more organized whereas flow at Re=800 was found to be more disorganized, with quicker vortex dissipation. This is attributed to the fact that as Reynolds number increases, the kinetic energy associated to each fluid particle also increases and momentum interchange between particles increases, leading to a quicker and higher disorganized vortex dissipation.

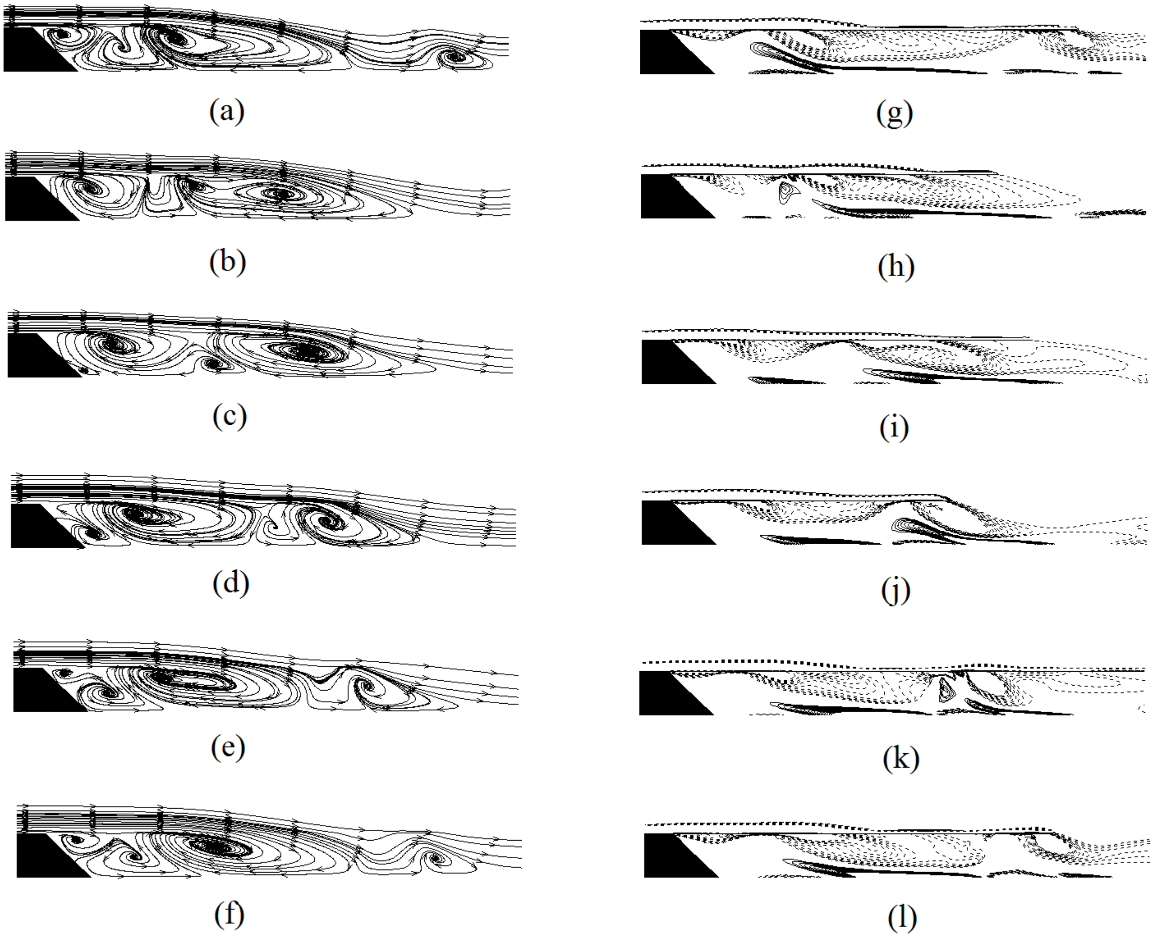
(a) (g)
(b) (h)
(c) (i)
(d) (j)
(e) (k)
(f) (l)

Figure 4.5: Streamline and corresponding Vorticity plots of vortex shedding cycle in the wake of backward facing inclined Step at Re=500, for $\theta=45^0$: (a, g) T/6; (b, h) T/3; (c, i) T/2; (d, j) 2T/3; (e, k) 5T/6; (f, l) T. No AFC is applied.

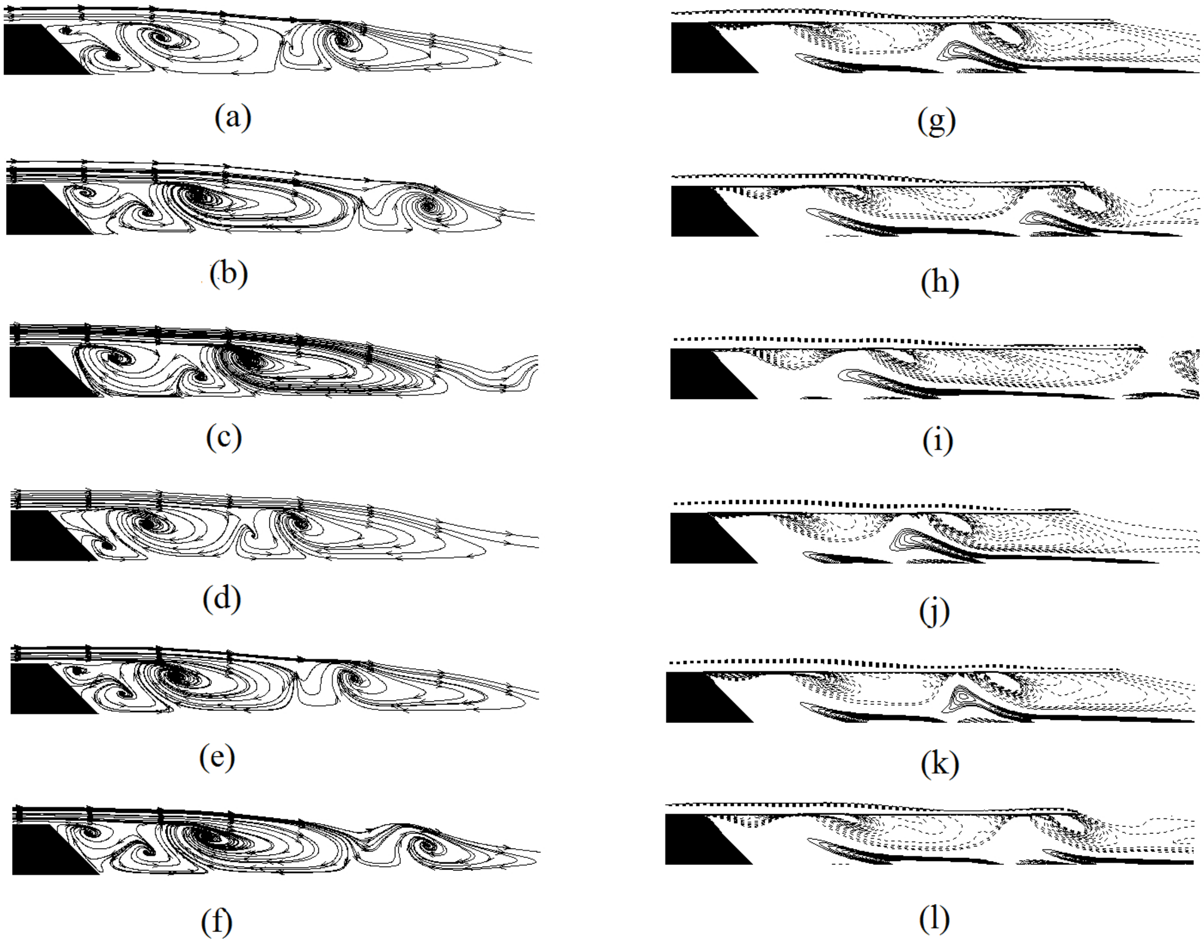

Figure 4.6: Streamline and corresponding vorticity plots of vortex shedding cycle in the wake of backward facing inclined step at Re=500, for θ=45° with ZNMF technique, x=0.193a, w=0.023, f=0.049, C_μ=0.0001 and amplitude, A=0.1: (a, g) T/6; (b, h) T/3; (c, i) T/2; (d, j) 2T/3; (e, k) 5T/6; (f, l) T.

Figure 4.6 presents the vortex shedding cycle for flow over the inclined step when $\theta=45^0$, ZNMF technique is applied. The frequency, amplitude and momentum coefficient of the flow control, are respectively, f=0.049, A=0.1 and C_μ=0.0001. The groove was placed at (x=1.953a, y=a) and the width of the groove was considered as w=0.023. From figure 4.6, it can be observed that the vortex shedding mechanism is the same as in case of flow over an inclined step without any AFC technique applied. The vortex shedding occurs in the rear of the step due to the interaction of the rolling up shear layer formed below the growing recirculating vortex with the neck of the vortex, causing the vortex separation and subsequently dissipating it in the wake of the step as seen in figure 4.6(g, h , i). Identical vortex shedding mechanism and pattern was observed in figures 4.5 and 4.6, in fact, in all simulations undertaken in the present study, irrespective of the angle of inclination, Reynolds number, AFC technique and regardless of the configuration employed, just some variations in the recirculation and neck lengths of the vortices in the wake of the step were spotted. The main differences observed in the downstream flow characteristics of the inclined step when AFC techniques were applied on the upstream horizontal surface, are related to the pressure variation on the upstream and inclined surfaces. In some cases, the separation of the boundary layer in the upstream length, due to the interaction of the injected jet into the upstream boundary layer could be clearly seen. It was also observed that upstream boundary layer oscillated in harmony with the injection and absorption of the fluid when ZNMF or FA techniques were applied, in these cases, the boundary layer thickness near the inclined step corner varied with the vortex shedding cycle, see figure 4.8 to 4.11. Whereas in case of flow over an inclined step without AFC, the boundary layer thickness was steady through the vortex shedding cycle, as observed in figure 4.5.

The effects of AFC frequency, f and groove position, were found to be minor regarding the recirculating vortices and upstream boundary layer variation, whereas the effects of amplitude, A and groove width, were found to be prominent, irrespective of the AFC technique, angle of inclination and Reynolds number analyzed.

When small fluid amplitudes were applied, $A \leq 0.1$, even for the optimum jet forcing frequency f=0.049, which according to Brunn and Nitsche (2006), needs to be around the natural vortex shedding frequency, and regardless of the jet configuration used ZNMF or FA, the boundary layer was slightly affected, the streamlines and vorticity contours, did not show any clear differences when compared to the ones obtained without AFC, see figure 4.5 and 4.6. At higher forcing amplitudes, along with the increase in the boundary layer thickness and flow separation upstream of the inclined step corner, the height of the recirculating vortex in the wake of inclined step tended to grow larger in size than the height of the step, as seen in streamline plots of figures (4.7-4.11). Notice that in figure (4.6), the size of the recirculating vortex in the wake was found to be similar to the one of figure (4.5), which in both cases was about the height of the step, the neck length also remained similar in both cases.

Figure 4.7 (a-f) present the streamline plots of vortex shedding cycle, for an inclination angle, $\theta=45^0$ at Re=800 and when FA is used, frequency, f=0.051, amplitude, A=0.5 and momentum coefficient, $C_\mu=0.0154$, groove width and location were the same as the ones employed in figure 4.6. Corresponding vorticity plots of the AFC fluid injection on the upstream surface into the boundary layer in a vortex shedding cycle, figure 4.7(g-l) are also introduced. A gradual increase of fluid injection into the upstream boundary layer can be observed in figure 4.7(k, l) and the decrease in the fluid injection can be seen in figure 4.7(g, i). The boundary layer on the upstream surface remains attached to the surface until reaching the inclined step corner and then separates forming the neck of the vortex, which then elongates along with the growing recirculating vortex on the wake of the step and interacts with the rolling up shear layer leading to vortex dissipation, as observed in the streamline plots.

To compare the effects of forcing amplitude, with respect to both flow control techniques, on the upstream boundary layer, figure 4.8 and 4.9 are presented. In figure 4.8, flow over the inclined step when $\theta=65^0$, Re=800, frequency f=0.045, amplitude A=1 and momentum coefficient $C_\mu=0.0093$, is presented, ZNMF is used, whereas in figure 4.9 the flow over the inclined step with θ=65^0, Re=800, f= 0.045, amplitude A=1 and momentum coefficient C_μ=0.0616, can be seen, FA is employed. Groove width and position were the same as in the previous cases, figure 4.6 and 4.7. it can be noted that the momentum coefficient used in figure 4.9 is around 7 times the one employed in figure 4.8. In the former case, figure 4.8, the fluid injection is releasing its energy inside the boundary layer, whereas in the latter case, figure 4.9, the jet injected is breaking the boundary layer causing it to separate before reaching the inclined step corner, then, reattaches just before reaching the groove, as presented in figure 4.9(j) and its respective streamlines in 4.9(d). This, upstream boundary layer separation at the inclined step corner, leads to an increase of the pressure acting on the inclined upper surface, leading to a drastic decrease of the lift acting on the body, due to the increase of the downward force acting on the upstream surface.

Due to the higher maximum velocity of the injected jet in case of figure 4.9, the recirculating vortex is also much larger and tends to grow bigger than in case of figure 8, indicating a boundary layer earlier separation. Pressure variation onto the upper and inclined surfaces, for the latest two cases presented, can be evaluated when seeing figure 4.14 (c) and (d), where for A = 1, it is observed, for the case of ZNMF, that the pressure onto the upper surface is much smaller than the one obtained when FA technique is applied. Although pressure distribution profiles for θ=65º are presented in this chapter, it was realized that the pattern was similar to the one observed at θ=45º.

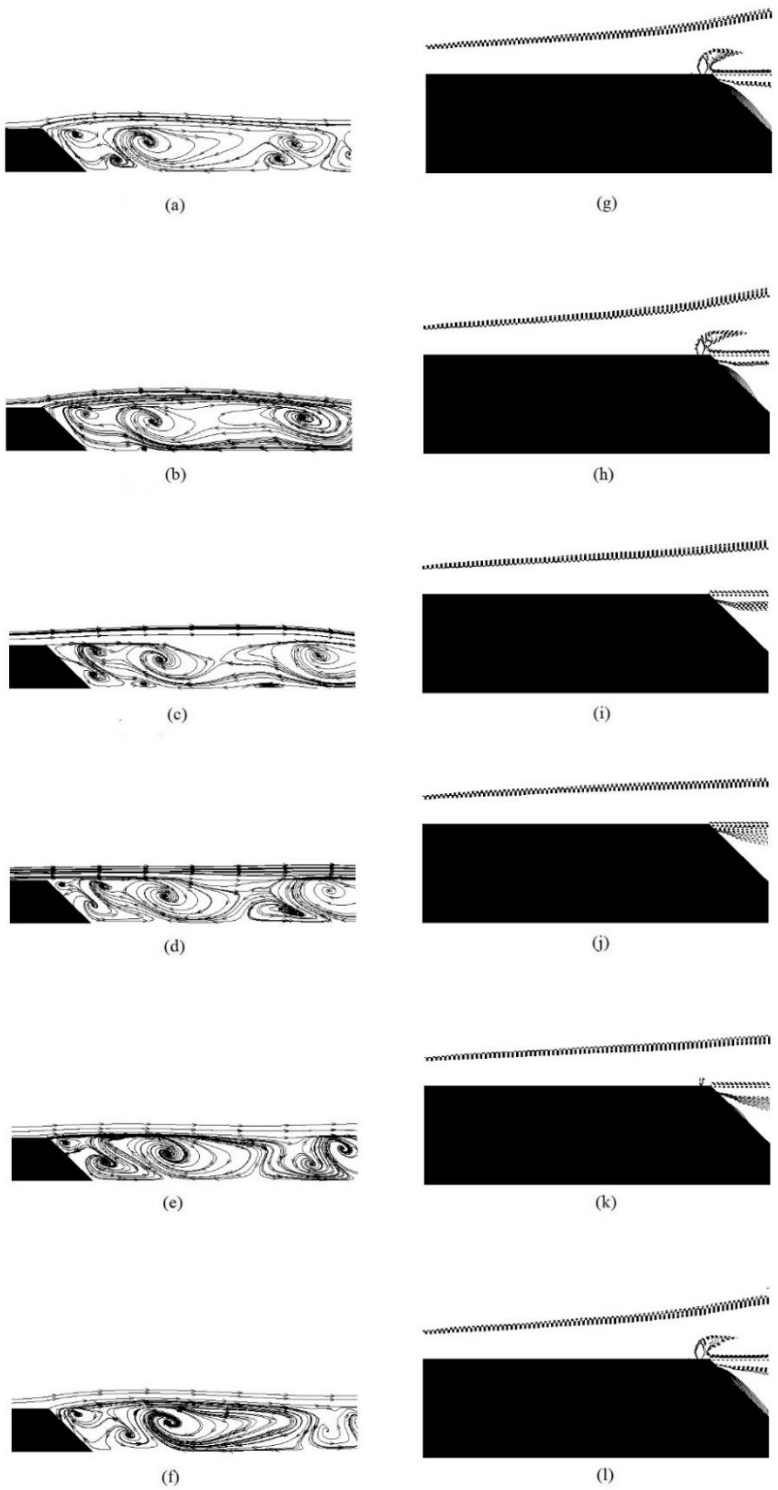

Figure 4.7: Streamline plots of vortex shedding cycle and corresponding Vorticity plots of AFC on the upstream surface of the inclined step at Re=800, with FA frequency 0.051, C_μ=0.0154, amplitude A=0.5 for θ=45°, w=0.023: (a, g) T/6; (b, h) T/3; (c, i) T/2; (d, j) 2T/3; (e, k) 5T/6; (f, l) T.

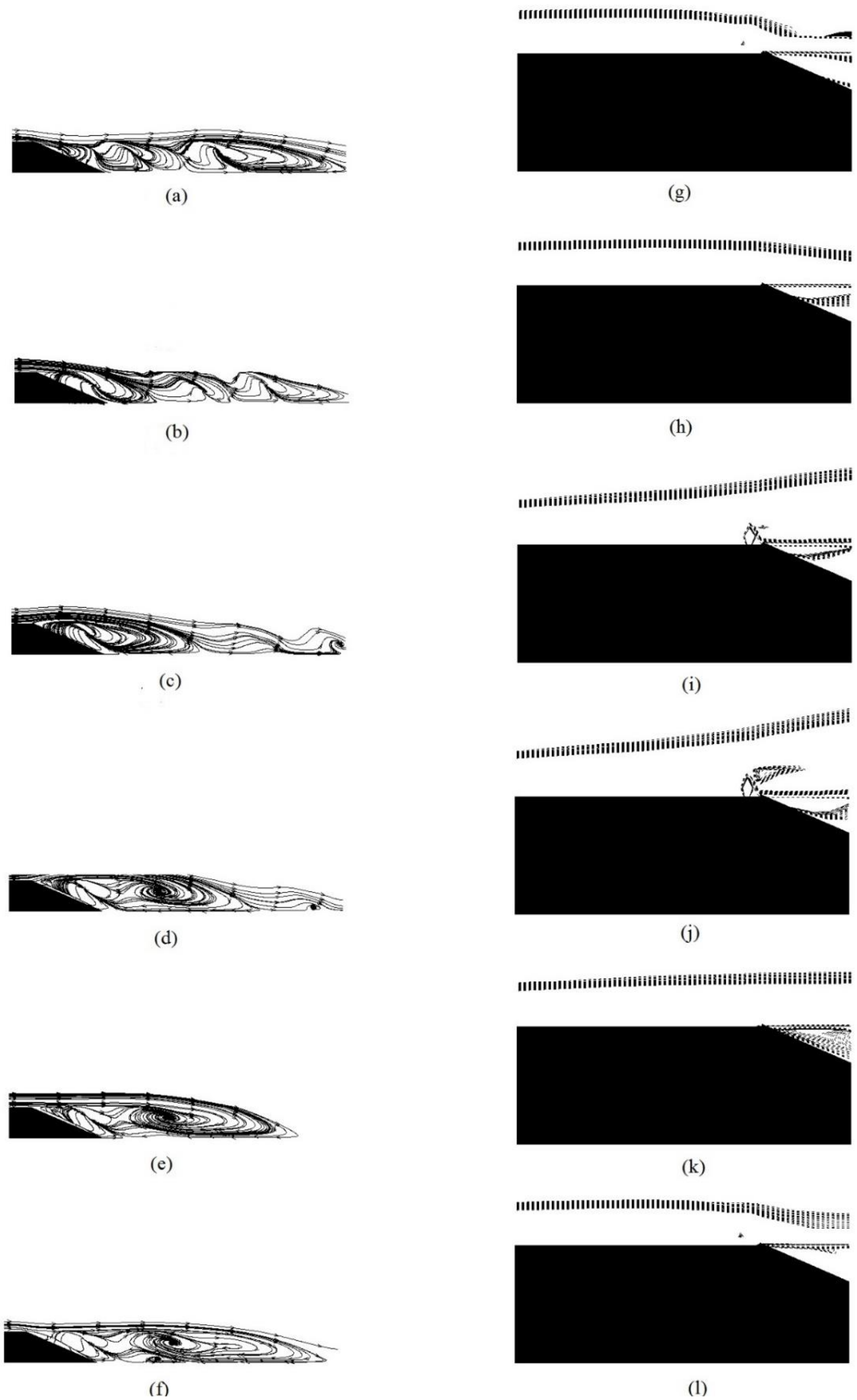

Figure 4.8: Streamline plots of vortex shedding cycle and corresponding Vorticity plots of AFC on the upstream surface of the inclined step at Re=800, with upstream ZNMF control frequency 0.045, amplitude A=1 for $\theta=65^0$, x= 0.193a, w=0.023, $C_\mu=0.0093$. (a, g) T/6; (b, h) T/3; (c, i) T/2; (d, j) 2T/3; (e, k) 5T/6; (f, l) T.

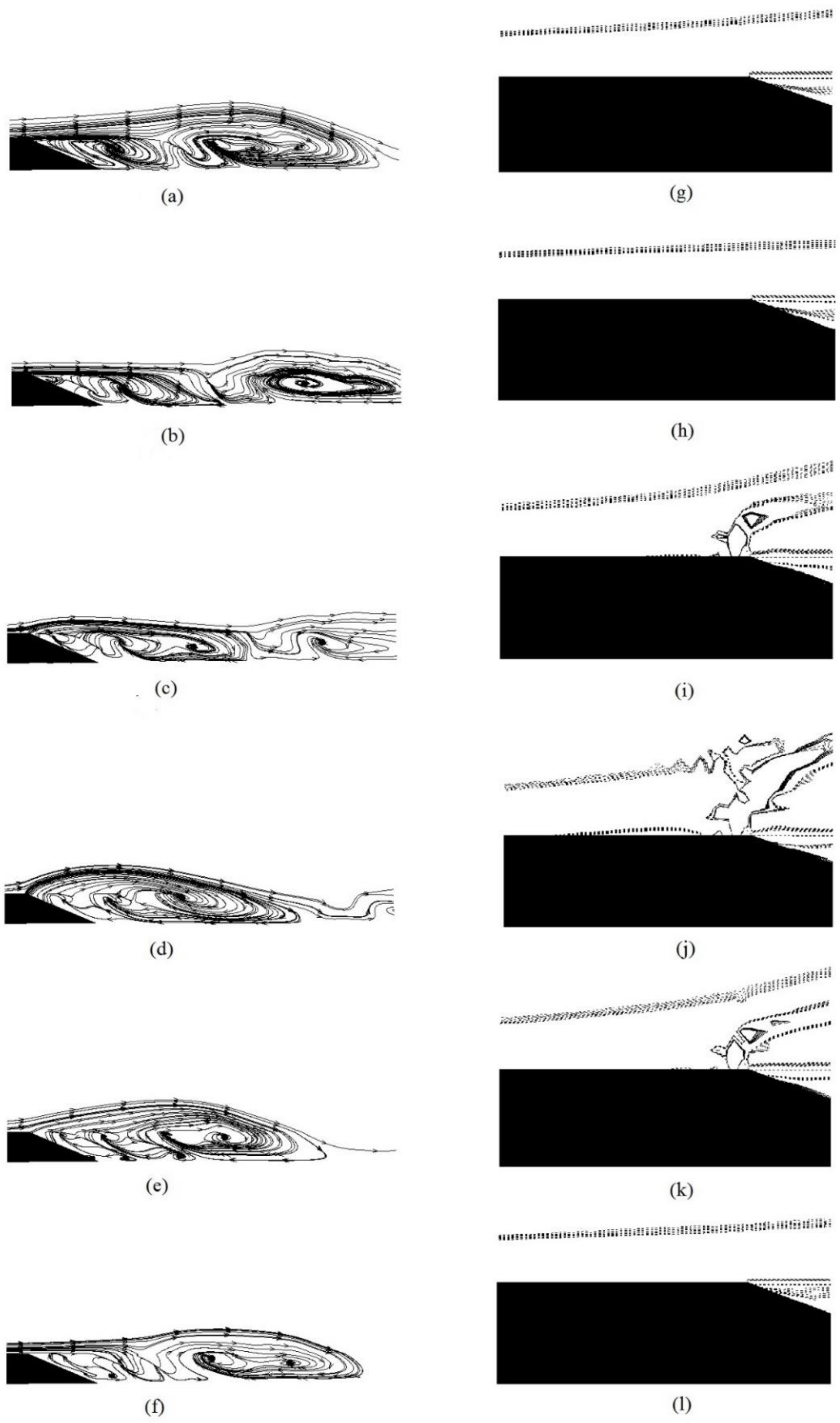

Figure 4.9: Streamline plots of vortex shedding cycle and corresponding Vorticity plots of AFC on the upstream surface of the inclined step at Re=800, with upstream FA flow control frequency 0.045, amplitude A=1 for $\theta=65^0$, x = 0.193a, w=0.023, $C_\mu=0.0616$: (a, g) T/6; (b, h) T/3; (c, i) T/2; (d, j) 2T/3; (e, k) 5T/6; (f, l) T.

To evaluate the effects of groove width on the upstream boundary layer, for both flow control techniques, three different groove widths of w=0.023, 0.048 and 0.073 were analyzed. Groove width affects the mass flow injected into the upstream boundary layer. Since momentum coefficient is directly proportional to groove width, its effects on flow properties are considerably. In figure 4.10, flow over the inclined step with $\theta=45^0$, Re=800, frequency f= 0.048, amplitude A=0.5 and momentum coefficient $C_\mu=0.0074$, is presented with ZNMF technique applied. In figure 4.11, flow over the inclined step with $\theta=45^0$, Re=800, frequency f= 0.051, amplitude A=0.5 and momentum coefficient $C_\mu=0.0489$ is presented with FA technique applied. In both cases, the maximum groove width of w=0.073 was considered. From figure 4.8, it can be observed that for ZNMF technique applied with w=0.023 and A=1, the fluid from the groove is induced within the upstream boundary layer. In case of figure 4.10, for a smaller amplitude A=0.5, the momentum coefficient is similar to figure 4.8 because of the increased width=0.072, resulting in similar behavior of the AFC Jet and boundary interaction. It can be inferred that momentum coefficient is an important parameter influencing the boundary layer. In figure 4.11, the injected jet is breaking the boundary layer causing it to separate before reaching the inclined step corner, and then it reattaches just before reaching the groove, as seen in figure 4.11(g, h, l) and its respective streamlines, figures 4.11(a, b. f). The phenomena described in figure 4.11 resembles characteristics seen in figure 4.9 and in both cases momentum coefficients are similar. It is also to be observed, when comparing figure 4.10 and 4.11, that momentum coefficient of the latter is about 7 times the former leading to boundary tripping seen in figure 4.11(g), (h) and (I). From figures 4.10 and 4.11, it can be observed that the boundary layer oscillates in harmony with the AFC jet frequency, indicating that at the Reynolds numbers analyzed, boundary layer fluctuations ae in resonance with the AFC technique applied. This upstream boundary layer separation, at the inclined step upper corner, leads to an increase in pressure acting on the inclined surface, leading to a drastic decrease in the lift acting on the inclined step. This phenomenon can also be seen in figure 4.10(c), (d), where the flow is attached to the upstream surface until reaching the inclined step corner, causing lower pressure on the upstream surface. Due to the AFC jet higher momentum coefficient, figure 4.11, the recirculating vortex is larger and tends to grow further than in case of figure 4.10, as observed form the streamline plots. The vortex size increase is a result of earlier separation of the boundary layer on the upstream surface of the step.

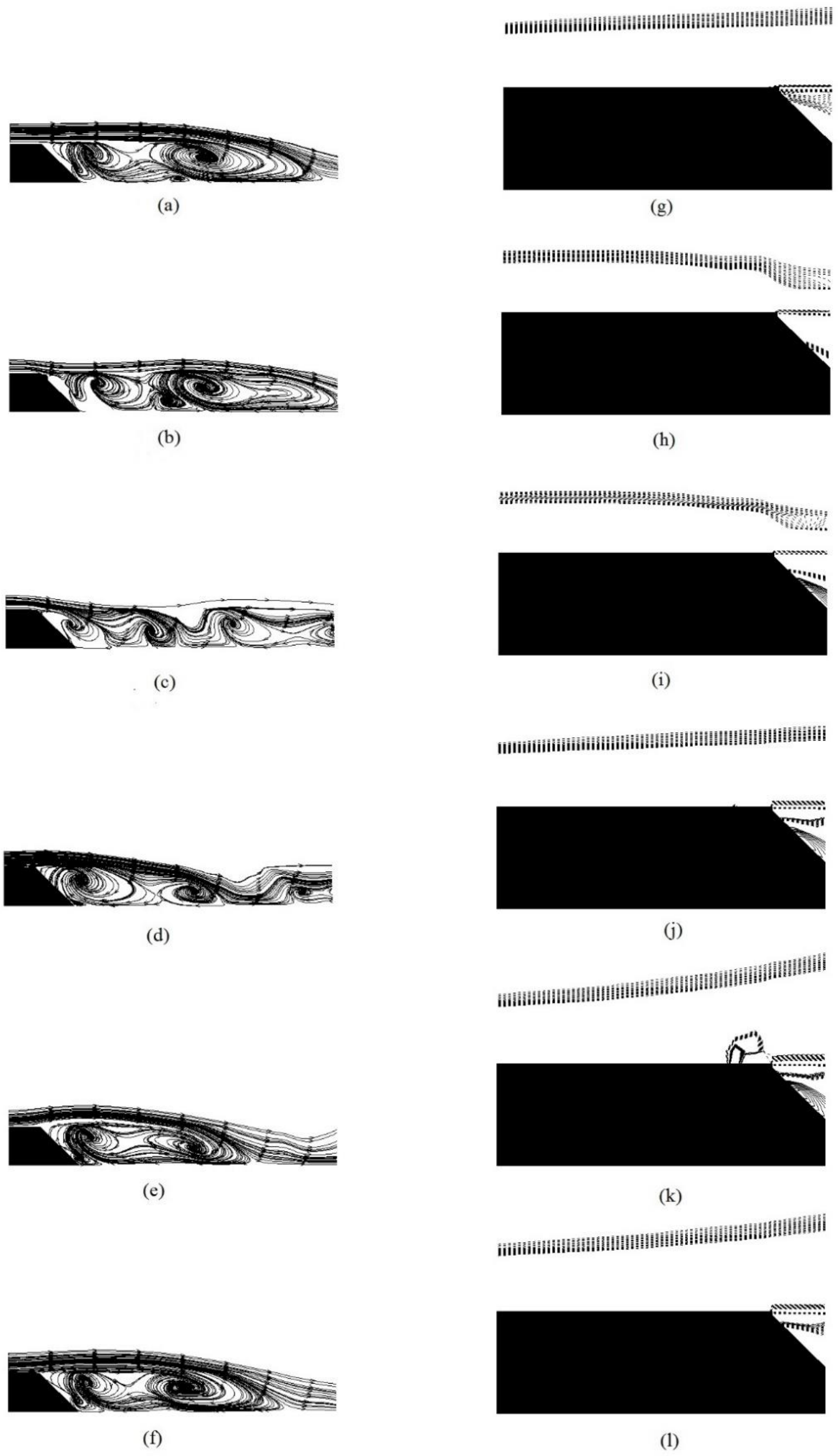
(a)
(g)
(b)
(h)
(c)
(i)
(d)
(j)
(e)
(k)
(f)
(l)

Figure 4.10: Streamline plots of vortex shedding cycle and corresponding Vorticity plots of AFC on the upstream surface of the inclined step at Re=800, with upstream ZNMF frequency, f=0.048, A=0.5, x = 0.193a and w= 0.073, C_{μ}=0.0074, θ=45°: (a, g) T/6; (b, h) T/3; (c, i) T/2; (d, j) 2T/3; (e, k) 5T/6; (f, l) T.

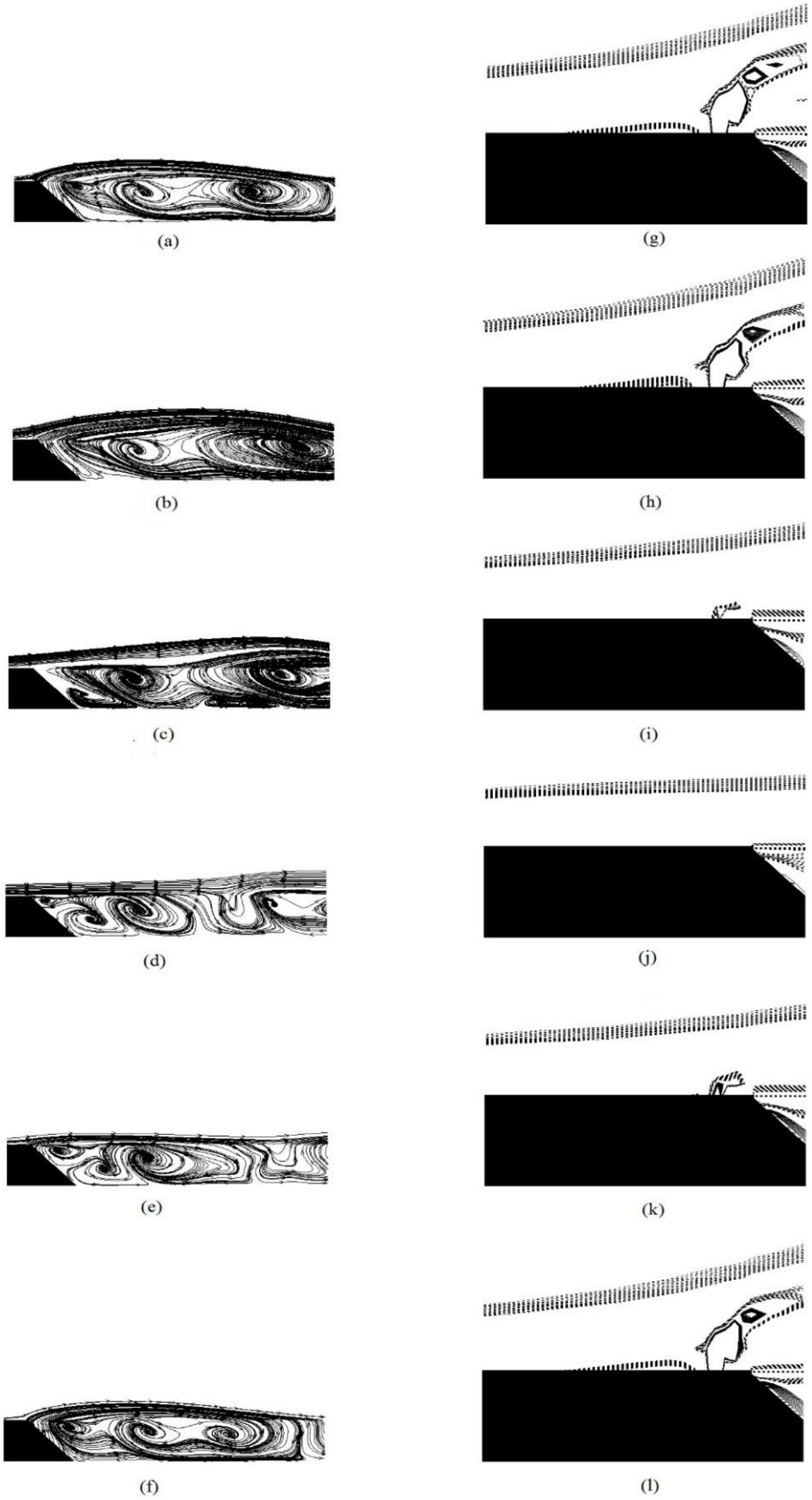

Figure 4.11: Streamline plots of vortex shedding cycle and corresponding Vorticity plots of AFC on the upstream surface of the inclined step at Re=800, with upstream FA frequency 0.051, amplitude, A=0.5, x = 0.193a, w= 0.073, C_{μ}=0.0489, $\theta=45^{o}$: (a, g) T/6; (b, h) T/3; (c, i) T/2; (d, j) 2T/3; (e, k) 5T/6; (f, l) T.

4.4.2 Effect of frequency and amplitude on Drag and Lift coefficient:

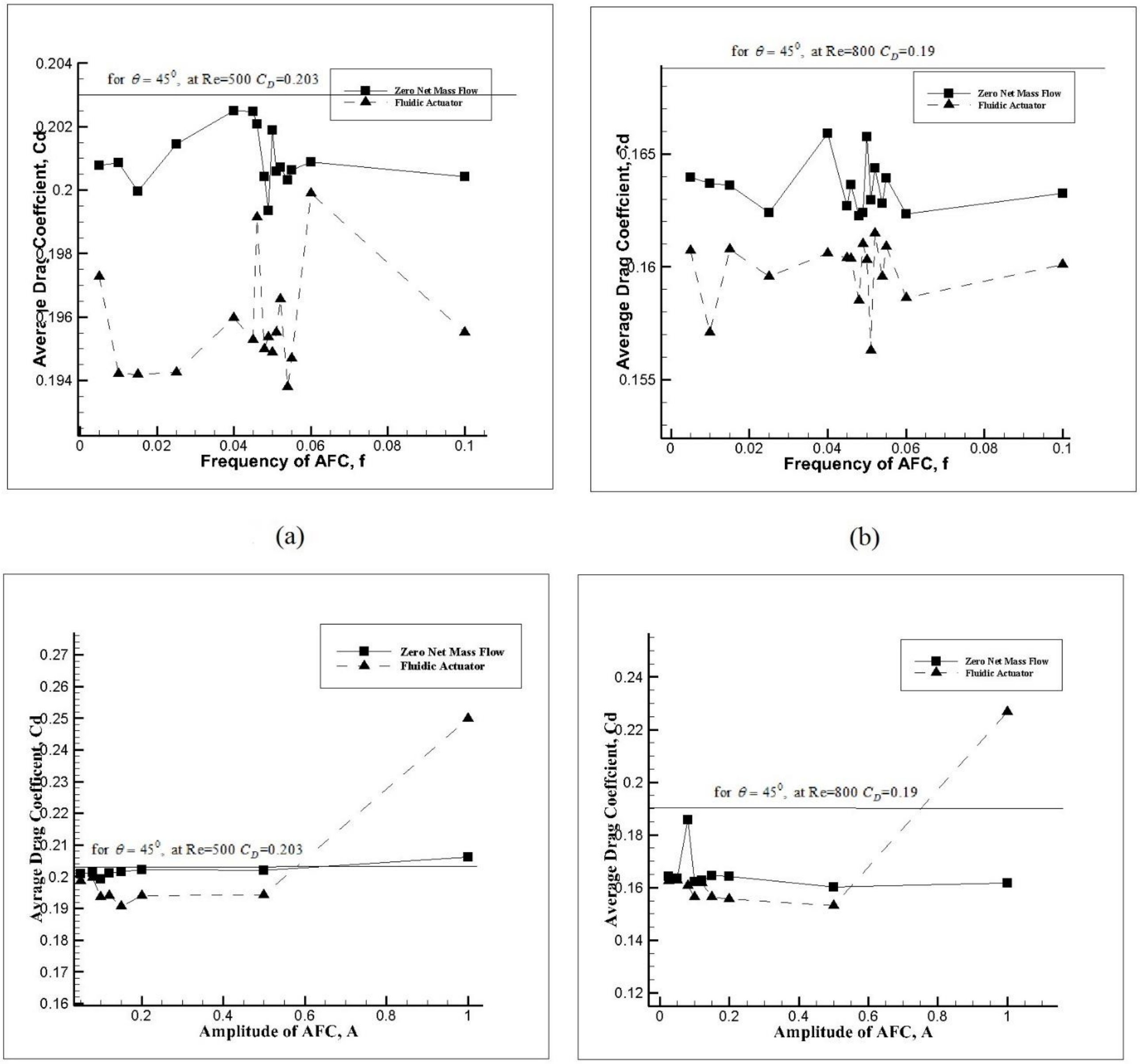

(a) (b)

(c) (d)

Figure 4.12: Average Drag coefficient versus frequency, f of active flow control (AFC) for θ=45° (a) Re=500, A=0.1 (b) Re=800, A=0.1, Average drag coefficient versus Amplitude, A of active flow control (AFC) for θ=45° (c) Re=500, f=0.049 for ZNMFA and f=0.054for FA, (d) Re=800, f=0.048 for ZNMFA and f =0.051 for FA. For all cases x=0.193a, w= 0.023.

Figures 4.12(a), (b) present the variation of average Drag coefficient as a function of the frequency f, applied on the upstream length, ul for $\theta=45^o$. The groove was placed at (x=1.953a, y=a), as seen in figure 4.2(b), a groove width, w=0.023 and jet amplitude, A=0.1 was considered. For comparison with flow over inclined step, the drag without AFC is also plotted. It can be observed that irrespective of the Reynolds number and AFC technique applied, the drag on the inclined step oscillates when the frequency of the flow control is varied around the natural vortex shedding one. Drag coefficient is most cases is smaller than the drag acting on the inclined step with no AFC technique applied, proving the effectiveness of the flow control, even at small forcing amplitudes. The drag was found to be minimum at frequencies ranging between f=0.045-0.055, indicating that the optimum frequency for Active flow control technique is around ±10% of the natural vortex shedding frequency of the inclined step without any flow control applied. The frequencies f=0.055 and f=0.045 seem to be the limits of drag coefficient oscillation, since for frequencies above and below them oscillation of the drag coefficient appears to disappear. This phenomenon completely agrees with the previous studies carried out by Brunn and Nitsche (2006), Leclerc et al (2006) and Joseph et al (2012), which reported that the optimum value of the AFC jet frequency, is the flow natural vortex shedding frequency. Figure 4.12(a), (b), exhibit a similar behavior when the parameters are varied, although ZNMF technique was found to be less effective than the fluidic actuator one in the case of drag reduction. For Reynolds number, Re=500, as observed in figures 4.14(a), (b), the pressure acting on the inclined surface, independent of the AFC technique, is higher when AFC frequency applied is around the natural vortex shedding frequency. At Reynolds number, Re=800, when comparing curves in figure 4.15(a), (b) characterized by the same frequency, pressure acting on the inclined surface in case of FA technique is higher than ZNMF technique, leading to a smaller drag acting on the inclined step.

Figure 4.12(c), (d), present the variation of average drag coefficient with active flow control amplitude A with respective optimum frequency, f for all the cases. It is interesting to see that the drag acting on the inclined step surface has a minor variation when ZNMF technique is applied, but for FA technique, when amplitude of the AFC is varied from 0.025 to 0.5 the drag is smaller when compared to ZNMF. At higher amplitudes, in case of FA the drag acting on the step is higher when compared to ZNMF. This effect can be attributed to the occurrence of boundary layer tripping as the amplitude increases as seen in figure 4.9 and reducing the pressure on the inclined surface. This behavior of the pressure acting on the inclined surface can be observed form figure 4.14(d), for A=1 the pressure acting on the inclined surface is minimum and is maximum at the amplitude for ZNMF as seen in figure 4.14(c) leading to lower drag acting on step in case of ZNMF than FA. When comparing figures 4.14(c) and (d), it can also be seen that for amplitudes ranging from A=0.05 to 0.5, the inclined surface pressure is slightly smaller for ZNMF than FA. Similar effect is also observed at Re=80 as seen in figures 4.15 (c) and (d).

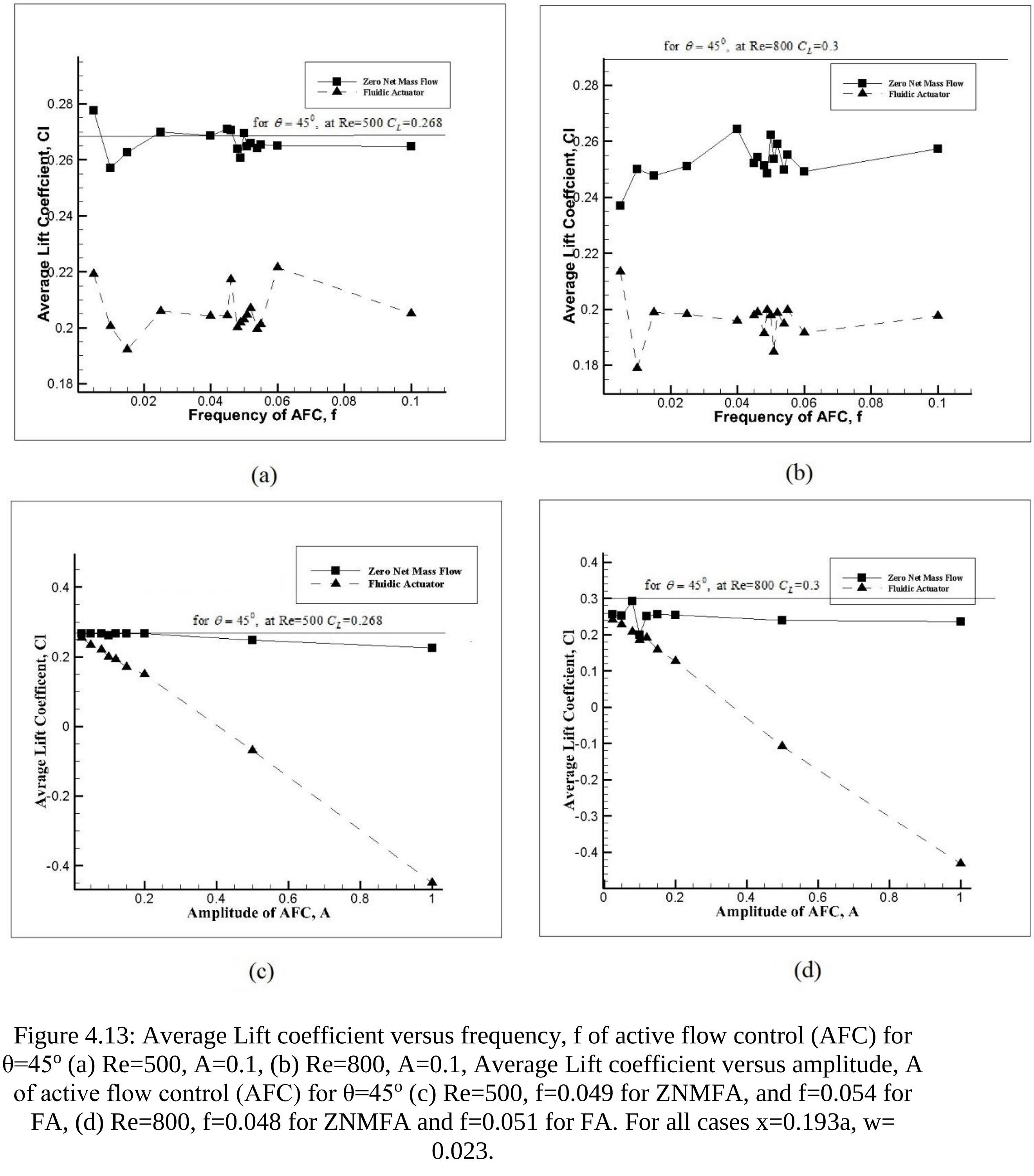

(a)

(b)

(c)

(d)

Figure 4.13: Average Lift coefficient versus frequency, f of active flow control (AFC) for θ=45^o (a) Re=500, A=0.1, (b) Re=800, A=0.1, Average Lift coefficient versus amplitude, A of active flow control (AFC) for θ=45^o (c) Re=500, f=0.049 for ZNMFA, and f=0.054 for FA, (d) Re=800, f=0.048 for ZNMFA and f=0.051 for FA. For all cases x=0.193a, w= 0.023.

Figure 4.13(a) and (b), present the variation of average lift coefficient with active flow control frequency f, for θ=45°. As seen in the case of the drag presented in figures 4.12(a) and (b), the lift acting on the inclined step oscillates when the frequency of the flow control is varied around the natural vortex shedding frequency. Since the lift on the inclined step is primarily dependent on the pressure acting on the upstream surface of the step, the lift behavior can be explained when evaluating the pressure profiles of the upstream surface. At Reynolds number, Re=500 for a given frequency, f, as observed in figures 4.14(a), (b), the pressure acting on the upstream surface in case of FA technique is higher than ZNMF technique, which results in a decrease of the lift acting on the inclined step as seen in figure 4.13 (a), (b). The same phenomena also appears at Re=800, as observed in figure 4.15(a), (b).

In figure 4.13(c), (d), the variation of average lift coefficient with active flow control amplitude A, is presented. For nearly all amplitudes studied and independent of the Reynolds number, the lift acting on the inclined step is smaller for FA technique than ZNMF due to higher pressure acting on the upstream surface, especially higher amplitudes as seen in figure 4.14(c), (d). At these high amplitudes for FA boundary layer tripping occurs leading to very high pressure on the upstream surface. At very small amplitudes of around 0.025, pressure on the upstream surface is slightly higher for ZNMF than FA. A similar behavior can also be observed for Re=800 in figure 4.15(c) and (d). According to the present results, for FA technique, it can be inferred that boundary layer tripping is likely to occur for jet amplitudes higher than 0.2 and evident for A=1.

In sharp contrast to the FA technique, the lift acting on the inclined step varies nominally for ZNMF technique when the amplitude, A of AFC is increased from 0.025 to 1, regardless of the Reynolds number used, as seen in figure 4.13(c) and (d). It can be attributed to the pressure variation on the upstream surface, as it is smaller when compared to FA technique, as observed when comparing figure 4.14(c), (d) for Re=500 and figure 4.15(c), (d) for Re=800. It is also interesting to realize, from figure 4.14(c) and 4.15(c) that in case of ZNMF maximum pressure on the upstream surface is obtained for minimum amplitude analyzed and for FA the maximum is obtained when using the maximum amplitude, see figure 4.14(d) and 4.15(d).

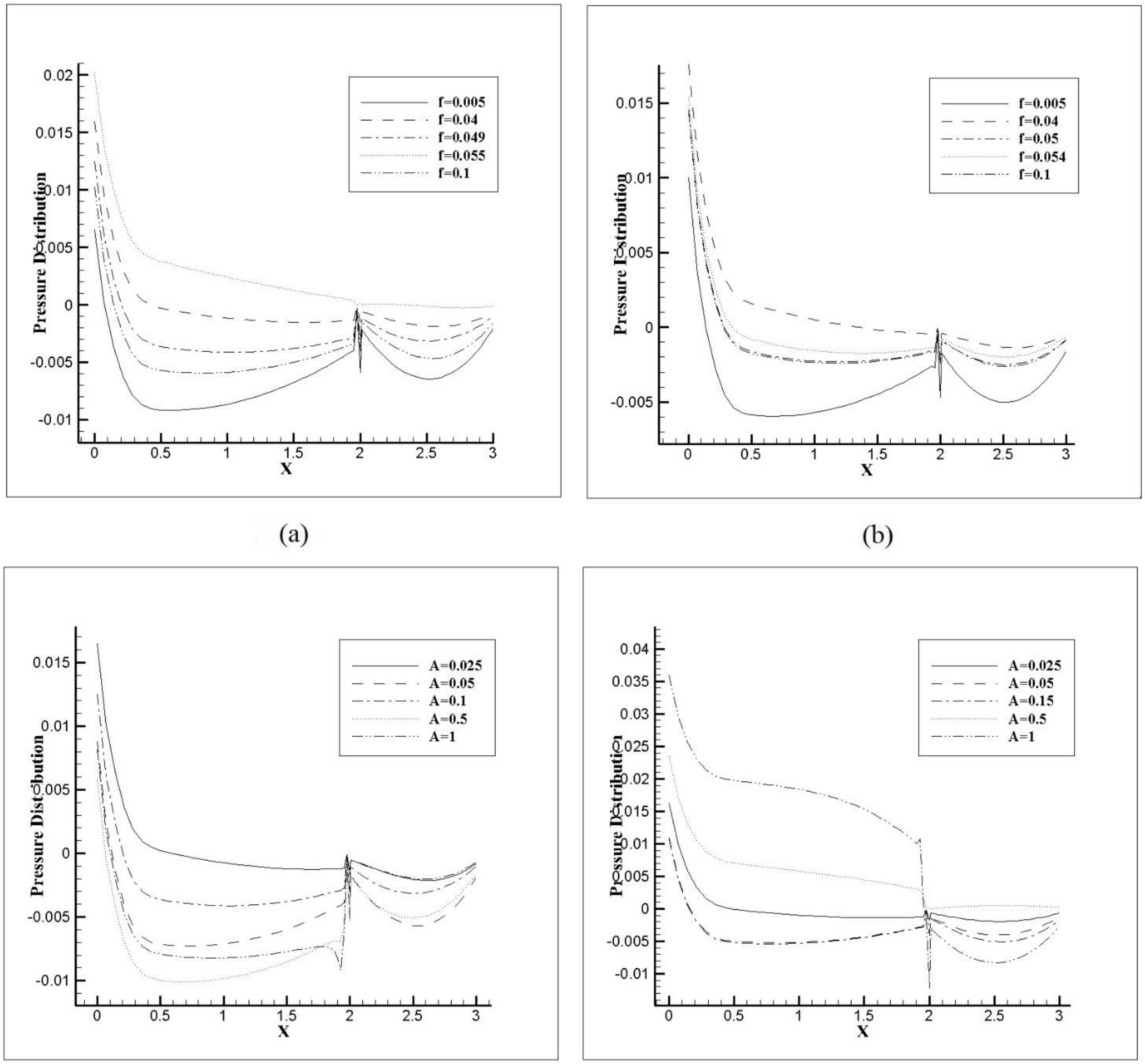

(a) (b)

(c) (d)

Figure 4.14: Instantaneous pressure Distribution plots on the inclined step surface for $\theta=45^0$at Re=500. For different frequencies f, Amplitude A=0.1 using (a) Zero Net Mass Flow technique (b) Fluidic Actuator technique. For different Amplitudes A, with respective optimum frequency, f using (c) Zero Net Mass Flow technique (d) Fluidic Actuator technique.

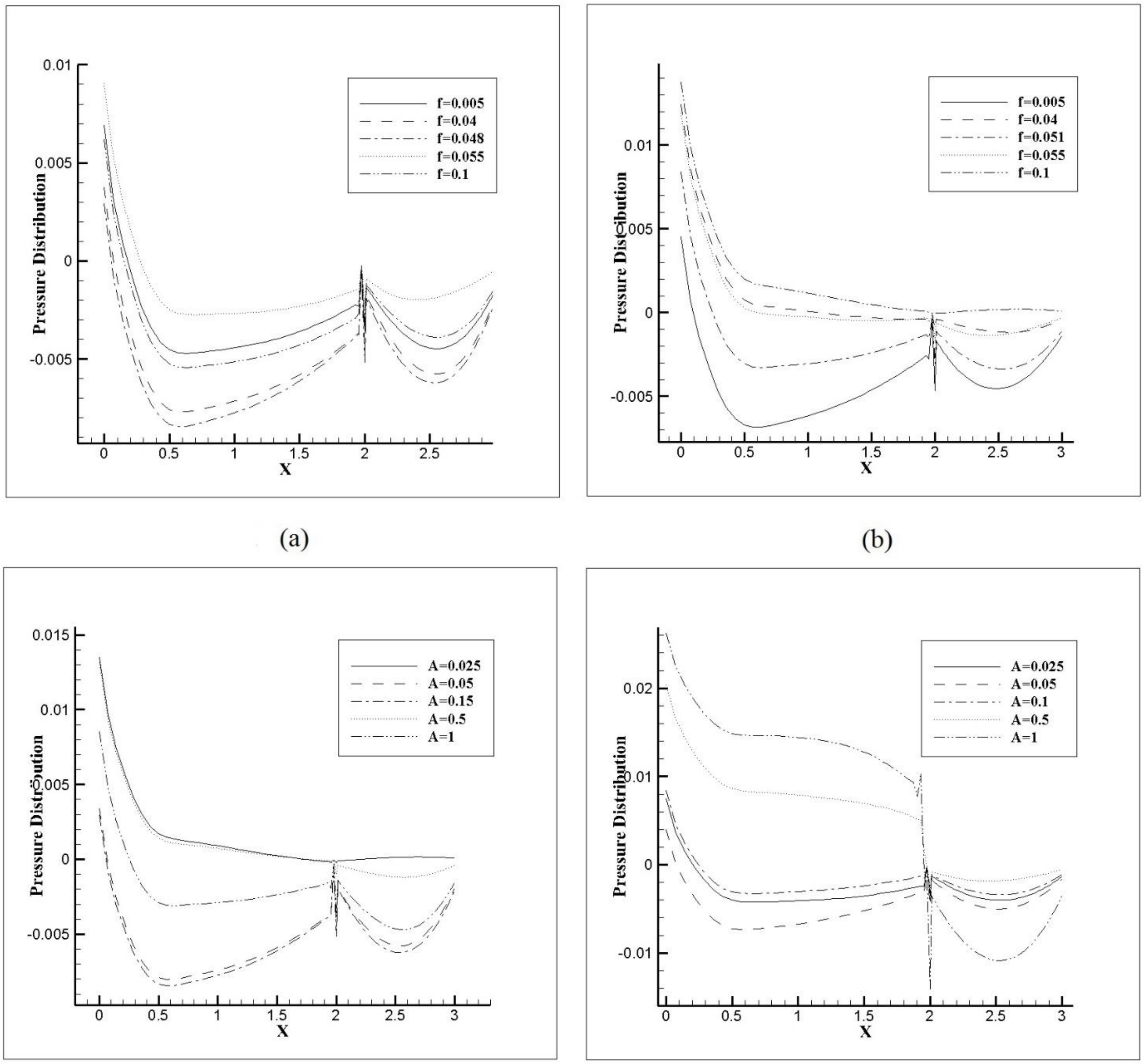

(a) (b)

(c) (d)

Figure 4.15: Instantaneous pressure Distribution plots on the inclined step surface for θ=45^{0}at Re=800. For different frequencies f, Amplitude A=0.1. (a) with Zero Net Mass Flow technique, (b) with Fluidic Actuator technique. For different Amplitudes A, the frequency was the optimum one for each case, (c) with Zero Net Mass Flow technique, (d) with Fluidic Actuator technique.

The instantaneous pressure distribution plots over the surface of the inclined step for ZNMF and FA, by varying the frequency f, and amplitude A, for Re=500 and θ=45º are introduced in figure 4.14. In figure 4.14(a), (b), the pressure distribution on the step surface is presented for different frequencies, f with application of ZNMF and FA techniques respectively. When comparing figures 4.14(a),(b) with 4.15(a),(b), it is realized that pressure on the inclined surface suffers a marginal variation as Reynolds number increases from 500 to 800, although it can also be seen that as Reynolds number increases, surface pressure tends to slightly decrease. An important phenomenon observed in figures 4.14 and 4.15, is that the pressure on the upstream surface, first decreases from the stagnation point, which is formed close to the leading edge, due to the abrupt change in the flow conditions caused by the sudden interaction of the free stream with the upstream surface, until reaching approximately the upper surface midpoint, pressure distribution then, tends to stabilize as the boundary layer develops on the upstream surface. This phenomenon is identical to the pressure distribution on the upper surface of an airfoil. Similarly, on the inclined surface, the pressure decreases until reaching the midpoint of the surface and then increases. This is due to the flow separation at the upper corner inclined surface, resulting in vortex dissipation in the wake along with the rolling up shear layer appearing at the lower edge of the inclined surface.

Figure 4.14(c), (d) present the pressure distribution on the step surfaces for different amplitudes, at their respective optimum frequency, f. In case of ZNMF technique, the pressure variation on the upstream surface with the increase in amplitude, A is much smaller when compared to fluidic actuator technique. In case of FA technique the pressure increases gradually with amplitude. This phenomenon can be attributed to increase in momentum coefficient with amplitude which is higher in case of FA than ZNMF leading to boundary layer tripping at higher amplitude causing higher pressure acting on the upstream surface.

It can be concluded that the amplitude, A is the primary factor influencing the stability of the upstream boundary layer. In all cases, the pressure fluctuations over the inclined step corner seem to be occurring irrespective of the flow conditions, especially at higher amplitude leading to boundary layer tripping causing large pressure fluctuation at the step corner as seen in figure 4.14(c), (d). It can also be observed that pressure fluctuations at the step corner are higher in case of FA than ZNMF due to higher momentum coefficient for a given amplitude, A of the AFC jet. It can also be seen from figure 4.14(d) and 4.15(d), for A=1 pressure acting on the upstream surface is maximum, indicating the occurrence of boundary layer tripping.

It was observed that as the inclination angle increases from 45º to 65º degrees, average drag coefficient decreases irrespective of the AFC frequency or amplitude applied. When frequency, f of AFC jet is varied the decrease is about 23% at Re =500 and a decrease of 25% at Re=800 for both ZNMF and FA techniques. For amplitude variation, decrease in average drag as angle of inclination increased from θ = 45º to 65º is about 23.6% for ZNMF at Re=500 and 24.6% at Re = 800. Similarly for FA, the decrease is about 22.6% at Re = 500 and about 25% at Re = 800 for ZNMF and FA respectively.

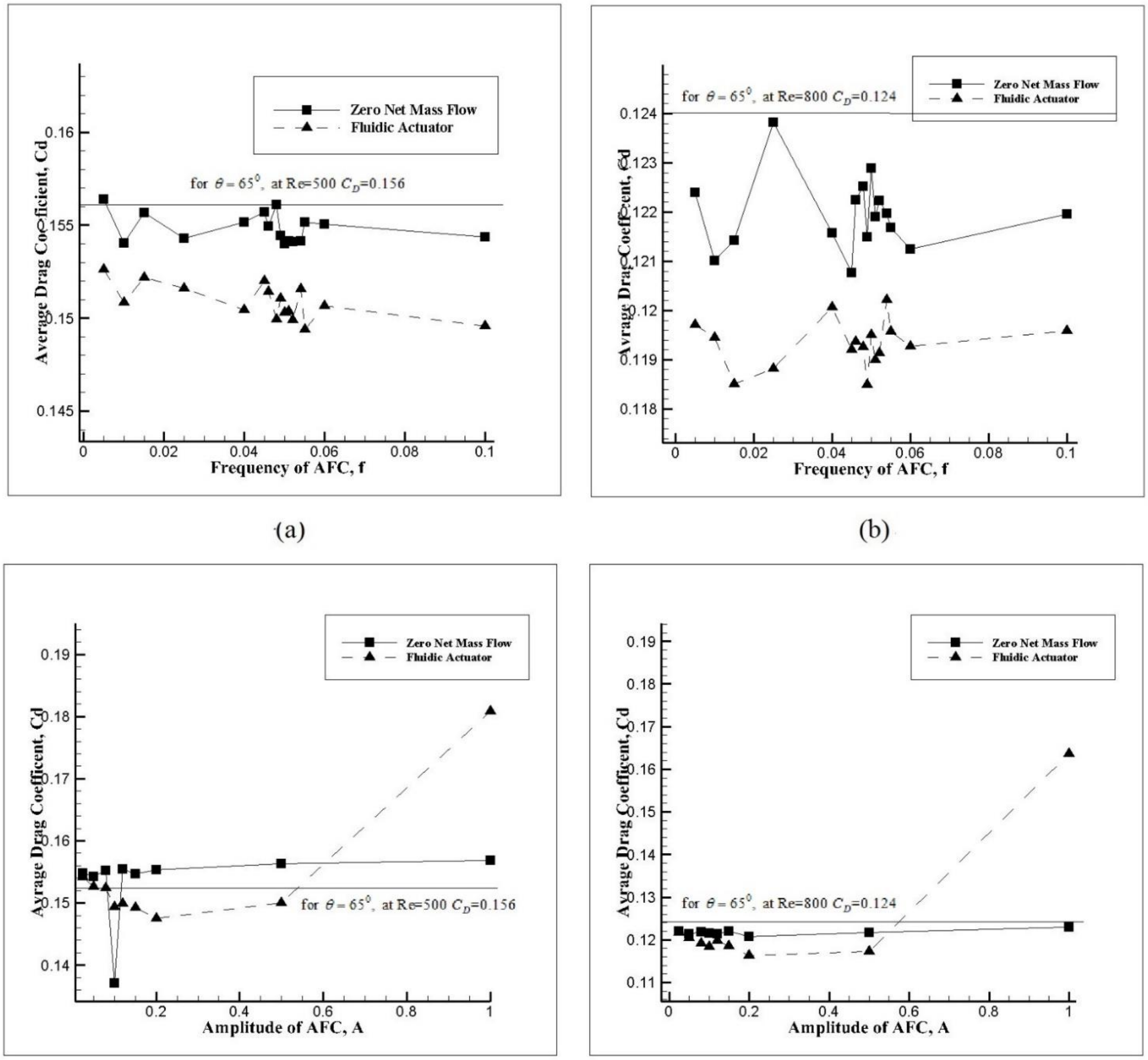

(a) (b)

(c) (d)

Figure 4.16: Average Drag coefficient versus frequency, f of active flow control (AFC) for θ=65° (a) Re=500, A=0.1 (b) Re=800, A=0.1, Average drag coefficient versus Amplitude, A of active flow control (AFC) for θ=65° (c) Re=500, f=0.045 for ZNMFA and f=0.055 for FA, (d) Re=800, f=0.045 for ZNMFA and f =0.049 for FA. For all cases x=0.193a, w= 0.023.

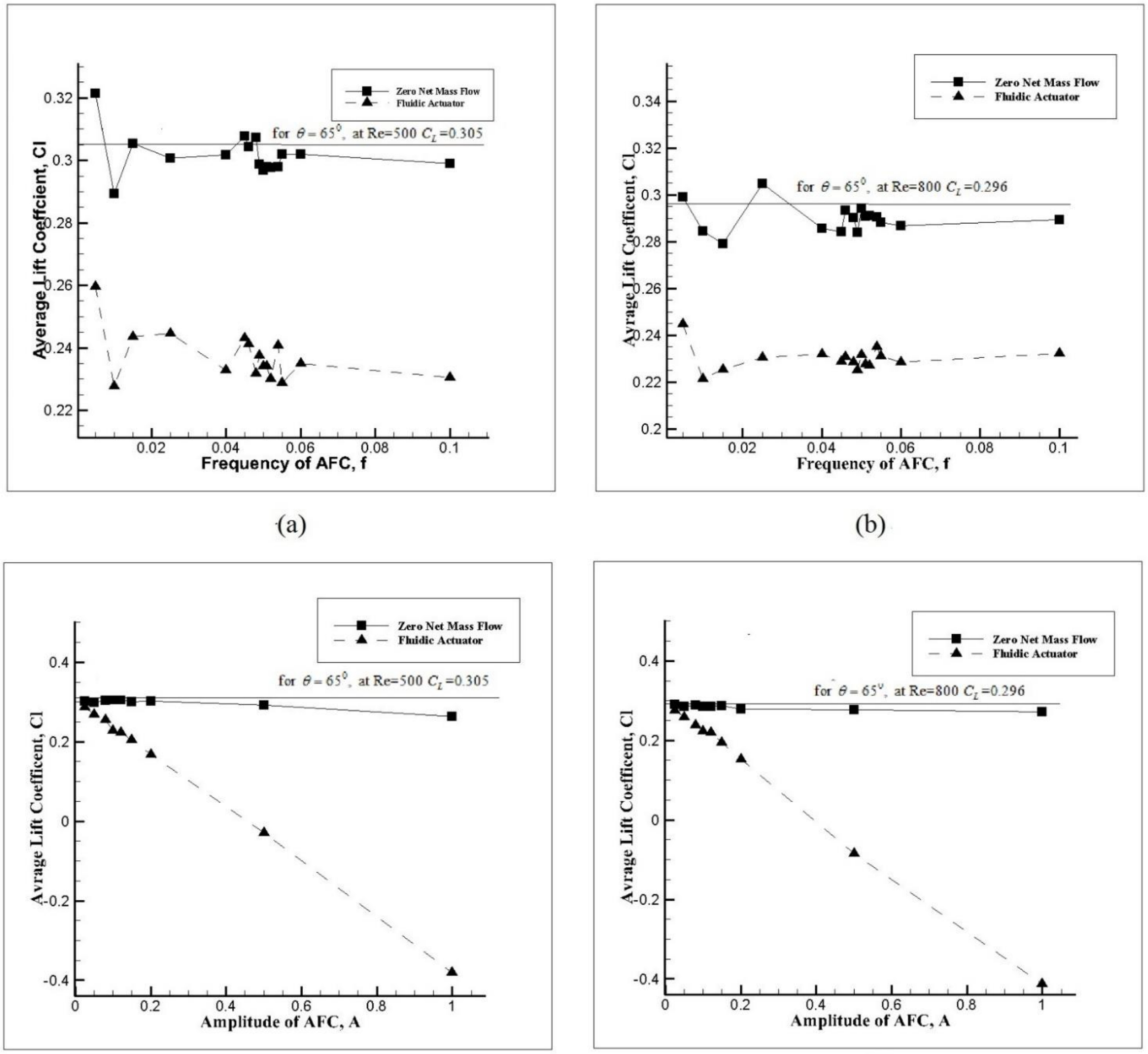

(a)

(b)

(c)

(d)

Figure 4.17: Average Lift coefficient versus frequency, f of active flow control (AFC) for θ=65° (a) Re=500, A=0.1, (b) Re=800, A=0.1, Average Lift coefficient versus amplitude, A of active flow control (AFC) for θ=65° (c) Re=500, f=0.045 for ZNMFA, and f=0.055 for FA, (d) Re=800, f=0.045 for ZNMFA and f=0.049 for FA. For all cases x=0.193a, w= 0.023.

As seen from figure 4.16 and 4.17, when θ increases from 45° to 65°, the average lift coefficient increases by approximately 12% with frequency, f for ZNMF at both Reynolds numbers. Similarly, for FA the increase in average lift coefficient is about 12% for Re=500 and about 15% for Re=800. The variation in average lift coefficient with amplitude for both ZNMF and FA and both Reynolds numbers studied was negligible, as the inclination angle increased from θ=45º to 65º. As presented in figure 4.18 and 4.19, a similar behavior of the pressure profiles acting on the body was obtained for $\theta=65^0$, Re=500 and Re=800.

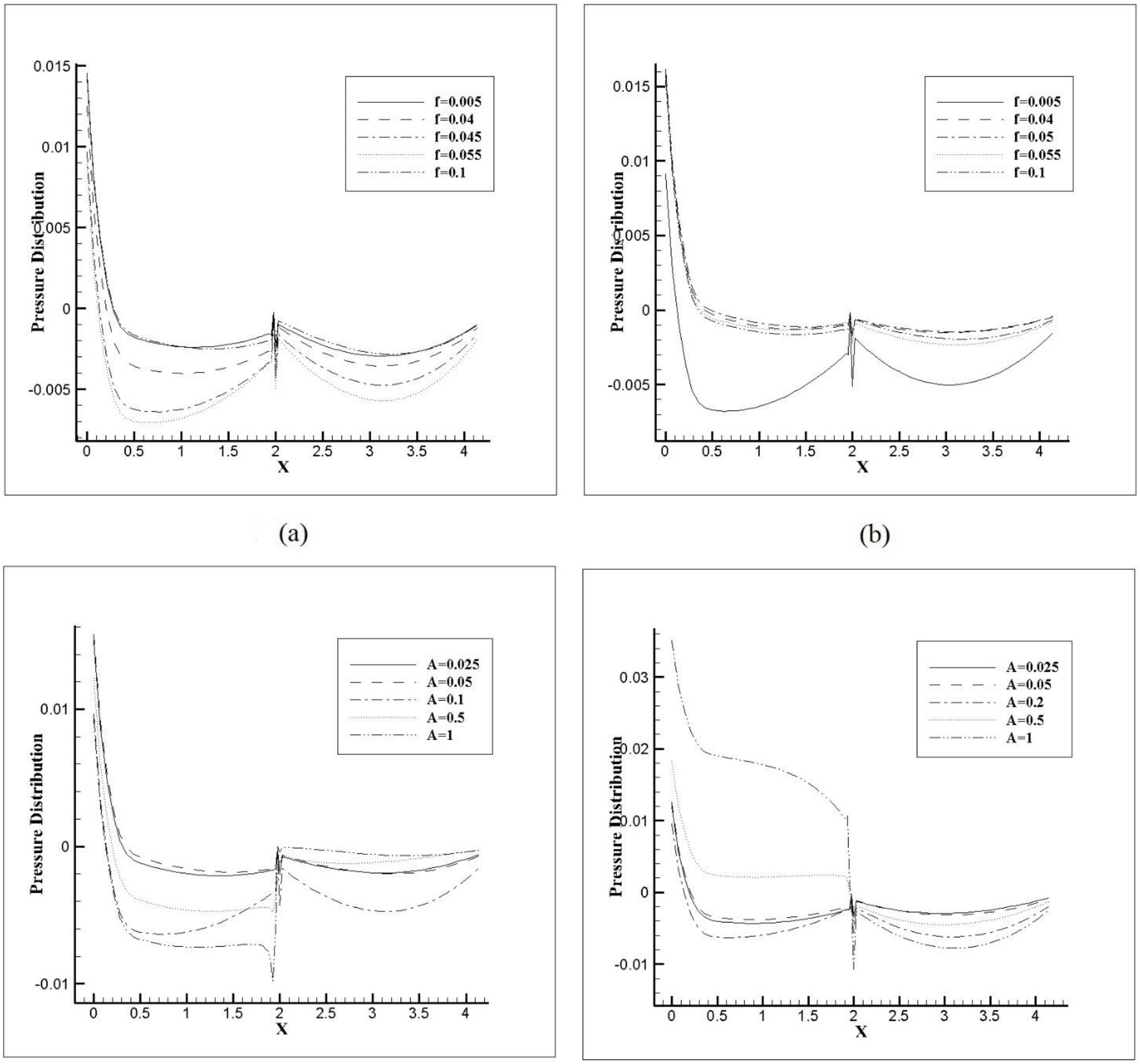

(a) (b)

(c) (d)

Figure 4.18: Instantaneous pressure Distribution plots on the inclined step surface for $\theta=65^0$at Re=500. For different frequencies f, Amplitude A=0.1 using (a) Zero Net Mass Flow technique (b) Fluidic Actuator technique. For different Amplitudes A, with respective optimum frequency, f using (c) Zero Net Mass Flow technique (d) Fluidic Actuator technique

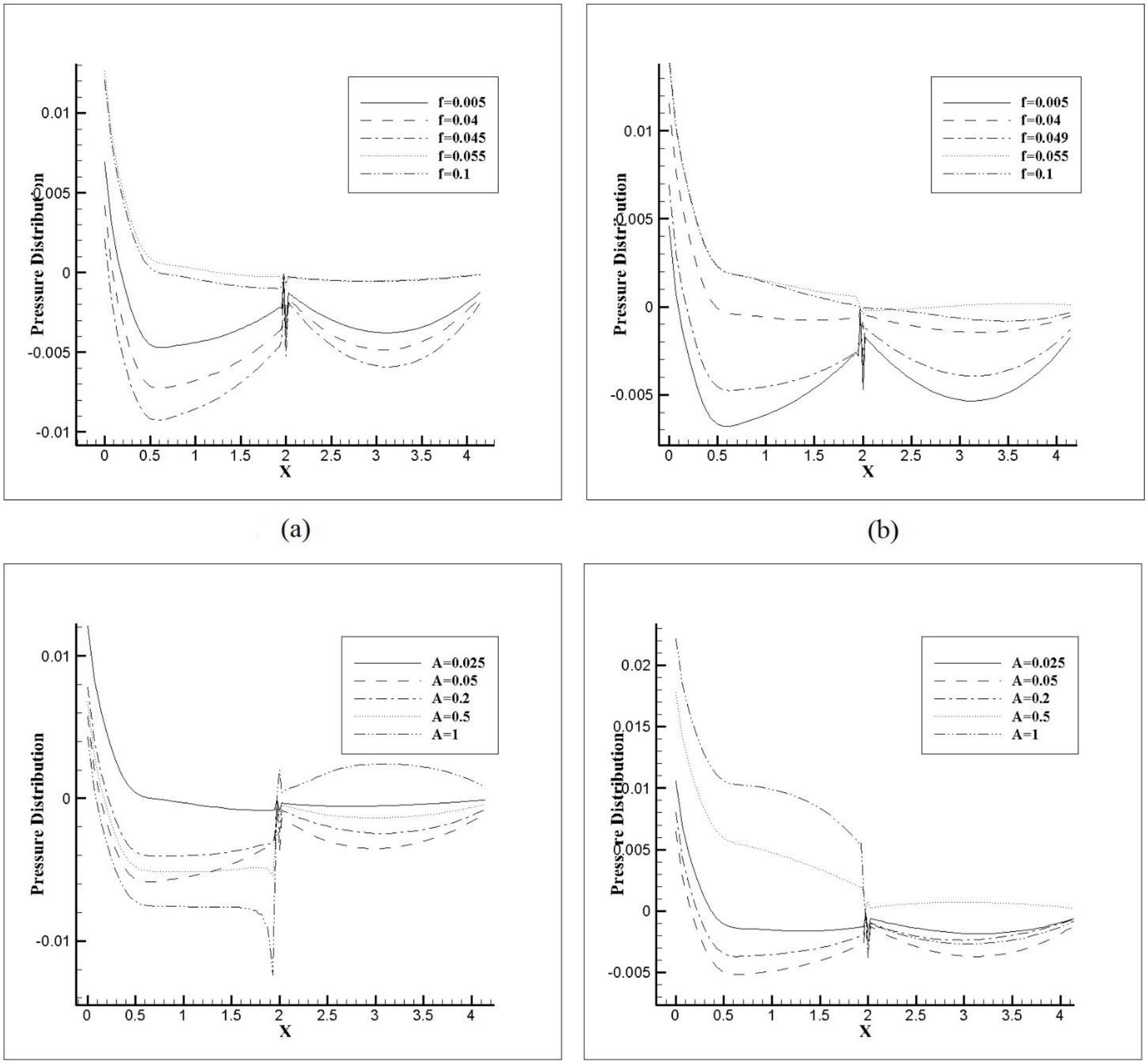

(a) (b)

(c) (d)

Figure 4.19: Instantaneous pressure Distribution plots on the inclined step surface for $\theta=65^0$at Re=800. For different frequencies f, Amplitude A=0.1. (a) with Zero Net Mass Flow technique, (b) with Fluidic Actuator technique. For different Amplitudes A, the frequency was the optimum one for each case, (c) with Zero Net Mass Flow technique, (d) with Fluidic Actuator technique

4.4.3 Effect of groove position and width on Drag and Lift coefficient:

Four different groove positions located on the upstream surface at (x=1.902a, y=a), (x=1.928a, y=a), (x=1.953a, y=a) and (x=1.976a, y=a) were simulated. In most of the cases studied, the penultimate position at (x=1.953a, y=a), is observed to exhibit the maximum effect on the body drag, as seen in figure 4.20(a), (b), especially for the case of fluidic actuator technique. When the groove is moved further upstream or downstream, leads to earlier boundary layer separation and the drag on the body increases. At this particular optimum groove position (x=1.953a, y=a), pressure on the inclined surface is maximum, as seen figure 4.22(a) and (b). When the groove is very close to the upper right edge, the boundary layer tends to become unstable and separate earlier leading to enhancement in vortex dissipation and increase in drag as seen in figure 4.20(a), (b). In case of ZNMF, technique the groove position has minor effects on the drag. It was observed that irrespective of groove position and Reynolds number, drag coefficient was reduced when any AFC technique is applied, especially at Re=800 as seen in figure 4.20(b) due to higher flow speed and momentum coefficient of the AFC jet injected into the boundary layer on the upstream when compared to figure 4.20(a), at Re=500 .

Figure 4.20(c), (d) present the variation of drag with the groove width, w. At Re = 500 and regardless of the flow control technique used, figure 4.20 (c), the drag acting on the body decreases as the groove width increases, this is can be attributed to the increase in momentum coefficient as the groove width increases. It can also be seen figure 4.22(c), (d), that pressure on the inclined surface increases with the groove width increase for both AFC techniques. Whenever the Reynolds number increases, at Re=800, figure 4.22(d), it can be seen that in case of the zero net mass flow technique, the drag initially decreases and then increases attaining the minimum value at w=0.048, but in case of fluidic actuator technique the drag increases with the width increase. Boundary layer is affected by two related parameters, velocity ratio U_{jet}/U_{∞} and momentum coefficient C_{μ}. At Re=500, as the momentum coefficient increases with the groove width, the AFC jet interacts effectively with the boundary layer causing decrease in drag coefficient as seen in figure 4.20(a) . At Re=800, due to higher momentum coefficient more energy is induced into the boundary layer leading to lower pressure acting on the inclined surface, thereby leading to increase in drag acting on the body, as seen by comparing figure 4.22(c), (d) with figure 4.23(c), (d). From figure 4.22 and 4.23 it can be observed that as Reynolds number is increased from 500 to 800, the increase in groove width leads to contrasting effects for the pressure acting on the inclined surface. At Re=500 as width increases, pressure acting on the inclined surface increases leading to reduction in drag acting on the step, but at Re=800 the increase in width leads to a decrease in pressure acting on the inclines surface causing the drag to increase. This can be attributed to the fact that as the groove width increases, especially for FA and at higher Reynolds number, boundary layer tripping occurs, as seen in figure 4.22(d) and 4.23(d).

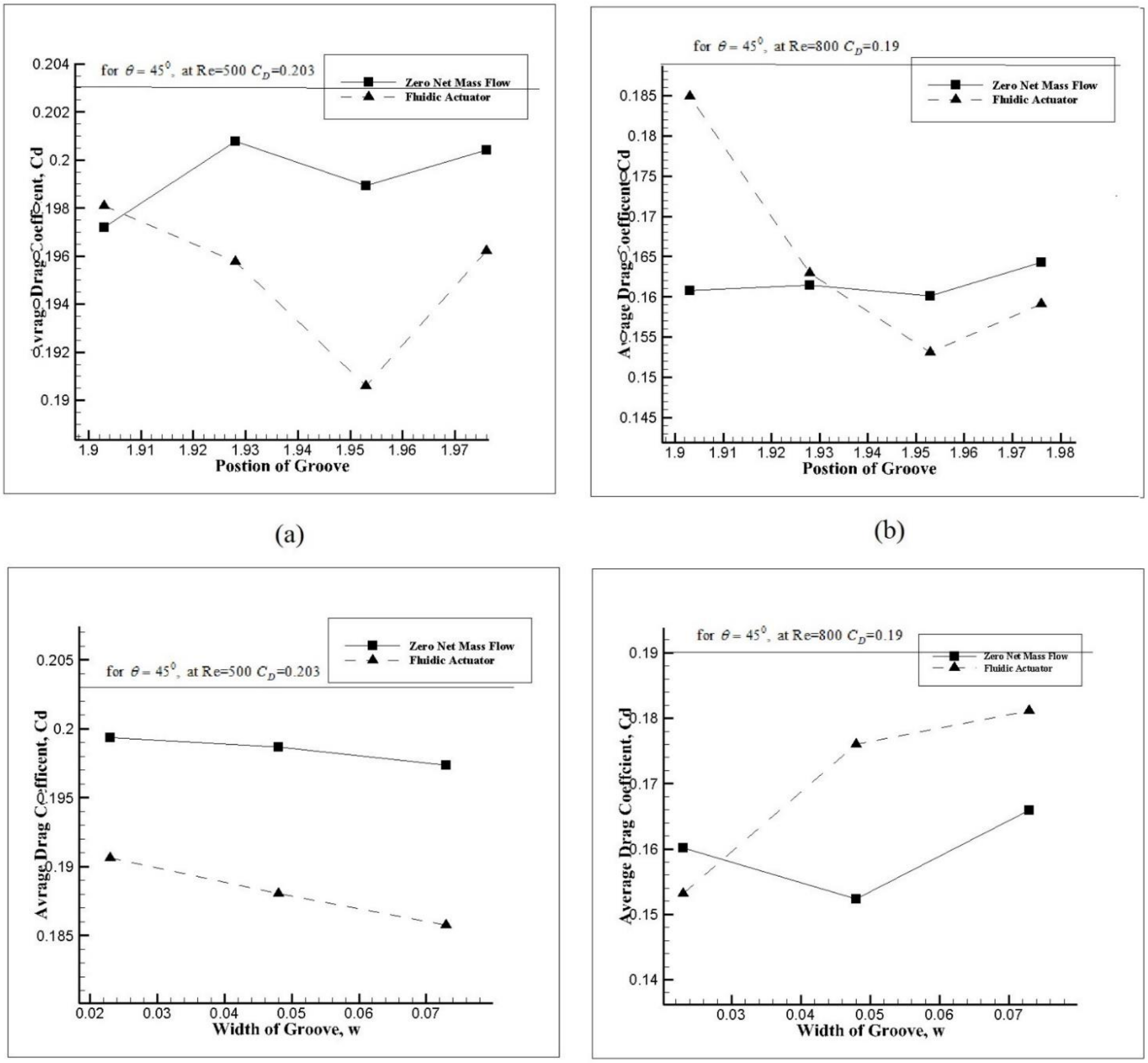

(a) (b)

(c) (d)

Figure 4.20: Average Drag coefficient versus groove position, (a) Re=500, (b) Re=800, groove width remained constant at w=0.023. Average Drag coefficient versus groove width w, groove position remained constant at x= 1.953a, (c) Re=500, (d) Re=800. For all cases, θ=45^o. At Re=500, f= 0.049 for ZNMFA and f=0.054 for FA, at Re=800, f=0.048 for ZNMFA and f=0.051 for FA.

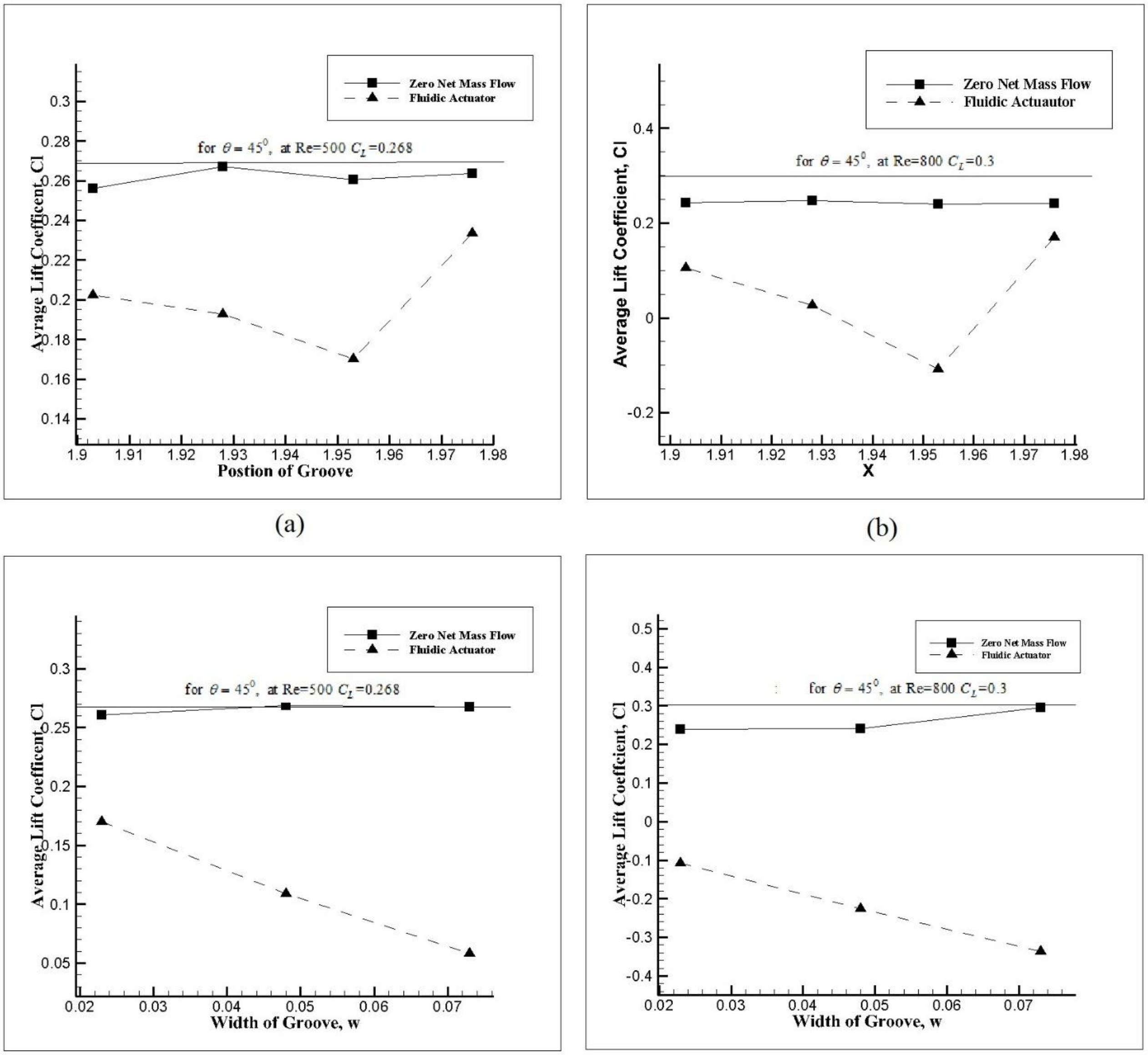

(a) (b)

(c) (d)

Figure 4.21: Average Lift coefficient versus groove position, (a) Re=500 (b) Re=800, groove width remained constant at w=0.023. Average Lift coefficient versus groove width, groove position remained constant at x= 1.953a, (c) Re=500, (d) Re=800. For all cases θ=45°, at Re=500, ZNMF configuration was f=0.049, A=0.1 and FA configuration was f=0.054, A=0.15 . At Re=800, , ZNMF configuration f=0.048, A=0.5 and FA configuration f=0.051, A=0.5 for FA.

Figure 4.21 presents the variation of lift coefficient for different groove position and width, w. The variation in lift acting on the body with respect to change in groove position and width was similar for both Reynolds numbers, as seen in figure 4.21(a), (b). In case of ZNMF technique the change in lift for different groove positions was negligible when compared to FA technique. This can be attributed to smaller variation in pressure on the upstream surface of the step as seen by comparing figure 4.22(a) with 4.22(b) and 4.23(a) with 4.23(b). From these figures it can also be seen that groove displacement has contrasting effects for the pressure acting on the upstream surface. For ZNMF, as groove is moved upstream, pressure on the upstream surface slightly decreases whereas in case FA the pressure increases. In case of FA, the optimum groove position to obtain minimum lift is x=1.953a which corresponds to maximum pressure acting on the upstream surface.

Figure 4.21(c), (d) present the variation of lift with the groove width, w. For ZNMF, regardless of the Reynolds number evaluated, a minimal variation of the lift acting on the body was observed with increase in groove width but in case of FA, lift decreased as the groove width increased. Momentum coefficient associated to FA is higher than for ZNMF, and it seems that for the groove widths evaluated, boundary layer is almost unaffected when using ZNMF. Clearly, when using FA, pressure on the upper surface, increases with groove width increase, generating a smaller lift, see figure 4.22(c), (d) and 4.23(c), (d). Notice as well that for ZNMF, the variation in pressure acting on the upstream surface is subtle, especially at Re=500.

Effects of lift coefficient at θ=65º and regardless of the Reynolds number, as seen in figure 4.25, was minor due to variation of groove position and width when ZNMFA was used as the variation in upstream pressure was observed to be negligible. Similar behavior was observed for θ=45º as seen in figure 4.21. For θ=65º and when FA was applied, it was observed that the minimum lift was obtained at groove position x=1.953a.

As mentioned in Mushyam, A. et.al. (2015), that the drag coefficient, C_D is smaller for θ=65º than θ=45º, indicating due to higher pressure acting on the inclined surface. As seen in figures 4.24 and 4.25, at θ=65º the minimum drag was obtained for a groove position of x=0.193a, at the same position as observed for θ=45º. Finally, at θ=65º, as groove width increase drag coefficient tends to decrease, independent of the Reynolds number. For Re=800 and θ=45º, as seen in figure 4.20(d), drag increases with the groove width increase. This change in tendency indicates that at θ=65º, smaller momentum coefficient leads to higher pressure on the inclined surface causing the drag coefficient to decrease.

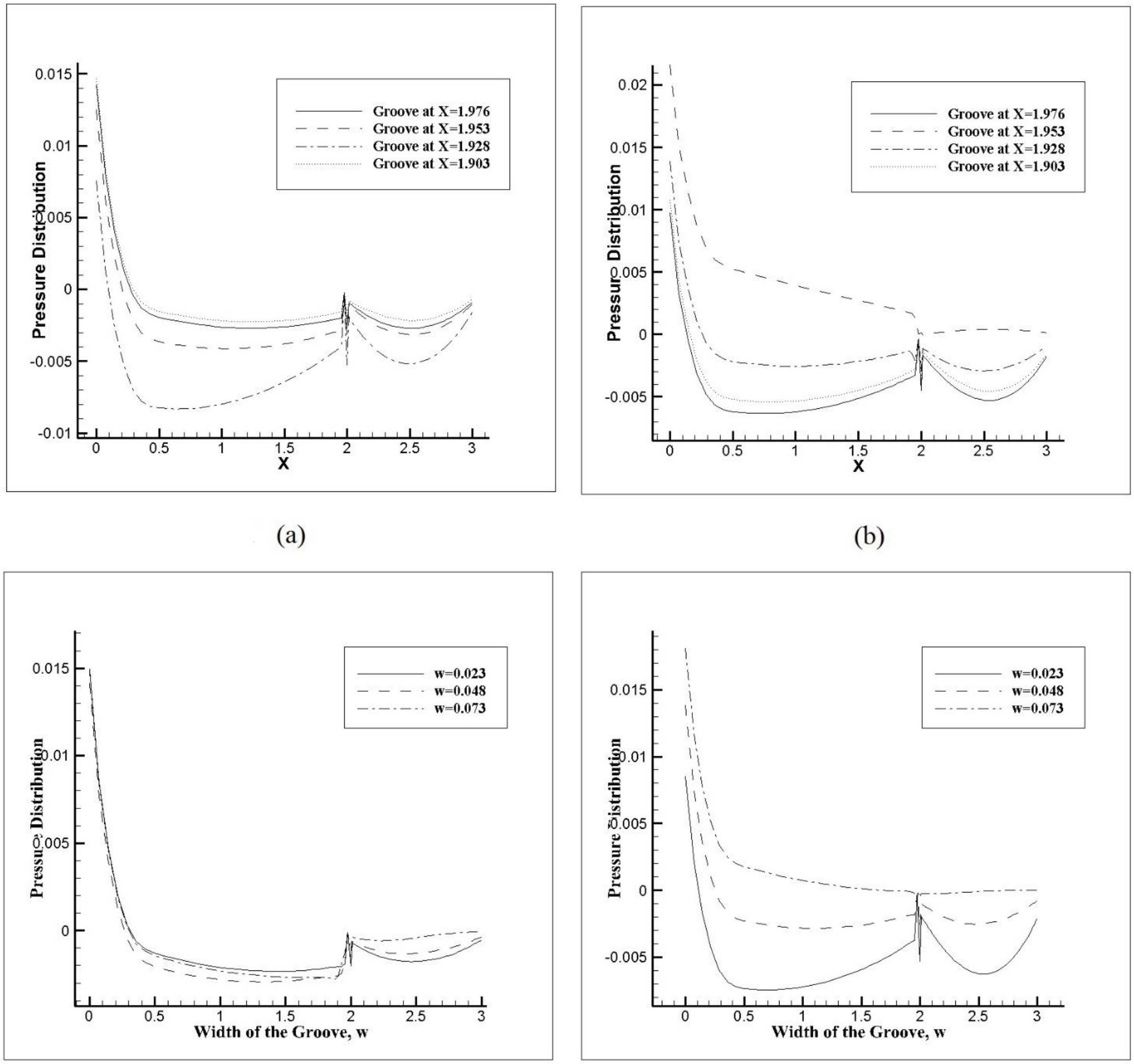

(a) (b)

(c) (d)

Figure 4.22: Instantaneous pressure distribution plots on the inclined step surface for θ=45º and Re=500. For different groove positions, groove width w=0.023, (a) Zero Net Mass Flow technique, (b) Fluidic Actuator technique. For different groove widths, groove position x=1.953a, (c) Zero Net Mass Flow technique, (d) Fluidic Actuator technique.

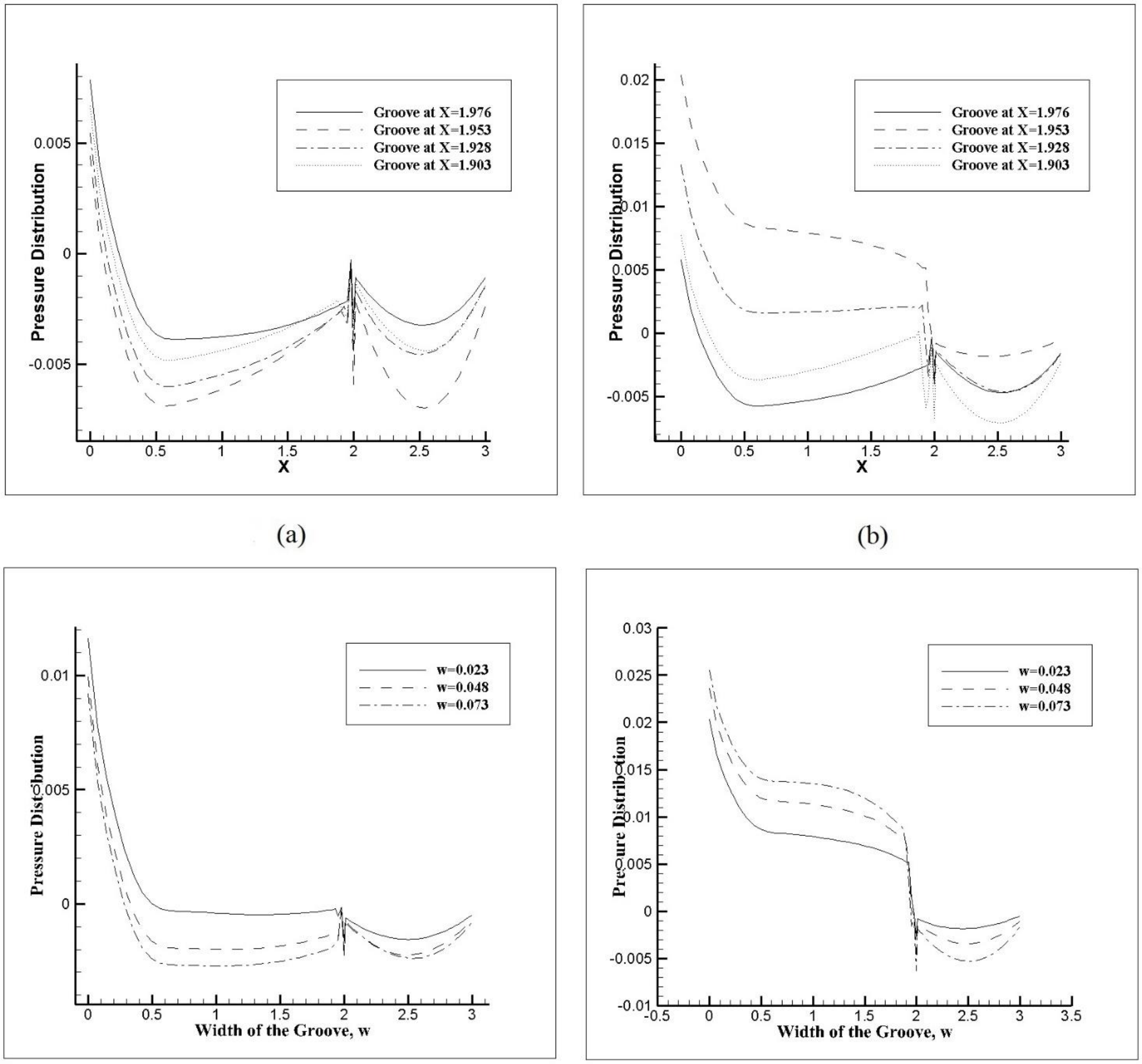

(a) (b)

(c) (d)

Figure 4.23: Instantaneous pressure distribution plots on the inclined step surface for θ=45º and Re=800. For different groove positions, groove width w=0.023, (a) Zero Net Mass Flow technique, (b) Fluidic Actuator technique. For different groove widths, groove position x=1.953a, (c) Zero Net Mass Flow technique, (d) Fluidic Actuator technique.

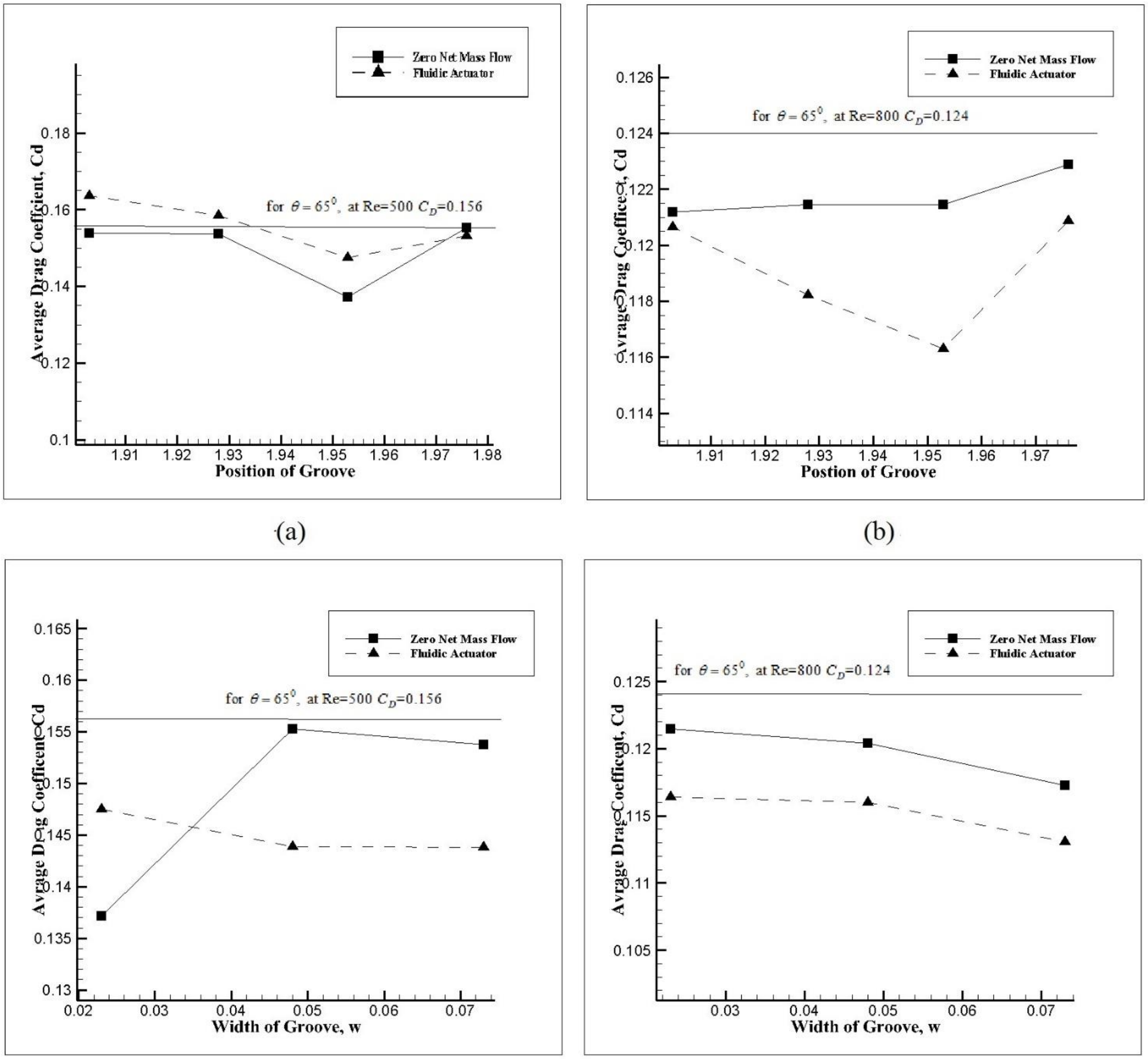

(a)

(b)

(c)

(d)

Figure 4.24: Average Drag coefficient versus groove position, (a) Re=500, (b) Re=800, groove width remained constant at w=0.023. Average Drag coefficient versus groove width w, groove position remained constant at x= 1.953a, (c) Re=500, (d) Re=800. For all cases, θ=65°. At Re=500, f= 0.045 for ZNMFA and f=0.055 for FA, at Re=800, f=0.045 for ZNMFA and f=0.049 for FA.

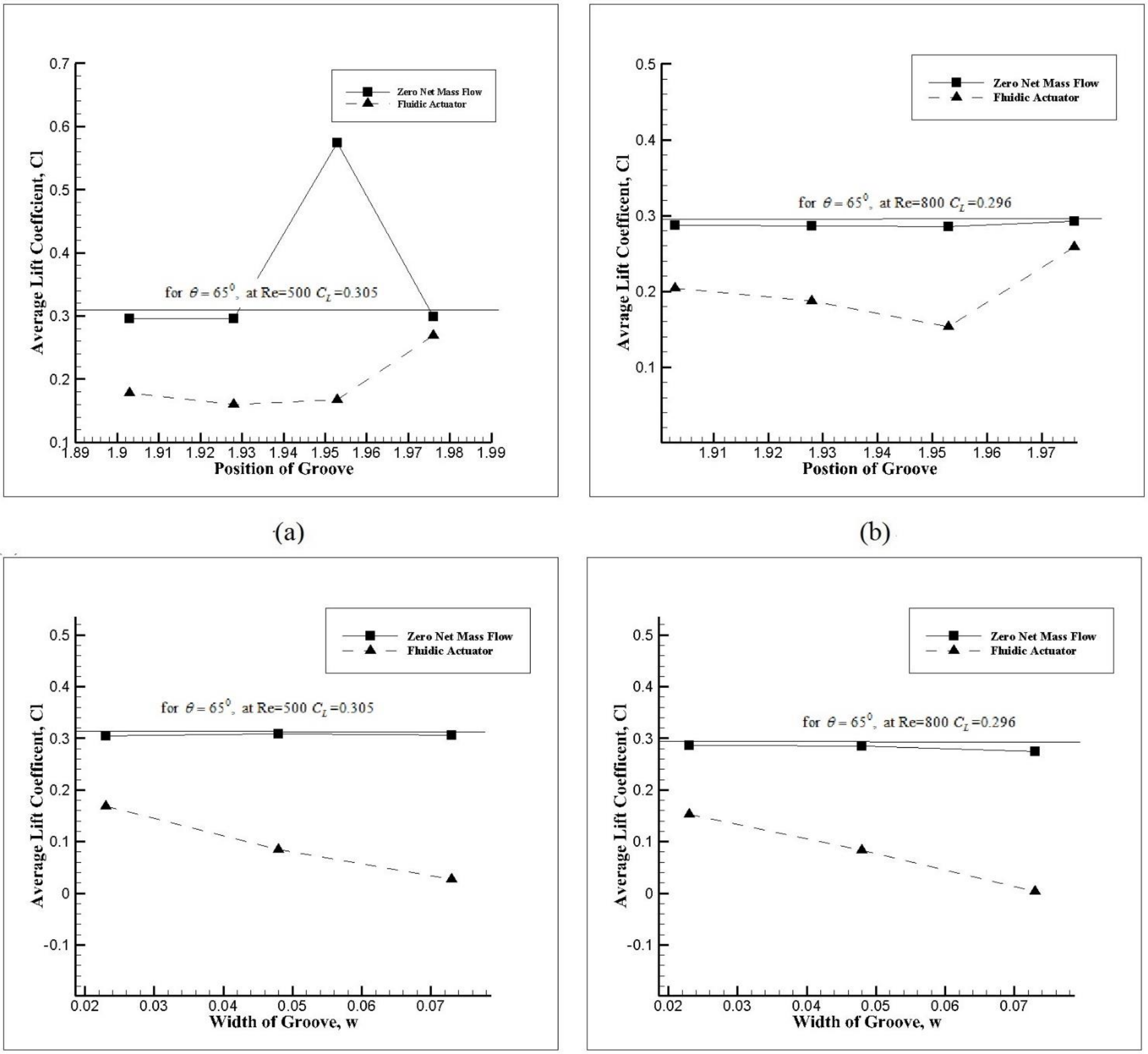

(a) (b)

(c) (d)

Figure 4.25: Average Lift coefficient versus groove position, (a) Re=500 (b) Re=800, groove width remained constant at w=0.023. Average Lift coefficient versus groove width, groove position remained constant at x= 1.953a, (c) Re=500, (d) Re=800. For all cases θ=65^o, at Re=500, ZNMF configuration was f=0.045, A=0.1 and FA configuration was f=0.055, A=0.2. At Re=800, ZNMF configuration f=0.045, A=0.12 and FA configuration f=0.049, A=0.2 for FA.

4.5. Conclusions:

- It was observed that the optimum frequency of AFC jet to influence the boundary layer, as found by previous researchers, is around the natural vortex shedding frequency.
- Fluidic actuator technique, for the cases simulated, was found to be more effective than ZNMF for drag reduction.
- Optimum groove position for drag reduction for ZNMF and in case of FA which minimizes both lift and drag, for both 45° and 65° angles of inclination was found to at x=0.1953a.
- Boundary layer separation on the upstream surface, also called as boundary layer tripping, occurred at higher amplitudes for FA.
- Downstream vorticity is deeply affected by the AFC jet forcing amplitude, especially when the boundary layer tripping occurs.
- The boundary layer at the inclined step upper corner oscillates in harmony with the AFC jet forcing frequency.
- AFC jet amplitude or the momentum coefficient was found to be the primary factor influencing the boundary layer stability on the upstream surface.
- Effects of groove width on the pressure acting on inclined surface of the step and drag acting on the body were found to be opposite at Reynolds number Re=500 and 800 for both FA and ZNMFA. At Re=500, as width increases pressure acting on the inclined surface also increase leading to decrease in drag coefficient. Whereas at Re=800, as the groove width increases leading to decrease in the pressure on inclined surface leading to an increase in drag coefficient.

References:

Anderson J.D. (1995) Computational Fluid Dynamics. McGraw Hill.

Aubrun S; McNally J; Alvi F; Kourta A. (2011). Separation flow control on a generic ground vehicle using steady microjet arrays. Exp. Fluids 51: 1177-1187.

Armaly, B. F., Durst, F., Peireira, J. C. F., Schonung, B. (1983). Experimental and theoretical investigation of backward-facing step flow. J. Fluid Mech. 127: 473– 96.

Armaly, B. F., Li A, Nie JH. (2003). Measurements in the three-dimensional laminar separated flow. Int. J. Heat and Mass Transfer. 46: 3573-3582.

Avdis A; Lardeau S; Leschziner M. (2009). Large Eddy Simulation of Separated Flow over a Two-dimensional Hump with and without Control by Means of a Synthetic Slot-jet. Flow turbulence Combust. 83: 343-370.

Chen Y.T., Nie J.H., Hsieh H.T., Sun L.J. (2006), Three-dimensional convection flow adjacent to inclined backward-facing step. Int. Journal of Heat and Mass Transfer. 49: 4795-4803.

Chowdhary H., Dhiman A., (2011). Two-Dimensional Laminar Fluid Flow and Heat Transfer over a Backward-Facing Step: Effects of Reynolds and Prandtl Numbers. Heat transfer research journal. 42, 4, 379-402

Bruneau CH; Creusé E; Depeyras D; Guilliéron P; Mortazavi I. (2012). Active and Passive Flow Control around Simplified Ground Vehicles. Journal of Applied Fluid Mechanics. 5; 1: 89-93.

Brunn A; Nitsche W. (2006). Active control of turbulent separated flows over slanted surfaces. International Journal of heat and Fluid flow. 26: 748-755.

Dandois J; Garnier E; Sagaut P. (2006). DNS/LES of active separation control. 6th International Ercofac workshop od direct Large-Eddy simulation. ERCOFAC SERIES. European research community on flow turbulence and combustion. 10: 459-466.

Dandois J; Garnier E; Sagaut P. (2007). Numerical simulation of active separation control by a synthetic jet. J. Fluid Mech. 574: 25-58.

Geropp D; Odenthal HJ. (2000). Drag reduction of motor vehicles by active flow control using the Coanda effect. Experiments in Fluids 28: 74-85.

Heinemann T; Springer M; Lienhart H; Kniesburges S; Othmer C; Becker S. (2014). Active flow control on a 1:4 car model. Exp. Fluids. 55: 1738.

Joseph P; Amadolèse X; Aider JL. (2012). Drag reduction on the 25º slant angle Ahmed reference body using pulsed jets. Exp. Fluids 52: 1169-1185.

Kumar Singh D; Bandyopadhyay G. (2012). Active Flow Control over the Car. Applied Mechanics and Materials. 110; 116: 2521-2528.

Lecrec C; Levallois E; Gallas Q; Gulliéron P; Kourta A. (2006). Phase locked analysis of a simplified car geometry wake flow control using synthetic jet. Proceedings of the FEDSM2006 ASME Joint US-European Fluids Engineering Summer Meeting. July 17-20, Miami, FL. Paper N 98469.

Lehugeur B; Gilliéron P; Ivanic T. (2006). Contribution de l'éclatement tourbillonnaire à la reduction de la trainee des véhicules automobiles: approche numérique. C.R. Mecanique 334: 368-372.

Lehugeur B; Gilliéron P; Bobillier P. (2008). Controle des structures tourbillonnaires longitudinales dans le sillage d'une géométrie simplifiée de véhicule automobile: approche expérimentale. Mécanique & Industries 9: 533-541.

Mestiri R; Ahmed-Bensoltane A; Keirsbulck L; Aloui F; Labraga L. (2014). Active flow control at the rear end of a generic car model using steady blowing. Journal of Applied Fluid Mechanics, 7; 4: 565-571.

Mushyam A., Bergada J.M., Nayeri C.N., A numerical investigation of laminar flow over a backward facing inclined step, Meccanica, doi: 10.1007/s11012-015-0335-5, online ISSN 1572-9648.

Newmann J; Wengle H. (2004). LES of controlled turbulent flow over a rounded step. Direct and Large Eddy simulation V, 557-564.

Park H; Cho J; Lee J; Lee D; Kim KH. (2013). Experimental study of synthetic jet array for aerodynamic drag reduction of a simplified car. Journal of Mechanical Science and Technology. 27; 12: 3721-3731.

Postl, D., Gross, A., Faselz, HF. (2003) Numerical investigation of low-pressure turbine blade separation control. AIAA-2003-614.

Roberts GO.(1971). Computational meshes for boundary layer problems. Proceedings of the Second International Conference on Numerical Methods and Fluid Dynamics, Lecture Notes in Physics. Springer-Verlag: New York. 8:171–177.

Rouméas M; Gilliéron P; Kourta A. (2008). Separated flows around the rear window of a simplified car geometry. J. of Fluid Engineering. ASME. Vol 130/021101-1:10

Rouméas M; Gilliéron P; Kourta A. (2009). Drag reduction by flow separation control on a car after body. Int. J. Numer. Meth. Fluids. 60: 1222-1240.

Sohankar, A., Davidson, L., Norberg, C., “Numerical simulation of unsteady flow around a square two dimensional cylinder,” 12th Australian Fluid Mechanics Conference, University of Sydney, Australia, 517-520, (1995).

Sohankar, A., Norberg, C., Davidson, L., "Low Reynolds number flow around a square cylinder at incidence: Study of blockage, onset of vortex shedding and outlet boundary condition,” Int Journal for Numerical Methods in Fluids,26, 39-56, (1998).

Sondergaard, R., Rivir, RB., Bons JP. (2002). Control of low-pressure turbine separation using vortex-generator jets. Journal of propulsion and power 18, 889-895.

Song S (2002). Reynolds number effects on a turbulent boundary layer with separation, reattachment and recovery. PhD thesis, Stanford University, USA.

5

3D flow over a Backward facing step with Active Flow Control

Abstract:
In this chapter, three dimensional flow over a backward facing step in turbulent flow regime and with application of active flow control technique (AFC) is analyzed. The turbulent flow past backward step is simulated using LES based Smagorinsky-Lilly sub-grid scale model. The motive for the present work is to study the effectiveness of active flow control in altering the ocurance and evolution of stream wise vortex in the wake of the backward step. In previous chapter two dimensional flow over Backward facing inclined step simulations with angles of inclination of 45° and 65° were carried out with application of active flow control on the upstream horizontal surface to influence the boundary layer and to analyse the effects on the downstream vortex shedding properties of the flow. Two different kinds of flow control techniques were analyzed in this study namely zero net mass flow actuators and fluidic actuators. Analysis of active flow control was carried out by varying the frequency, to study their respective effects on the flow and vortex dissipation in the wake of the step.

Nomenclature.

a	Height of the Backward step	(m)
A	Amplitude of the AFC jet	
C_D	Drag coefficient	
C_L	Lift coefficient	
C_μ	Momentum Coefficient	
C_s	Smagorinsky constant	
f	Non-dimensional frequency of AFC,	
f_v	Dimensional frequency	(H_z)
F_D	Dimensional drag force	(N)
F_f	Flux through face f of the control volume	
F_L	Dimensional lift force	(N)
h	Height of the physical domain	
$\hat{n}$	Outward normal of the surface S	
p	Non dimensional Pressure	
Re	Reynolds number	
S	Surface of the control volume	
t	Non-dimensional Time	
ul	Upstream length of the physical domain	
dl	Downstream length of the physical domain	
u	Non-dimensional Velocity Y direction	
u_{av}	Average half cycle velocity of the AFC jet	(m/s)
U	Free stream velocity in X direction at the inlet	(m/s)
v	Non-dimensional Velocity Y direction	
V_{afc}	Non-dimensional Velocity Y direction of the jet	
w	Width of the groove, non-dimensional	
W	Groove width	(m)
$\forall$	Control Volume	(m^3)

x	Non-Dimensional Eulerian coordinates in horizontal direction	
x_p	Dimensional horizontal coordinate of the physical domain	(m)
y	Non-Dimensional Eulerian coordinates in vertical direction	
y_p	Dimensional vertical coordinate of the physical domain	(m)
ρ	Fluid density	(Kg/m^3)
ρ_{jet}	Actuating jet density	(Kg/m^3)
Ψ	Additional default amplitude of the AFC jet	

Abbreviations.

AFC	Active flow control
ZNMF	Zero net mass flow
FA	Fluidic Actuator

5.1. Introduction.

The use of Active Flow Control (AFC) applied to ground vehicles has to be regarded as a new technology. So far, the expectations of enhancing aerodynamic performance, usually decreasing drag force, have been validated by many researchers, yet, the technology is far from being fully understood and ready to be implemented in real vehicles. Important parameters like, the most adequate location or locations of the (AFC) devices, the groove width or output jet diameters, the jet inclination angle, the actuating jet configuration, whether constant blowing, constant suction, pulsating jets with zero net mass flow, pulsating jets with positive mass flow, the amplitude, frequency and momentum coefficient associated to pulsating jets and the ratio jet velocity versus incoming flow velocity for constant blowing jets, are among the parameters which need to be evaluated for any given application.

The vast majority of the studies undertaken using (AFC) were two dimensional, some examples are, Suzuki (2006), Dandois et al (2007), Chabert et al (2014), Avdis et al (2009), Newmann and Wengle (2004) and Cerretelli and Kirtley (2009). In Suzuki, Avdis et al and Cerretelli and Kirtley, flow over a hump was evaluated, pulsating actuation was employed in the three cases, Sukuki considered the actuator position obtaining the optimum position to minimize downstream vortex shedding, fluid injection was always perpendicular to the surface, Avdis et al and Cerretelli and Kirtley injected fluid almost tangential to the surface. It was observed that unsteady blowing drastically reduced the momentum required, particularly when the non-dimensional frequency employed was close to the flapping instability of the shear layer. Dandois et al (2007), Newman and Wengle (2004) and Chabert et al (2014), focused their work in understanding the flow over a rounded ramp, having closed similarities with the previous studies. The first two papers were numerical, respectively, the turbulence models and Reynolds numbers were, DNS/LES at Reynolds 28275 and LES at

Re=9100, Chabert et al paper was experimental and they evaluated the flow at Re = $2*10^6$. As many previous authors, they observed that using periodic forcing is more effective since it acts on the natural instabilities of the flow.

Very recently, researchers have focused on studypaping the effect of using (AFC) on three dimensional Ahmed bodies. In reality, the majority of the papers were experimental, some good examples are Aubrun et al (2011) and Joseph et al (2012), in both cases a 25º slanted angle Ahmed body was studied, several Reynolds numbers of the order of $1.4*10^6$ as well as several momentum coefficients and Strouhal numbers, for the second case, were considered, different (AFC) geometric configurations were evaluated. Joseph et al observed that optimum actuation frequencies were closed to the shear layer natural frequency, when grooves were located slightly downstream of the separated point, and they were about two times the shear layer natural frequency when grooves were located upstream. They observed that the wake was fully three dimensional, the three dimensionality was concentrated in the shear flow region, were absolute and convective instabilities exists, as reported among others by Cherry et al (1984). In reality, it is generally understood as 3D effects over an Ahmed body, when the lateral vortices are included in the equation, such lateral vortices were indeed studied experimentally by Lehugeur et al (2008), Kourta and Leclerc (2013), Krentel et al (2010), Mestiri et al (2014), Park et al (2013), Tounsi et al (2016), and numerically by Rouméas et al (2008), (2009), Bruneau et al (2012), Lehugeur et al (2006), Lehugeur and Gilliéron (2006), Krajnovic and Basara (2010). In most of these studies lateral vortices were tried to minimize via using Active flow actuation located along the two lateral slanted edges, see for example, Lehugeur et al (2006) (2008), Lehugeur and Gilliéron (2006), Bruneau et al (2012), Mestiri et al (2014), Park (2013). In some other cases, lateral vortices were modified using groves located at the slanted surface upper edges, see Krajnovic and Basara (2010), Rouméas et al (2009). Blowing, suction, a combination of both or even periodic forcing, was employed in the different studies, despite of the actuation strategy used, in any of the researches presented it was possible to get rid of the lateral vortices, usually it was possible to modify the lateral vortices inclination angle or reducing its strength, but preventing it from appearing has not yet been achieved. Typical drag reductions of about 10% were often obtained. When employing constant suction or blowing, typical velocity ratios of $(u/U_\infty) = 0.6$ were used, but especially when performing experimental studies, velocity ratios above 2 were often used, Aubrun et al (2011). When using periodic forcing, momentum coefficients typically employed, ranged between $0.5*10^{-4}$ to almost 0.1, smaller momentum coefficients were required if the actuation slot was placed near the shear layer separation point. In fact, the effectiveness of the (AFC) application directly depends on two main parameters, the slot position, and momentum coefficient, or velocity ratio when constant actuations is used. Actuating frequency, although important, has a secondary effect on the downstream vortex shedding. Actuating jet inclination angle employed in the vast majority of the cases is of 90º, perpendicular to the suface. As a conclusion, it can be stated that Ahmed body three dimensional structures, although known, it is very difficult to completely dissipate them, (AFC) can simply reduce vortices intensity, delay the separation region, displace the vortices downstream, modify lateral vortices inclination angle or a combination of the previous modifications. It appears as if a combination of active and passive flow control should be the final solution if drag coefficient is to be drastically reduced.

When studying three dimensional structures at the rear of a bluff body, another important case which resembles a vehicle rear is the so called the square back Ahmed body, having many similarities to the rear of a lorry. As in the previous cases presented, not many papers have considered this geometry and considering the implementation of active flow control devices on it. Some of the most relevant papers in this field are: Parkin et al (2014), Bruneau et al (2010; 2012-2014), Krajnovic and Fernandes (2011), Rouméas et al (2006, 2009), Krentel and Nitsche (2013). It is to be noticed that all these papers except the last one are numerical. Parkin et al, used LES to evaluate the flow at Re=23000, four actuation slots were located at the vehicle rear, upper and lower edges, two slots were allocated at the upper and lower horizontal surfaces, and the other two were allocated at the vertical wall, all slots injected fluid perpendicular to the respective walls. Maximum drag reduction was obtained when all slots were employed, momentum coefficients used ranged between 0.002 and 0.016 and optimum Strouhal numbers ranged between 0.09 and 0.135, these Strouhal numbers were approximately half of the strouhal number associated to the natural vortex shedding case. Krajnovic and Fernandes (2011) also employed LES to simulate the flow at Reynolds 2000 and 20000, three different slot configurations were evaluated, one of them similar to the one employed by Parkin et al. In this case nevertheless, flow was injected at an angle of 45° versus the body surface. Zero net mass flow actuators were employed obtaining the optimum performance for a momentum coefficient of 0.015 and a strouhal number of 0.17. From all groove configurations studied, the most effective one was the one Parkin et al also used. Rouméas et al (2006, 2009), presented a 3D numerical simulation of a square back Ahmed body based on the Lattice Boltzmann Method. They located blowing devices around the entire square back periphery, constant blowing was employed, the jet was injected at an angle of 45° versus the body surface and velocity ratios used ranged between $(u/U_\infty) = 0.5$ and 1.5, the Reynolds number evaluated, based on the body length, was $2.8*10^6$. In Bruneau et al research (2010; 2012-2014), two different Reynolds numbers of 30000 and 8276 were numerically evaluated, three different slot positions located at the rear vertical side were studied, periodic blowing as well as passive control using porous layers were tested separately, the combination of both, active and passive control methodologies was also analysed. The results demonstrated that coupling passive and active flow control was the optimum solution, obtaining a drag coefficient decrease of 31%. When just the active actuation was employed, maximum drag reductions of 21% were obtained when using velocity ratios of $(u/U_\infty) = 0.6$ and 0.9, the corresponding momentum coefficients were $8*10^{-3}$ and $1.8*10^{-2}$. Synthetic jets were used. The results they obtained agreed well with what was obtained by Rouméas et al (2009), although the Reynolds number was $2.8*10^6$. One of the latest experimental investigations on square back Ahmed bodies, is the one undertaken by Krentel and Nitsche (2013), two different incoming flow angles versus the Ahmed body central axis of 0 and 15° were used. Active actuating devices were positioned around the rear perimeter, as in the case of Rouméas et al (2006, 2009), two jet inclination angles of 0 and 45° versus the rear vertical wall were checked, the optimum momentum coefficient for each angle was respectively $2.3*10^{-3}$ and $4.7*10^{-4}$, the optimal Strouhal number was 0.17. They observed that for the optimal forcing parameters, the shear layer was characterized by a decrease in turbulent momentum flux, as a result, the momentum transfer from the outer flow into the recirculation region, increased.

5.2. Problem Statement.

5.2.1 Physical domain

Figure 5.1 presents the physical domain of the backward step geometry inside a channel. Flow over a backward facing step with upstream length, ul=2a and downstream length, dl=20a. Flow over the step was simulated in 3D in turbulent regime using LES turbulence modeling, at Reynolds number Re=3200 to 1024000. No slip boundary condition was used at all solid boundaries. As the flow is unconstrained at the top, free slip boundary conditions was used at the top, which was located at a distance of 8a, according to Sohankar et al. (1995). In order to simulate a far field downstream boundary, Neumann boundary condition was used at the outlet, the outlet boundary was located at a distance of 20a downstream of the inclined step lower vertex, as suggested by Sohankar et al. (1998).

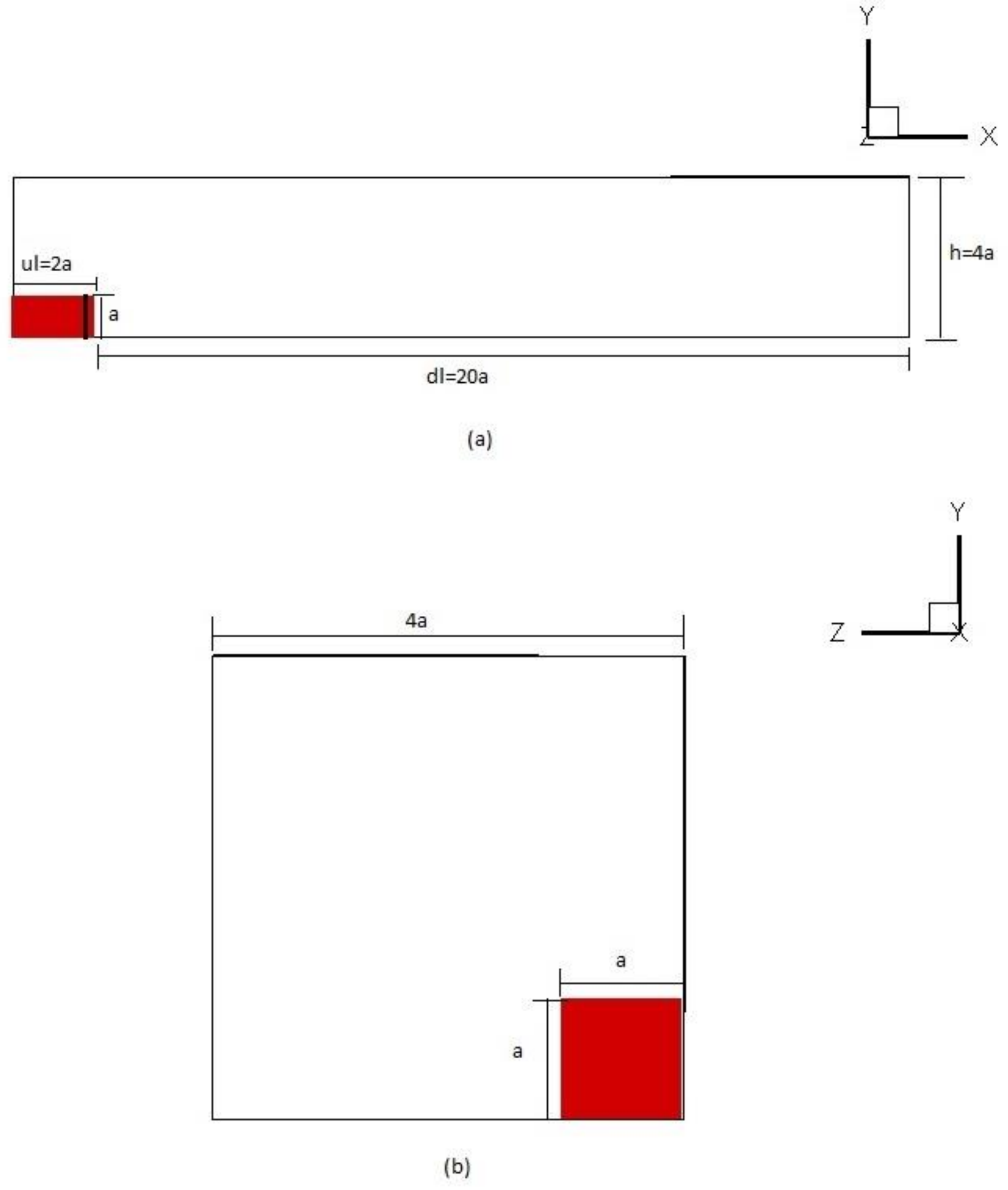

(a)

(b)

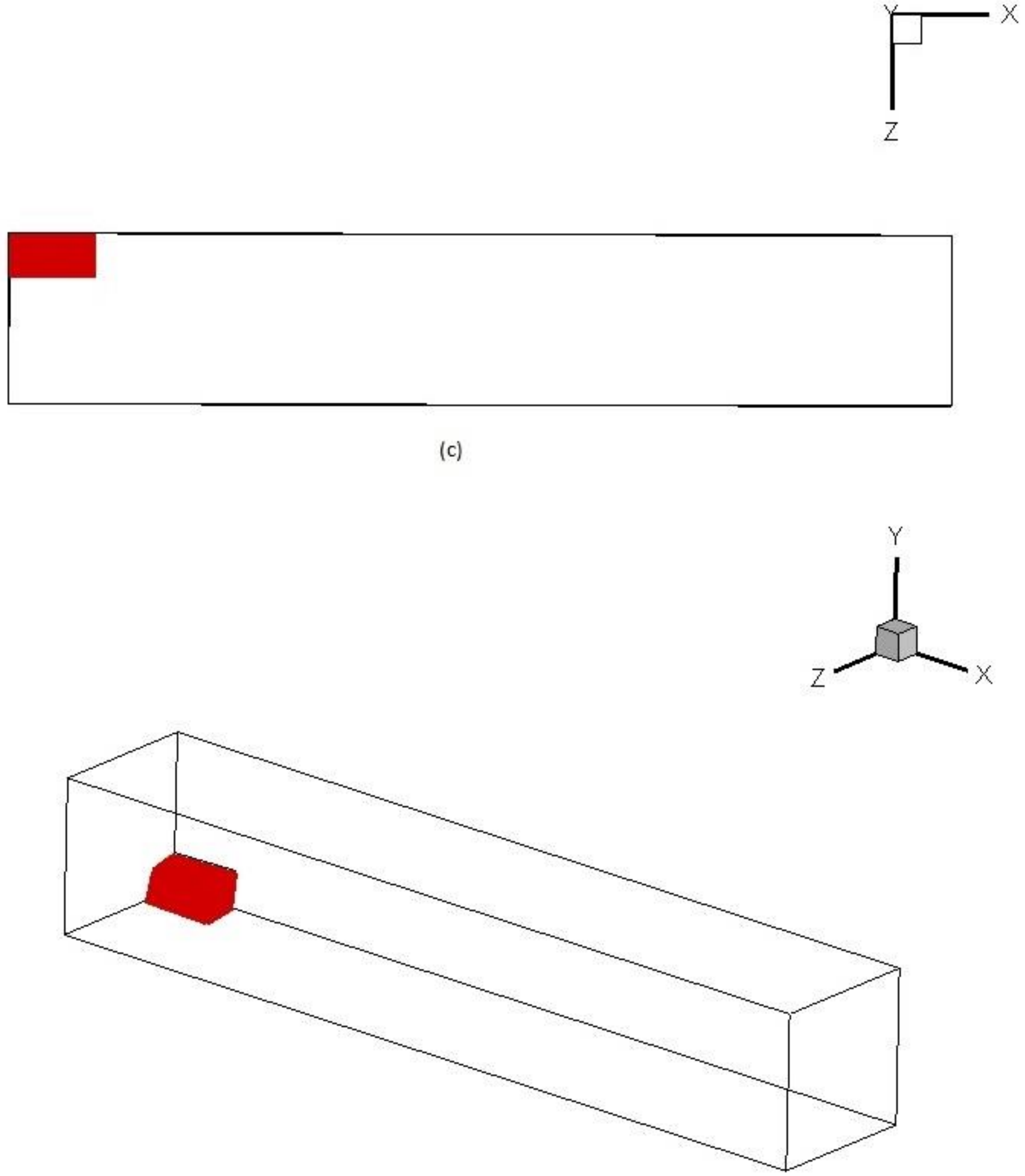

(c)

(d)

Figure 5.1: Physical Domain of the Inclined Step (a)Side View (b) Front View (c) Top View and (d) 3D view of the Backward step enclosed in a channel.

Figures 5.2(a), (b), present the grid of the proposed problem. An orthogonal non-uniform structured grid was chosen, since it is most appropriate to simulate the flow dynamics. Figure 5.2a, shows the three sub-domains of the grid. The first sub domain is the region over the upstream surface of the inclined step. Second sub-domain is located on the right side of the backward step. The region over the second sub-domain and on the right side of the first sub-domain is the third sub-domain. Structured grid has been generated in the three sub-domains using the stretching transformation proposed by Roberts (1971), which refines the grid in the vicinity of the solid walls.

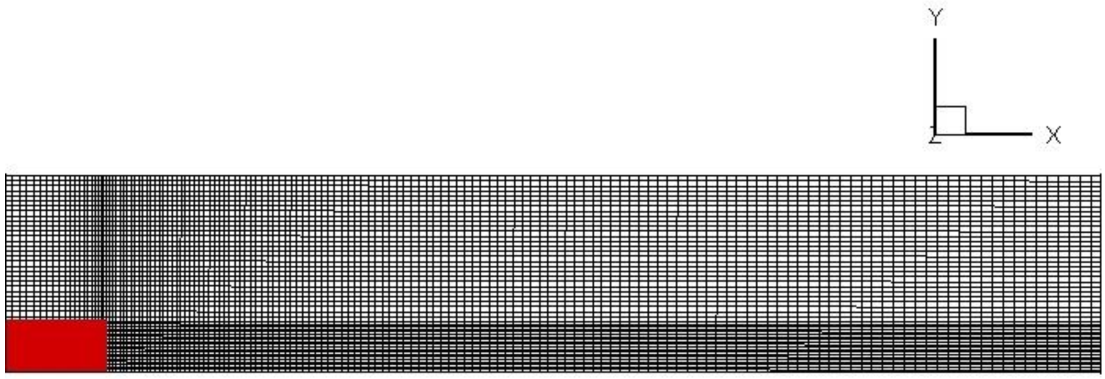

(a)

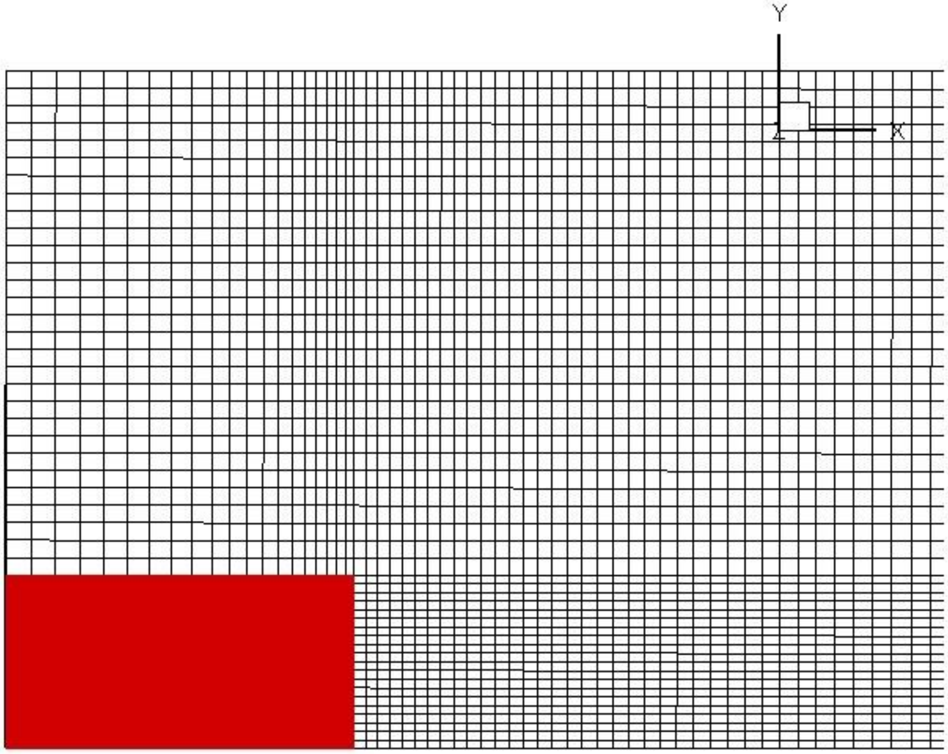

(b)

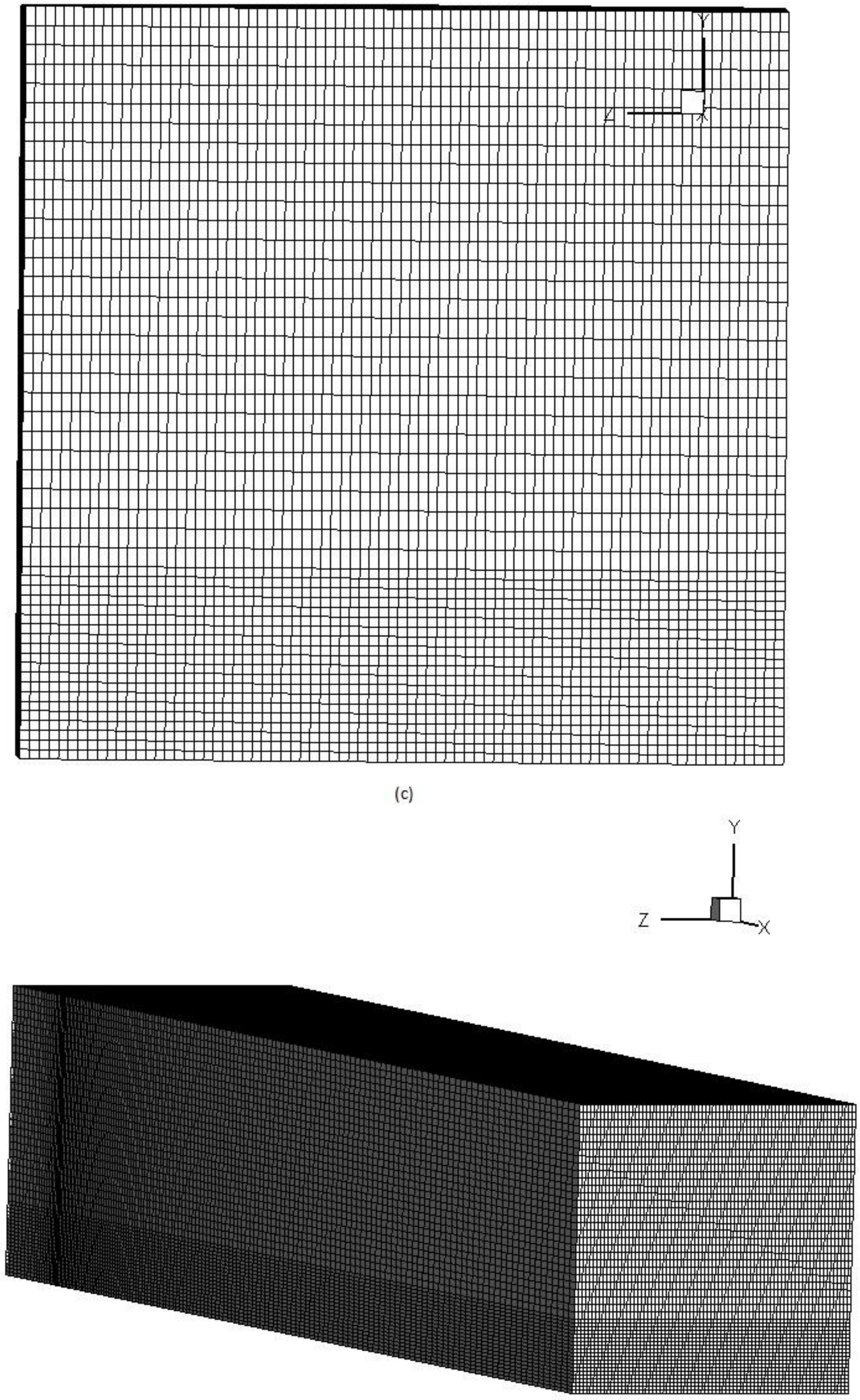

(c)

(d)

Figure: 5.2 Non uniform structured grid for discretization of the domain. (a) Side view (b) Closer side view of the grid point collocation at the wall of the step for accurate resolution of the boundary layer (c) Front view (d) 3D view of grid enclosing physical domain

Simulations were performed using two different types of active flow control techniques, zero net mass flow and fluidic actuators. Two different non-dimensional frequencies, f = 0.055 and 0,065 and non-dimensional velocity amplitude A=0.1 was used for both the flow control techniques at Re=512000 and 1024000. The grove was placed at (x =1.953, z = 1) as seen in figure 5.1 (a). These studies were carried out to understand the effects of the active flow control techniques on the horizontal surface boundary layer development, stream wise vortex and the subsequent downstream flow.

5.2.2 Governing Equations.

Smagorinsky-Lilly Large Eddy Simulation (LES) model was used to model turbulent flow over the backward step. The momentum and continuity equations for subgrid-scale turbulent model are presented as:

$$\frac{\partial u_i}{\partial t} + u_j \frac{\partial u_i}{\partial x_j} = -\frac{1}{\rho}\frac{\partial p}{\partial x_i} + \frac{\partial}{\partial x_j}\left((\nu + \nu_t)\frac{\partial u_i}{\partial x_j} \right) \tag{5.1}$$

$$\frac{\partial u_i}{\partial x_i} = 0 \tag{5.2}$$

Where ν_t is the subgrid-scale turbulent viscosity. The smagorinsky model can be summarized as below:

$$\tau_{ij} - \frac{1}{3}\tau_{kk}\partial_{ij} = -2\mu_t \overline{S}_{ij} \tag{5.3}$$

$$\mu_t = \rho (C_s \Delta)^2 \left| \overline{S} \right| \tag{5.4}$$

Where the filter width $\Delta = (volume)^{\frac{1}{3}}$ and where $\overline{S}_{ij}$ is the rate of strain tensor for the resolved scale defined by

$$\overline{S}_{ij} = \frac{1}{2}\left(\frac{\partial u_i}{\partial x_j} + \frac{\partial u_j}{\partial x_i} \right) \tag{5.5}$$

$$\left| \overline{S} \right| = \sqrt{2 \overline{S}_{ij} \overline{S}_{ij}} \tag{5.6}$$

C_s is smagorinsky constant with value ranging from 0.1 to 0.2. The finite volume approach was chosen for the simulation.

Simulations have been carried out with non-dimensional form of Navier-Stokes equations. To non-dimensionalize the equations, the height of the step, a, was taken as the characteristic length, the free stream velocity U, was taken as the characteristic velocity, the characteristic pressure was ρU^2 and the characteristic time was defined as the characteristic length divided by the characteristic velocity a/U. Reynolds number was defined as $\mathrm{Re} = \frac{\rho U a}{\mu}$. The fluid was considered incompressible and viscosity was taken as constant. Flow was considered as isothermal.

5.2.3 Numerical Strategy and Boundary Conditions.

A second-order Adams Bashforth-Crank Nicholson scheme for temporal discretization was applied to Navier Stokes equations in finite volume formulation to obtain equation is the continuity equation applied over a control volume. The consequent system of equations were solved by using the bi-conjugate gradient stabilized method.

A brief description boundary conditions used in the simulation at various boundaries follows.

At the inlet, uniform free stream condition for velocity and Neumann boundary condition for pressure were used.

$$u = U, \quad v = 0, \quad \frac{\partial p}{\partial x} = 0 \tag{5.7}$$

In all solid boundaries, no-slip boundary condition for velocity and normal gradient condition for pressure was employed.

$$u = 0, v = 0 \text{ and } \nabla p.\hat{n} = 0 \tag{5.8}$$

Where $\hat{n}$ is the unit normal vector perpendicular to the surface.

The outlet boundary, right side of figure 5.1(a), posed the biggest difficulty in computational modeling, especially when studying flows with unsteady wake or convecting vortices. The definition of this boundary condition is of paramount importance, since it not only changes the flow pattern but also affects convergence. For the present case the derivative of all dependent variables was taken equal to zero, which is known as Neumann Boundary Condition (NBC), condition presented in equation (5.9).

$$\frac{\partial \phi}{\partial x} = 0, \quad \phi = u, v, p; \tag{5.9}$$

The distance between the inclined step bottom edge and outlet boundary, where the Newman boundary condition is applied, was considered as 20a as seen in figure 5.1.

MAC (Marker and Cell) method with velocity and pressure coupling was applied using a predictor-corrector strategy. In the present study, the respective pressure correction factor in all the neighboring cells were also considered, notice that this is a further improvement with respect to the original MAC method and minimizes the error involved in the calculation. In this method the momentum equations are solved to calculate provisional values for the velocity components for the next time step using the predictor step and thereafter calculating the pressure and velocity correction factors for achieving the incompressibility condition of mass conservation.

5.2.4 Zero-net mass flow control technique.

In this technique the flow control is induced into the flow upstream of the step in such a way that the net mass flow from the groove is zero. A sinusoidal form of wave equation was used to induce the active flow control technique as presented in equation 5.10.

$$u=0$$

$$v=A.\sin(2\pi f t) \tag{5.10}$$

Where u and v are respectively the non-dimensional horizontal x-component and vertical y-component of fluid velocity, f is the non-dimensional frequency of the active flow control jet and t is the non-dimensional time. A is the non-dimensional velocity amplitude of the oscillating jet $A=V_{jet}/U$.

5.2.5 Fluidic Actuator flow control technique.

In fluidic actuators, the flow control is induced into the flow upstream of the step in such a way that the net mass flow from the groove is outwards. This is applied by inducing a default amplitude Ψ added to the sinusoidal form of wave equation used in zero net mass flow technique as presented in equation (5.11).

$$u=0$$

$$v= \Psi +A.\sin(2\pi ft) \tag{5.11}$$

Where Ψ is the additional default non-dimensional velocity amplitude, in the present study the default amplitude Ψ was considered equal to the amplitude A of the jet, so that the minimum velocity of the injected jet is zero.

The primary difference between zero net mass flow and fluidic actuator techniques is that, in case of former the fluid is injected and absorbed into the upstream boundary layer, but in case of fluidic actuator the fluid is only injected. In both cases the fluid is injected perpendicular to the upstream surface, since as mentioned in Sondergaad et al (2002) and Postl et al (2003), perpendicular forcing is most effective.

5.3. Results and Discussion.

This section is divided into two parts, initially the unsteady flow dynamics of 3D flow over an inclined step with flow on the side of the step is analyzed is analyzed with the help of streamline, Swirl and vorticity plots at various Reynolds numbers ranging from Re=3200 to 1024000. Secondly, flow over a backward step with incorporation of AFC technique in a groove positioned on the side of the step is analyzed and presented with average lift and drag coefficients as a function of AFC frequency.

5.3.1 3D Flow over a Backward Step.

In order to visualize unsteady turbulent flow over a backward step, in the present section simulations from Reynolds number, Re=3200 to 1024000 are presented in figure 5.3 to 5.14, with the help of instantaneous streamlines, swirl and vorticity contour plots. In this section the all the flow cases presented are without application of AFC, while in the next section presents the flow with AFC techniques applied to the side to the backward step. In all cases, an upstream length, ul=2a was considered. The flow remains turbulent at these Reynolds numbers, since as determined by Armaly et al (1983) the flow over an inclined step is laminar whenever Reynolds number is below 1200.

The onset of span wise vortex in case of the backward facing step, occurs due to interaction of the shear layers generated at the edge of the top and side surfaces of the step as observed in figures 5.1 (a) and (c) respectively. The shear layers generated when the flow separated from the surface at the edge of the step interact with each other behind the rear surface of the step in the wake leading to the evolution of the span wise vortex. The rolling up shear layer is also seen to be formed due to the interaction between the growing span-wise vortex in the wake of the step and the solid boundary located below the vortex. As the rolling up shear layer develops, its intensity increases, causing the entrainment of the rolling up shear layer into the core of the growing recirculating span-wise vortex at the rear of the backward step, which leads to the dissipation of the vortex from the neck and it is consequently shed into the wake of the step.This mechanism is different from the shedding mechanism in case of generic bluff body, where vortex shedding occurs due to the flapping motion of the upper and lower vortices appearing at the body trailing edge, vortices shed alternately into the wake.

Figure 5.3 and 5.4 present the flow over a backward step at Re = 3200. From figure 5.3(a) a recirculating region is seen immediately behind the rear face of the step. The recirculating region is formed due to the interaction of the fluid from the top and side surfaces of the step immediately after the rear face of the step. It was also observed that this recirculating region behind the backward step grows in size with time and until reaching a saturation point. This phenomena was observed at all Reynolds numbers from Re=3200 to 1024000 and the length of the recirculating region increases with Reynolds number as seen from figures 5.3(a), 5.5(a)to 5.12(a). The boundary layers on the top and side surfaces of the step were found to be stable. Two types of inviscid critical points, namely ‘center’ and ‘saddle’ can be seen from the figure 5.3(c). A critical point is a location where slope of streamline becomes indefinite; the point of zero velocity is referred to as the ‘center’ while the point where two streamlines running in opposite direction touch each other is referred to as the ‘saddle’. From the present study it was observed that the saddle point is shed in wake downstream of the step with dissipation of the stream-wise vortex. Figure 5.3(b) presents the streamline plot indicating development of swirling motion of fluid in the wake of the step. This can also be seen in figure 5.3(c) and (d) in swirl contour and vector plots but the Reynolds number of the flow appears to be inadequate for the evolution and development of the span-wise vortex due to the interaction of the fluid from the top and side of the backward step due to lower kinetic energy of the flow. The development of the rolling up shear layer can be clearly seen in figure 5.3 (c) along with the velocity vector indicating the direction of flow in that plane and its interaction with the swirling motion of the fluid in the wake of the step.

Figure 5.4 (d) presents the instantaneous streamline plot of the flow in the wake of the step with embedded swirl indicating the intensity of the flow at various position in the wake of the step. The rolling up shear layer formed due to the swirling motion of the fluid in the wake of the step, moves into the growing span-wise vortex in the wake only to be dissipated downstream in the form of vortical structure. Figure 5.4(a) shows the Iso-surface plots of swirl contour in the wake of the step and 5.4(b) presents the close up view of the wake pattern in the immediate vicinity of the rear of the backward step with streamlines indicating the pattern of the fluid interaction from the top and side of the backward step at Re=3200. Similar wake and vortex dissipating patterns were observed for Reynolds number ranging rom Re=3200 and 1024000, emphasizing the global nature of the flow.

From quantitative observations of simulations, it was also found that as the flow at Re=3200 is more organized whereas flow at Re=102400 was found to be more disorganized, with random span-wise vortex dissipation in the wake. It indicates that, apart from larger recirculating region behind the rear face of the backward step, flow in more disorganized and with increased random dissipation in the wake with increase in Reynolds number. This is attributed to the fact that as Reynolds number increases, the kinetic energy associated to each fluid particle also increases and momentum interchange between particles increases, leading to a quicker and higher disorganized vortex dissipation.

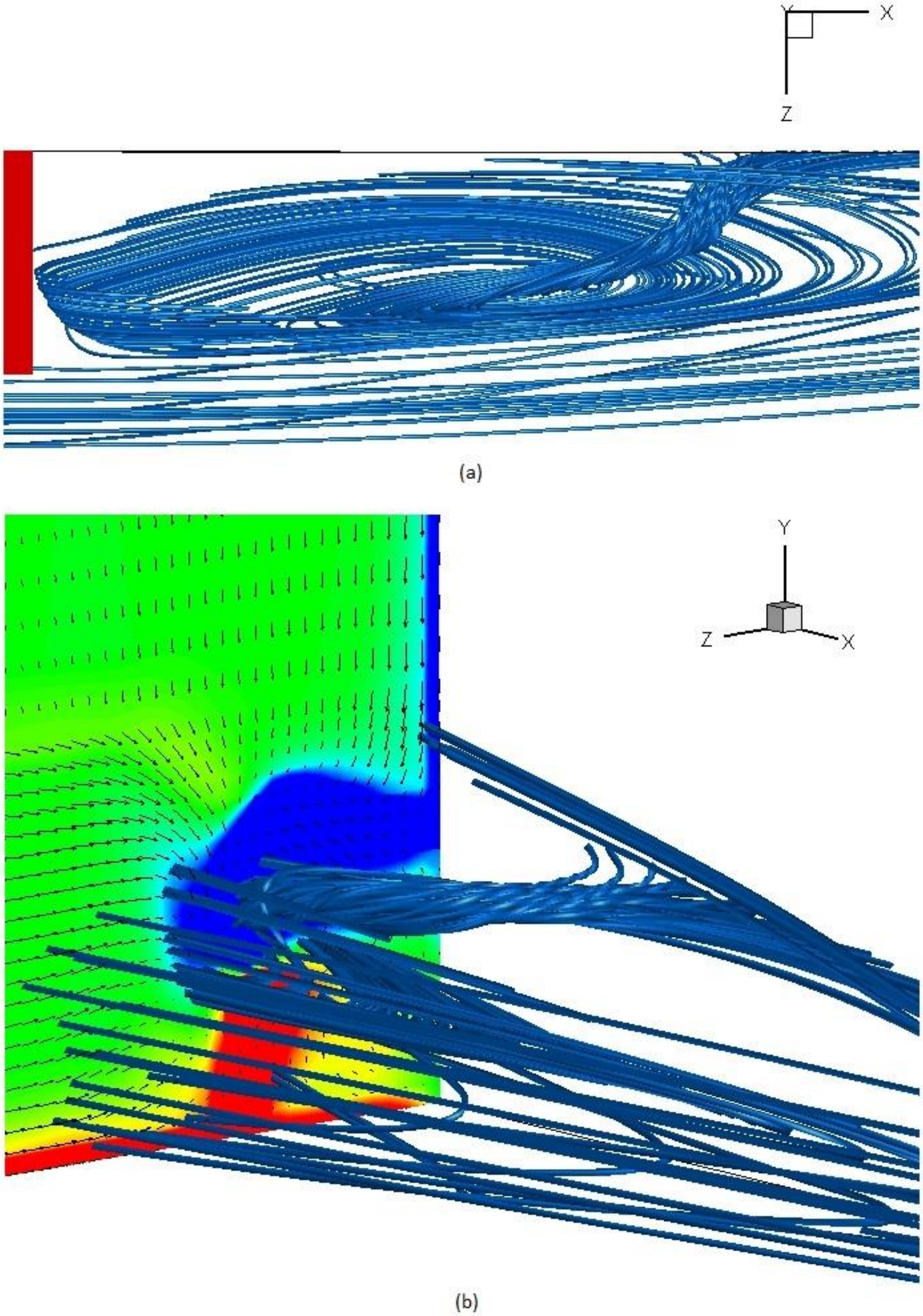

Figure 5.3: Streamline plots of flow over backward step at Re=3200 (a) Top View (b) Side View

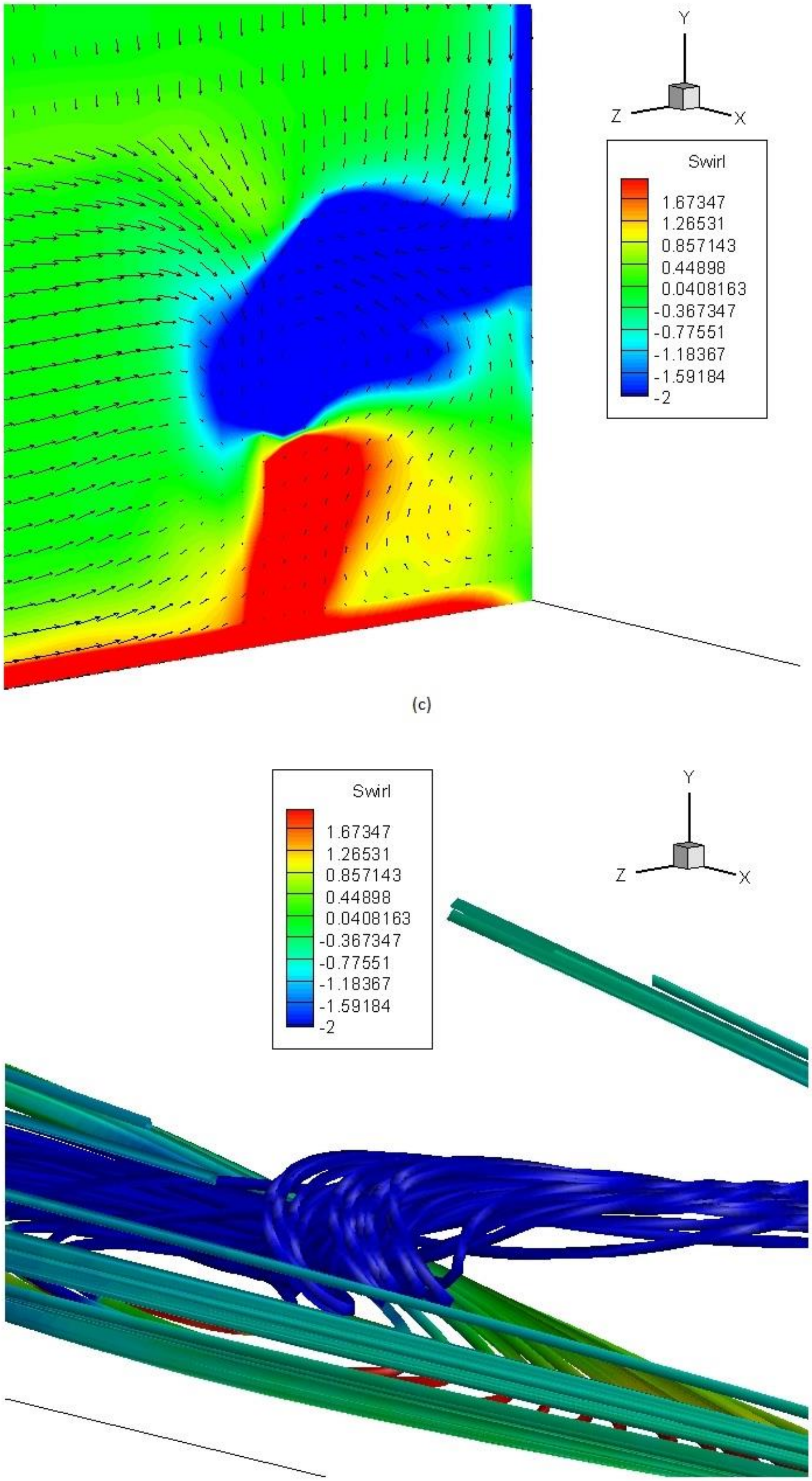

(c)

(d)

Figure 5.3: Side View of flow over backward step at Re=3200 (c) Instantaneous swirl contour plot with velocity vectors on YZ plane (d) Corresponding Streamline plot with swirl contour

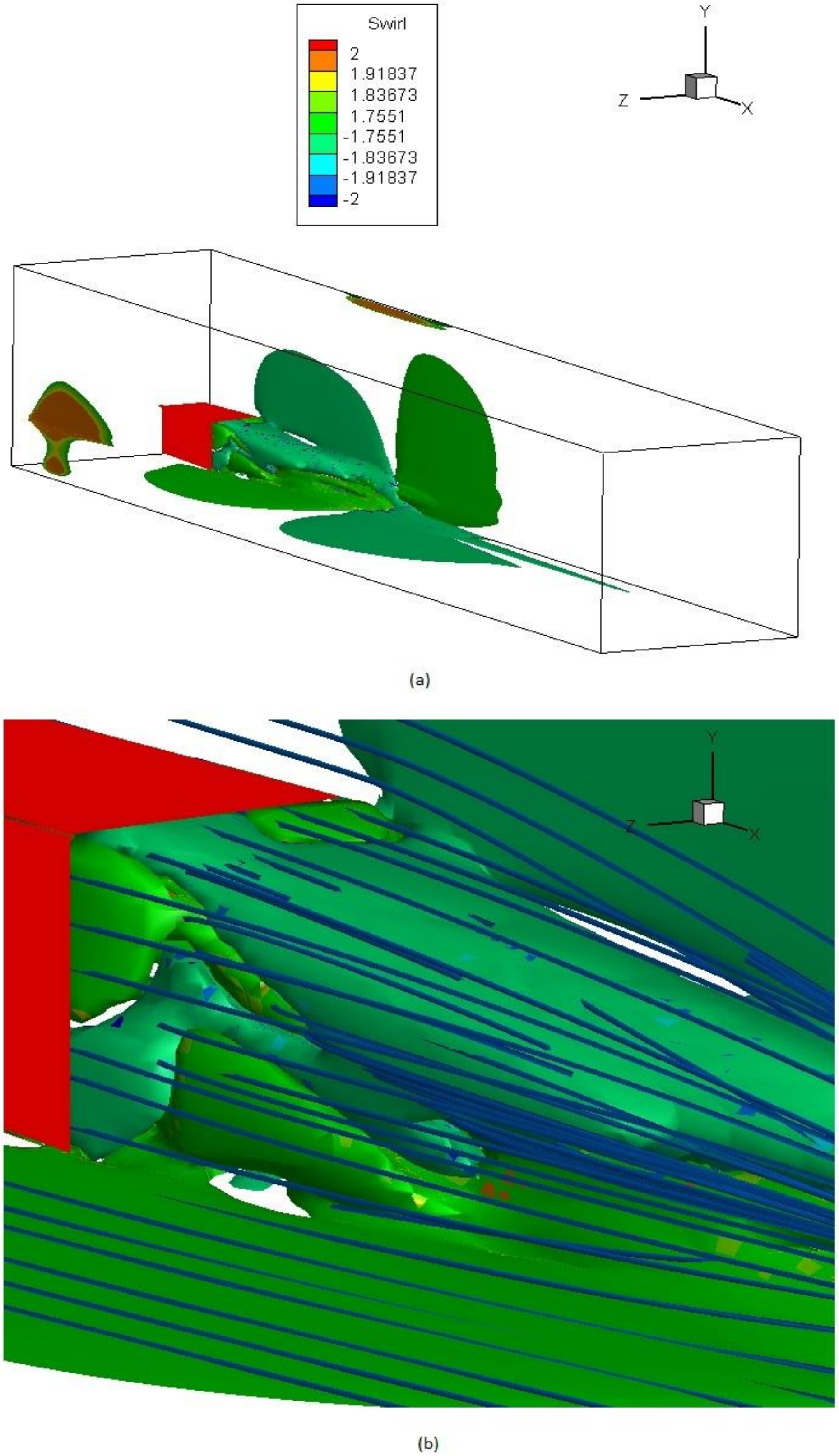

Figure 5.4: (a) Iso-Surface plots of Swirl contour for flow over backward step at Re=3200
(b) Close-up of wake of the backward step with Streamlines

Figure 5.5 presents the flow over a backward step at Re = 6400. From figure 5.5 (a) a recirculating region is seen immediately behind the rear face of the step. The recirculating region formed due to the interaction of the fluid from the top and side surfaces of the step immediately after the rear face of the step. Figure 5.5 (b) indicate the onset of span wise vortex in the wake of the backward facing step at Re=6400, due to interaction of the shear layers generated at the edge of the top and side surfaces of the step as observed in figures 5.1 (a) and (c) respectively. It can also be seen from 5.5 (b) that because of the evolution of a stronger stream-wise vortex due to higher kinetic energy of the flow than in case of Re=3200, from the interaction of shear layers generated from the flow separated at the edge of the top and side surfaces of the step in the wake, leads to formation of a stronger rolling up shear causing a stronger vortex core and swirling motion of the fluid on the bottom surface of the physical domain. The span-wise vortex core and the fluid motion of the rolling up shear layer in the YZ plane can be seen form contour and vector plot in figure 5.5 (c). As the rolling up shear layer intensity increases, causing the entrainment of the rolling up shear layer into the core of the growing recirculating span-wise vortex at the rear of the backward step, which leads to the dissipation of the vortex from the neck and it is consequently shed into the wake of the step as seen in figure 5.5 (c), 5.6 (c), 5.7 (c) and 5.8 (c).

It was also observed that along with the recirculating region behind the backward step the intensity of the span-wise vortex also increases leading to suppression of the vortex core on the bottom surface of the physical domain. This phenomena can be seen from Reynolds number, Re=3200 to 1024000 as seen from figures 5.3(a), (b) and (d), 5.5(a), (b) and (d) to 5.12(a), (b) and (d). This can be attributed to increase in Reynolds number of the flow leading to an exponential increase in the flow kinetic energy. Figure 5.11 and 5.12 present the flow over a backward step at Re = 512000 and 1024000. Figure 5.11(a) and 5.12(a) show a much larger recirculating region behind the rear face of the backward step with former smaller than the latter as discussed before due to the increase in the Reynolds number. Figure 5.11(b) and 5.12 (b) presents the streamline plot indicating development of a stronger span-wise vortex in the wake of the step than at lower Reynolds number when compared to figures 5.5 (b) to 5.10(b). The intensity and evolution of span-wise vortex is more in case of Re=1024000 than at Re=512000 as seen from the swirl contour and stream plots in figures 5.11 (c), (d) and 5.12 (c), (d). The development of the rolling up shear layer and its interaction with stream-wise vortex can be seen in figure 5.11 (c) and 5.12 (c) along with the velocity vector indicating the direction of flow in YZ plane in the wake of the step. Figure 5.11 (d) and 5.12 (d) presents the instantaneous streamline plot of the flow in the wake of the step with embedded swirl indicating the intensity of the flow at various position in the wake of the step, showing a more evolved and stronger stream wise in case of Re=1024000 than at Re=512000.

Figure 5.13(a) shows the Iso-surface plots of swirl contour in the wake of the step and 5.13(b) presents the close up view of the wake pattern for Re=1024000 in the wake of the backward step with streamlines indicating the pattern of the fluid interaction from the top and side of the backward step. The disorganized and random dissipation in the wake of the backward step in the form of vertical structures is more at higher Reynolds number than at lower Reynolds numbers. This phenomena can be observed by comparing figures 5.4 (a) and 5.13 (a). Figures 5.14(b) and (b) present the swirl and X-vorticity contour plots on XY plane at z=0.5. The random and disorganized dissipation and small scale eddys can be seen clearly indicating the shedding of small vertical structures in the wake of the step. Similar dissipation patters and flow behavior was also found at Re=512000. The global flow properties and interactions in the wake were observed to be similar for Reynolds number ranging from Re=3200 and 1024000. Non-dimensional frequency of vortex dissipation, deduced from the FFT analysis of Z-axis velocity of the flow at a point, in the span-wise vortex as seen figures 5.11 and 5.12 was found to be, f=0.055 at Re=512000 and f=0.065 at Re=1024000.

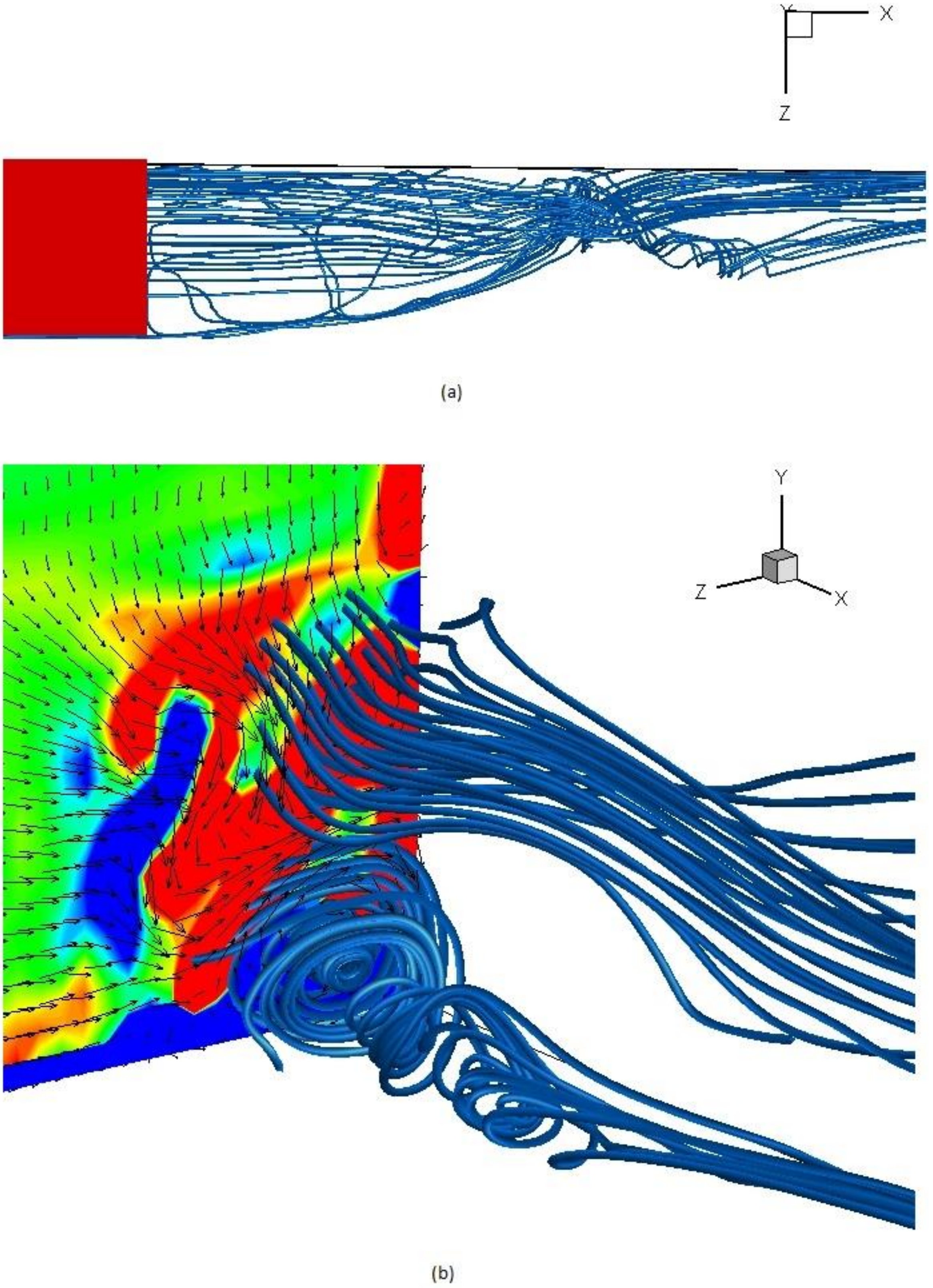

Figure 5.5: Streamline plots of flow over backward step at Re=6400 (a) Top View (b) Side View

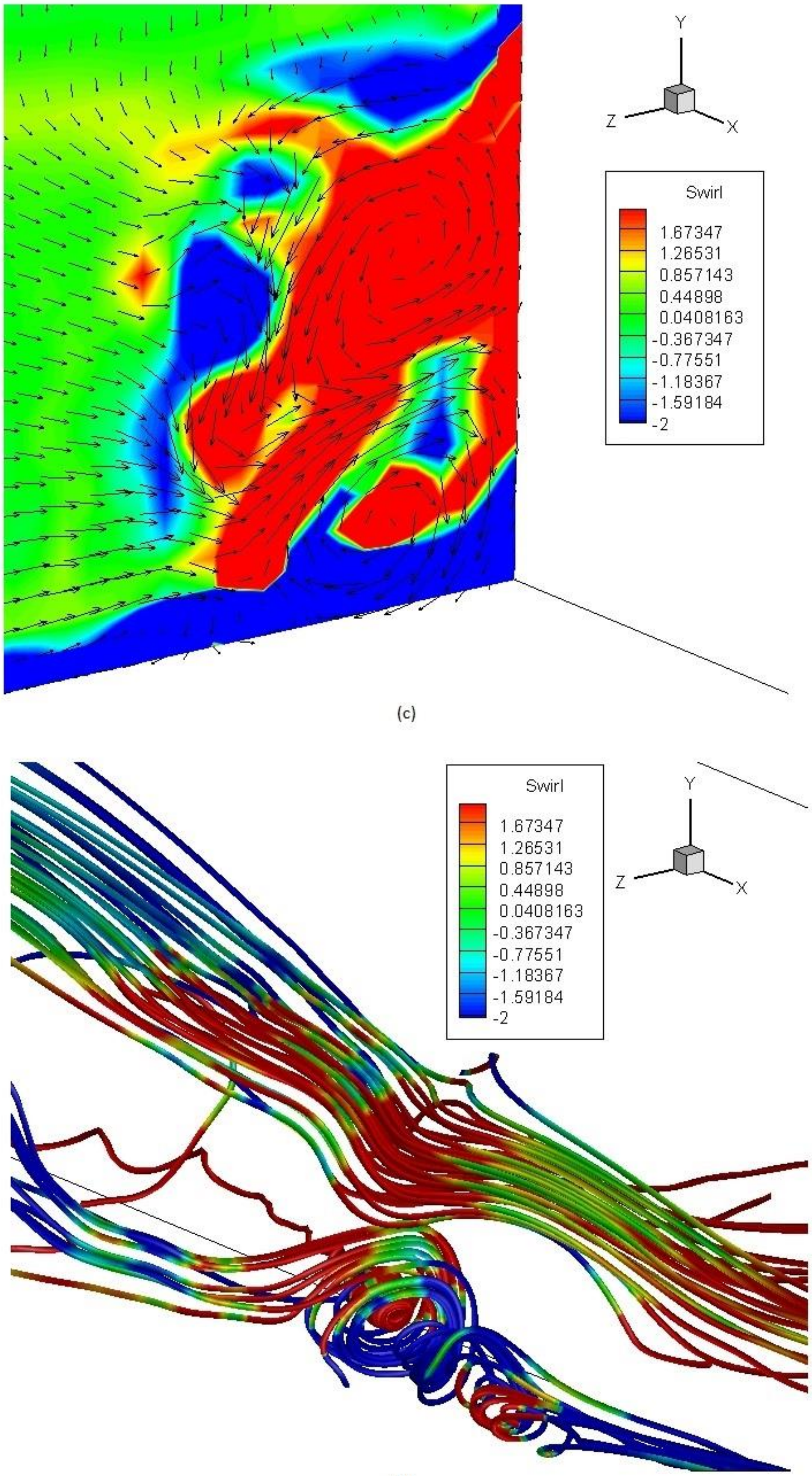

(c)

(d)

Figure 5.5: Side View of flow over backward step at Re=6400 (c) Instantaneous swirl contour plot with velocity vectors on YZ plane (d) Corresponding Streamline plot with swirl contour

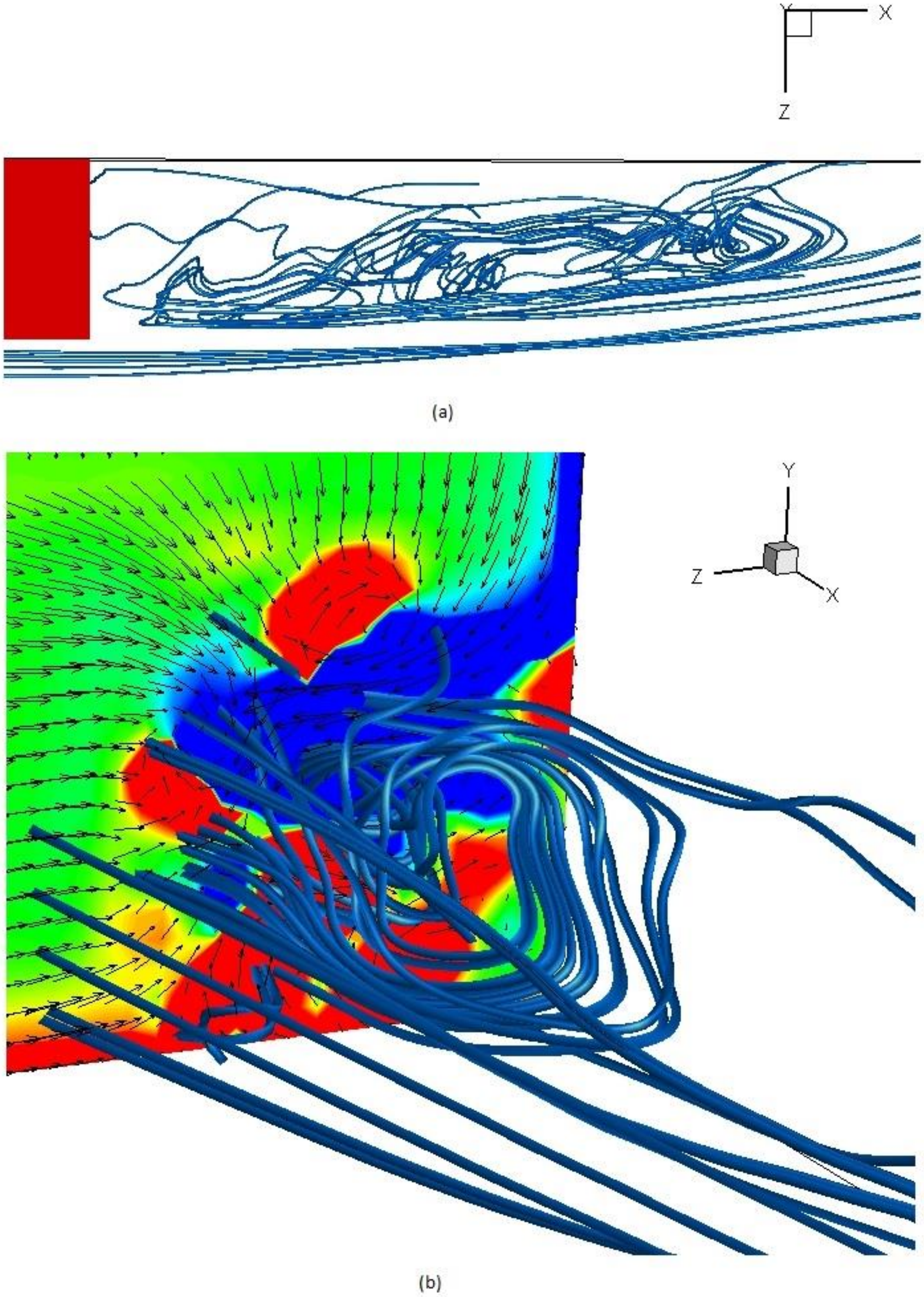

Figure 5.6: Streamline plots of flow over backward step at Re=16000 (a) Top View (b) Side View

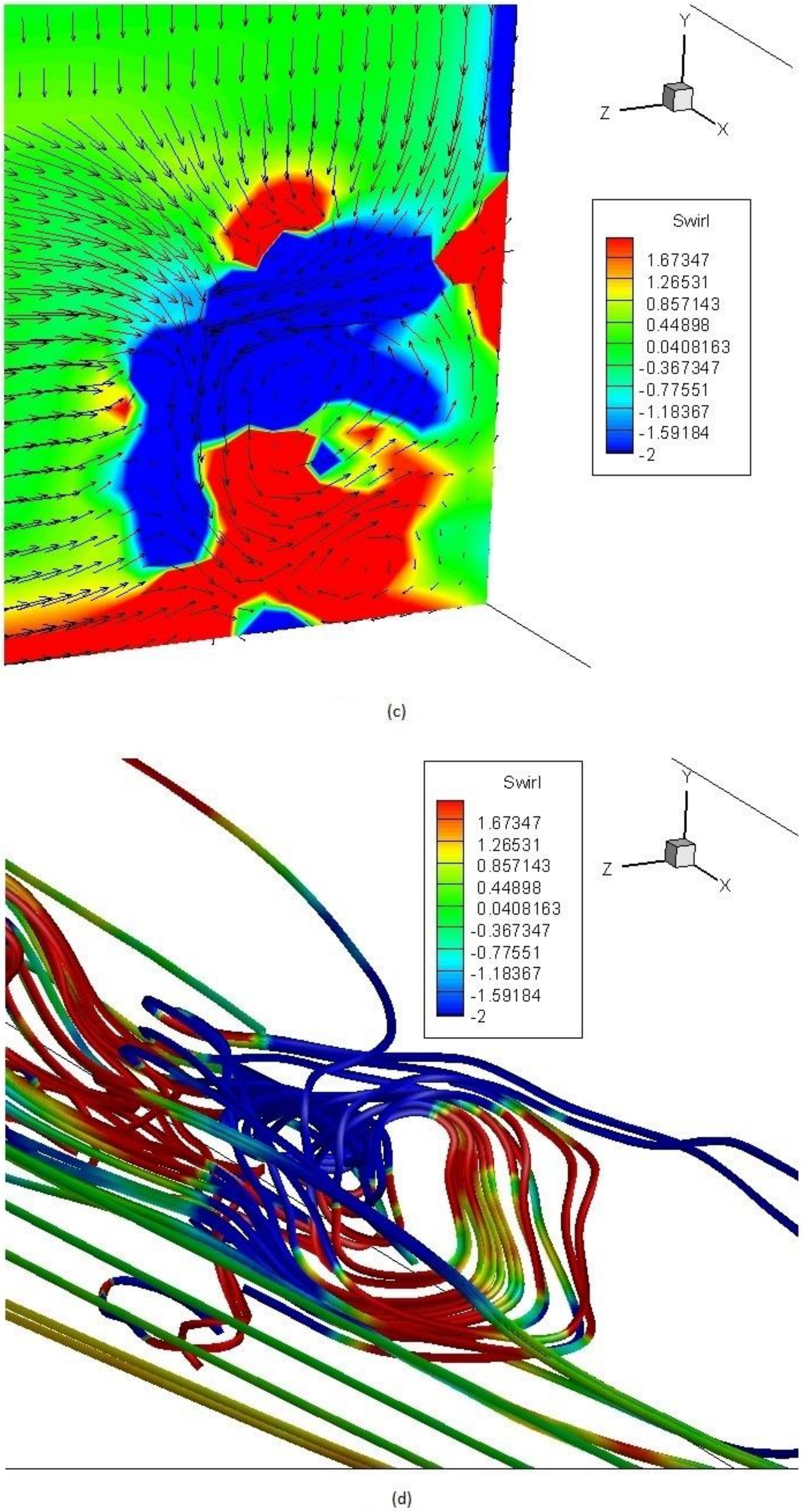

Figure 5.6: Side View of flow over backward step at Re=16000 (c) Instantaneous swirl contour plot with velocity vectors on YZ plane (d) Corresponding Streamline plot with swirl contour

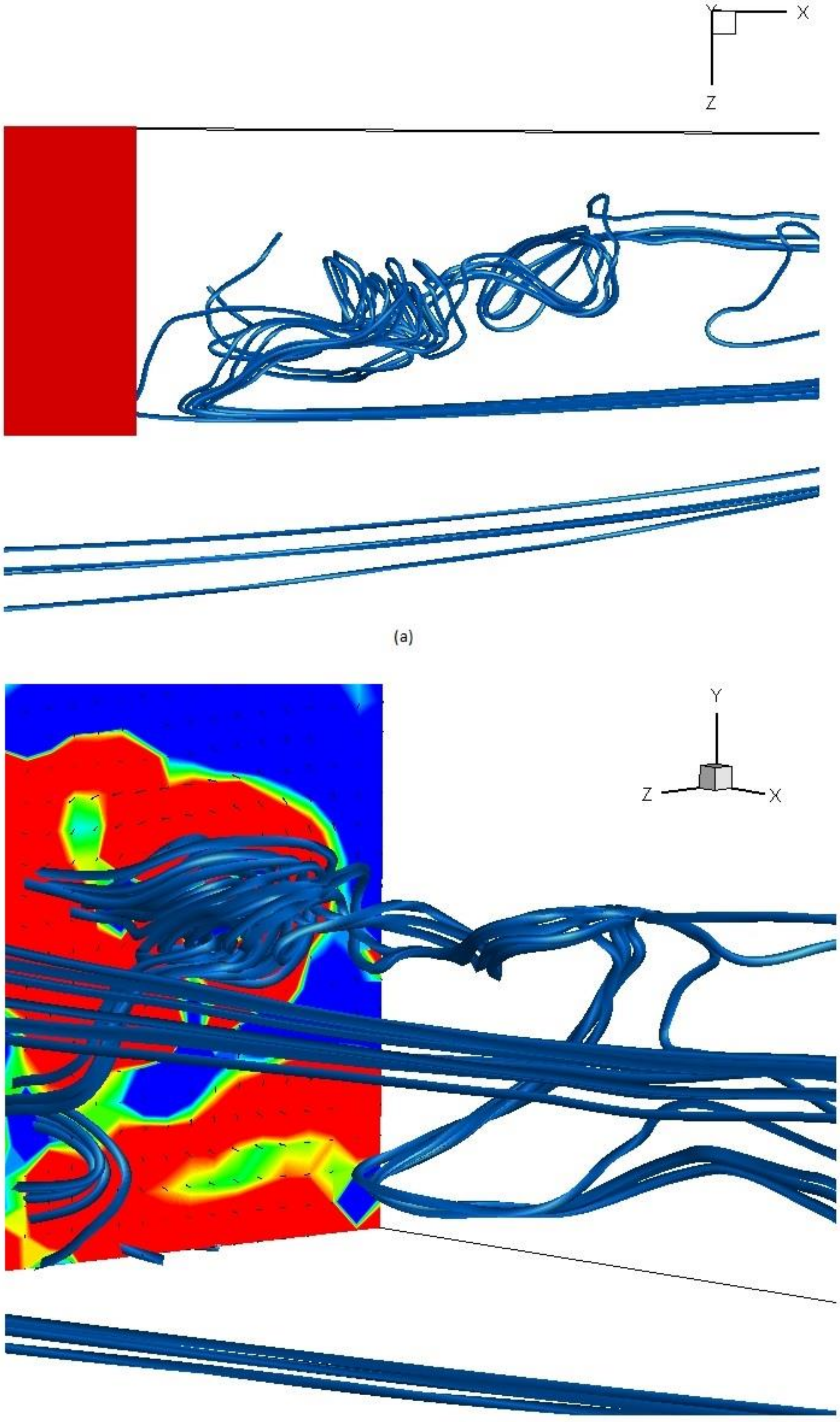

(a)

(b)

Figure 5.7: Streamline plots of flow over backward step at Re=32000 (a) Top View (b) Side View

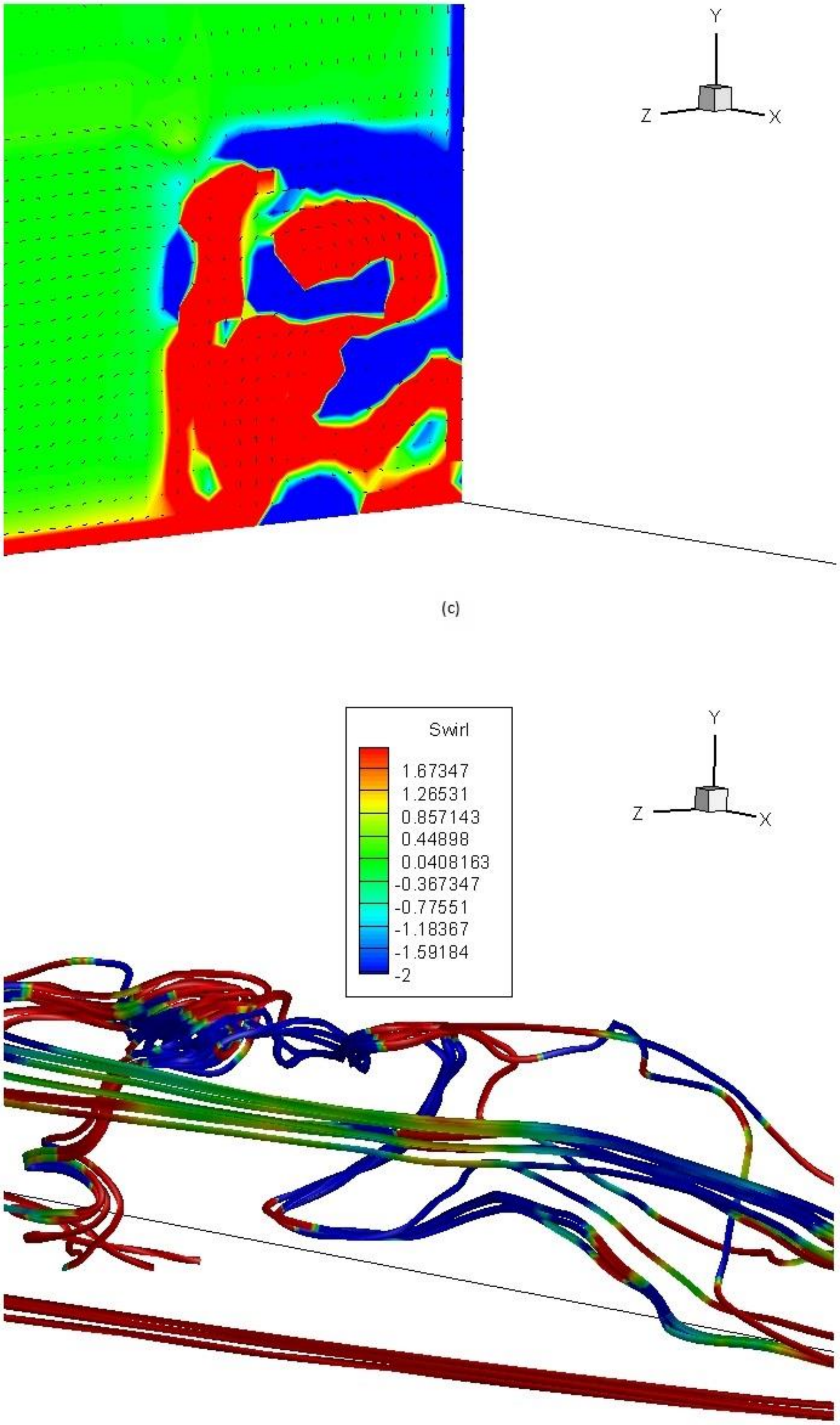

(c)

(d)

Figure 5.7: Side View of flow over backward step at Re=32000 (c) Instantaneous swirl contour plot with velocity vectors on YZ plane (d) Corresponding Streamline plot with swirl contour

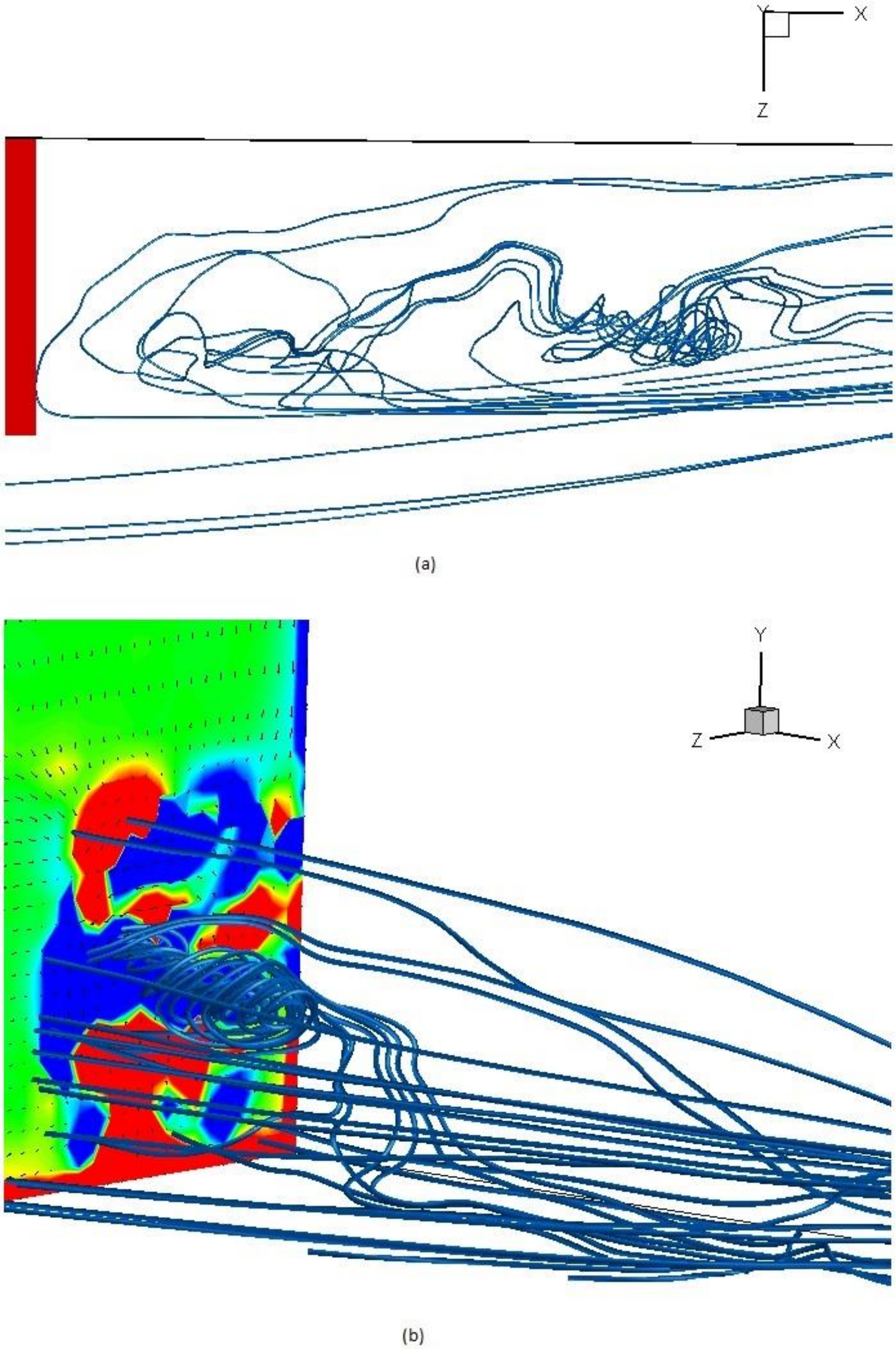

Figure 5.8: Streamline plots of flow over backward step at Re=64000 (a) Top View (b) Side View

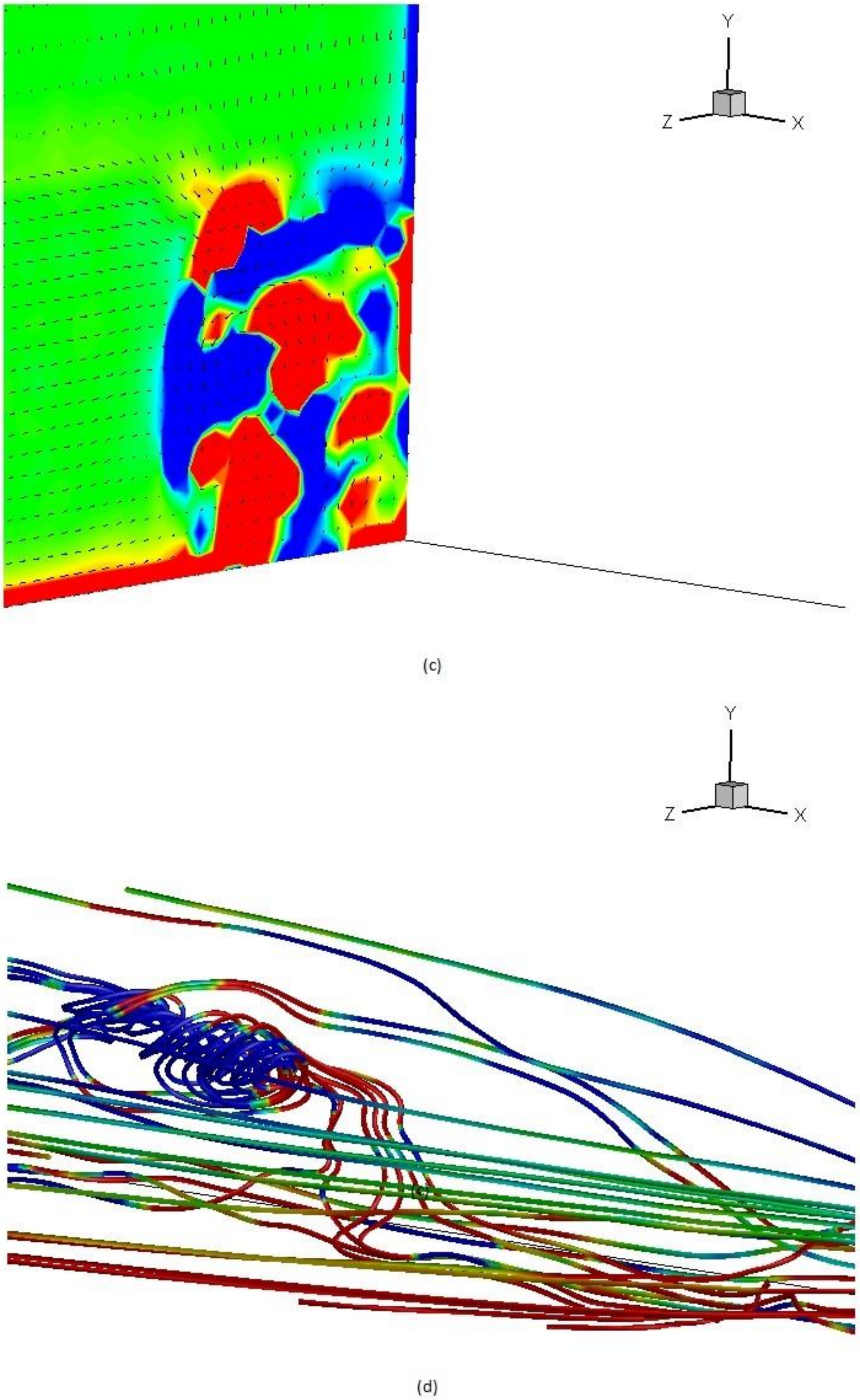

Figure 5.8: Side View of flow over backward step at Re=64000 (c) Instantaneous swirl contour plot with velocity vectors on YZ plane (d) Corresponding Streamline plot with swirl contour

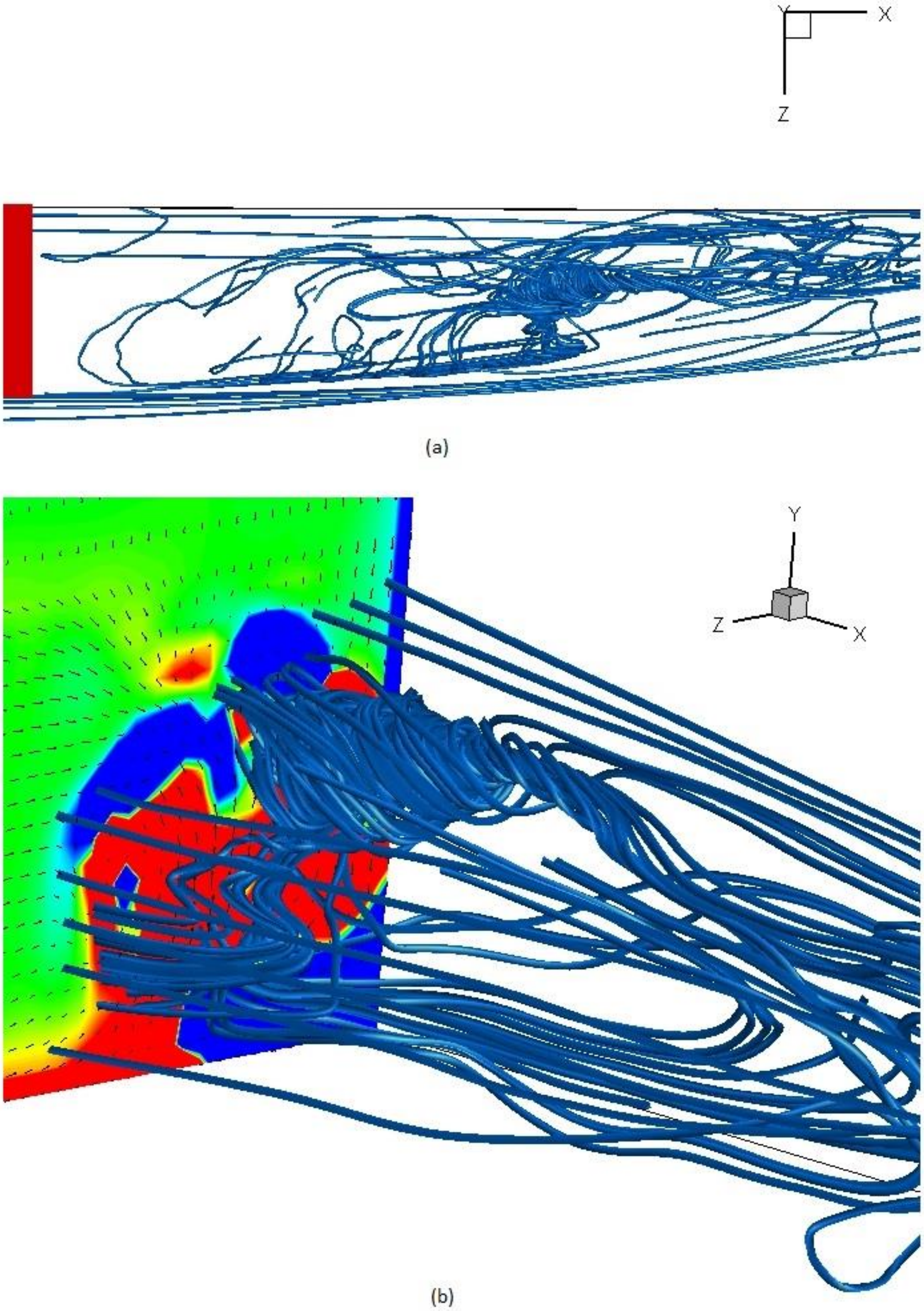

Figure 5.9: Streamline plots of flow over backward step at Re=128000 (a) Top View (b) Side View

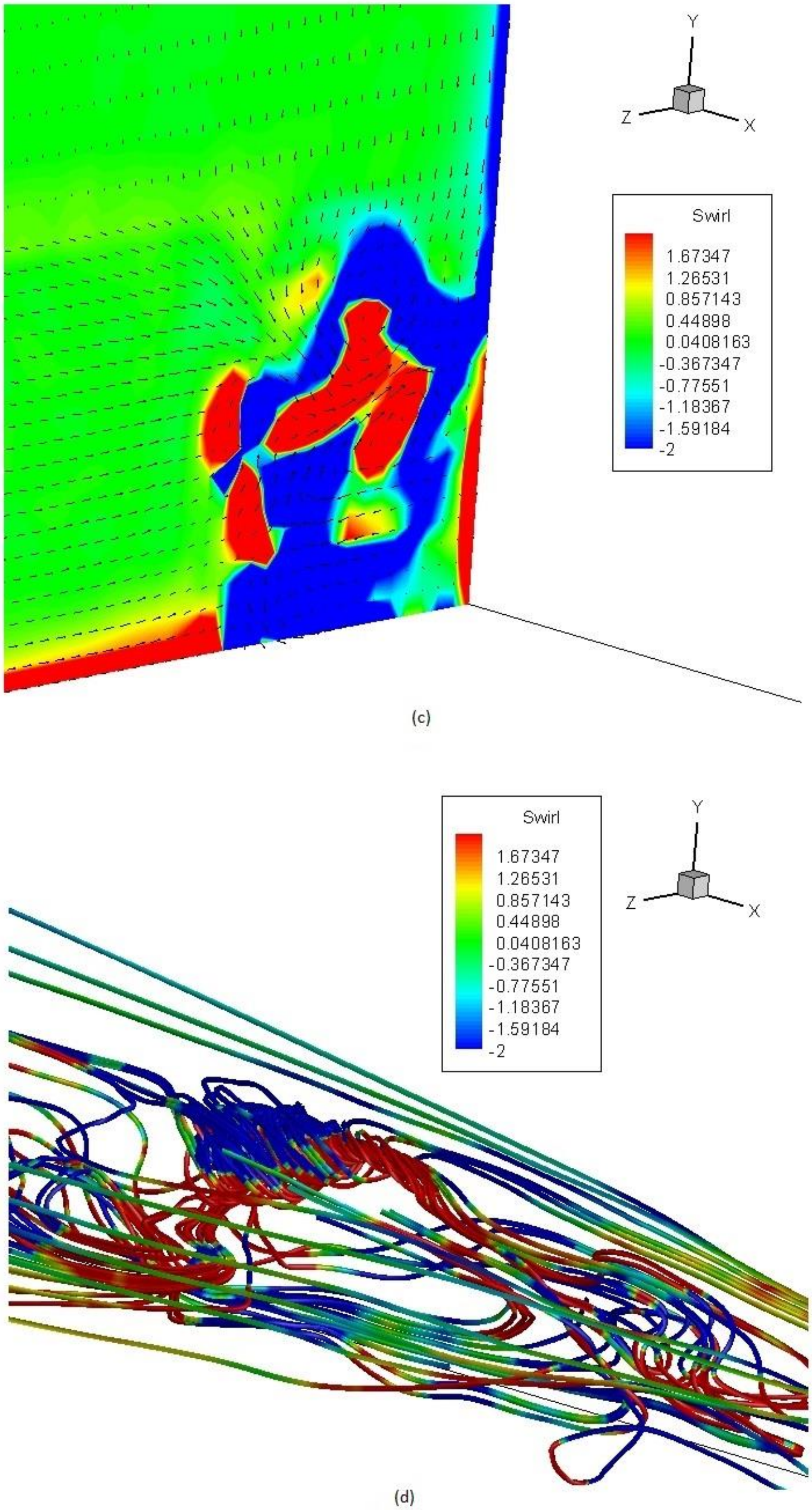

(c)

(d)

Figure 5.9: Side View of flow over backward step at Re=128000 (c) Instantaneous swirl contour plot with velocity vectors on YZ plane (d) Corresponding Streamline plot with swirl contour

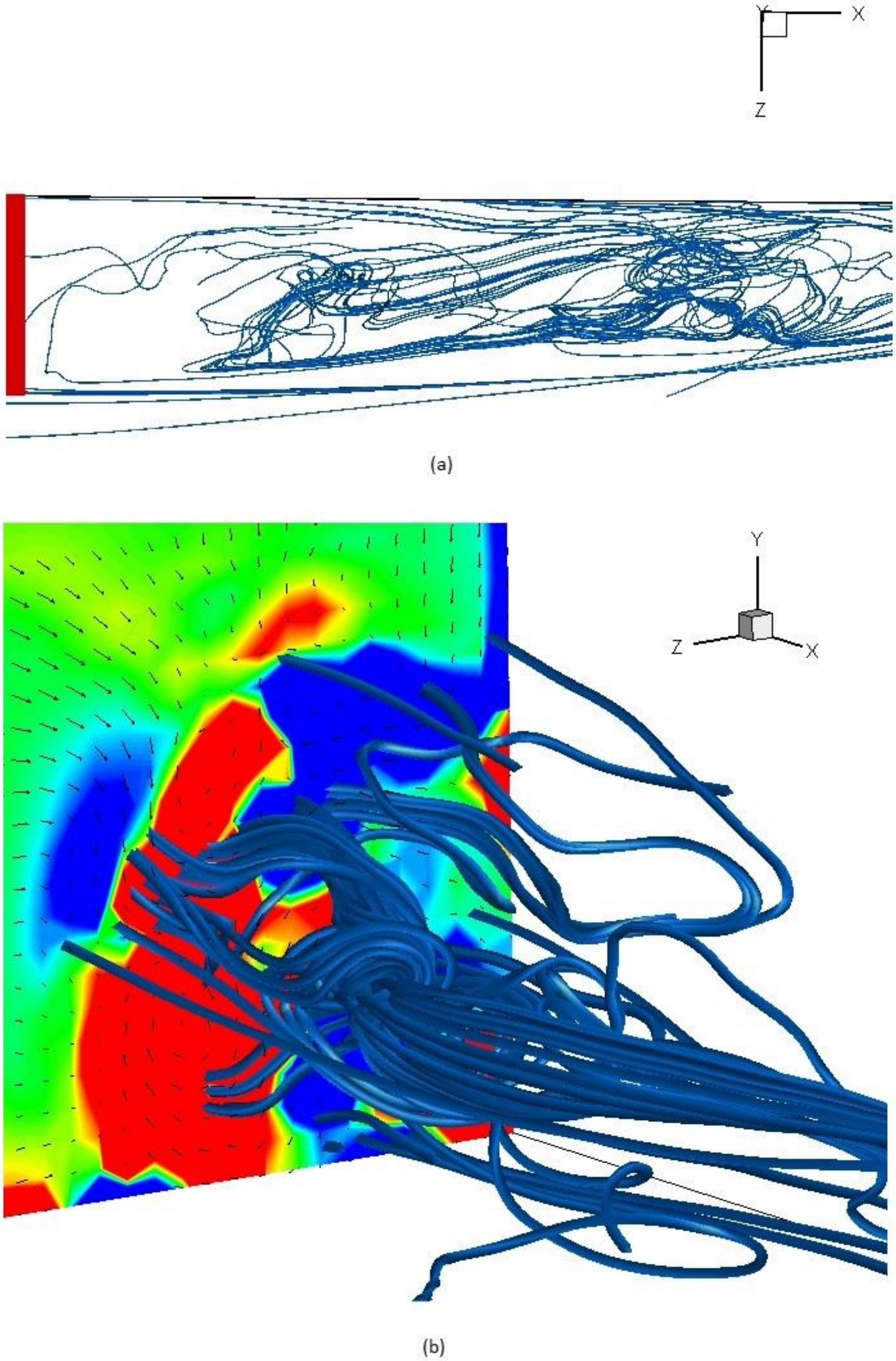

(a)

(b)

Figure 5.10: Streamline plots of flow over backward step at Re=256000 (a) Top View (b) Side View

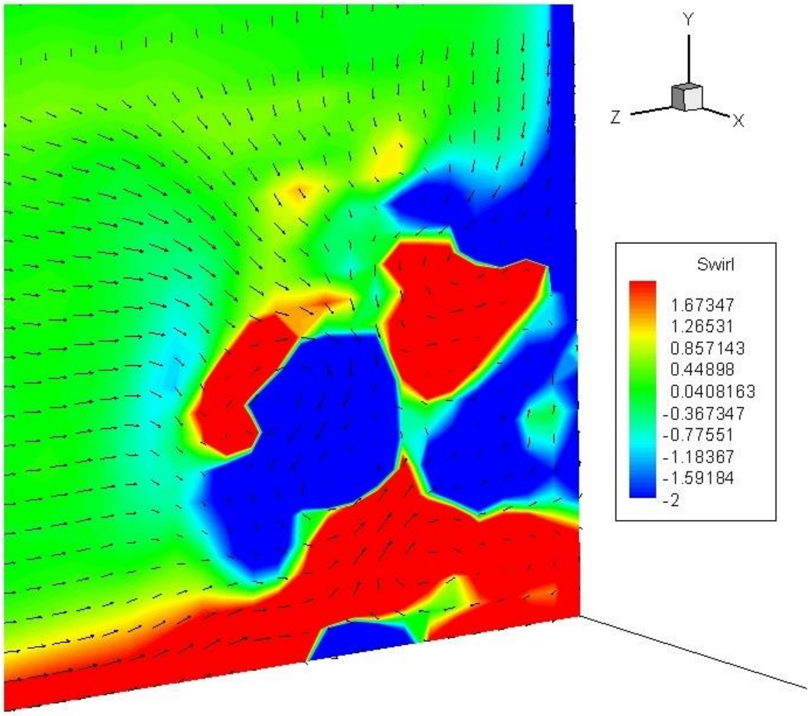

(c)

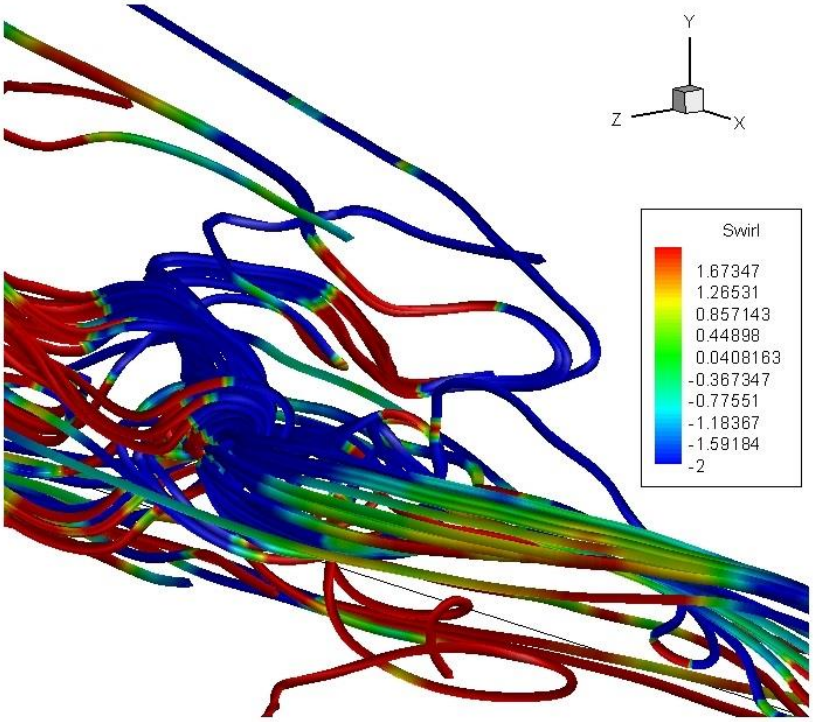

(d)

Figure 5.10: Side View of flow over backward step at Re=256000 (c) Instantaneous swirl contour plot with velocity vectors on YZ plane (d) Corresponding Streamline plot with swirl contour

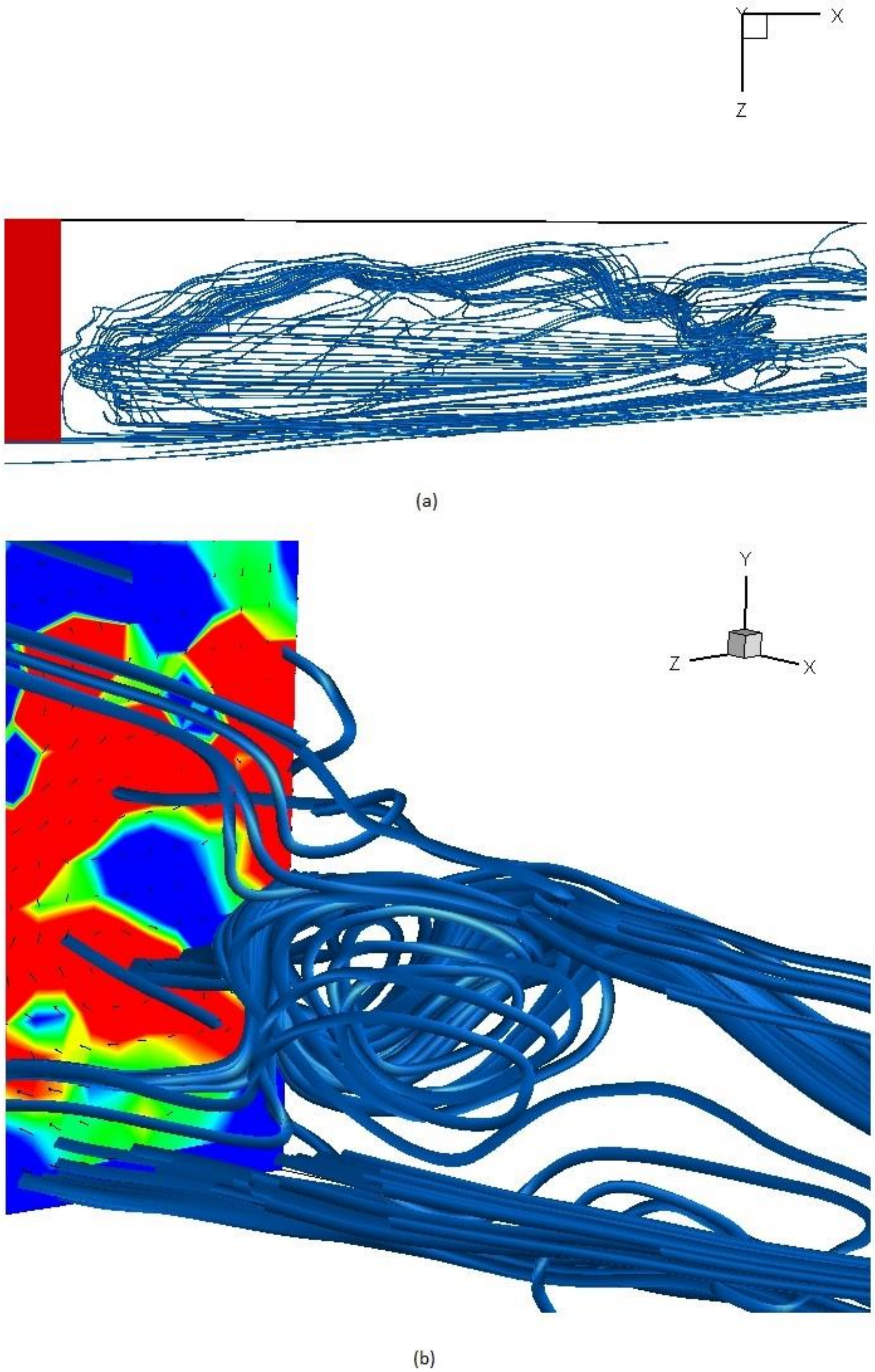

Figure 5.11: Streamline plots of flow over backward step at Re=512000 (a) Top View (b) Side View

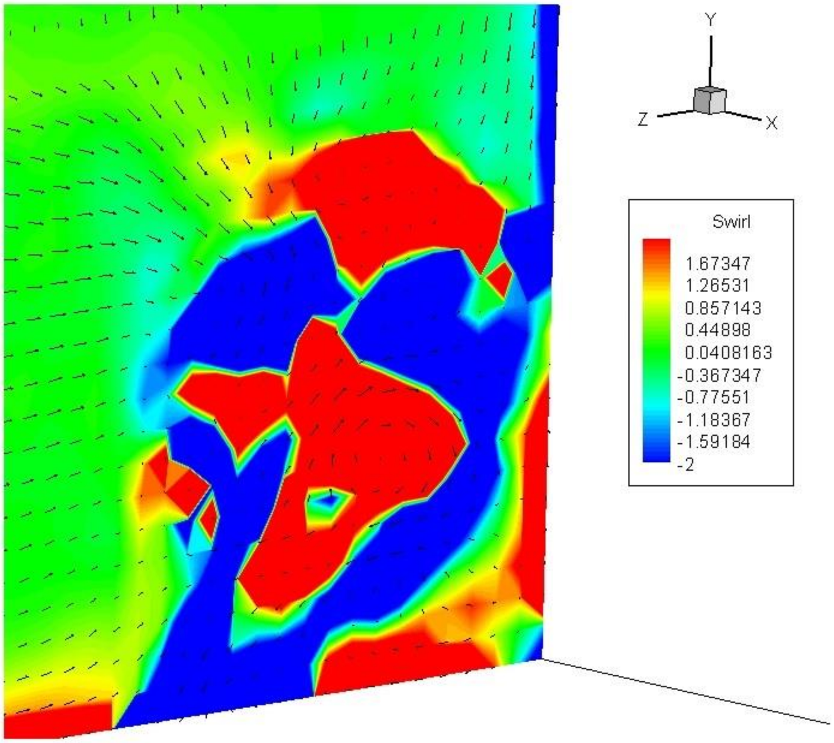

(c)

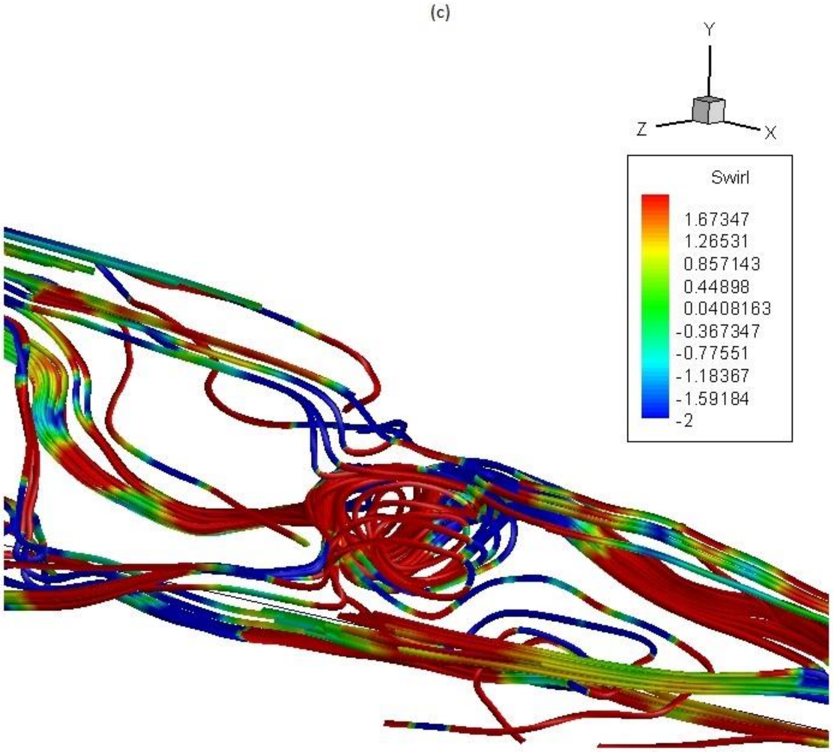

(d)

Figure 5.11: Side View of flow over backward step at Re=512000 (c) Instantaneous swirl contour plot with velocity vectors on YZ plane (d) Corresponding Streamline plot with swirl contour

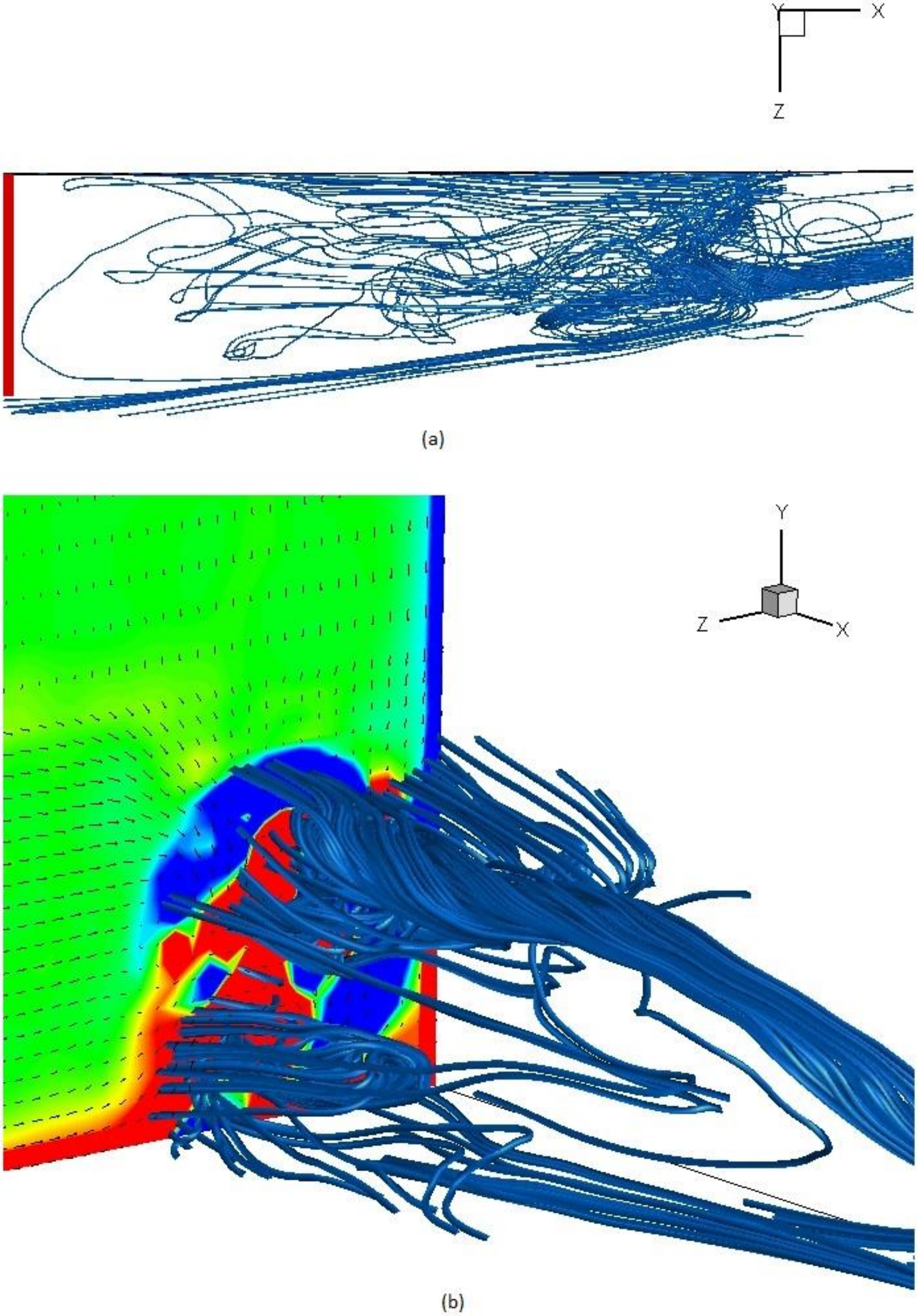

Figure 5.12: Streamline plots of flow over backward step at Re=1024000 (a) Top View (b) Side View

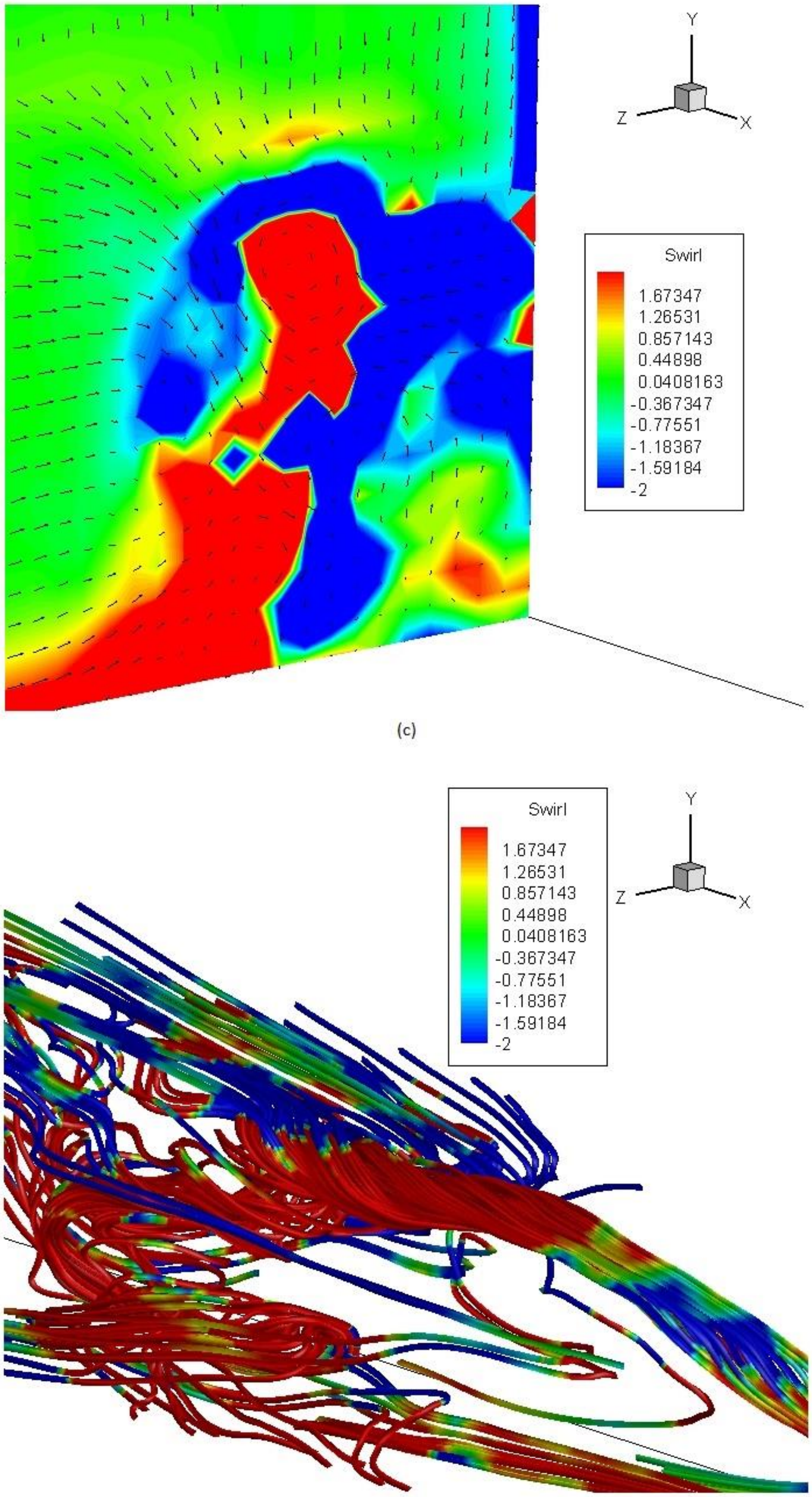

(c)

(d)

Figure 5.12: Side View of flow over backward step at Re=1024000 (c) Instantaneous swirl contour plot with velocity vectors on YZ plane (d) Corresponding Streamline plot with swirl contour

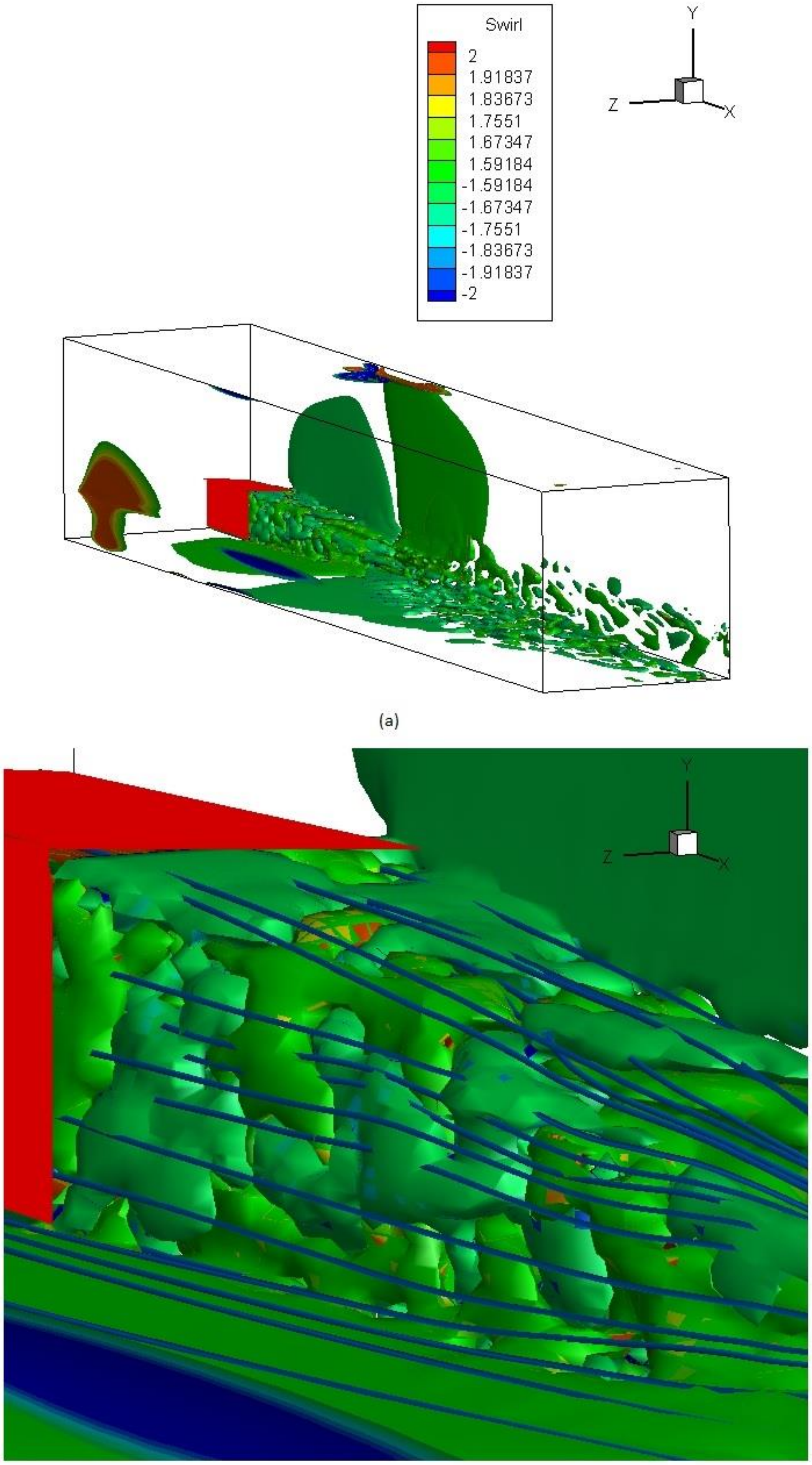

(a)

(b)

Figure 5.13: (a) Iso-Surface plots of Swirl contour of flow over backward step at Re=1024000 (b) Close-up of wake of the backward step with Streamlines

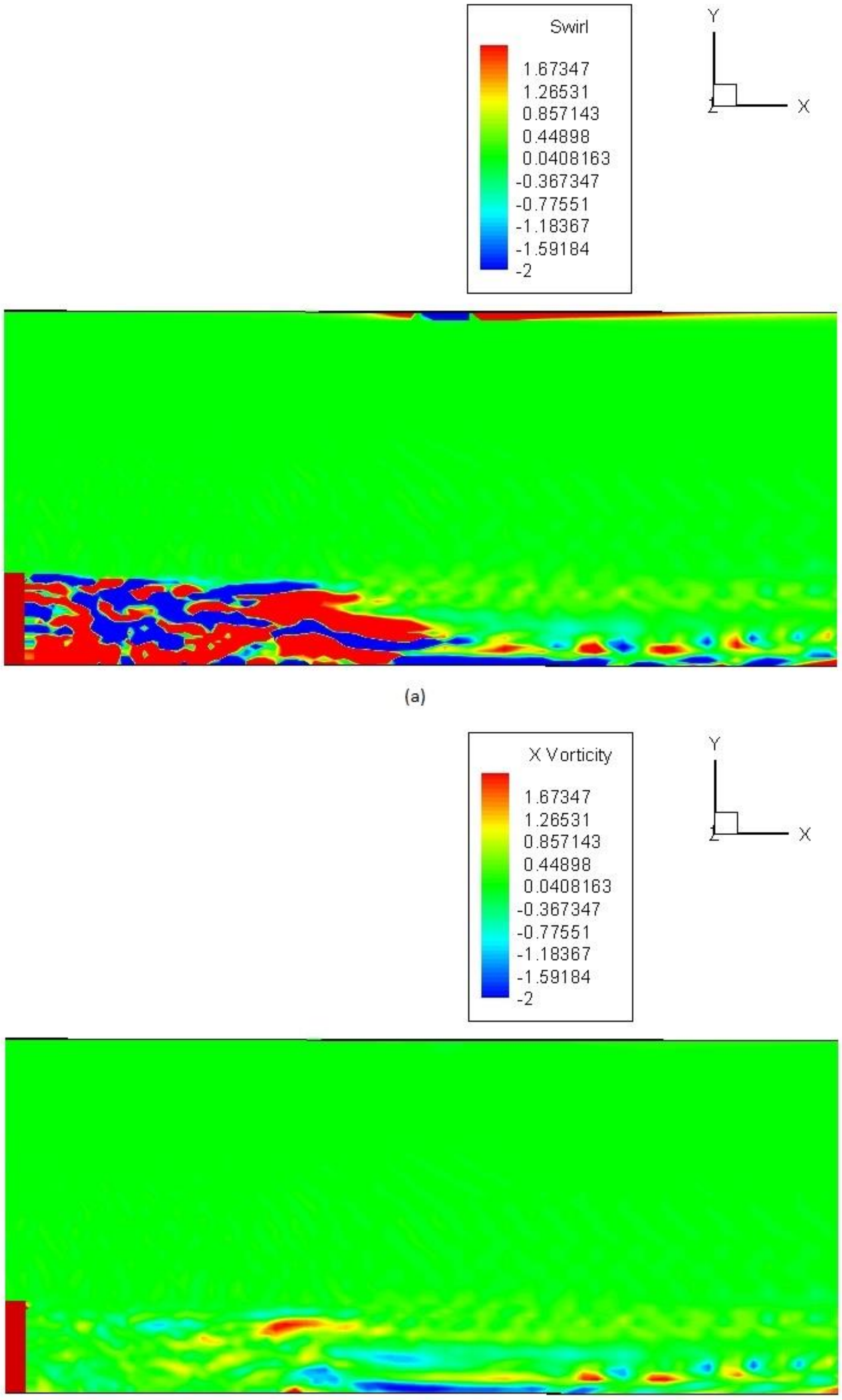

(a)

(b)

Figure 5.14: Side View of flow over backward step at Re=1024000 on XY plane at z=0.5 (a) Instantaneous Swirl contour plot (b) Instantaneous X-Vorticity contour plot with velocity vectors

5.3.2 3D Flow over a Backward Step with Active Flow Control.

Figure 5.15 and 5.16 presents present the flow over a backward step at Re = 51200 with ZNMF and FA techniques applied respectively. The frequency, amplitude and momentum coefficient of both the flow control, are respectively, f=0.055, A=0.1 and C_μ=0.0001. The groove was placed at (x=1.953, z=1) and the width of the groove was considered as w=0.023. From figure 5.15, it can be observed that the flow interactions and properties of wake is the same as in case of flow over a backward step without any AFC technique applied when compared to figure 5.11. It can be seen from figures 5.11(a) and 5.15(a) that the recirculating region in the wake of the backward step is smaller in the case of latter case than in former due to application of ZNMF technique on the side surface of the step. It can also be seen that the intensity and development of the span-wise vortex in the wake of the backward step is suppressed and diminished when ZNMF technique is applied at Re=512000 on side of the step as seen in figure 5.15(b) when compared to figure 5.11(b). The swirling motion of the fluid in the wake of the step as seen in figure 5.15(b) and (d) is similar to the vortex seen in figure 5.3(b) and (d) at Re=3200 where the development of the span-wise vortex is suppressed to inadequate kinetic energy of the fluid at that Reynolds number. It can be concluded that due to the application of the ZNMF technique on the side of the step, the evolution of span wise vortex is diminished due to the absorption and inducing of fluid, as in case of ZNMF technique, into the boundary layer leading to suppression of interactions of the shear layers and kinetic energy in the wake of the step causing suppressed swirling motion of fluid as in the case of Re=3200 shown in figure 5.3 (b).

Figure 5.16 shows the onset of the span-wise vortex in the wake of the step when FA technique is applied to side surface of the step. The configuration of the flow control is the same as in case of figure 5.15 with f=0.055, A=0.1, w=0.023, C_μ=0.0001 and the groove was placed at (x=1.953, z=1). From figure 5.16, it can also be observed that wake interactions and global properties of flow are same as in case of flow over a backward step without any AFC technique applied when compared to figure 5.11. It can be observed from figures 5.11(a) and 5.16(a) that the recirculating region in the wake of the backward step is slightly smaller in the case of latter case than in former due to application of FA technique on the side surface of the step, but larger than in case of ZNMF technique applied to the side of the step as seen in figure 5.15(a). It can also be seen that the onset and development of the span-wise vortex in the wake of the backward step, as seen in figure 5.16(b) and (d), is higher than when ZNMF technique is applied at Re=512000 on side of the step, as seen in figure 5.15(b) and (d). But when comparing figure 5.11(b) and (d) with 5.16(b) and (d) the intensity and development of the span-wise vortex in the wake of the step is suppressed in case of latter than former due to the inducing of fluid into the boundary layer on the side surface of the step as in case of FA technique leading to suppression of interactions in the wake of the step. In case of figure 5.16(b) and (d) the span-wise vortex is also closer towards the bottom surface of the physical domain than as seen in figure 5.11(b) and (d). The span-wise vortex evolution in the wake of the step as seen in figure 5.16(b) is similar to the vortex seen in figure 5.5(b) at Re=6400 where the onset and evolution of the span-wise vortex occurred. It can be concluded that in case of application of FA technique on the side of the step, the evolution and development of span-wise vortex is higher than in case of ZNMF technique due to the inducing of fluid, as in case of FA technique, into the boundary layer leading to enhanced interactions of the shear layers and kinetic energy in the wake of the step.

The boundary layers, in case of both figures 5.15 and 5.16, on the top and side surfaces remain stable as in the case of figure 5.11. The vortex dissipation mechanism remains similar to flow at Re=512000 without any AFC technique applied, when comparing figures 5.11(c), 5.15(c) and 5.16(c), and occurs due to the interaction of rolling up shear layer formed at the bottom surface of the step with the swirling motion of the fluid above leading to subsequent dissipation in the wake of the backward step.

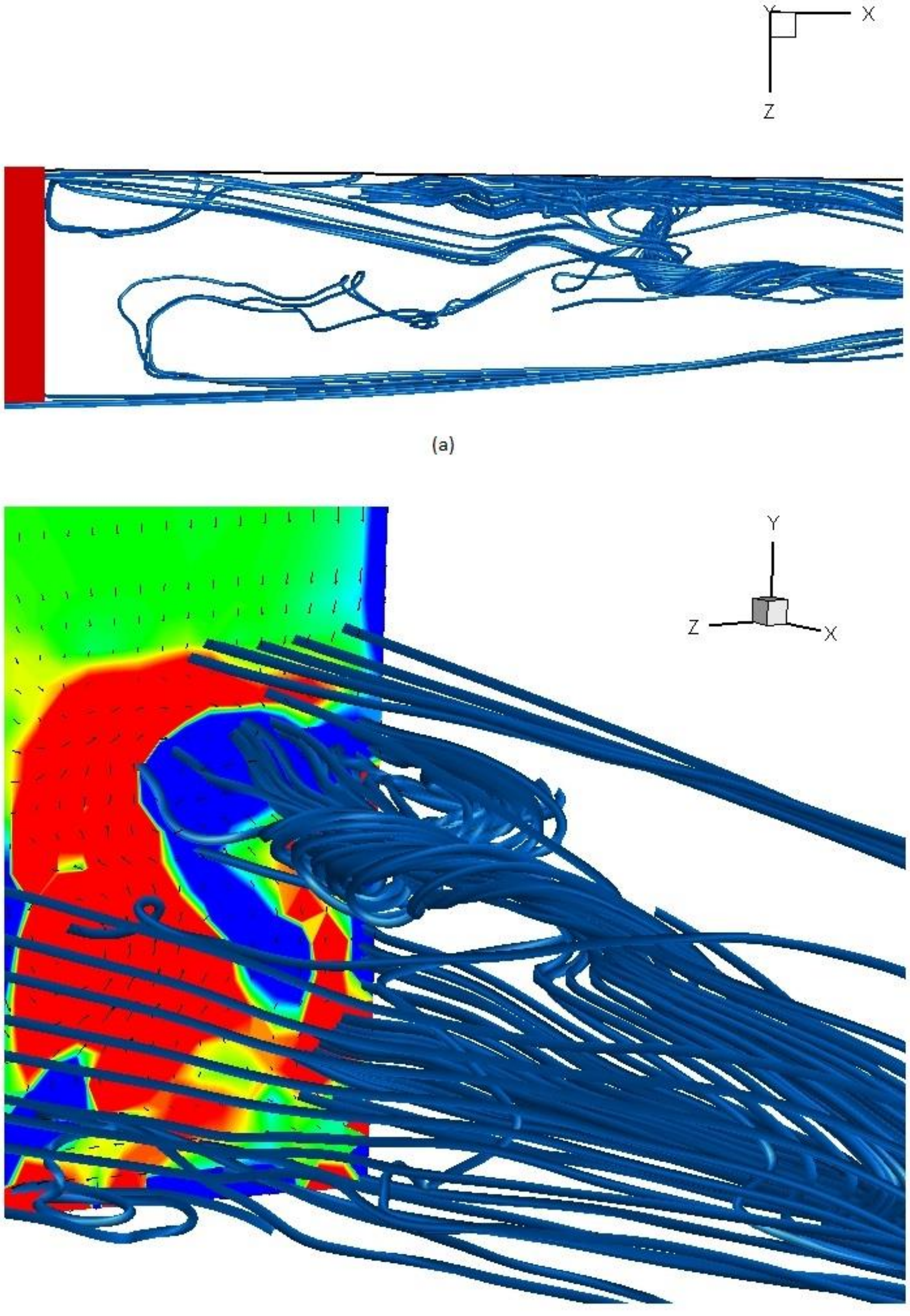

(a)

(b)

Figure 5.15: Streamline plots of flow over backward step with ZNMF technique at Re=512000, f=0.055 and A=0.1 (a) Top View (b) Side View

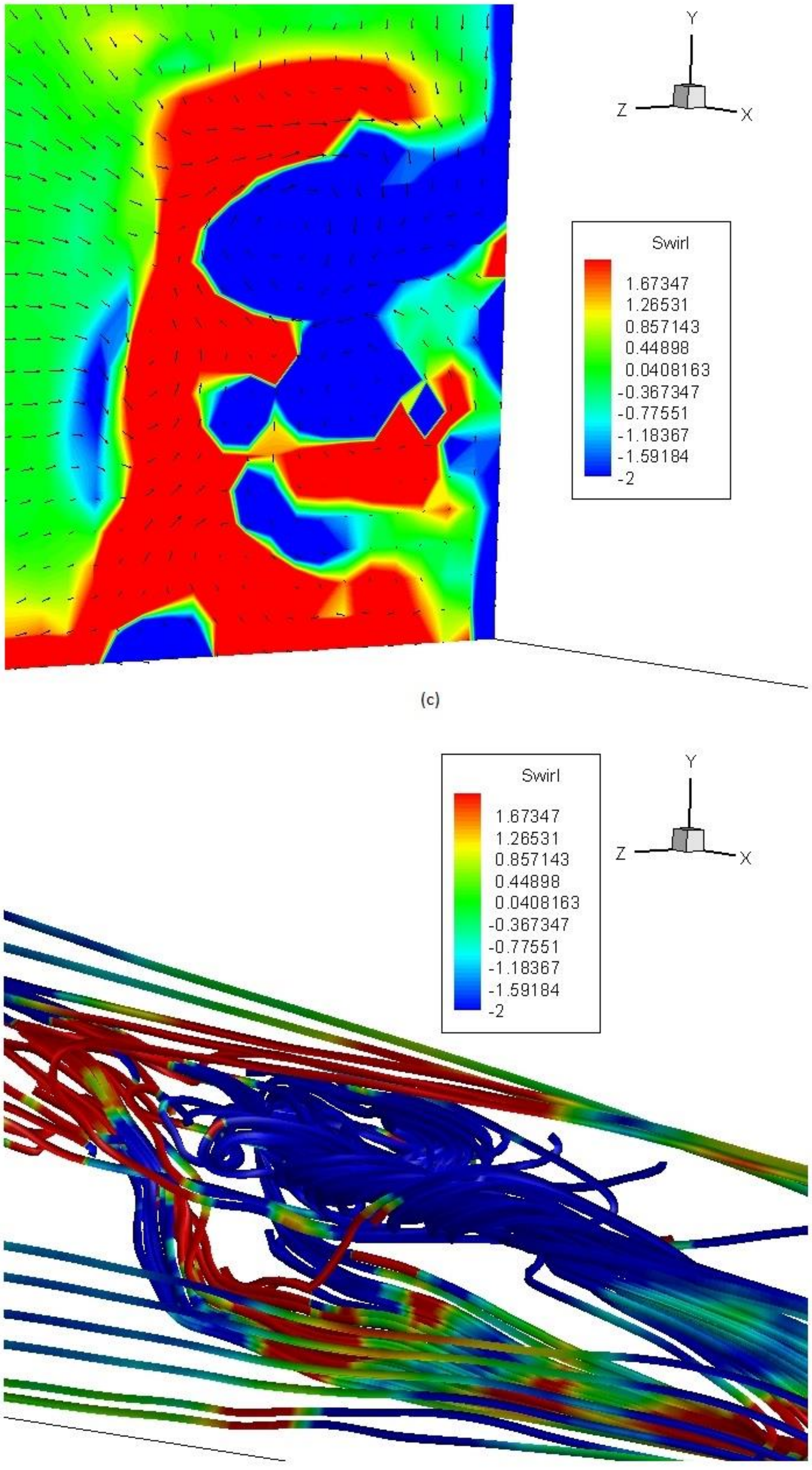

(c)

(d)

Figure 5.15: Side View of flow over backward step with ZNMF technique at Re=512000, f=0.055 and A=0.1 (c) Instantaneous swirl contour plot with velocity vectors on YZ plane (d) Corresponding Streamline plot with swirl contour

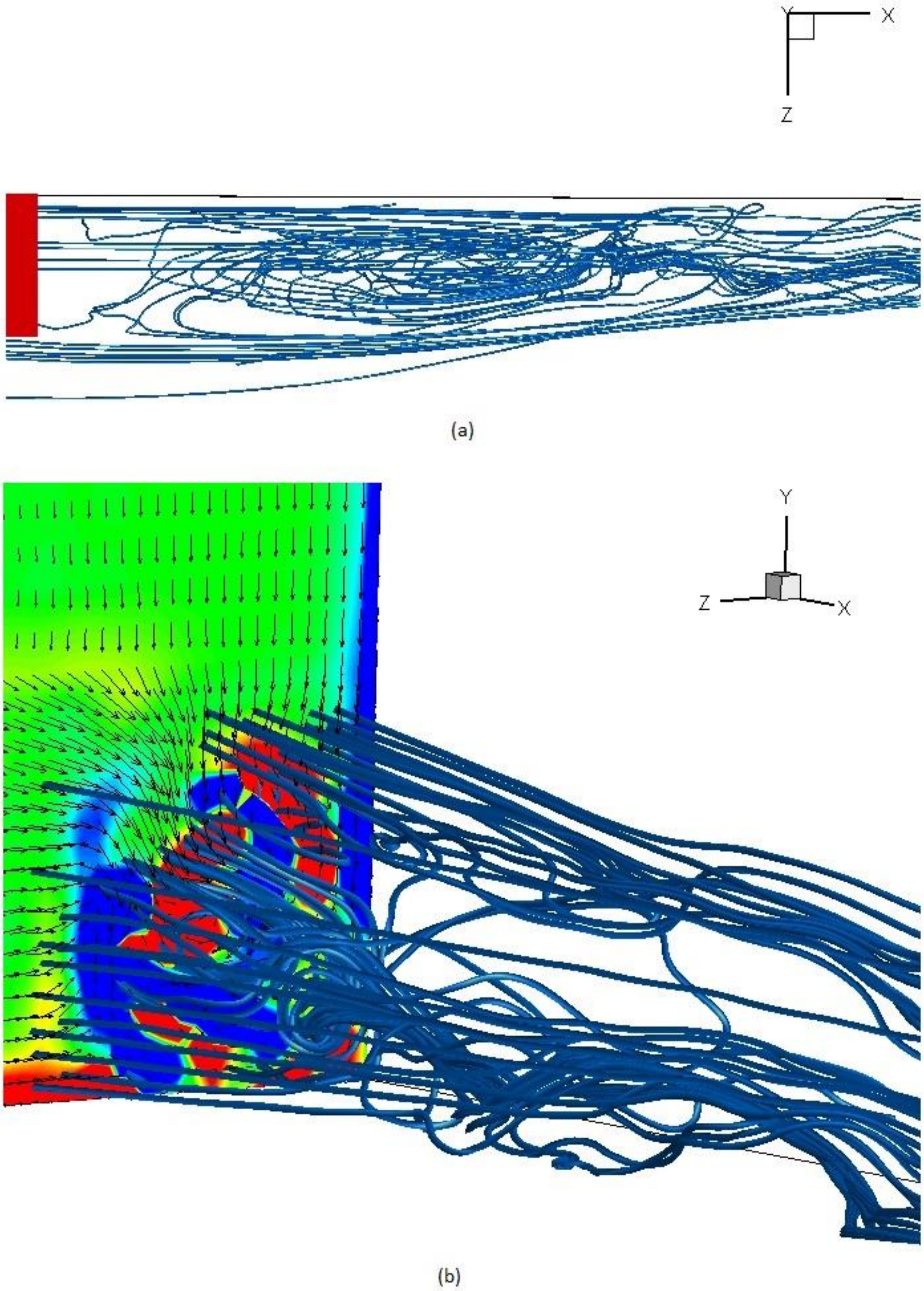

Figure 5.16: Streamline plots of flow over backward step with FA technique at Re=512000, f=0.055 and A=0.1 (a) Top View (b) Side View

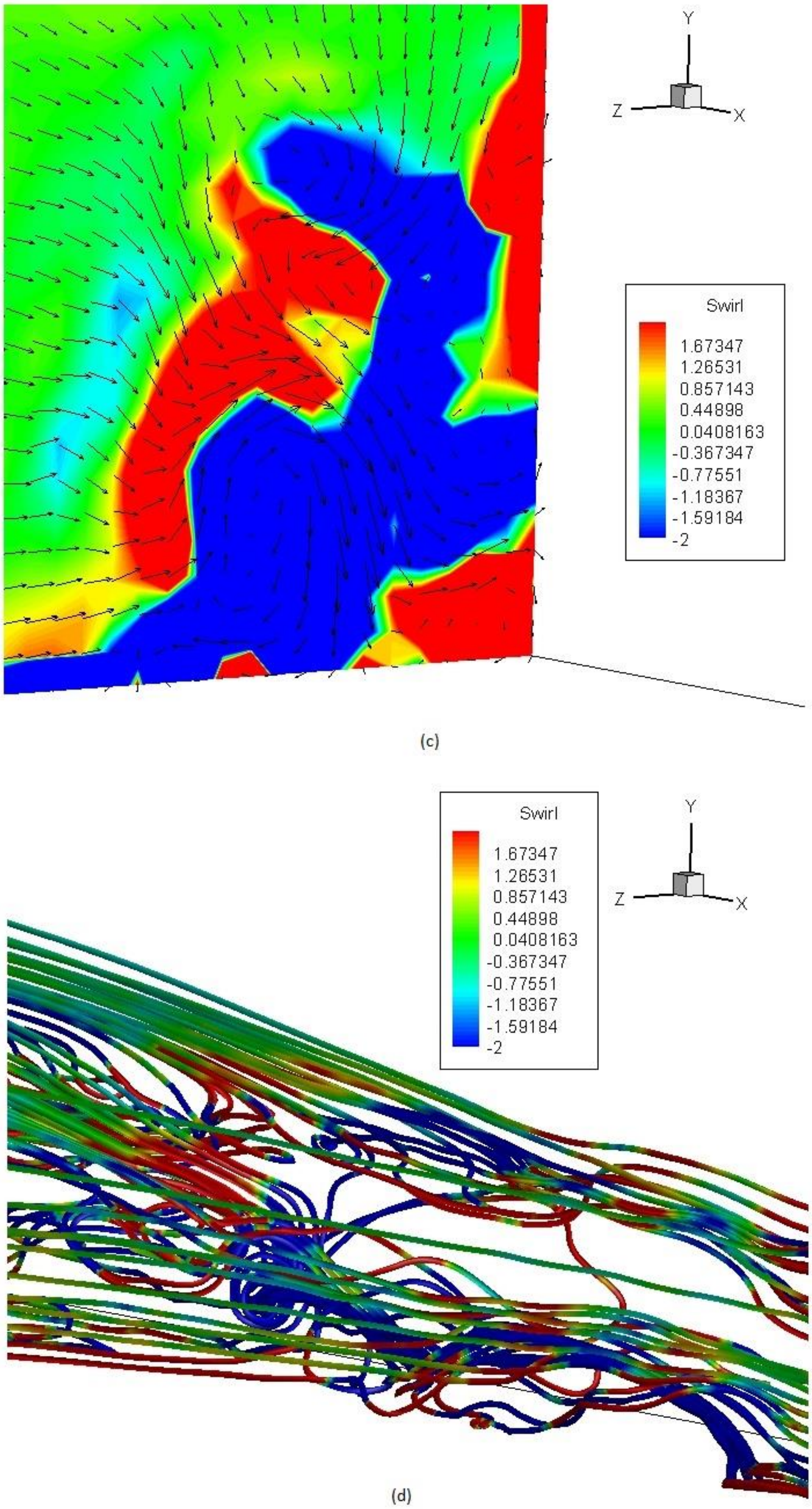

Figure 5.16: Side View of flow over backward step with FA technique at Re=512000, f=0.055 and A=0.1 (c) Instantaneous swirl contour plot with velocity vectors on YZ plane (d) Corresponding Streamline plot with swirl contour

The frequency of vortex dissipation, deduced from the FFT analysis of Z-axis velocity of the flow at a point in the span-wise vortex as seen figure 5.12 was found to be f=0.065 at Re=1024000. The flow over backward step at Re=102400 was evaluated at two actuating frequencies of AFC, f=0.055 and 0.065 to compare the effects of change in frequency on the properties of the wake of the backward step. Figure 5.17 and 5.18 presents present the flow over a backward step at Re = 102400 with ZNMF and FA techniques applied respectively. The frequency and amplitude of both the case are f=0.055 and A=0.1 respectively. The groove was placed at (x=1.953, z=1) and the width of the groove was considered as w=0.023. From figure 5.17 and 5.18, it can be observed that the flow interactions and properties of wake is the same as in case of flow over a backward step without any AFC technique applied when compared to figure 5.12. As in case of Re=512000, it can be seen from figures 5.12(a) and 5.17(a) that the recirculating region in the wake of the backward step is smaller in the case of latter case than in former due to application of ZNMF technique on the side surface of the step. From figures 5.12(b) and 5.17(b), it can also be seen that the evolution of span-wise vortex in the wake of the backward step doesn’t occur when ZNMF technique is applied at Re=1024000 on side of the step. It can be concluded that due to the application of the ZNMF technique on the side of the step, is very effective in averting the evolution of span wise vortex in the wake of the step by effectively altering the interactions of the shear layers and kinetic energy in the wake of the step, through the absorption and inducing of fluid, as in case of ZNMF technique, into the boundary layer. A similar behavior wake and the span-wise vortex evolution can also in figures 5.19(b) and (d) where the span-wise vortex is also completely suppressed when ZNMF technique is applied at frequency, f=0.065 and A=0.1.

Figure 5.18 shows the onset of the span-wise vortex in the wake of the step when FA technique is applied to side surface of the step. From figure 5.18, it can be observed that wake interactions and global properties of flow are same as in case of flow over a backward step without any AFC technique applied when compared to figure 5.12. It can be observed from figures 5.12(a) and 5.18(a) that the recirculating region in the wake of the backward step is of similar size as the former, but larger than in case of ZNMF technique applied to the side of the step as seen in figure 5.17(a). It can be seen that the onset and development of the span-wise vortex in the wake of the backward step, as seen in figure 5.18(b) and (d), is higher than when ZNMF technique is applied at Re=1024000 on side of the step, as seen in figure 5.17(b) and (d). But when comparing figure 5.12(b) and (d) with 5.16(b) and (d) the intensity and development of the span-wise vortex in the wake of the step is largely suppressed in case of latter than former due to the inducing of fluid into the boundary layer on the side surface of the step as in case of FA technique leading to suppression of interactions in the wake of the step. By comparing figures 5.17(b) and (d) and 5.18(b) and (d), it can be concluded that FA is effective in suppressing the evolution and development of the span-wise vortex in the wake of the step but ZNMF technique is more effective in suppression of the evolution of the span-wise vortex. When comparing figure 5.18(b), (d) and 5.22(b), (d), it can be observed that evolution of span-wise vortex is completely averted as seen in figures 5.17(b) and (d). It can be deduced that FA is more effective at natural dissipation frequency for the flow, in case figure 5.22(b) and (d), for Re=1024000 at f=0.065 than at f=0.055 as in case of figure 5.18(b) and (d). The boundary layers in all the cases of figures 5.17, 5.18, 5.19 and 5.22 on the top and side surfaces remain stable as in the case of figure 5.12. The effects of AFC frequency, f are higher on the wake properties and span-wise vortex evolution in in case of FA technique than ZNMF technique. Figures 5.20 and 5.23 present the flow and vortex dissipation pattern in the wake of the backward step with ZNMF and FA technique applied at f=0.065 and A=0.1. Flow pattern and random vortex dissipation in the wake of the step remain similar to figure 5.13 at Re=1024000 without any AFC technique applied to the backward step and also for Re=512000. The random dissipation in the wake can also be seen in swirl and X-vorticity plots in figures 5.21 and 5.24 due to high Reynolds number of the flow leading to greater kinetic energy and wake shear layer interactions.

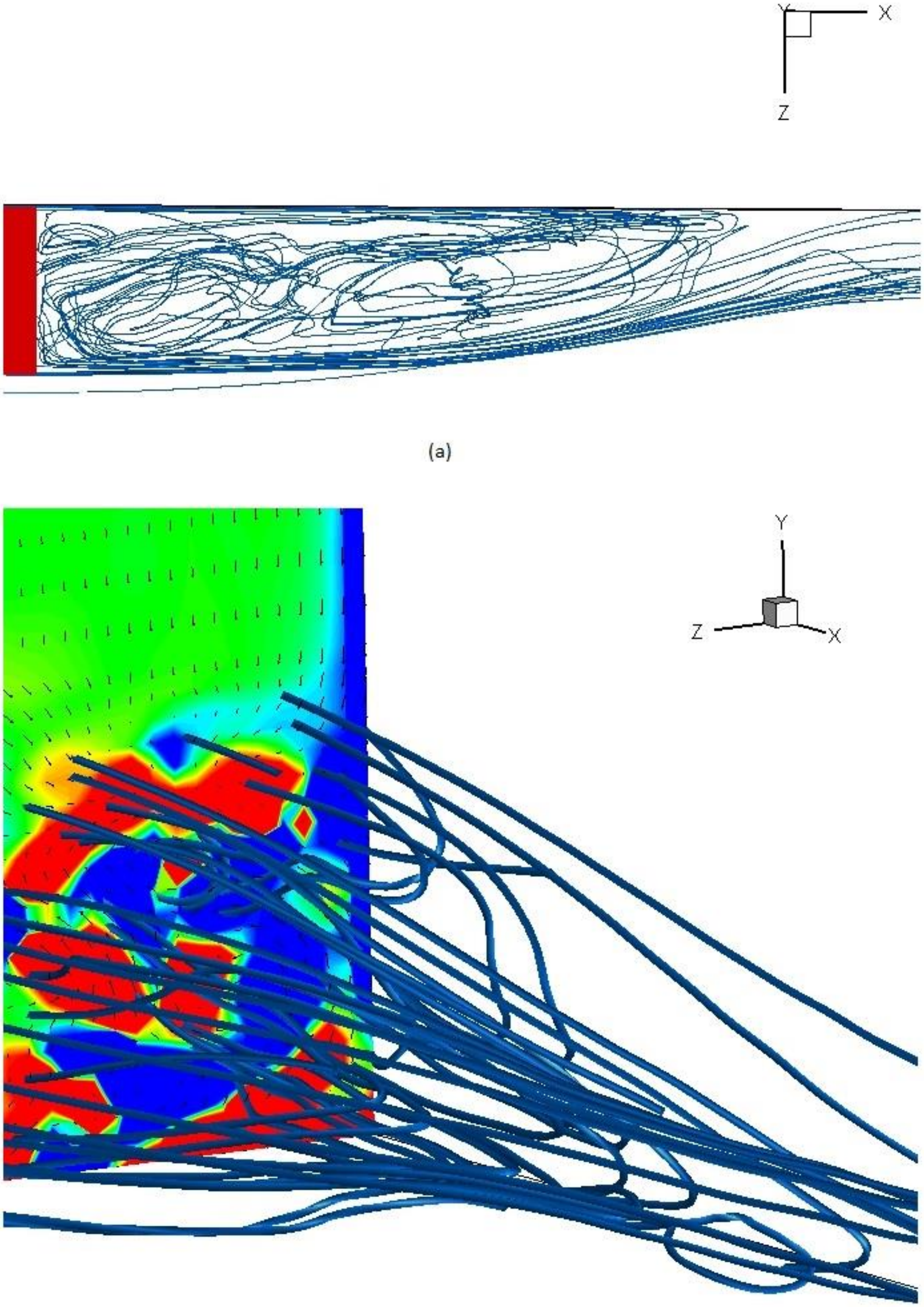

Figure 5.17: Streamline plots of flow over backward step with ZNMF technique at Re=1024000, f=0.055 and A=0.1 (a) Top View (b) Side View

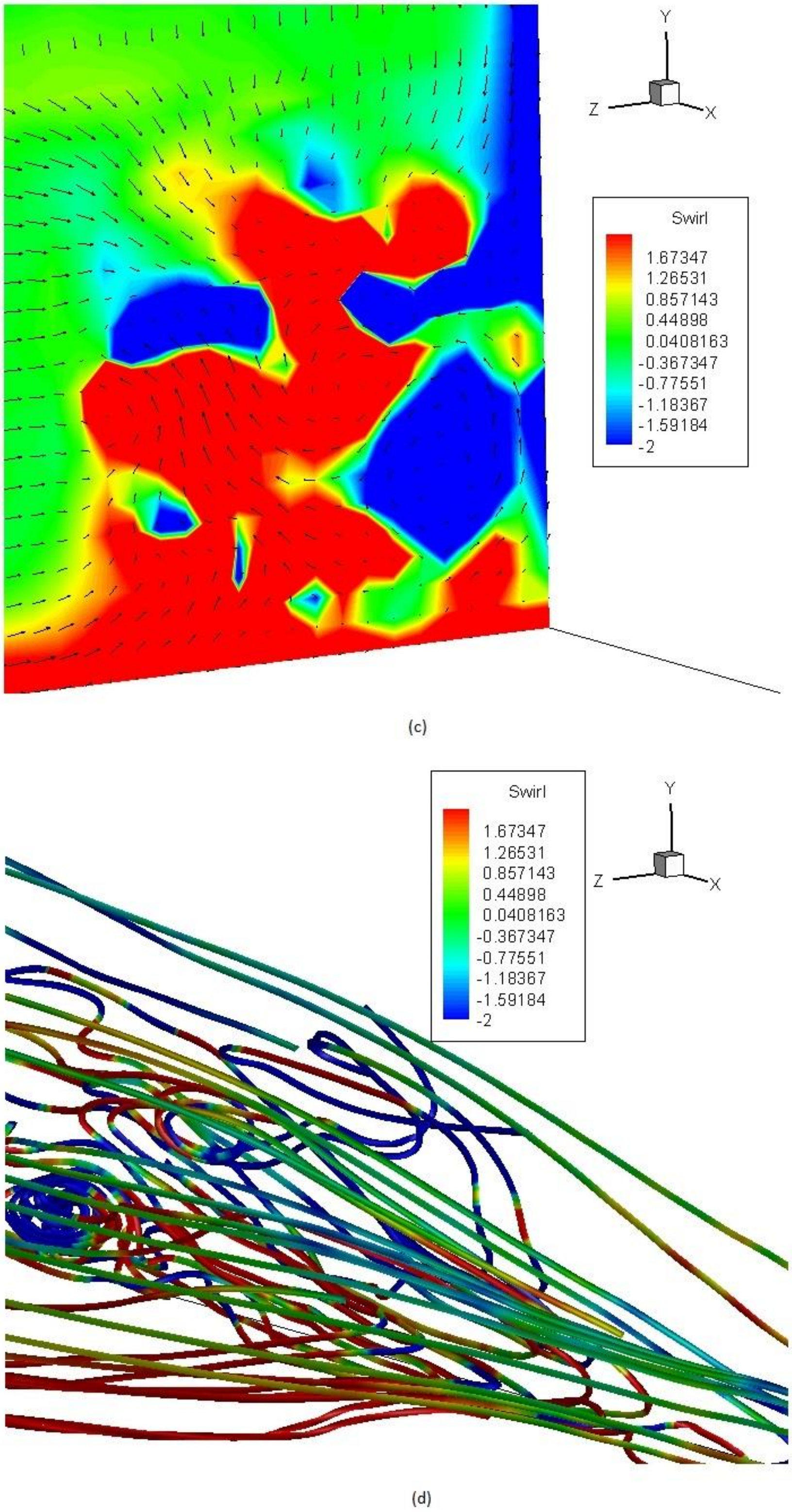

Figure 5.17: Side View of flow over backward step with ZNMF technique at Re=1024000, f=0.055 and A=0.1 (c) Instantaneous swirl contour plot with velocity vectors on YZ plane (d) Corresponding Streamline plot with swirl contour

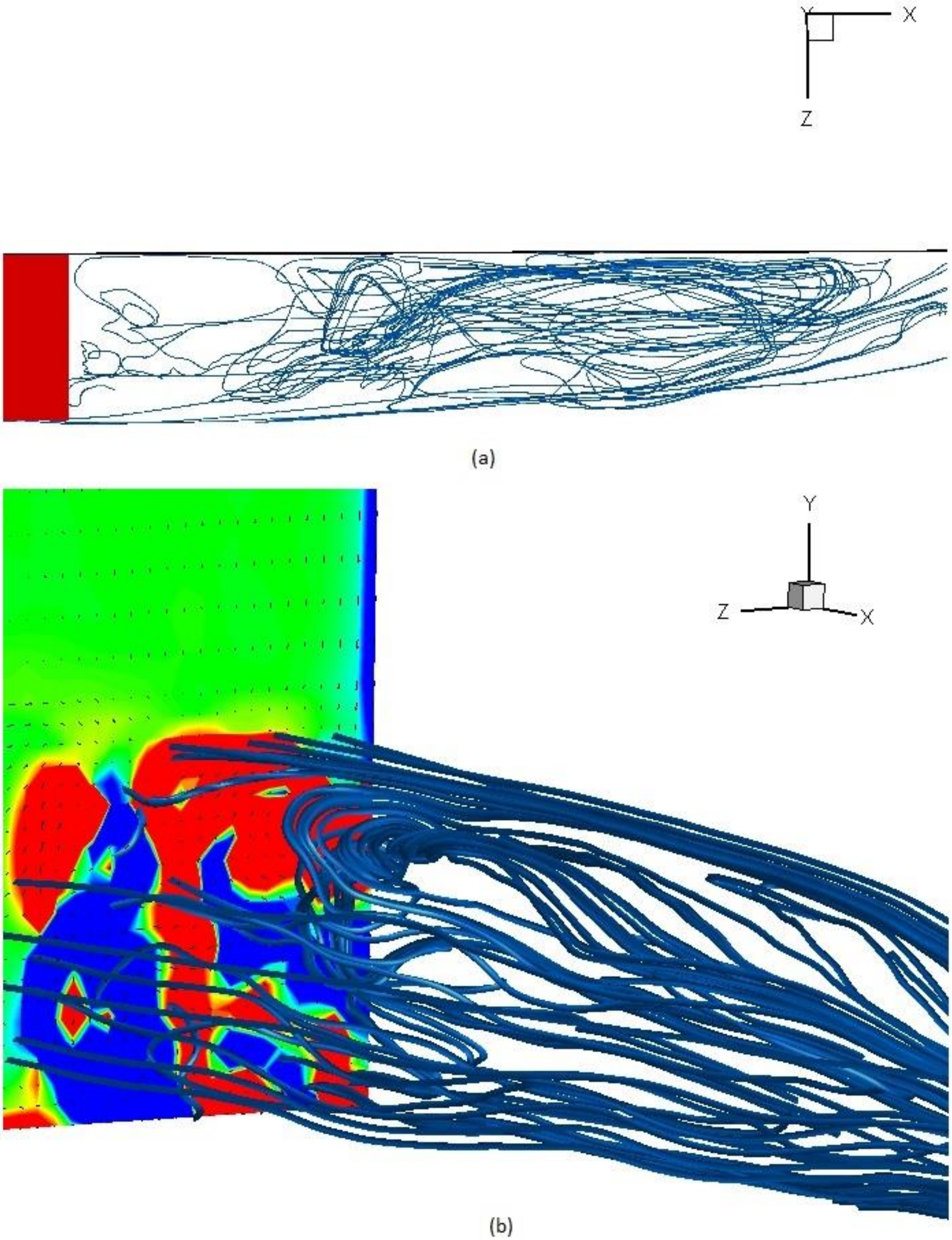

Figure 5.18: Streamline plots of flow over backward step with FA technique at Re=1024000, f=0.055 and A=0.1 (a) Top View (b) Side View

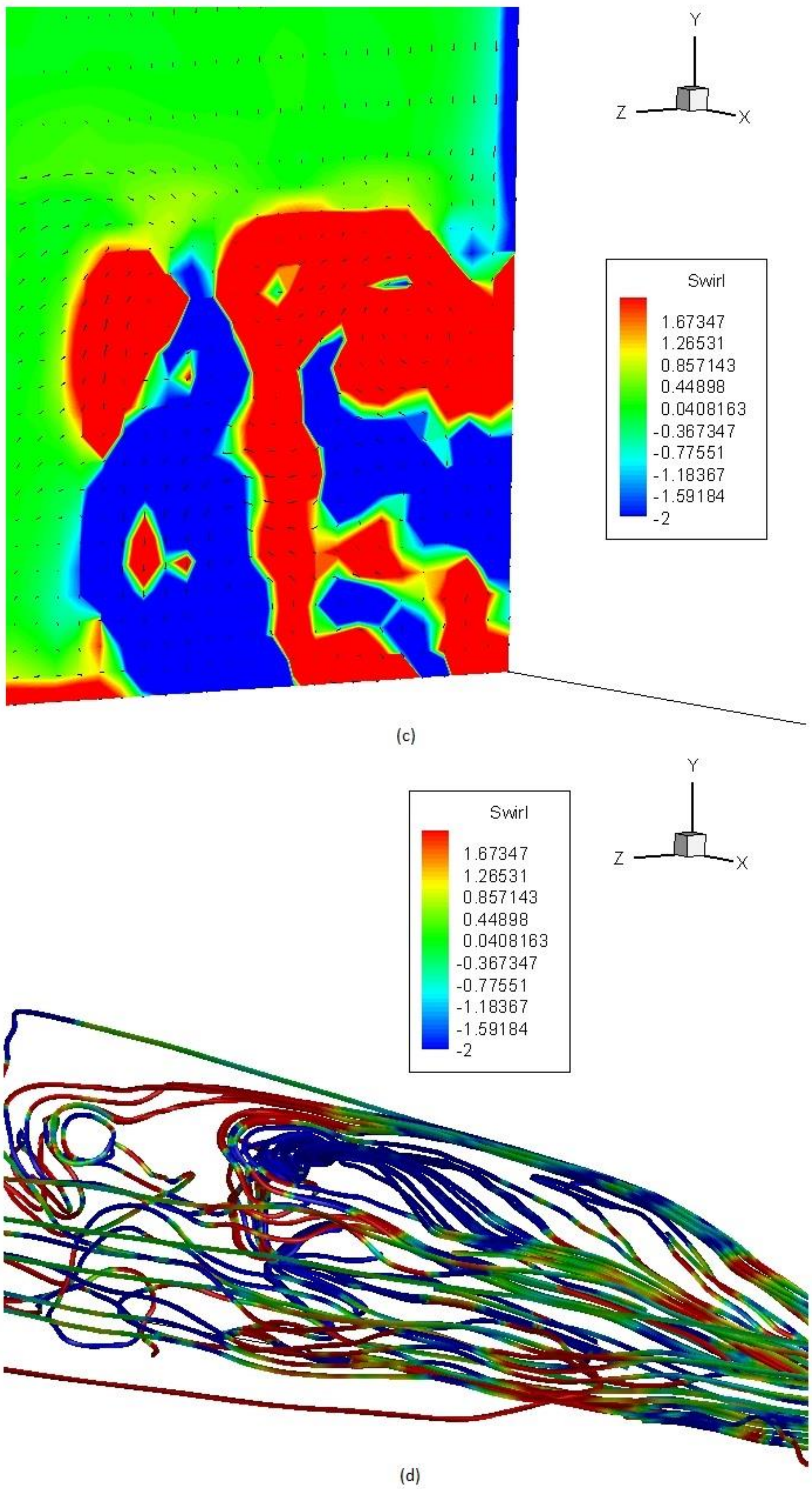

Figure 5.18: Side View of flow over backward step with FA technique at Re=1024000, f=0.055 and A=0.1 (c) Instantaneous swirl contour plot with velocity vectors on YZ plane (d) Corresponding Streamline plot with swirl contour

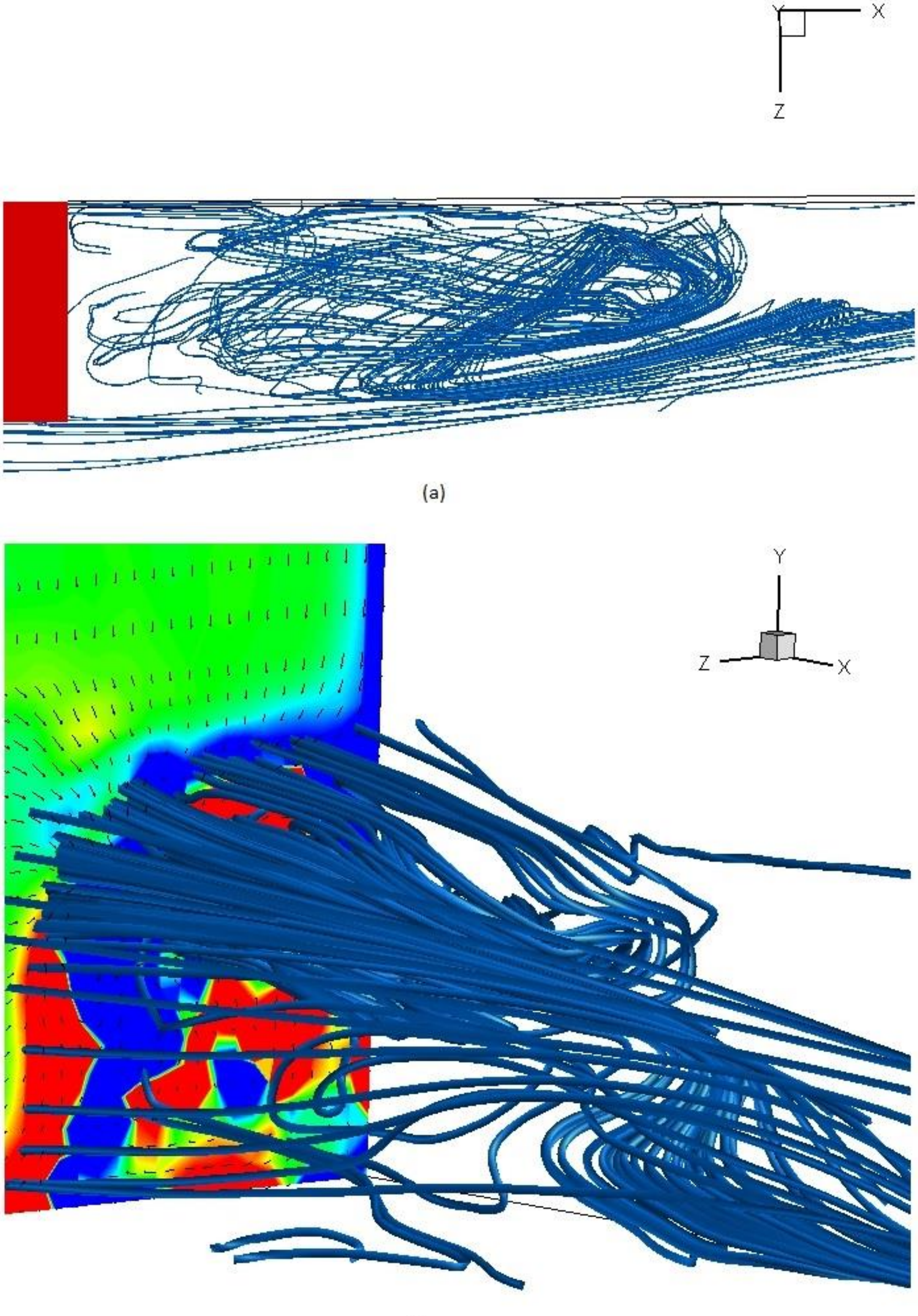

(a)

(b)

Figure 5.19: Streamline plots of flow over backward step with ZNMF technique at Re=1024000, f=0.065 and A=0.1 (a) Top View (b) Side View

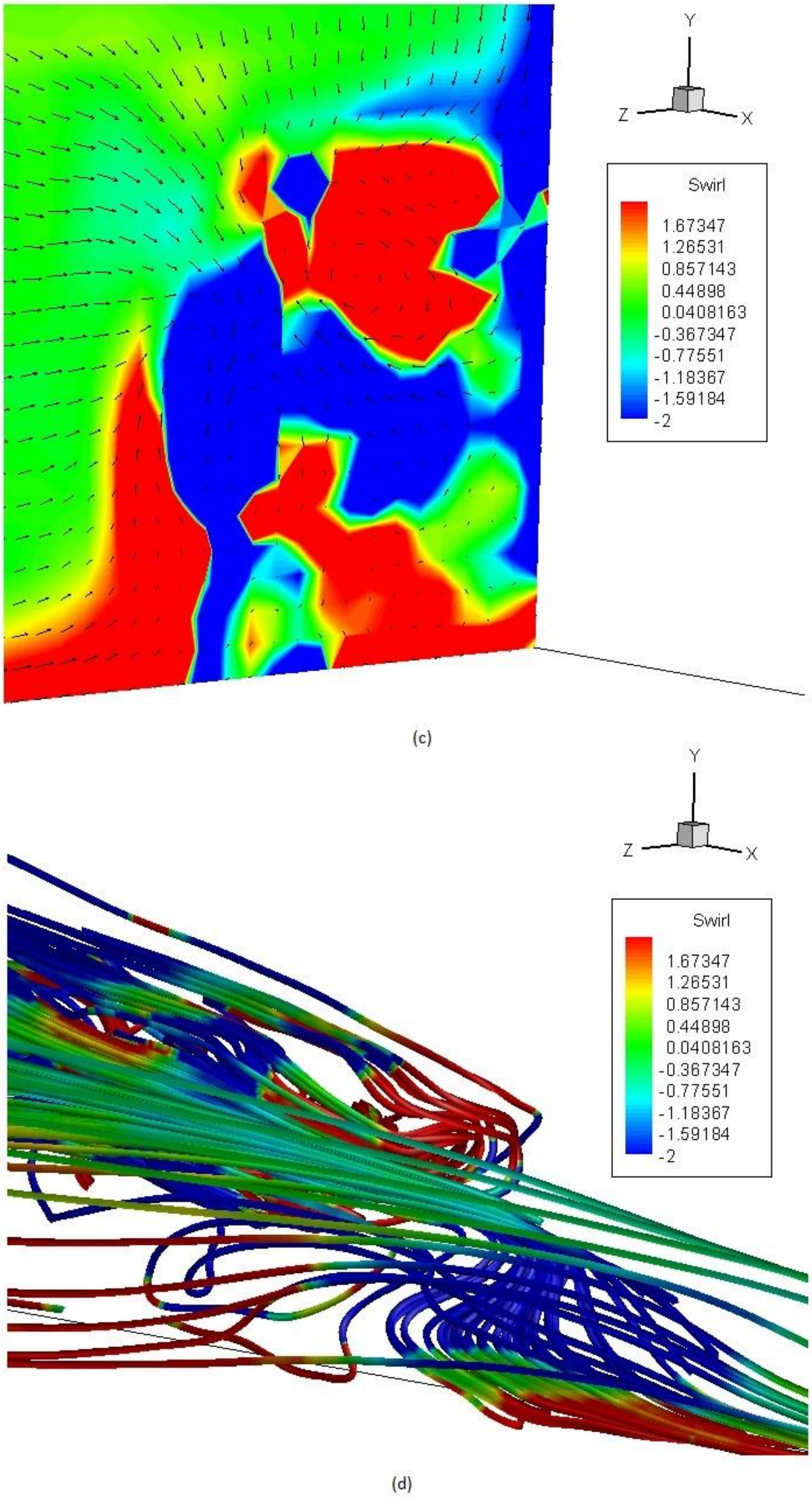

Figure 5.19: Side View of flow over backward step with ZNMF technique at Re=1024000, f=0.065 and A=0.1 (c) Instantaneous swirl contour plot with velocity vectors on YZ plane (d) Corresponding Streamline plot with swirl contour

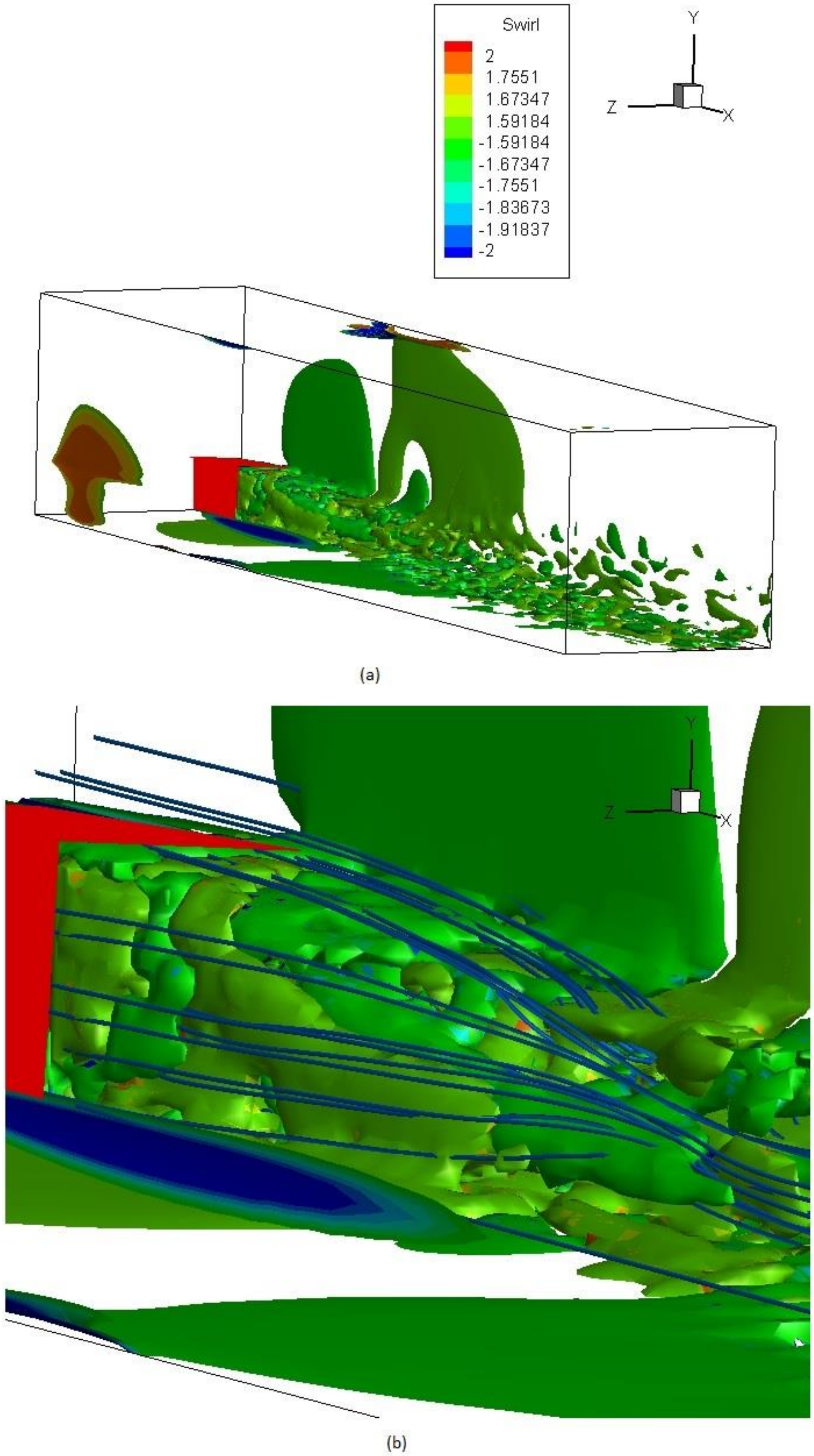

Figure 5.20: Flow over backward step with ZNMF technique at Re=1024000, f=0.065 and A=0.1 (a) Iso-Surface plots of Swirl contour (b) Close-up of wake of the backward step with Streamlines

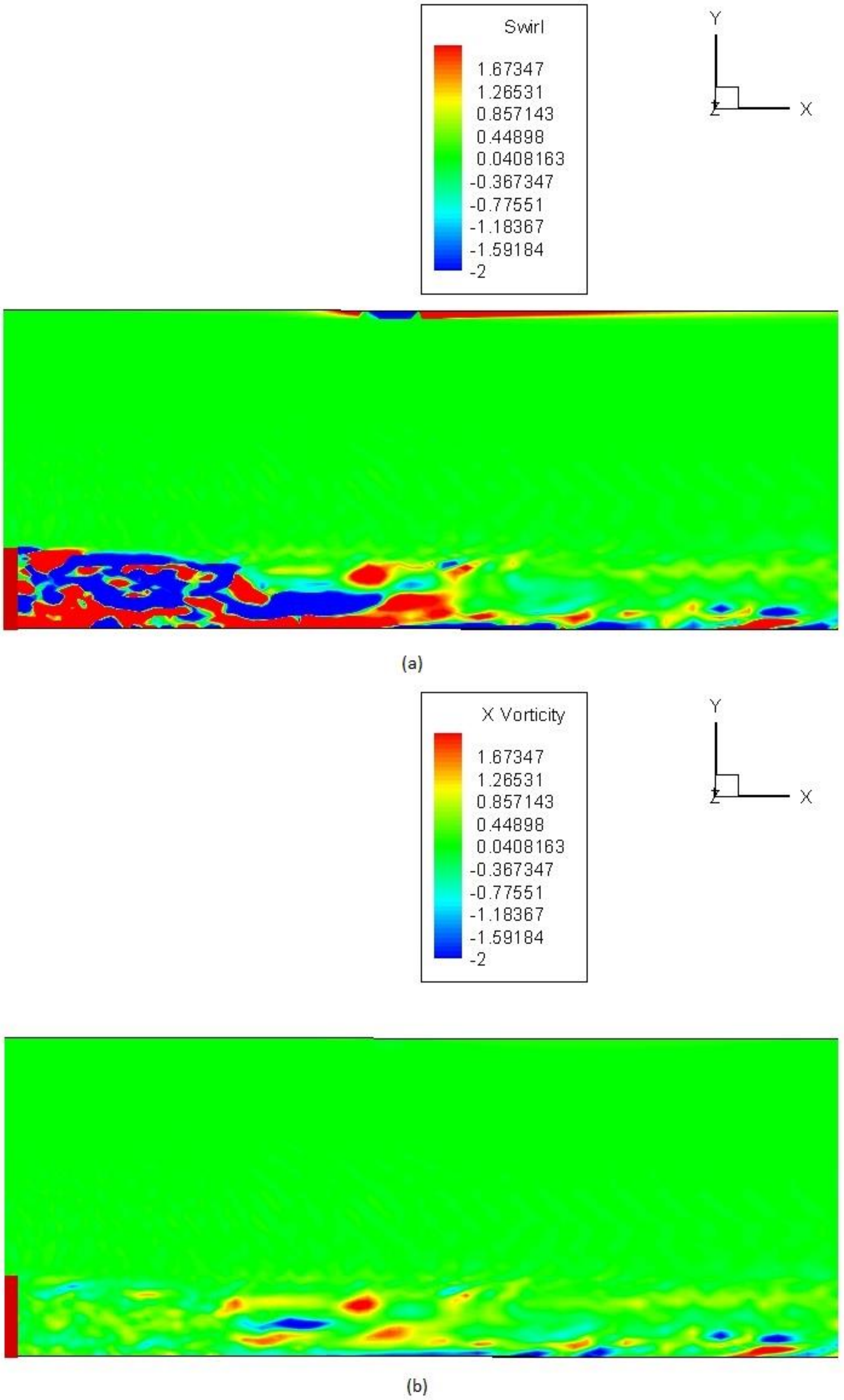

Figure 5.21: Side View of flow over backward step at Re=1024000 with ZNMF technique at Re=1024000, f=0.065 and A=0.1 on XY plane at z=0.5 (a) Instantaneous Swirl contour plot (b) Instantaneous X-Vorticity contour plot with velocity vectors

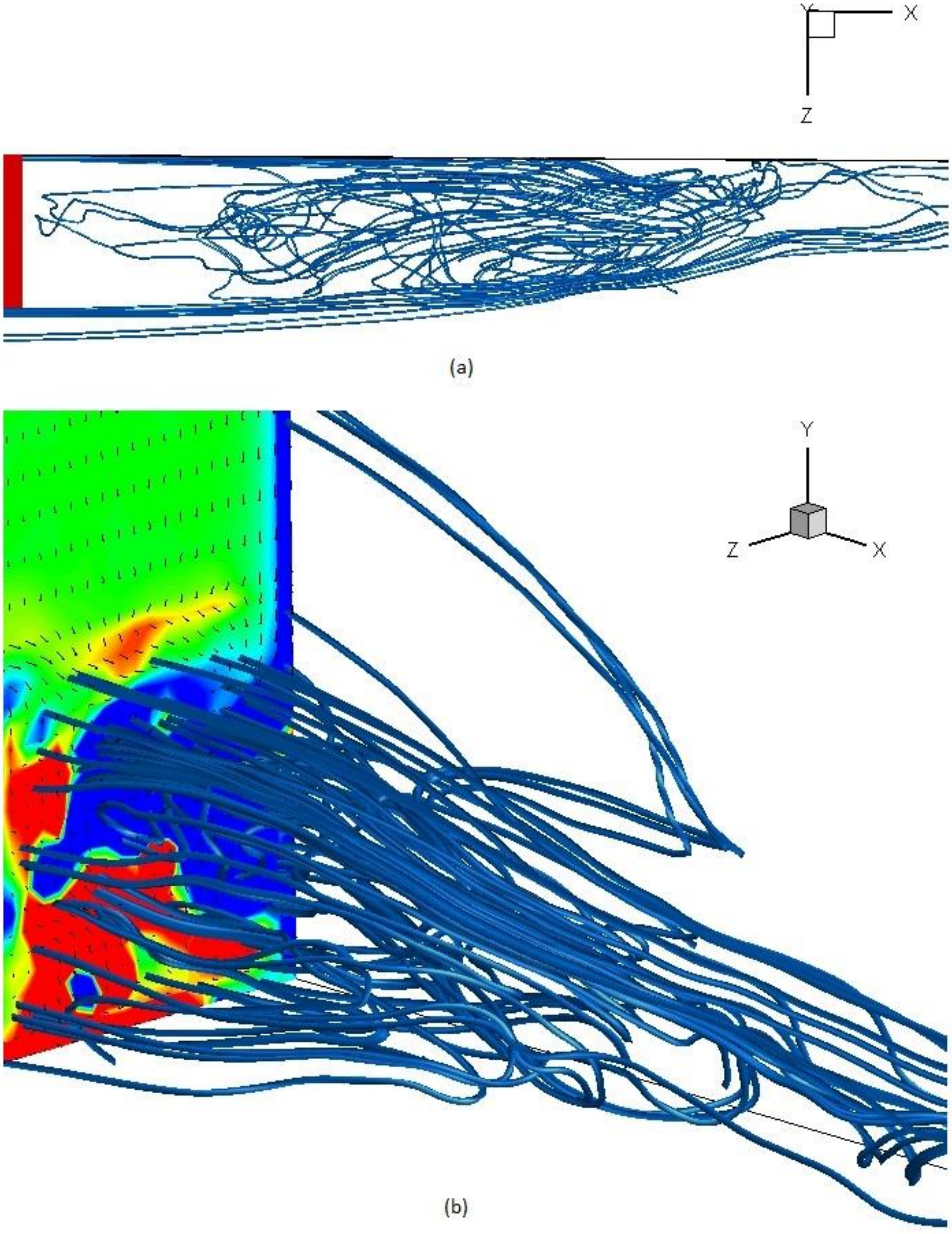

Figure 5.22: Streamline plots of flow over backward step with FA technique at Re=1024000, f=0.065 and A=0.1 (a) Top View (b) Side View

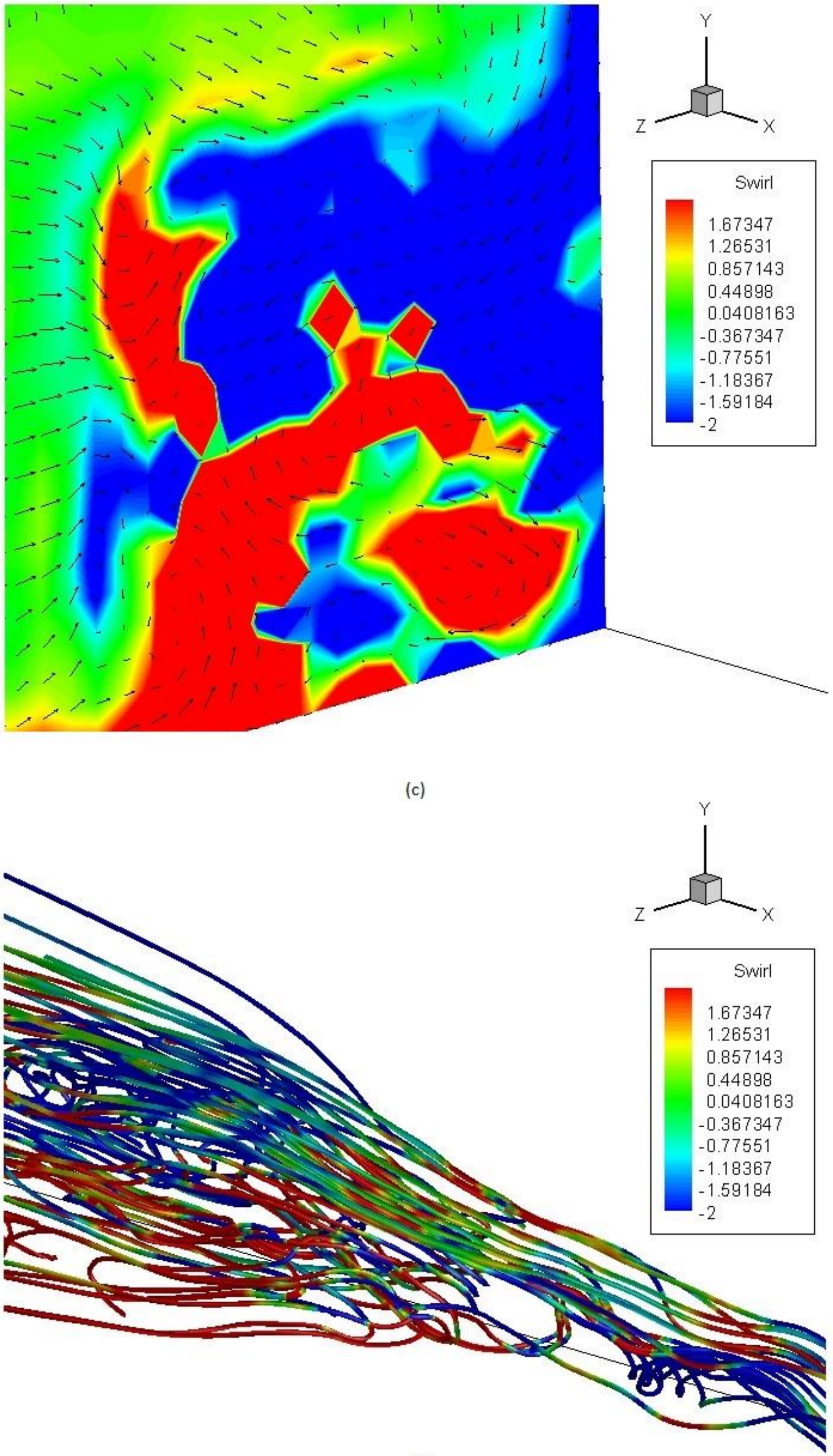

Figure 5.22: Side View of flow over backward step with FA technique at Re=1024000, f=0.065 and A=0.1 (c) Instantaneous swirl contour plot with velocity vectors on YZ plane (d) Corresponding Streamline plot with swirl contour

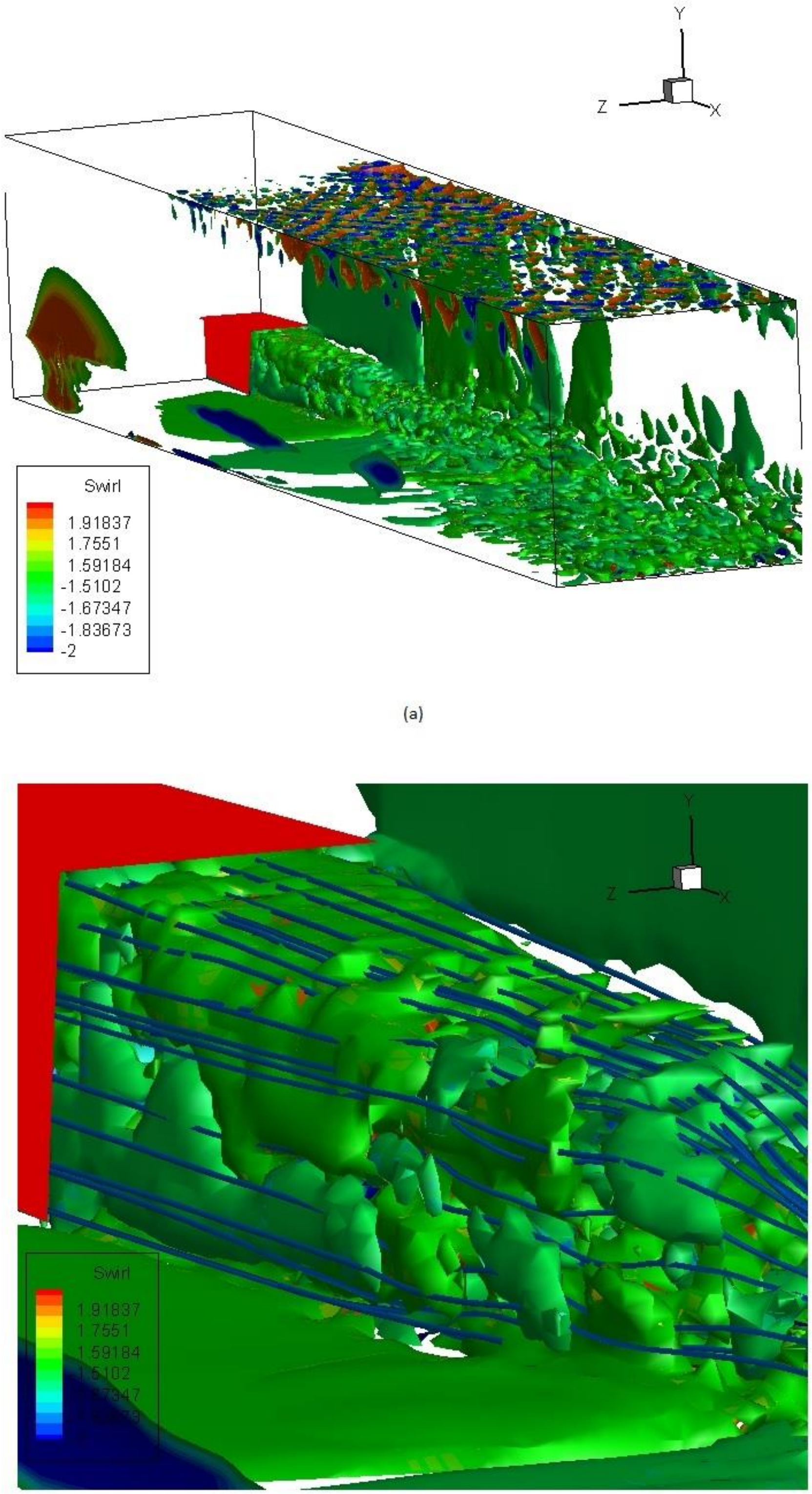

(a)

(b)

Figure 5.23: Flow over backward step with FA technique at Re=1024000, f=0.065 and A=0.1 (a) Iso-Surface plots of Swirl contour (b) Close-up of wake of the backward step with Streamlines

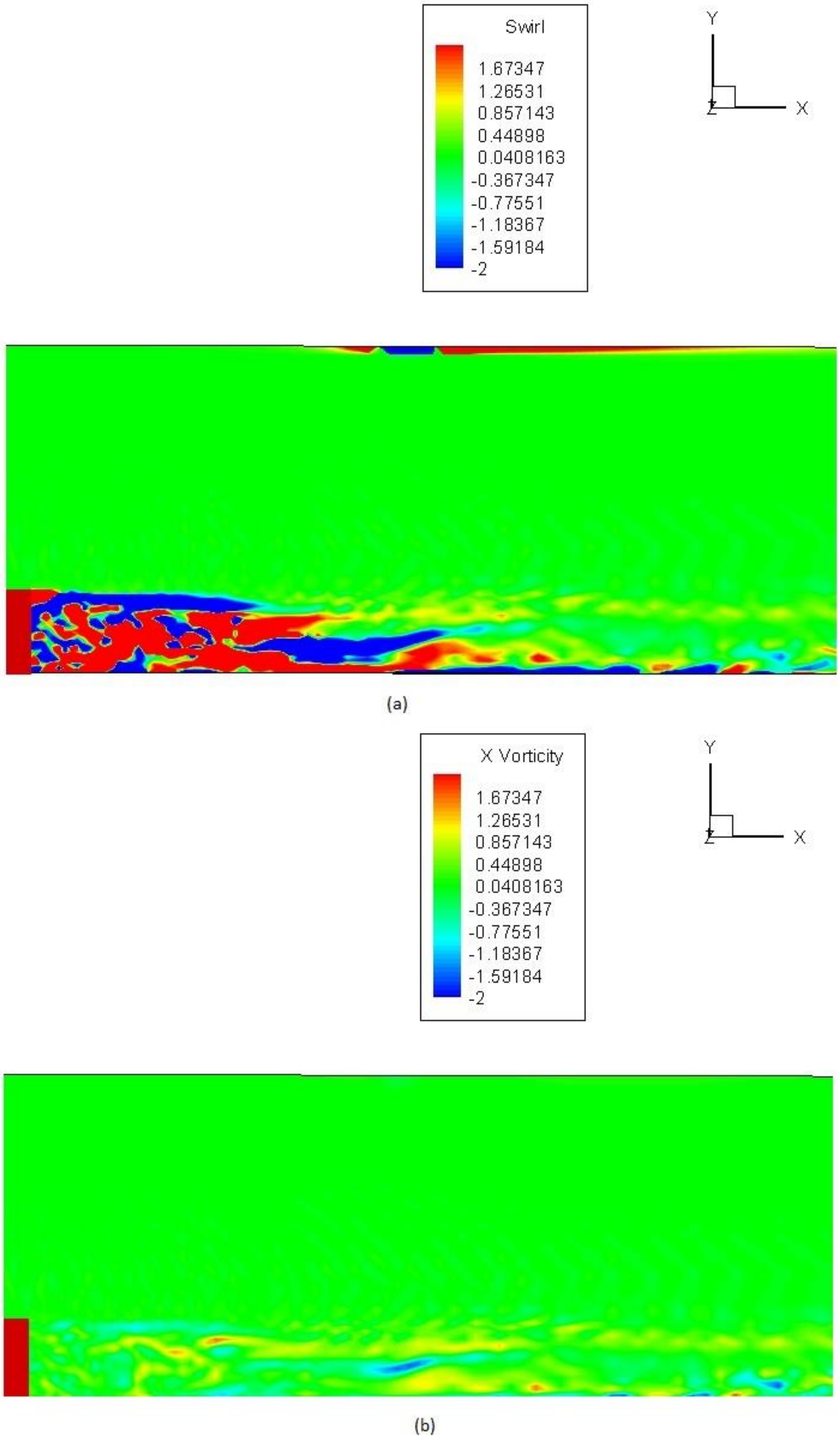

Figure 5.24: Side View of flow over backward step at Re=1024000 with FA technique at Re=1024000, f=0.065 and A=0.1 on XY plane at z=0.5 (a) Instantaneous Swirl contour plot (b) Instantaneous X-Vorticity contour plot with velocity vectors

5.3.3 Average Drag and Lift coefficients:

Table 1 presents drag and lift coefficient acting on the backward step at Re=512000 when actuated with AFC jet at the natural dissipating frequency, f=0.055. It can be seen that with application of ZNMF technique the drag acting on the body is 61.7% smaller when compared to FA technique and this can be attributed to decrease in pressure acting on the rear face of the backward step. The change in lift coefficient in negligible due to minor variation in pressure on the top surface of the backward step as the AFC groove is placed on the side surface of the step.

Re=512000	**ZNMF**	**FA**
C_D	**0.0141**	**0.0228**
C_L	**-0.1807**	**-0.1809**

Table 1: Drag and Lift co-efficient of Backward step at Re=512000 with f=0.055 and A=0.1

Re=1024000	**ZNMF**	**FA**
C_D	**0.0185**	**0.0286**
C_L	**-0.1778**	**-0.1714**

Table 2: Drag and Lift co-efficient of Backward step at Re=1024000 with f=0.065 and A=0.1

Table 2 presents the drag and lift coefficient acting on the backward step at Re=1024000 when actuated with AFC jet at the natural dissipating frequency, f=0.055. It can be seen that with application of ZNMF technique the drag acting on the body is 54.59% smaller when compared to FA technique and this can be attributed to decrease in pressure acting on the rear face of the backward step. The change in lift coefficient in this case also is negligible due to minor variation in pressure on the top surface of the backward step as the AFC groove is placed on the side surface of the step. It can be concluded that drag acting on the body is minimum when ZNMF technique is applied on the backward step. The groove can also be placed on the top surface of the step to alter the lift acting on the body and this study can be of further analysis with applications in aircraft wings and automobile performance.

5.4. Conclusions:

- It was observed that a recirculation region is formed in the wake of the step behind the rear face of the backward step and length of the recirculating region increases with Reynolds number of the flow.
- The evolution and development of the span-wise vortex due to the interaction of the shear layers in the wake of the step and the onset of span-wise vortex was found to be Re=6400.
- The shear layer interactions and vortex dissipation increases with increase in Reynolds number leading to more random dissipation at higher Reynolds number.
- ZNMF technique was found to be more effective in suppression of span-wise vortex evolution than FA technique especially at higher Reynolds number, Re=1024000
- FA technique is more effective when flow is actuated at the natural dissipating frequency for suppressing the span-wise vortex.
- The drag acting on the step is much smaller in case of ZNMF technique than FA technique applied on the side of the backward step.
- The variation in lift acting was found to be between ZNMF and FA due to the minor variation in pressure acting on the top surface.

References:

Aider JL; Beaudoin JF; Wesfreid JE; (2010). Drag and lift reduction of a 3D bluf-body using active vòrtex generators. Exp. Fluids 48: 771-789.

Aubrun S; McNally J; Alvi F; Kourta A. (2011). Separation flow control on a generic ground vehicle using steady microjet arrays. Exp. Fluids. 51:1177-1187.

Aubrun S; Alvi F; Leroy A; Kourta A. (2010). Active flow control of the 3D separation on a Ahmed body using steady microjets arrays. Proceedings of the ASME 3rd joint US-European fluids engineering summer meeting and 8th international conference on nanochannels, microchannels and minichannels. FEDSM-ICNMM2010, August 1-5, Montreal, Canada.

Avdis A; Lardeau S; Leschziner M. (2009). Large Eddy Simulation of Separated Flow over a two-dimensional hump with and without control by means of a synthetic jet. Flow Turbulence Combust. 83:343-370.

Barsotti DL; Boetcher SKS. (2013). Optimizing jets for active wake control of ground vehicles. Proceedings of the ASME 2013 International mechanical engineering congress and exposition IMECE2013 November 15-21 San Diego, USA.

Bruneau CH; Creusé E; Depeyras D; Gilliéron P; Mortazavi I. (2010). Coupling active and passive techniques to control the flow past the square back Ahmed body. Computers & Fluids 39: 1875-1892.

Bruneau CH; Creusé E; Depeyras D; Gilliéron P; Mortazavi I. (2012). Active and passive flow control around simplified ground vehicles. Journal of Applied Fluid Mechanics 5; 1: 89-93.

Bruneau CH; Creusé E; Depeyras D; Gilliéron P; Mortazavi I. (2012). Numerical simulation and control of the flow around one or two Ahmed bodies. Proceedings of the ASME fluids engineering summer meeting FEDSM2012 July 8-12, Rio Grande, Puerto Rico.

Bruneau CH; Creusé E; Gilliéron P; Mortazavi I. (2014). Effect of vortex dynamics on the drag coefficient of a square back Ahmed body: Application to the flow control. European Journal of Mechanics B/Fluids. 45: 1-11.

Bruneau CH; Khadra K; Mortazavi I. (2013). Analysis and active control of the flow around two following Ahmed bodies. Proceedings of the ASME fluids engineering division summer meeting FEDSM2013 July 7-11, Incline Village, Nevada, USA.

Brunn A; Nitsche W. (2006). Active control of turbulent separated flows over slanted surfaces. International Journal of Heat and Fluid Flow 27: 748-755.

Cerretelli C; Kirtley K. (2009). Boundary layer separation control with fluidic oscillators. Journal of Turbomachinery. 131: 041001.

Chabert T; Dandois J; Garnier E. (2014). Experimental closed-loop control of flow separation over a plain flap using slope seeking. Exp. Fluids. 55:1797.

Cherry NJ; Hillier R; Latour MEMP. (1984). Unsteady measurements in a separated and reattaching flow. J Fluid Mech. 144: 13-46.

Dandois J; Garnier E; Sagaut P. (2007). Numerical simulation of active separation control by a synthetic jet. J Fluid Mech. 574: 25-58.

Heinemann T; Springer M; Lienhart H; Kniesburges S; Othmer C; Becker S. (2014). Active flow control on a 1:4 car model. Exp. Fluids 55:1738.

Joseph P; Amandolèse X; Aider JL. (2012). Drag reduction on the 25º slant angle Ahmed reference body using pulsed jets. Exp. Fluids 52:1169-1185.

Kourta A; Leclerc C. (2013). Characterization of synthetic jet actuation with application to Ahmed body wake. Sensors and Actuators 192: 13-26.

Krajnovic S; Basara B. (2010). LES of the flow around Ahmed body with active flow control. M. Deville, TH Lê and P. Sagaut (Eds.): Turbulence and Interactions, NNFM 110: 247-254.

Krajnovic S; Fernandes J. (2011). Numerical simulation of the flow around a simplified vehicle model with active flow control. International Journal of Heat and Fluid Flow. 32: 192-200.

Krentel D; Nitsche W. (2013). Investigations on active drag control on a bluf body with cross-wind. A. Dillmann et al. (Eds.). New Results in Numer & Exp. Fluid Mech. NNFM121: 177-184.

Krentel D; Muminovic R; Brunn A; Nitsche W; King R. (2010). Application of active flow control on genèric 3D car models. R King (Ed.): Active Flow Control II, NNFM 108: 223-239.

Kumar Singh D; Bandyopadhyay G. (2012). Active flow control over a car. Applied Mechanics and Materials. 110; 116: 2521-2528.

Leclerc C; Levallois E; Gallas Q; Gilliéron P; Kourta A. (2006). Phase locked analysis of a simplified car geometry wake flow control using synthetic jet. Proceedings of FEDSM2006 ASME joint US-European Fluids Engineering summer Meeting. July 17-20 Miami USA.

Lehugeur B; Gilliéron P. (2006). Active control of vortex breakdown phenomenon in the wake of a simplified car geometry. Proceedings of FEDSM2006 ASME joint US-European Fluids Engineering summer Meeting. July 17-20 Miami USA.

Lehugeur B; Gilliéron P; Ivanic T. (2006). Contribution de l'éclatement tourbillonnaire à la réduction de la traînée des véhicules automobiles: approche numérique. C.R. Mecanique 334: 368-372.

Lehugeur B; Gilliéron P; Bobillier P. (2008). Contrôle des structures tourbillonnaires longitudinales dans le sillage d'une géométrie simplifiée de véhicule automobile: Approche expérimentale. Mécanique & Industries 9: 533-541.

Mestiri R; Ahmed-Bensoltane A; Keirsbulck L; Aloui F; Labraga L. (2014). Active flow control at the rear end of a Generic car model using steady blowing. Journal of Applied Fluid Mechanics, 7; 4: 565-571.

Metka M. (2013). Flow control on the Ahmed body vehicle model using fluidic oscillators. Proceedings of the ASME 2013 International mechanical engineering congress and exposition IMECE2013, November 15-21 San Diego USA.

Newmann J; Wengle H. (2004). LES of controlled turbulent flow over a rounded step. R. Friederich et al. (Eds). Direct and Large-Eddy Simulation V. 557-564.

Park H; Cho JH; Lee J; Lee DH; Kim KH. (2013). Experimental study on synthetic jet array for aerodynamic drag reduction of a simplified car. Journal of Mechanical Science and Technology 27; 12: 3721-3731.

Parkin DJ; Thomson MC; Sheridan J. (2014). Numerical analysis of bluf body wakes under periodic open-loop control. J. Fluid Mech. 739: 94-123.

Rouméas M; Gilliéron P; Kourta A. (2006). Analysis and control of near-wake flow on a simplified car geometry. Proceedings of FEDSM2006 ASME joint US-European fluids engineering summer meeting, July 17-20 Miami, USA.

Rouméas M; Gilliéron P; Kourta A. (2008). Separated flows around the rear window of a simplified car geometry. Journal of Fluids Engineering 130: 021101

Rouméas M; Gilliéron P; Kourta A. (2009). Drag reduction by flow separation control on a car after body. Int. J. Numer. Meth. Fluids. 60: 1222-1240.

Rouméas M; Gilliéron P; Kourta A. (2009). Analysis and control of the near-wake flow over a square-back geometry. Computers & Fuids 38: 60-70.

Suzuki T. (2006). Effects of a synthetic jet acting on a separated flow over a hump. J Fluid Mech. 547: 331-359.

Tounsi N; Mestiri R; Keirsbulck L; Oualli H; Hanchi S; Aloui F. (2016). Experimental study of flow control on bluff body using piezoelectric actuators. Journal of Applied Fluid Mechanics, 9; 2: 827-838.